Università degli Studi di Padova
Dipartimento di Fisica e Astronomia "Galileo Galilei"

CORSO DI DOTTORATO DI RICERCA IN FISICA
CICLO XXX

Nuclear structure of the semi-magic tin isotopes close to ^{100}Sn: lifetime measurements of low-lying states in ^{106}Sn and ^{108}Sn

Tesi redatta con il contributo finanziario dei Laboratori Nazionali di Legnaro

Coordinatore: Ch.mo Prof. Gianguido Dall'Agata

Supervisori: Dott. José Javier Valiente Dobón
Dott. Alain Goasduff

Dottorando: Marco Siciliano

Abstract

The structure of nuclei with few nucleons outside the double-shell closure $Z = N = 50$ has attracted large theoretical and experimental interest in the last years. Several studies were performed in this region to examine the evolution of the nucleon-nucleon interaction when going towards ^{100}Sn and eventually deduce the proton shell closure. Along the Sn isotopic chain, the excitation energies of the first 2^+ and 4^+ states are well known and rather constant. On the contrary, the $B(E2; 2^+ \to 0^+)$ transition strengths follow a kind of bell-shape behaviour. If a generalized seniority scheme is naïvely considered, the *a priori* expectation is an inverted parabola showing the maximum collectivity at mid-shell and smoothly decreasing towards the shell closures $N = 50, 82$. However, such simplistic prediction does not reproduce the experimental results. In fact, for the neutron-deficient Sn isotopes the experimental $B(E2; 2^+ \to 0^+)$ values, even if they suffer from large experimental uncertainties, seem to have a smoother trend that is almost constant for $104 \leq A \leq 112$. In addition, for such neutron-deficient region there is a lack of information on the $B(E2; 4^+ \to 2^+)$ values, whose knowledge would make a more robust physical interpretation when approaching $N = 50$. Since now theoretical calculations have been performed during the last decades, but up to date none of them is able to reproduce consistently the trend of the experimental reduced transition probabilities for the full Sn isotopic chain.

Despite fusion-evaporation reactions are appropriate for the population and the investigation of neutron-deficient nuclei, the presence of the 6^+ seniority isomers in even-even Sn isotopes prevents the measurement of the direct lifetime of the low-lying 2^+ and 4^+ states. Thus, until now the information on the $B(E2; 2^+ \to 0^+)$ in this region has been obtained only via safe or relativistic Coulomb excitation measurements, which allow a direct population of the low-lying states of interest.

The experiment discussed in this thesis was devoted to the measurement of the lifetimes of the low-lying states 2^+ and 4^+ for ^{106,108}Sn, in order to derive the reduced transition probabilities $B(E2)$, by using the Recoil Distance Doppler-Shift (RDDS) method. In order to overcome the problems mentioned above, the nuclei of interest were populated via multi-nucleon transfer reaction where a ^{106}Cd beam, provided by one separated-sector cyclotron of the GANIL facility (France) at the energy of 770 MeV, impinged onto a 0.715 mg/cm^2 thick ^{92}Mo target. After the target a 1.6 mg/cm^2 thick ^{24}Mg foil was used as degrader for

slowing down the reaction products: because of the two different velocities of the recoils, for every γ-ray transition two components were present in the Doppler-corrected energy spectrum and the ratio between their area depends on the target-degrader distance and on the lifetime of the state. This measurement is complementary to the Coulomb excitation method and it represents the very first direct lifetime measurement in the neutron-deficient Sn isotopes.

The complete identification of the reaction products was obtained on an event-by-event basis using the VAMOS++ magnetic spectrometer. In coincidence with VAMOS++, γ rays were detected by 8 AGATA Triple Clusters, placed at backward angles in a compact configuration. The AGATA spectrometer is a γ-tracking array, which relies on Pulse Shape Analysis (PSA) for the identification of the interaction points and on γ-ray tracking algorithm for the reconstruction of the interaction path through the detectors. During the analysis, large efforts were devoted to the analysis of AGATA in order to restore and push the capabilities of the apparatus. Thanks to the combination of the magnetic spectrometer together with the choice of the reaction mechanism, it was also possible to reconstruct the Q-value of the reaction. Such information was crucial for the success of the lifetime measurement because it allowed to control the feeding from higher-lying states. Then, by combining the information of the first interaction point in the AGATA detectors, provided by the γ-ray tracking algorithm, with the recoil velocity vector determined by VAMOS++, the Doppler correction of the γ rays emitted in-flight can be performed on a event-by-event basis. Because of the crucial importance of the γ-ray energy resolution for the RDDS method, particular attention was devoted to the improvement of the Doppler correction. The experimental method was validated by remeasuring the known lifetime of the first 2^+ state in ^{106}Cd and ^{104}Cd, obtaining $\tau(2^+) = 10.4(2)$ ps and $\tau(2^+) = 8.0(5)$ ps, respectively. The two results are in agreement with the adopted literature values and they have a smaller error.

Finally, due to the power of this experimental setup, it was possible to measure the lifetimes of the 2^+ and 4^+ excited states for ^{106,108}Sn. In order to reduce the error, for ^{108}Sn several tests on both Decay-Curve Method (DCM) and Differential Decay-Curve Method (DDCM) will be discussed, where the final results are $\tau(4^+) = 3.7(2)$ ps and $\tau(2^+) = 0.76(8)$ ps (adopted literature $\tau(2^+) = 0.69(17)$ ps). For ^{106}Sn, instead, the lifetime of the low-lying excited states was extracted only via DCM and it resulted in $\tau(4^+) = 5.2(39)$ ps and $\tau(2^+) = 1.3(7)$ ps.

The reduced transition probabilities $B(E2)$, deduced from the measured lifetimes, were compared with Large-Scale Shell-Model (LSSM) calculations. Such basic nuclear feature have proved to be incredibly sensitive to the form of the wave function: in particular the new $B(E2; 4^+ \to 2^+)$ value of ^{108}Sn clearly showed that high seniority components of the wave function are of extreme importance to define the transition probabilities in this region. This result questions the validity of other theoretical predictions, which have been considering the seniority truncation, in reproducing consistently the trend of the experimental $B(E2)$ values. In addition, the comparison of the experimental results with the LSSM calculation pointed out the possible presence of a small isovector component in the effective charges, that is in agreement with other measurements in the region. However, the origin of such component is an open question because, even if all the $0\hbar\omega$ excitations in the valence space have been taken into account, also some truncations have been applied to the valence space considered in the LSSM calculations. Further experimental and theoretical insight will be required to fully address this last observation.

Contents

1. Introduction 9
- 1.1. The atomic nucleus . . . 10
  - 1.1.1. Nuclear Hamiltonian . . . 12
  - 1.1.2. Nuclear shell model . . . 13
  - 1.1.3. Effective interactions . . . 16
  - 1.1.4. M-scheme representation . . . 20
- 1.2. Seniority scheme . . . 21
- 1.3. Heavy-ion reactions . . . 23
  - 1.3.1. Coulomb excitation reactions . . . 24
  - 1.3.2. Multi-nucleon transfer reactions . . . 24
  - 1.3.3. Fusion-evaporation reactions . . . 28
- 1.4. Gamma-ray spectroscopy . . . 31
  - 1.4.1. Electromagnetic transitions in atomic nuclei . . . 31
  - 1.4.2. Internal conversion . . . 34
  - 1.4.3. Gamma-ray detection: interaction of radiation with matter . . . 36
- 1.5. What is known along Z=50 . . . 40
  - 1.5.1. Physical motivation of the experiment . . . 43
  - 1.5.2. The experiment . . . 43

2. Experimental Setup 45
- 2.1. The GANIL accelerator complex . . . 45
- 2.2. AGATA spectrometer . . . 46
  - 2.2.1. Pulse shape analysis . . . 50
  - 2.2.2. Tracking . . . 53
- 2.3. VAMOS spectrometer . . . 55
  - 2.3.1. Multi-wire entrance detector . . . 56
  - 2.3.2. Focal plane detector setup . . . 58
  - 2.3.3. Event reconstruction . . . 59
- 2.4. Differential plunger device . . . 60

3. Presorting and Calibration **65**
3.1. AGATA spectrometer 65
3.1.1. Energy calibration 65
3.1.2. Cross-talk correction 66
3.1.3. Dead and unstable segments 66
3.1.4. Time alignment 69
3.1.5. Pulse shape analysis 70
3.1.6. Neutron damage correction 71
3.1.7. Tracking 72
3.2. VAMOS spectrometer 74
3.2.1. Ionization chamber 74
3.2.2. Drift chambers 79
3.2.3. Multi-wire entrance detector 81
3.2.4. Multi-wire focal plane 82
3.3. Plunger device 84

4. Experimental Data Analysis **87**
4.1. Ion identification 87
4.1.1. Atomic number identification 88
4.1.2. Charge state identification 91
4.1.3. Atomic mass identification 94
4.1.4. Yields of beam-like recoils 94
4.2. Doppler correction 100
4.2.1. Energy loss inside VAMOS 101
4.2.2. AGATA position 102
4.3. Reconstructed Q-value 104
4.4. Recoil distance Doppler-shift method 105
4.4.1. Decay-curve method 105
4.4.2. Differential decay-curve method 108

5. Results from Lifetime Measurements **111**
5.1. Cadmium isotopic chain 111
5.1.1. ^{106}Cd 112
5.1.2. ^{104}Cd 114
5.2. Tin isotopic chain 118
5.2.1. ^{108}Sn 119
5.2.2. ^{106}Sn 124
5.2.3. Odd-mass Sn 126

6. Theoretical Interpretation **129**
6.1. B(E2) systematics along the Sn isotopic chain 129
6.2. Proton excitation across the Z=50 shell closure 131
6.3. Effect of seniority in LSSM calculations 134
6.3.1. Seniority-truncated predictions 135
6.4. Theoretical results and discussion 136

7. Conclusions and Further Perspectives **141**
7.1. Conclusions . . . 141
7.2. Future perspectives . . . 142

A. Optimisation of the Experiment **147**
A.1. Target: material and thickness . . . 148
A.2. Degrader: material and thickness . . . 151
A.3. Beam: energy . . . 154

B. Tracking Optimisation **155**

Bibliography **161**

List of Figures **175**

List of Tables **189**

1

Introduction

There's something that doesn't make sense. Let's go and poke it with a stick.

by Steven Moffat

In the last century atomic nuclei have been subject to many experimental studies aimed at investigating their structure and at understanding the reaction mechanism among them. Until recent years, the investigation was limited to stable nuclei, or nuclei close to stability, since stable targets and beams were available. Then, the availability of exotic or radioactive beams have enabled to study nuclei far from the valley of stability, creating new challenges for theoretical models and shedding light on a much larger region of the Segrè chart. Up to date about 3600 nuclei have been studied in laboratories, out of a total of more than 7000 estimated to exist in the universe. A similar effort has been put in place to build theoretical models to explain the nuclear realm. However, our limited knowledge of the nuclear interaction and the difficulties in dealing with a many body problem have prevented to achieve a unified description of the structural properties through the entire nuclear landscape. In absence of a unified theory, various models have been developed, based on effective interactions derived from experimental observations in specific regions of masses. As a consequence, predictions are mainly limited to systems a few nucleons away from experimentally observed nuclei, and extrapolations to exotic regions, far away from the valley of stability, suffer from large uncertainties.

Why has nuclear physics attract so much interest in the last century?
First of all, the nucleus is one of the building blocks of nature and understanding how protons and neutrons are bound together and what is the exact form of their interaction, is a main subject for fundamental physics. Then, since the nucleus is a many-body quantum system, it has also proven itself to be an effective quantum-physics laboratory, with a rich phenomenology. In addition, the information on nuclear structure is crucial for other fields of physics. For example, the understanding of stellar nucleosynthesis and of the astrophysical phenomena depends on the knowledge which can be achieved on very exotic nuclei, i.e. on nuclei with a large excess of protons or neutrons with respect to the stable ones. Finally, nuclear physics has also a large and direct impact to the society and the everyday life, from the production of energy to the nuclear medicine.

The last decade has witnessed both quantitative and qualitative progress in shell-model studies, which have resulted in a remarkable gain in our understanding of the structure of the nucleus. New effective nucleon-nucleon interactions have been constructed that contain both two- and three-body contributions. Information on the single-particle energies and two-body residual interactions can be derived from the experimental observables, such as single-particle energies, reduced transition probabilities and quadrupole moments [1], and it can be used to predict the structure of more complex nuclear configurations. Thus, experimental data are needed in order to make robust predictions. The structure of nuclei with few nucleons outside the double-shell closure $Z = N = 50$ has attracted large interest in the last years. Several studies were performed in this region to examine the robustness of the proton shell closure when $N = 50$ is approached.

The work presented in this thesis, based on an experiment performed at the Grand Accélérateur National d'Ions Lourds in Caen (France), is devoted to the investigation of the quadrupole correlations in the vicinity of the proton drip-line, by directly measuring the lifetime of low-lying states in neutron-deficient tin isotopes. The neutron-deficient tin isotopes were populated via multi-nucleon transfer reactions, providing a complementary method to the Coulomb excitation experiments performed until this work in this region.

The next sections will outline the physical motivations for the experiment and its relevance in the field of modern nuclear physics. In addition, the nuclear theories are introduced, focusing the attention on the features of nuclear shell-model approaches which are used in the interpretation of the experimental results. Furthermore, few concepts about reaction mechanisms, in particular multi-nucleon transfer, Coulomb-excitation and fusion-evaporation reactions, and the methods of γ-ray spectroscopy will be briefly described.

1.1. The atomic nucleus

The atomic nucleus is a many-body system of strongly-interacting fermions of two kinds: protons and neutrons. For the microscopic world the use of quantum field theory and perturbation methods has proved successful in providing an effective description of many phenomena. From the theoretical point of view, being a many-body system, the atomic nucleus should give origin to the same problems encountered in condensed-matter physics. On the other hand, there are fundamental differences which make it a much more difficult system to study. In fact, the fermions composing the nucleons have themselves an internal structure. The interaction between nucleons is thus much more complex than the electromagnetic force and many-body forces do play an important role in nuclear interactions. In addition, while in condensed-matter physics the system can be considered infinite and this provides possible approximations of the physics problem, nuclear systems are composed by a limited number of nucleons. Nonetheless, considering that modern nuclear interactions fit the nucleon-nucleon scattering data very well, at least the two-body part is well under control. Differently from the atomic case, the nucleons are not subject to a central field, since the nucleon-nucleon interaction is dominated by short-range components. However, the first experimental observations revealed a shell structure similar to the electrons in an atom, and it turned out that the structure of nuclei could be described by a shell model with a central mean field and a residual interaction between nucleons. As example of such experimental observation, Figure 1.1 represents the excitation energy of the first 2^+ state as

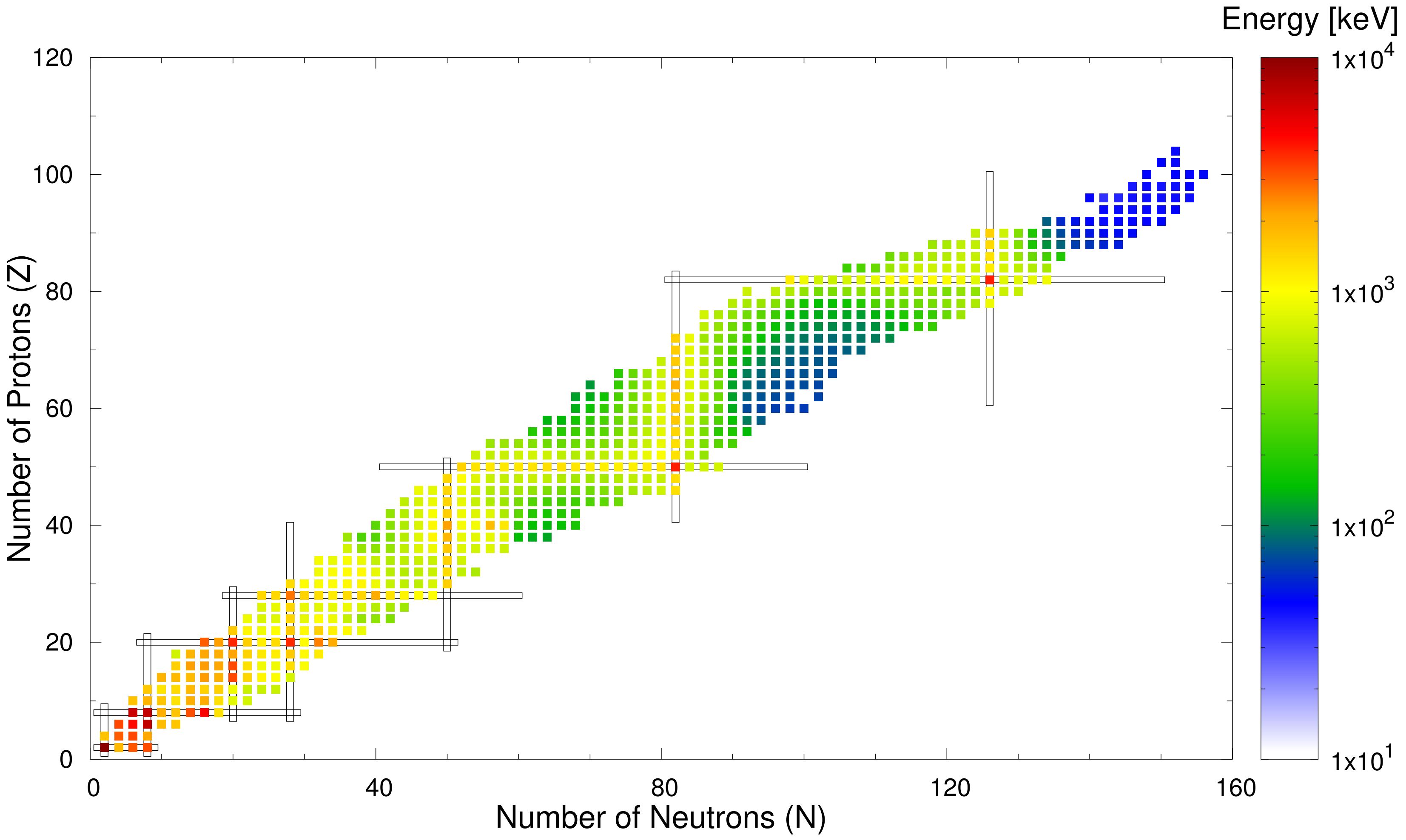

Figure 1.1.: Measured excitation energy of the first 2^+ state as a function of the proton and neutron numbers for all the known even-even nuclei. In proximity of the shell closures (black rectangles) the excitation energy rapidly increases. Data taken from Reference [2].

a function of the proton (Z) and neutron (N) numbers for all the known even-even nuclei: the rapid increase of the excitation energy suggests the existence of shell closures happening for specific numbers of proton and neutrons called magic numbers.

1.1.1. Nuclear Hamiltonian

The nuclear Hamiltonian, the atomic nucleus being a many-body quantum system, can be written as [3]

$$H = \sum_{i=1}^{A} T_i + \sum_{i,j}^{A} V_{ij} \quad , \tag{1.1}$$

where A is the number of nucleons, T_i denotes the kinetic energy of every single nucleon and V_{ij} is the two-body interaction potential[1] (here possible contributions from a higher many-body interactions are neglected) The eigenstate equation of this Hamiltonian can only be solved for very light nuclei. Heavier systems can presently not be solved due to the lack of numerical calculation power of current computers.

One can assume the existence of a single-particle potential V_i which absorbs most of the V_{ij} potential. Thus, the nuclear Hamiltonian can be written as

$$\begin{aligned} H &= \left(\sum_{i=1}^{A} T_i + \sum_{i=1}^{A} V_i \right) + \left(\sum_{i,j}^{A} V_{ij} - \sum_{i=1}^{A} V_i \right) \\ &= \sum_{i=1}^{A} H_i^{s.p.} + \sum_{i,j}^{A} H_{ij}^{res} \quad , \end{aligned} \tag{1.2}$$

where $H_i^{s.p.}$ is the single-particle Hamiltonian, while H_{ij}^{res} is the residual interaction, i.e. the fraction of the two-body interaction which is not absorbed by the single-particle potential. Moreover, the experimental evidence of the conservation of angular momentum, parity and energy restricts the choice of the potential shape. Finally, shell effects similar to the atomic case are observed in the nuclear excitation energies as well as in the separation energies of nucleons: the eigenstates of $H^{s.p.}$ should reproduce these phenomena.

The separation of the nuclear Hamiltonian into $H^{s.p.}$ and H^{res} reduces the calculation problem to the diagonalization of the residual interaction inside the wave-function space, defined by the not-perturbed Hamiltonian. On one side, the excellent results, coming from the employment of a mean field theory together to the related single-particle model, shows that the nucleon-nucleon interaction can be treated inside the nuclear system. On the other hand, because of the limited calculation power of the current computers, the solution of the nuclear problem usually cannot be extended inside the whole Hilbert space. Thus, an approximation of the exact solution is necessary, which brings the complete Hilbert space to be separated in three parts (Figure 1.2):

- the *inert core* where all the orbits are completely occupied;

---

[1] In principle the potential V contains the N-body interactions of the particles, where a two-body contribution is predominant.

- the *valence space* corresponding to the orbits that include the degrees of freedom necessary for the description of the physical phenomena;
- the *external space* where all the orbits are always empty.

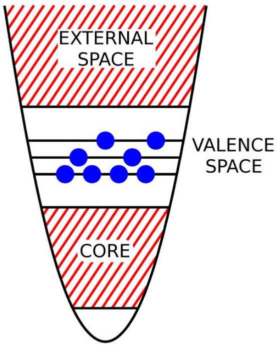

Figure 1.2.: Schematic drawing of the Hilbert space truncation. Adapted from Reference [4].

1.1.2. Nuclear shell model

The first step for addressing the nuclear problem consists in the study of a non-interacting model. In such model, each nucleon is assumed to be moving in an external field, created by the remaining $A-1$ nucleons [5, 6].

As a first approximation, the mean-field potential can be represented by a 3D harmonic oscillator potential V_c, which is a central potential and allows analytical solution for the Schrödinger equation. The resulting Hamiltonians for the *i-th* nucleon is

$$H_i^{s.p.} = \frac{1}{2}M_i v_i^2 + \frac{1}{2}M_i \omega^2 r_i^2 \quad , \tag{1.3}$$

where M_i is the nucleon mass, v_i its velocity, r_i its radial distance from the centre of the nucleus, ω a parameter which can be deduced from the dimensions of the nucleus. The eigenfunctions are calculated as

$$\Psi_{n,l,m_l,s,m_s}(r,\theta,\phi) = R_{n,l}(r) Y_l^{m_l}(\theta,\phi)\chi_{1/2}^{m_s} \quad , \tag{1.4}$$

where l is the quantum number associated to the orbital angular momentum, s is the spin quantum number ($s = 1/2$ for both protons and neutrons), m_l and m_s their projection on the polar axis, and n an integer quantum number. The polar coordinates used to define the position in the space are r, θ and ϕ. $Y_l^{m_l}(\theta,\phi)$ are the usual spherical harmonics, and $\chi_{1/2}^{m_s}$ are the spin wave functions. The radial part of eigenfunctions is represented by

$$R_{n,l}(r) = \sqrt{\frac{2^{l-n+2}\,(2l+2n+1)!!\alpha^{2l+3}}{\sqrt{\pi}n!\,[(2l+1)!!]^2}}\, e^{-\frac{1}{2}\alpha^2 r^2} r^l \sum_{k=0}^{n} \frac{(-1)^k\, 2^k n!\,(2l+1)!!\,\left(\alpha^2 r^2\right)^k}{k!\,(n-k)!\,(2l+2k+1)!!} \quad , \tag{1.5}$$

where $\alpha^2 = \frac{M\omega}{\hbar}$. The eigenvalues of this Hamiltonian are (similarly to the well-known 1D harmonic oscillator)

$$\begin{aligned} E_{n,l} &= \left(2n + l + \frac{3}{2}\right)\hbar\omega \\ &= \left(N + \frac{3}{4}\right)\hbar\omega \quad . \end{aligned} \tag{1.6}$$

Since $E_{n,l}$ is not a function of m_l, s and m_s, the energy level degeneration is $2(2l + 1)$ for both protons and neutrons. The number of nucleons when shell-closure effects become evident are called *magic numbers*. In Figure 1.3 the single-particle level scheme for a 3D harmonic oscillator is presented, showing both the degeneracy of the orbitals and the magic numbers.

From the comparison between the experimental shell closures reported in Figure 1.1 and the single-particle level scheme of Figure 1.3, the harmonic oscillator potential justifies only some of the experimentally observed magic numbers (2, 8, 20) while other magic numbers (28, 50, 82, 126) are not predicted by this model. Various modifications of the potential were attempted, but the most effective one was the insertion of the spin-orbit coupling. In atomic physics, this term stems from a relativistic correction, whereas in nuclear physics it has been derived by analogy with the atomic case. The expression of the spin-orbit interaction is [7–9]

$$V_{so} = V_{ls}\frac{\partial V_c}{\partial r}\vec{l}\cdot\vec{s} \quad , \tag{1.7}$$

where V_{ls} is a phenomenological constant. This interaction splits levels with the same $\vec{l}$ but with different total angular momentum $\vec{j} = \vec{l} + \vec{s}$. As a consequence, the separation between the two split levels is proportional to $(2l + 1)$, and both m_l and m_s are no longer good quantum numbers. Figure 1.3 shows that, introducing this potential, also the magic numbers 28, 50, 82, 126 are correctly reproduced.

Nowadays, the shell model offers a very comprehensive view of the nuclear structure [9, 11], but still with important shortcomings. One problem emerges with the calculations for light nuclei. Here, the dimensions of the Hamiltonian matrix are small enough to allow a diagonalization in the full space. These calculations should thus in principle be correct; on the contrary they fall short in reproducing the experimental data [12–14]. This has been attributed to the lack of three-body forces in the nuclear Hamiltonian: their introduction improves the agreement with spectroscopic data. A second problem is evident when performing calculations in heavier nuclei using a closed core, a valence space and a renormalized interaction. A paradigmatic example of a remarkable failure is the well-known doubly-magic nucleus ^{48}Ca, whose neutron shell closure $N = 28$ cannot be predicted via shell-model calculations using a first-principle renormalized interaction. In order to reproduce that magic number it is necessary to fit the matrix elements of the interaction on the experimental data[2]. However, despite the mentioned important progresses, a comprehensive picture of the nuclear phenomenology is still lacking.

---

[2] The adjustments needed for reproducing the $N = 28$ shell closure interest the monopole part of the interaction [11] and they have been proved compatible with a three-body force origin [15, 16]

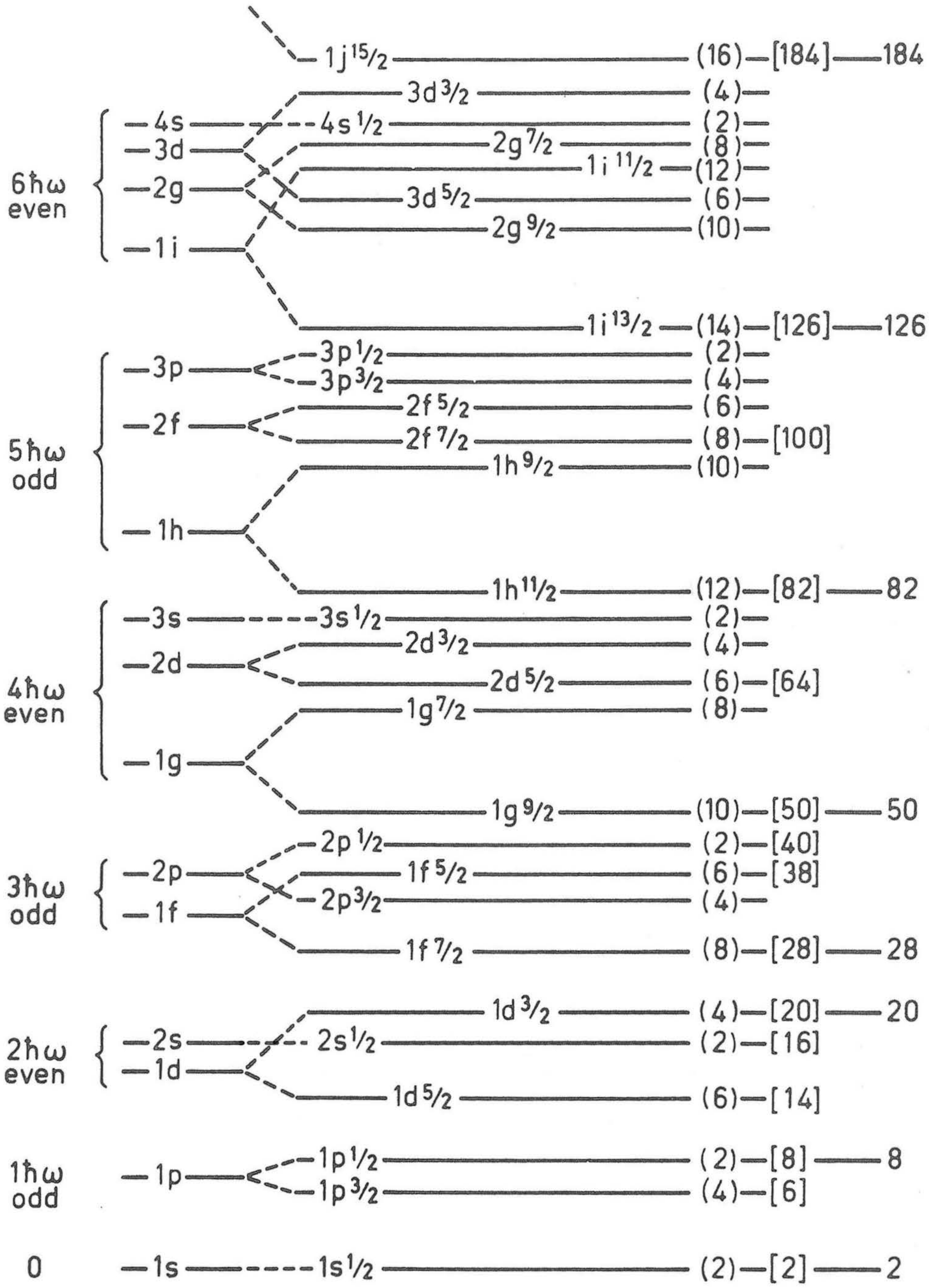
1j 15/2 (16)—[184]—184
3d 3/2 (4)—
4s 4s 1/2 (2)—
3d 2g 7/2 (8)—
6ħω even
1i 11/2 (12)—
2g 3d 5/2 (6)—
2g 9/2 (10)—
1i
1i 13/2 (14)—[126]—126
3p 3p 1/2 (2)—
3p 3/2 (4)—
2f 2f 5/2 (6)—
2f 7/2 (8)—[100]
5ħω odd
1h 9/2 (10)—
1h
1h 11/2 (12)—[82]—82
3s 3s 1/2 (2)—
2d 3/2 (4)—
2d 2d 5/2 (6)—[64]
4ħω even
1g 7/2 (8)—
1g
1g 9/2 (10)—[50]—50
2p 1/2 (2)—[40]
3ħω odd
2p 1f 5/2 (6)—[38]
1f 2p 3/2 (4)—
1f 7/2 (8)—[28]—28
1d 3/2 (4)—[20]—20
2ħω even
2s 2s 1/2 (2)—[16]
1d 1d 5/2 (6)—[14]
1ħω odd
1p 1p 1/2 (2)—[8]—8
1p 3/2 (4)—[6]
0 1s 1s 1/2 (2)—[2]—2

Figure 1.3.: Single-particle levels when the spin-orbit term is added to the harmonic oscillator Hamiltonian. Figure taken from References [9, 10] and then corrected for the erroneous effect of the V_{so} term on the $2s_{1/2}$ orbital.

1.1.3. Effective interactions

The non-interacting shell model is a simple theory which accounts for some observations, but is still a crude approximation of the full problem of the description of the nucleus [6]. This is mostly due to the fact that particles are assumed not to interact with each other. In reality, the potential V_{ij} of Equation 1.1 is not a simple mean-field potential, but it contains pairwise interactions (in general it contains many-body terms). Considering that the atomic nucleus is a many-body system, in order to calculate its energy spectrum and study the nuclear properties the many-body Schrödinger equation $H\Psi = E\Psi$ with H must be solved. For this purpose the energy matrix elements $\langle\phi_k|\, H\, |\phi_l\rangle$ have to be constructed and then diagonalized: these matrix elements of a given interaction between many-particle states can be expressed in terms of two-body matrix elements.

Before performing any shell model calculation, the definition of the valence space, which will be considered in the calculation, is crucial. Usually this space consists in a harmonic-oscillator shell, called major shell or $0\hbar\omega$, where the number of configurations and the matrices dimensions should remain treatable.

The restriction of the Hilbert space to a smaller model space is therefore inevitable and then the employment of both effective interactions and operators is crucial. Regarding the Schrödinger equation, the problem can be schematized as

$$H\psi = E\psi \rightarrow H_{eff}\psi_{eff} = E\psi_{eff} \quad . \tag{1.8}$$

Phenomenological interactions

The method to define a phenomenological interaction is an iterative procedure, defined starting from experimental data, such as energy levels and electromagnetic properties. This process consists in the minimization of the least squares between the calculated and the experimental spectra. However, when the considered spaces become too large, such a procedure is impossible. In fact a large space entails choosing a schematic interaction, which depends on parameters that are determined by phenomenological adjustment on a large number of nuclei. As example of this kind of interaction, the space fp is deeply discussed in the work of W.A. Richter and collaborators [17].

The advantage of this empirical approach is that it is not necessary to explicitly specify the interaction in order to correlate experimental energy spectra. Moreover, the matrix elements obtained in this way may have optimum values with respect to a reproduction of experimental energies: this procedure should yield the most suitable effective two-body matrix elements in a given restricted model space. On the other hand, the disadvantage of using a phenomenological interaction is that the number of parameters is usually very large, even for a reduced valence space. For example, in the sd space where the dimensions remain reasonable, it is possible to determine the 63 matrix elements by fitting experimental data [18]. Another objection is the fact that the selection of experimental states, which are thought to be described well in the assumed model space, may become rather arbitrary. Then, in order to minimize the effect of states that are erroneously included in the fit, the number of experimental states taken into account should be larger than the number of two-body matrix elements that have to be determined.

Realistic interactions

In the case of realistic interaction, the two-body matrix elements are not obtained from a fit to experimental data, but they are calculated from the free nucleon-nucleon interaction. In particular, they are extracted from potentials that reproduce the phase shifts during nucleon-nucleon scattering in a energy window varying up to 300 MeV or some properties of the deuteron, such as its binding energy. For example, the parametrization can be developed to take into account only the lower partial waves (S-, P- and D-waves) or to describe the phase shift of all partial waves.

Unfortunately, direct application of a realistic interaction in a shell-model calculation does not lead to an acceptable agreement with the spectroscopic data. This is due to the fact that a shell-model calculation is necessarily restricted to a finite, truncated model space. For a reasonably complete description in terms of a realistic interaction, a so-called effective interaction is needed: for a given configuration space this effective interaction can in principle be constructed starting from the free nucleon-nucleon interaction when all the processes that take place outside the chosen configuration space are accounted for in terms of perturbation theory. However, such a derivation of an effective interaction is complicated and difficult, in particular because of problems of convergence of the involved perturbation expansions.

In addition to that, such microscopic descriptions of the nuclei are affected by two main problems: the knowledge of the nucleon-nucleon interaction and the complexity of numerical calculations generated by the N-body problem, in particular taking into account the presence of the repulsive core.

The determination of the interaction potential between two nucleons has been an open question since the 1930s, but so far there is no method capable of deducing such a force from the quantum chromodynamics and the constituents of the nucleons. Nucleon-nucleon diffusion experiments and the properties of deuteron provide only part of the matrix elements of the nuclear interaction. In fact, the nucleon-nucleon interaction is well known at long range ($r > 2$ fm), where it is presented by the exchange of a pion, and at medium range (1 fm $< r < 2$ fm), where it is represented by the exchange of two pions and a meson ω. On the other hand, the short-range repulsion ($r < 0.8$ fm) is due to a complex set of phenomena (multiple exchanges of pions and heavy mesons, interactions between mesons, meson-nucleon resonances in intermediate states, etc.), which cannot be explicitly included, so they are empirically simulated. In addition to that, phenomenological adjustments are also necessary for the long-range and medium-range components of the force: effective values, different from those experimentally known, are requested for the meson-meson coupling constants and/or the meson masses in modern form of the potentials, such as Paris [19], Bonn [20] or Argonne [21].

The repulsive hard core of realistic interactions leads to very large or even infinite matrix elements. In response to this problem, the G-matrix technique [22, 23] makes it possible to get rid of the very short-range repulsive part and describes the diffusion of two free nucleons in the infinite nuclear material. By definition, it gives the transition amplitude between the states of two nucleons propagating independently in the nucleus before and after collision. Its matrix elements are therefore defined as states with two independent nucleons inside the nucleus and thus represents an effective interaction for nucleons in independent states. The order of magnitude of the G-matrix elements is reasonable: thanks to Pauli exclusion principle, nucleon-nucleon collisions within the nucleus have a small probability and for a given collision many of the final states are not available because they are occupied by the other nucleons.

Finally, the most recent approaches construct potentials based on the chiral field theory. The term of the chiral Lagrangian are classified by the term $\left(\frac{Q}{\Lambda_\chi}\right)^\nu$, where $Q \approx m_\pi$ (140 MeV), $\Lambda_\chi \approx 700$ MeV is a cut-off parameter and corresponds to the maximum potential energy avoiding short-range repulsion and ν is the chiral power order. In this context the hierarchy of nuclear forces appears naturally with not only nucleon-nucleon interactions, but also with three and N-body forces, as a function of the disturbance development order [24, 25]. In Figure 1.4 an example of the hierarchy of the nuclear forces as function of $\left(\frac{Q}{\Lambda_\chi}\right)^\nu$ is presented. In the leading order (LO) the nucleon-nucleon amplitude is made up by two momentum-independent contact terms ($\approx Q^0$): one is the tensor force, which is necessary to describe the deuteron and explains NN scattering, while the other contributes only in S waves, providing the short- and intermediate-range interaction. The $\nu = 1$ order is absent because its contributions vanish due to parity and time-reversal invariance. Therefore, the next-to-leading order (NLO) is $\nu = 2$ and it has again two main terms: the first is the two-pion exchange, which creates a more sophisticated description of the intermediate-range interaction but its contribution is rather weak; the second, instead, is the two-nucleon interaction, which contribute in both S and P waves. The operator structure of these contacts include a spin-orbit term besides central, spin-spin, and tensor terms. Thus, essentially all spin-isospin structures necessary to describe the two-nucleon force phenomenologically have been generated at this order. The main deficiency at this stage of development is an insufficient intermediate-range attraction. Then, the next-to-next-to-leading order (NNLO or N^{2}LO) introduces for the first time the three-nucleon forces, even if their contribution is very weak [26–29]. Despite the complexity of the possible considered configurations, such realistic forces do not reproduce the saturating properties of the nuclear material and they cannot simultaneously describe the radius and the binding energies of the nuclei. This fact can be explained by noting that the mean distance between nucleons in the nuclei is of the order of 2.4 fm and thus belongs to the medium- and long-range parts of the interaction, which are certainly better understood and described. On the other hand, the short-range part contains the repulsive terms necessary for the Pauli exclusion principle and the saturation properties.

It has been demonstrated [30] that it is possible to strictly separate the nuclear Hamiltonian into a monopolar part H_m and a multipolar component H_M:

$$H = H_m + H_M \quad . \tag{1.9}$$

The first, sensitive to Hartree-Fock variations, is responsible for the saturation properties and for the behaviour of the individual energies; the second, instead, is responsible for the correlations and for the detailed spectroscopy. In fact the multipolar part proves to be similar to the realistic interaction and to have good properties [30], such as being independent of the regularization procedure (G-matrix, etc.) and including also the case of the chiral potentials. Current advances in the description of the nuclear structure from first principles (so-called “ab-initio” description) suggest that the phenomenological corrections introduced on the monopolar part of realistic interactions come from the three-body forces that were not incorporated so far [15, 31, 32].

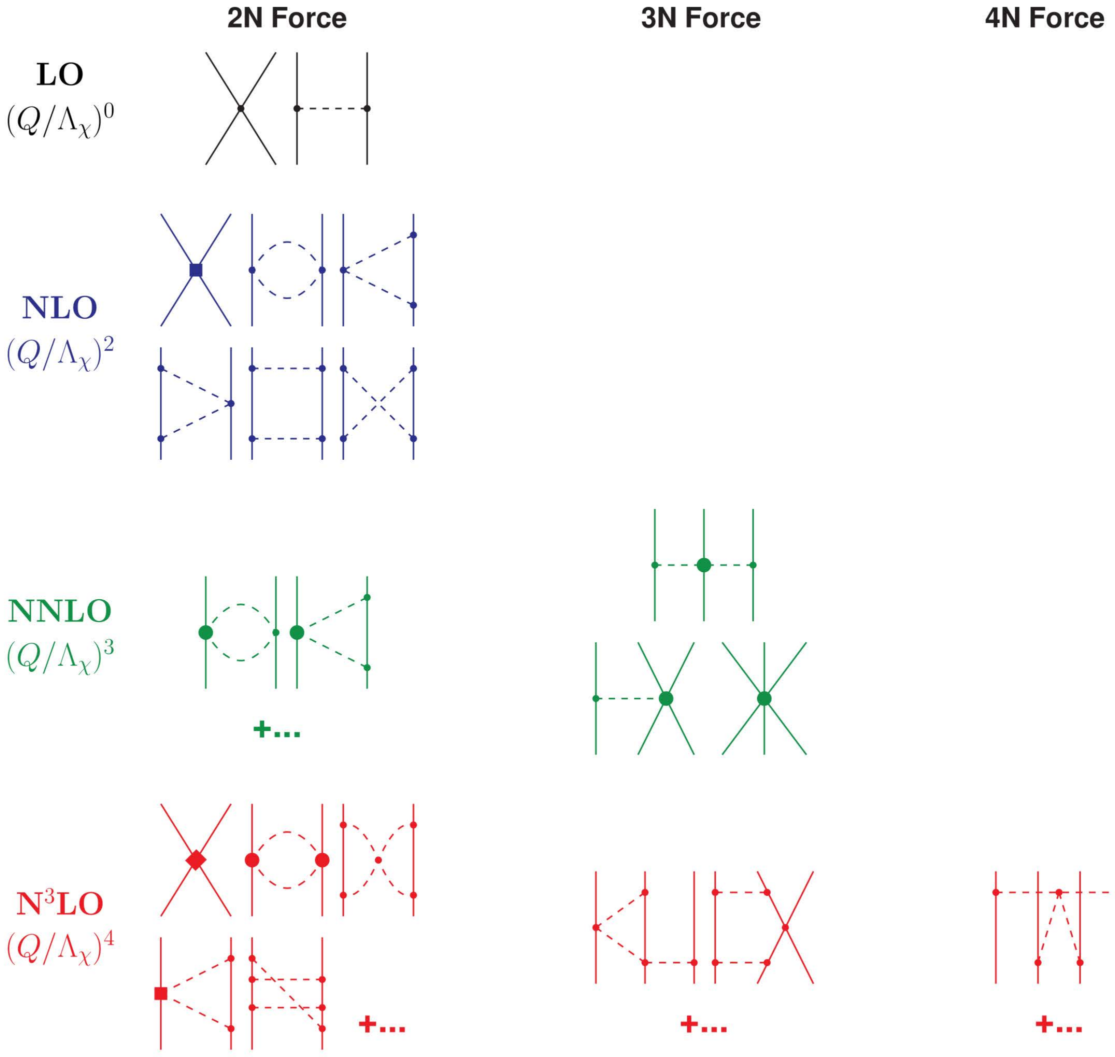
2N Force
3N Force
4N Force
LO
$(Q/\Lambda_\chi)^0$
NLO
$(Q/\Lambda_\chi)^2$
NNLO
$(Q/\Lambda_\chi)^3$
+...
N^{3}LO
$(Q/\Lambda_\chi)^4$
+...
+...
+...

Figure 1.4.: Hierarchy of the nuclear forces inside the chiral perturbation theory, classified according to the chiral order ν and described as a function of $\left(\frac{Q}{\Lambda_\chi}\right)^\nu$ (see text). Solid and dashed lines represent nucleons and pions, respectively. Small dots, large solid dots, solid squares and solid diamonds denote vertices of interaction index equal to 1, 2, 3 and 4 respectively. Taken from Reference [24].

1.1.4. M-scheme representation

One possible choice of the eigenvector basis, used for the description of the wave function, is given by the so-called *m-scheme* representation, which consists in all the possible Slater determinants, related to the distribution of N-particles inside p-orbitals, labelled with $|nljm\tau\rangle$ where n is the *principal quantum number*, l is the *angular momentum*, τ is the third component of the *isospin* and identifies if the nucleon is a proton ($\tau = -1/2$) or a neutron ($\tau = 1/2$), j and m are the *total angular momentum* and its projection along a specified axis respectively. The only symmetries taken into account are those related to the conservation of the parity, of the angular momentum projection J_z and of the isospin projection T_z. Via such a representation the nuclear wave function is defined as

$$\psi_{a_1 ... a_N}(r_1, ..., r_N) = det \begin{bmatrix} \phi_{a_1}(r_1) & ... & \phi_{a_1}(r_N) \\ ... & \phi_{a_k}(r_j) & ... \\ \phi_{a_N}(r_1) & ... & \phi_{a_N}(r_N) \end{bmatrix} = \prod_k a^\dagger_{a_k} |0\rangle \quad , \tag{1.10}$$

where ϕ_{a_k} is the wave function of the *k-th* single particle, placed inside the a_k orbit (for simplicity the label $|nljm\tau\rangle$ is summarised with a_k), and r_k is the position vector of the *k-th* nucleon. Thanks to the simplicity of the m-scheme representation, the matrix elements of a N-body system differs just by a phase from the matrix element of a not-interacting 2-body system. However, because all the possible states are taken into account, the dimension of the generated matrices is maximum and proportional to the combination of z-protons and n-neutrons distributed inside D_π and D_ν, respectively:

$$Dim \propto \begin{pmatrix} D_\pi \\ z \end{pmatrix} \times \begin{pmatrix} D_\nu \\ n \end{pmatrix} \quad . \tag{1.11}$$

Because of such a large dimension, in the past the m-scheme representation could be used only for describing the very light and the first double-magic nuclei, for which the shell model seemed to be less valid [4]. As example of such large dimension, the number of non-zero matrix element inside a full $0\hbar\omega$ valence space is shown in Figure 1.5 as a function of the neutron and proton numbers.

This problem was partially solved in 1989 thanks to the code ANTOINE [11, 33, 34]. This code can easily manage matrices with dimension up to 10^{12}, diagonalising them iteratively via Lanczos algorithm [35].

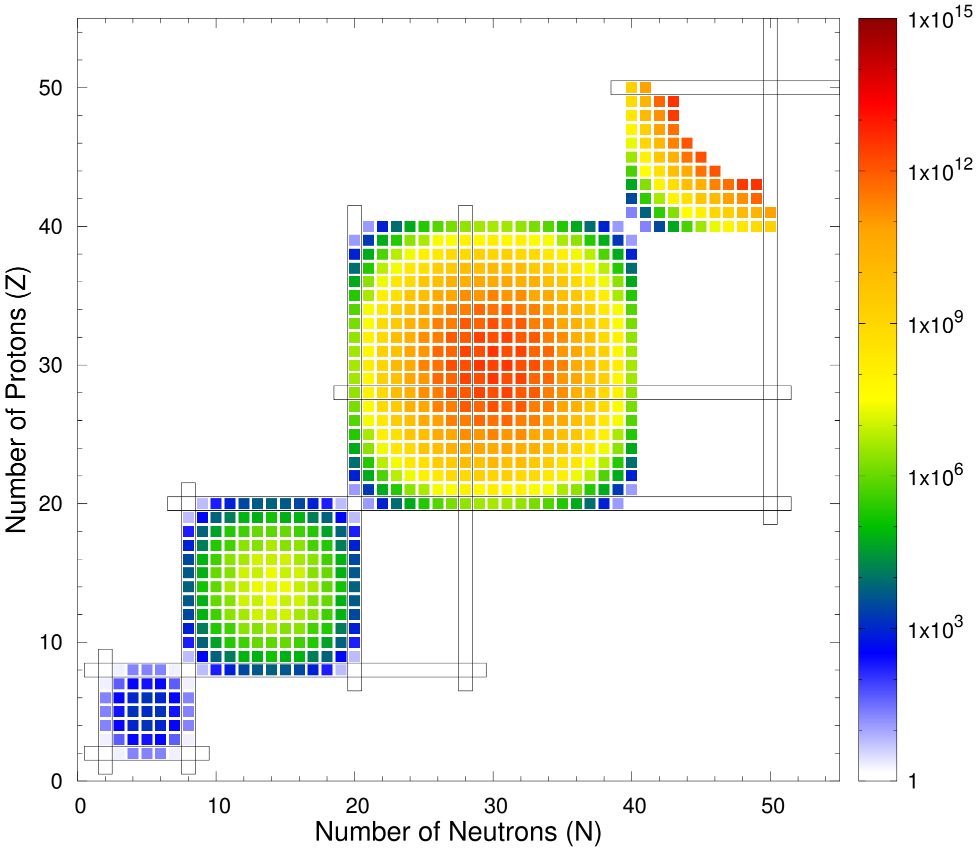

Figure 1.5.: Number of non-zero matrix elements (given by the colour axis) considering full $0\hbar\omega$ valence spaces as a function of the proton and neutron numbers. For $N, Z > 40$ ($l = 3$ major shell) the dimensions of the matrices exceed the capacity of standard computers when using the full major shell, illustrating the importance of the space truncation in this region. The rectangles with black outline represents the shell closures.

1.2. Seniority scheme

In this thesis the quadrupole correlations at $N = Z = 50$ will be investigated via lifetime measurement of low-lying states in neutron-deficient Sn isotopes. Considering that tin isotopes are well-known semi-magic nuclei, the seniority should represent a “good” quantum number for describing their Hamiltonian. In particular, the experimental results will be discussed and interpreted in the light of seniority evolution and truncation along the isotopic chain. Thus, for a clear understanding of the following discussions, it is important to introduce the concept of seniority.

In a multi-particle system with n valence nucleons, the similar nucleons couple together to angular momentum $J = 0$ because of the pairing force. For this reason almost all the even-even nuclei have 0^+ as ground. Then, because of the restrictions imposed by the Pauli exclusion principle, only few values of the total angular momentum J are permitted. In fact, not all angular momentum coupling of two identical nucleons are possible, so the maximum angular momentum J^{max} that can be created with n nucleons in a shell of momentum j is given by

$$J^{max} = nj - \frac{n(n-1)}{2} \quad . \tag{1.12}$$

The seniority is defined as the number v of unpaired nucleons, i.e. nucleons that are not coupled to angular momentum $J = 0$ [3]. In first approximation this quantity is a good quantum number for semi-magic nuclei. In these isotopes the n neutron or protons outside the doubly-magic core will mainly have a j^n configuration, where j is the lowest energy orbital outside the core. For example, in the case of neutron-deficient tin isotopes, the first neutrons outside the $Z = N = 50$ shell closure will predominantly occupy the $1g_{7/2}$ shell, as it can be deduced from Figure 1.3.

In a j^n configuration the conservation of the seniority quantum number provides a useful simplification in the description of the nuclear structure, called seniority scheme. For example, various interactions and matrix elements can be classified in terms of whether or not they conserve seniority. The seniority scheme predicts that the low-spin excited energy levels should have energies independent on the number of nucleons outside the core. It also provides an analytical estimate of the electromagnetic transition strengths between these states, for which a parabolic behaviour is expected [36]. A schematic illustration, showing the reduced transition probability $B(E2; J \to J-2)$ for seniority-dominated transitions, is presented in Figure 1.6.

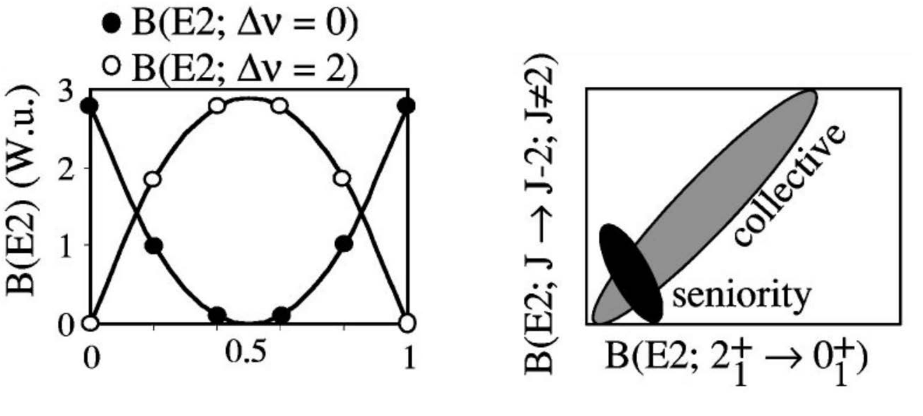

Figure 1.6.: (Left) Calculated $B(E2; J \to J-2)$ values for seniority conserving (full dots) and non-conserving (open dots) transitions as a function of the fractional filling of the main shell. (Right) Schematic illustration of $B(E2; J \to J-2)$ plotted against $B(E2; 2^+ \to 0^+)$ for seniority- and collectivity-dominated transitions. Figure adapted from Reference [36].

The seniority scheme often gives rise to the so-called seniority isomers. In a j^n configuration the states at low energy are usually the ones with low seniority [37], because breaking a pair of nucleons coupled to $J = 0$ has an energetic cost. As a result, the ground state of even-even semi-magic nuclei has $v = 0$, while the lowest yrast levels almost always have only one broken pair of nucleons, i.e. seniority $v = 2$. In addition, because the energies of the $v = 2$ states are independent of the number of nucleons n, all energy differences of seniority $v = 0$ and $v = 2$ states in the n-particle configuration are identical to those in the two-particle system [3]. Along the tin isotopic chain, indeed, the excitation energy of both the first 2^+ and 4^+ states is rather constant, how it is presented later in Figure 1.16.

In the mentioned case of the neutron-deficient tin isotopes, when neutrons fill the $1g_{7/2}$, the maximum angular momentum is 6. These maximally-aligned states are usually isomeric with a lifetime larger than 1 ns. This is due to a combination of low transition rate to the underlying level and of a small transition energy: on one side the $E2$ strength between levels with $v = 2$, as the low-lying yrast states in semi-magic nuclei, are hindered, especially when the j shell is half filled [38]; on the other side the energy differences between excited low-spin yrast levels become smaller going towards the maximally-aligned state.

1.3. Heavy-ion reactions

Nuclear reactions are a very complex quantum mechanical process which depends on the structure of the involved nuclei and on the reaction mechanism. Although the boundaries between various processes are not sharp, one can still classify them according to the reaction impact parameter, transferred angular momentum, energy and so on [39–41]. Figure 1.7 shows that with increasing impact parameters the interaction evolves from fusion reactions, which require a substantial overlap of the two nuclei, through deep inelastic processes, to quasi-elastic reactions, which are associated with the most grazing-type collisions [42]. At even larger impact parameter nuclei feel only Coulomb force, and only Coulomb excitation is observed.

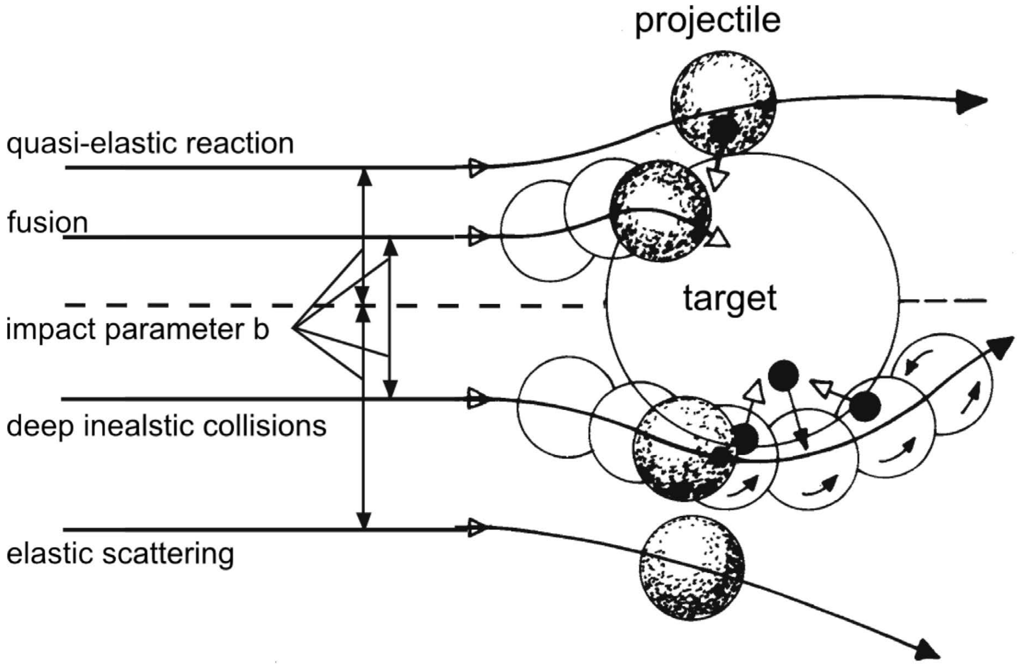

Figure 1.7.: Classification of heavy-ion collisions as a function of the impact parameter. Figure adapted from Reference [43].

1.3.1. Coulomb excitation reactions

Coulomb excitation is the physical process in which a target nucleus is excited by the electromagnetic field of a projectile nucleus, or vice versa [44–46]. The primary advantage in using sub-barrier Coulomb excitation is the inherent exclusion of any strong force component in the excitation process.

The cross section for the excitation process can be calculated in detail for low energies, i.e. for energies below the Coulomb barrier. At these energies, the charge distributions of the two nuclei do not overlap, due to the Coulomb repulsion, and the electromagnetic interaction plays a dominant role. For the intermediate energies, the cross section for the Coulomb excitation process was calculated in a semi-classical approximation: the cross section depends on the minimum impact parameter b_{min} and in this energy regime it is calculated as [47]

$$b_{min} = \left[cot\left(\frac{\theta^{c.m.}_{max}}{2}\right) + \frac{\pi}{2} \right] \frac{Z_p Z_t e^2}{\gamma m_0 v^2} \tag{1.13}$$

with the maximum scattering angle in the centre of mass system $\theta^{c.m.}_{max}$, the reduced mass of the two nuclei m_0, the Lorentz factor γ and the velocity v of the projectile in the laboratory system. The calculation for the cross section yields

$$\sigma \approx \left(\frac{Ze^2}{\hbar c}\right)^2 \frac{B(E\lambda; 0 \to \lambda)}{e^2 b_{min}^{2\lambda-2}} \frac{1}{\lambda - 1} \tag{1.14}$$

for the transition multipolarity $\lambda \geq 2$, the charge of the target nucleus Z in the case of projectile excitation.

Due to the proportionality of σ and $B(E\lambda)$, the reduced transition probabilities can be obtained from measurements of Coulomb excitation cross-section. At intermediate energies and above, one-step processes (i.e. the direct transition from the ground state to the excited state) are dominating the population of excited states and among these $E2$ transitions are favoured, as it can be deduced from Equation 1.14. Therefore, in even-even nuclei the Coulomb excitation process populates predominantly the first 2^+ states.

1.3.2. Multi-nucleon transfer reactions

In heavy-ion collisions, Multi-Nucleon Transfer (MNT) reactions play a considerable role, and both pick-up and stripping of nucleons occur. Transfer reactions represent the natural transition from the quasi-elastic regime to the more complex deep inelastic one [48]. In a single collision it is possible to transfer several nucleons and large angular momentum between the projectile and the target.

In the last decade, the renewed interest in transfer reactions has been mainly due to the realization that MNT reactions could be used to populate nuclei moderately rich in neutrons with cross sections large enough to study their structure [49]. This renewed interest benefited from the construction of the new generation large solid angle spectrometers based on trajectory reconstruction (VAMOS++, PRISMA, etc.), providing at the same time large overall efficiency and good identification of reaction products.

In *quasi-elastic* reactions the projectile has lost only a moderate amount of energy and has exchanged only few nucleons with the target nucleus. Such reactions close to the Coulomb barrier are assumed to correspond to collisions where the surfaces of the two ions have just been in grazing contact, and they essentially keep their identity [41]. Quasi-elastic reactions populate well defined quantum states with a high degree of selectivity, usually at rather low excitation energy and with (relatively) high spins. In addition, the angular distributions often exhibit a single peak at the grazing angle.

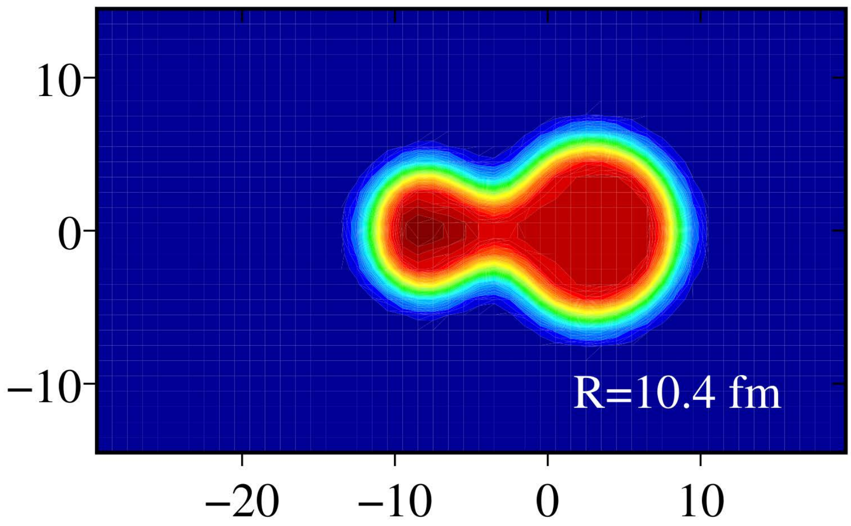

Figure 1.8.: Microscopic Density-Constrained Time-Dependent Hartree-Fock study of ^{48}Ca+^{132}Sn at the energy $E_{c.m.}$ = 140 MeV, showing a contour plot of the mass density at internuclear distance R = 10.4 fm. During the formation of the “neck” between the reaction fragments, the nucleons transfer takes place entailing an exchange of mass and momentum. Figure taken from Reference [50].

In *deep-inelastic* reactions (or strongly damped collisions) the distribution of masses and kinetic energies of the reaction products often present a broad distribution. Moreover, an appreciable fraction of the incident kinetic energy has been converted into internal excitation energy. The primary products are also found to be essentially binary: they result from the two heavy nuclei staying together for a longer time than that of direct reactions, but not long enough for the two systems to fuse into a compound nucleus [40]. Such collision time and large energy losses suggest that the excitation of surface modes allows the two ions to stay in close contact for time sufficient to exchange large number of nucleons. Very often this mechanism is described via the creation of a “neck” between the two colliding partners, as it is predicted, for example, by Time-Dependent Hartree-Fock calculations (see Figure 1.8). During the time window when the neck between the ions is created, there is a large energy loss, but the system still retains memory of how it was formed by showing, for example, a forward-peaked angular distribution. The two nuclei involved in the reaction are characterized by a large exchange of nucleons, towards the charge equilibration (i.e. N/Z ratio of compound nucleus).

For a given mass asymmetry in the entrance channel, the contribution of quasi-elastic or deep-inelastic components in a reaction depends mainly on the projectile energy, but also on the mass of the colliding partners and on the detection angle. The height of the Coulomb barrier, by using the two point charges expression, can be written as

$$E_B = \frac{Z_t Z_p e^2}{r_C} \quad , \tag{1.15}$$

where Z_t and Z_p are the atomic number of target and projectile, respectively, and r_C is the interaction distance. For projectile energy higher than the Coulomb barrier the deep-inelastic contribution to the total cross-section becomes more and more important.

For both MNT and deep-inelastic collisions a unified theory has not been defined yet [51] and the different existing models are able to reproduce just few aspects of such reactions. On the other hand, for MNT reactions close to the Coulomb barrier the reaction process can be described in semi-classical approximation[3]. Thanks to such approximation, the equations related to the motion of the colliding partner can be considered as describing classical trajectories. Then, by treating the transfer reaction in first order perturbation theory and approximating the true trajectory with a parabolic parametrization around the turning point, the probability for a given transfer process from the entrance channel α to the channel β may be written as [48, 52, 53]

$$P_{\beta\alpha} = \sqrt{\frac{1}{16\pi\hbar^2 \left|\ddot{r_0}\right| K_{a_1'}}} \left|f_{\beta\alpha}(0,r)\right|^2 g(Q_{\beta\alpha}) \quad , \tag{1.16}$$

where $\ddot{r_0}$ is the radial acceleration at the distance of closest approach for the grazing partial wave, the coefficient $K_{a_1'}$ contains the binding energy of the single particle state a_1' entering in the transition, $f_{\beta\alpha}(0,r)$ is the transferred-particle form factor at large distances and $g(Q_{\beta\alpha})$ is the adiabatic cut-off that depends on the optimum Q-value of the reaction. From Equation 1.16 it is clear that the transfer processes are mainly governed by two contributions:

- *form factors*, spectroscopic information of colliding nuclei and dynamics
- *optimum Q-value* consideration, regarding the balance of the internal and binding energy in the phase space of the colliding nuclei

Due to the characteristic behaviour of the binding energy in the nuclear chart, the process is essentially governed by the lighter partner of the reaction. In general, the use of lighter stable projectiles on heavy targets results in population of only proton stripping and neutron pick-up channels.

The form factor is a matrix element between initial and final states in the transfer process and reflects nuclear structure properties of the donor and acceptor, weighting the relative importance of different channels. The form factor is equal to

$$f_{\beta\gamma}(\vec{k},\vec{r}) = \langle\omega_\beta|\,(V_\gamma - U_\gamma)\,|\omega_\gamma\rangle \quad , \tag{1.17}$$

where $\vec{k}$ is the transferred momentum, $\vec{r} = \frac{1}{2}\left(\vec{r_\beta} + \vec{r_\gamma}\right)$ is the centre of mass distances, $|\omega_i\rangle$ constitute a dual base obtained from the overlap matrix, U and V are the nuclear potential and the coupling interaction respectively. At large distances, for the transferred particle the form factor can be written as

---

[3] Semi-classical approximation is valid also at the energies above the Coulomb barrier since the wave length associated with the relative motion is much smaller than the interaction region (sum of the two nuclear radii) [48].

$$f_{\beta\gamma}(0,r) \approx \frac{1}{K_{a'_1} r} e^{-K_{a'_1} r} \quad , \tag{1.18}$$

where the asymptotic behaviour of the form factor is governed by the coefficient $K_{a'_1}$. For single-particle states close to the Fermi energy the decay length of the one-transferred particle form factor is of the order of 1.2 fm, thus at large distances the transfer form factor prevails over the nuclear component of the inelastic form factor.

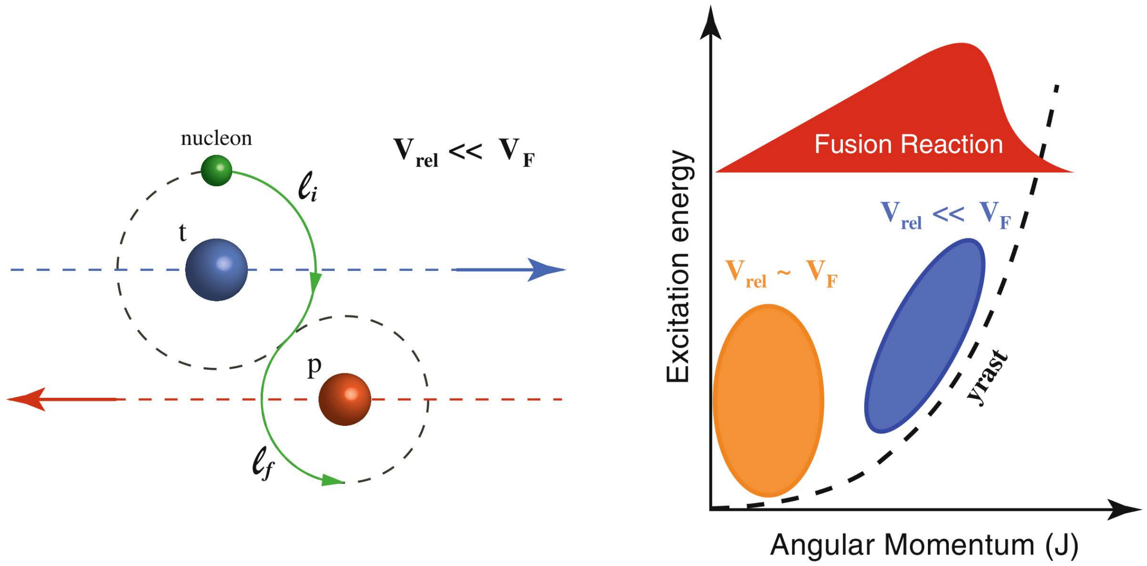

Figure 1.9.: (left) Schematic design of the angular momentum transfer in the case of transfer reactions between a target t and a projectile p at energies close to the Coulomb barrier. The angular momenta of the orbiting nucleons of the initial l_i and final state l_f would be perpendicular to the scattering plane and their projections will have opposite sign. (right) Schematic representation of the states populated in the plane excitation energy versus angular momentum degrees of freedom for the two regimes described in the text: small relative velocities ($E_{rel} \ll E_F$) and higher transfer energies ($E_{rel} \approx E_F$). The region of population for fusion-evaporation reactions has been depicted for comparison. Figure adapted from Reference [54].

As it was previously introduced by Equation 1.16, the transfer probability is affected by an adiabatic cut-off that depends on the optimum Q-value of the reaction:

$$g(Q) = e^{-\frac{(Q-Q_{opt})^2}{\hbar^2 \ddot{r}_0 K_{a'_1}}} \quad . \tag{1.19}$$

Such cut-off function $g(Q)$ defines the actual value of the transition probability whose maximum is at the optimum Q-value. This derives from the requirement that the trajectory of entrance and exit channels matches smoothly close to the turning point where the contribution of the form factor peaks [55]. The bombarding energy dependence of the cut-off function is contained in the $\ddot{r_0}$ term that defines its width (inversely proportional to the collision time). Lowering the bombarding energy increases collision time and squeezes Q-value window, thus reducing the average number of transferred neutrons. On the other side, by increasing the bombarding energy the grazing distance is decreased, thus leading to more intimate collision in the grazing region.

The optimum Q-value is calculated as

$$Q_{opt} \approx \left(\frac{Z_x}{Z_t} - \frac{Z_x}{Z_p} \right) E_B + \left(\frac{m_x}{m_p} - \frac{m_x}{m_t} \right) (E_p - E_B) + \frac{m_x \ddot{r_0}}{m_p + m_t} \left(R_t m_{pl} - R_p m_{tl} \right), \quad (1.20)$$

where E_B is the height of the Coulomb barrier, Z_i and m_i are the proton number and the mass of the *i-th* particle, while x, p and t stay for the transferred particle, the projectile and the target before the reaction, while pl and tl stay for the projectile-like and the target-like fragments after the reaction, respectively. By observing the equation above, for the neutron transfer $Q_{opt} \approx 0$ and this implies that in first approximation the optimum Q-value can be considered constant along an isotopic chain, as it was assumed during the optimisation of the experimental setup, as it is presented in Appendix A (see Table A.3). On the other hand, the optimum Q-value for charge particle transfer is both system and energy dependent.

The knowledge of the states directly populated in a MNT reaction has a significant bearing on the application of such reactions in the γ-ray spectroscopy. In the case of transfer reactions at energies close to the Coulomb barrier, since the relative kinetic energy is very small if compared with the Fermi kinetic energies ($E_{rel} \ll E_F$), the transfer of a nucleon happens as it is sketched in Figure 1.9 (left), i.e. the angular momenta of the orbiting nucleons of the initial l_i and final state l_f would be perpendicular to the scattering plane and their projections will have opposite sign. Thus, the maximum transfer angular momentum is given by

$$|l_{transf}| = |l_i + l_f| = |l_i| + |l_f| \quad . \quad (1.21)$$

At a higher energies ($E_{rel} \approx E_F$), due to the larger relative angular momentum between the two nuclei, one tends to have a similar population of the states $j_f = l_f \pm 1/2$. Therefore, these two regimes will populate two very different regions in an excitation energy versus angular momentum plot, as illustrated in Figure 1.9 (right). The transfer mechanism, due to the angular momentum matching conditions discussed above, makes possible a strong yrast population.

1.3.3. Fusion-evaporation reactions

A fusion-evaporation reaction can occur for a strong overlap between the projectile and target charge distribution, leading the two colliding partners to fuse together. The resulting compound nucleus, which has "forgotten" its origin, is formed in a highly excited state with a high angular momentum and the excitation energy is redistributed between the nucleons as they rearrange themselves. If the compound nucleus is stable against fission, the excitation energy is released via particle (protons, neutrons, alpha particles, etc.) evaporation and then γ-ray emission. In the evaporation process the amount of removed excitation energy depends on the binding energy of the evaporated particles and on the Coulomb barrier, that protons need to overcome to escape the nucleus. A schematic drawing, presented in Figure 1.10, shows the production and decay mechanism of a compound nucleus.

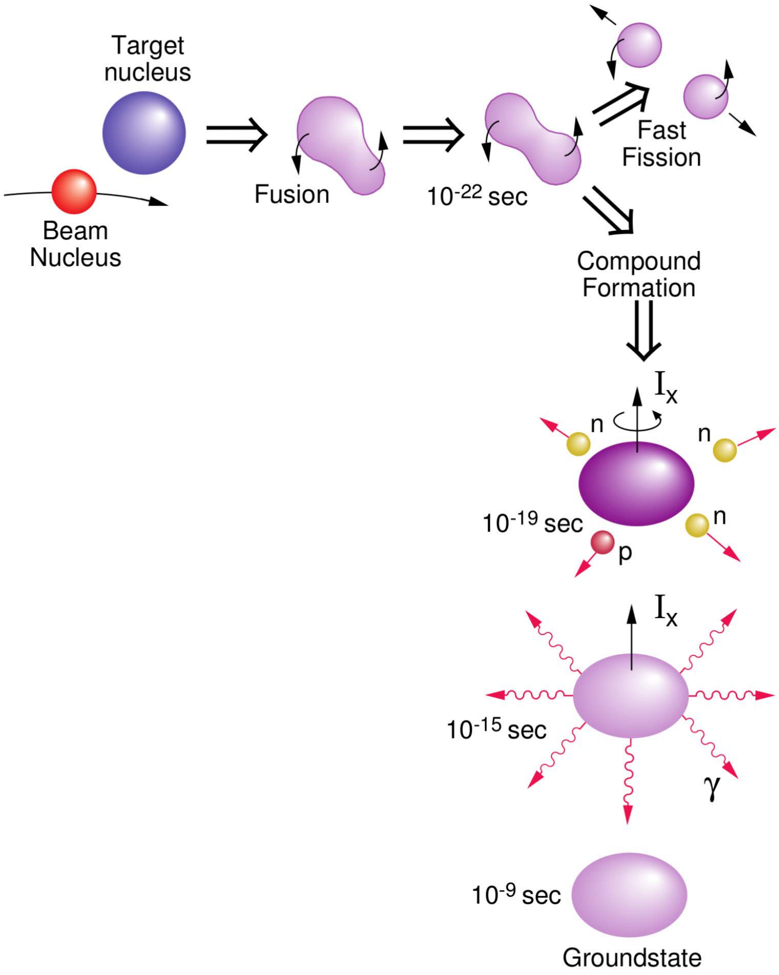
Target nucleus
Beam Nucleus
Fusion
10^{-22} sec
Fast Fission
Compound Formation
I_x
n
n
n
p
10^{-19} sec
I_x
10^{-15} sec
γ
10^{-9} sec
Groundstate

Figure 1.10.: Different steps of a fusion-evaporation reaction ending up in the ground state of the newly formed nucleus. The average time scale of each step in case of heavy compound-nucleus formation is indicated. Taken from References [56, 57].

The fusion cross section defines the formation probability of the compound nucleus, which will eventually decay via several fusion-evaporation channels or by fission. Therefore,

$$\sigma_{fusion} = \sum_{ER} \sigma_{ER} + \sigma_{fission} \tag{1.22}$$

where σ_{ER} is the cross section of an individual evaporation residue and $\sigma_{fission}$ denotes fission cross section. This effect can be seen in Figure 1.11 (a) that presents a sketch of the fusion-evaporation cross section with respect to the excitation energy of the compound nucleus. The total fusion cross section rises with increasing beam energy, however the fusion evaporation cross section decreases when the fission process starts to compete. This effect can also be seen in the lowering of the cross section of the individual evaporation channels with increasing number of evaporated neutrons. When the excitation energy is not sufficient for any further particle evaporation, the final nucleus is still formed in a highly excited state, the so called *entry region*. The γ-ray emission competes with particle evaporation and is the dominant decay mode at excitation energies below the neutron-separation energy and in the vicinity of the yrast line. The de-excitation path starting from the compound nucleus is presented in Figure 1.11 (b): the region where the yrast line is reached depends on the position of the entry region, which is determined by the fusion-evaporation entrance channel and in particular by the excitation energy of the compound nucleus.

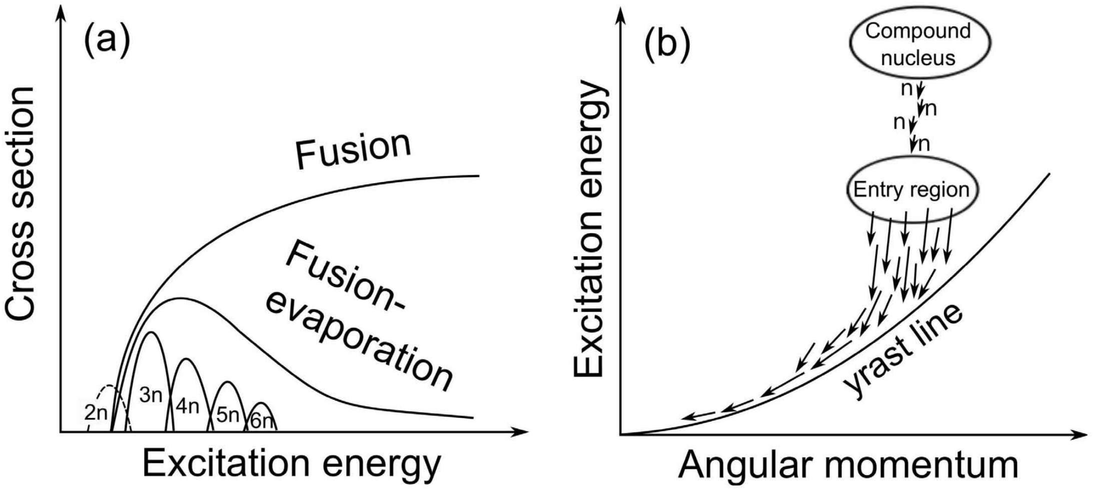

Figure 1.11.: (a) Schematic illustration of the fusion-evaporation cross-section with respect to the excitation energy of the compound nucleus. The cross section of fusion and fission rises with increasing energy; as the fission cross section becomes more competitive with the increasing excitation energy of the compound nucleus, the fusion-evaporation cross section starts to decrease. As example, the neutron-evaporation channels have been added, while the $2n$ channel is presented by a dashed line as the fusion barrier cuts this exit channel. (b) The de-excitation path to the yrast line of the final nucleus, produced in the entry region through the evaporation of neutrons from the compound nucleus. The $4n$ evaporation channel has been drawn as an example and the arrows from the entry region downward denote emitted γ rays. Taken from Reference [58].

In this sense, fusion-evaporation reactions favour the study of collective behaviour of nucleons in proton-rich nuclei by employing in-beam γ-ray spectroscopy. These reactions provide a unique possibility to study nuclear properties under conditions unattainable via other types of reactions.

1.4. Gamma-ray spectroscopy

Gamma spectroscopy is a fundamental tool in nuclear physics, as it provides essential information on the structure of nuclei. In fact, the study of γ-ray emission and of its competing process, such as internal conversion, allows to assign spin and parity to the nuclear levels or to test the nuclear wave function through the measurement of the electromagnetic transition strengths.

1.4.1. Electromagnetic transitions in atomic nuclei

One of the most common de-excitation modes of the atomic nucleus is via the emission of γ rays. The electromagnetic radiation produced by a nucleus can be described in terms of a multipole expansion. This is convenient because transitions between nuclear levels, which have a well defined spin and parity, carry away a precise amount of angular momentum thus giving origin to selection rules that limit the number of possible multipolarities [59, 60]. Moreover, as it will be shown soon, the highest multipolarities are much hindered with respect to the lower ones: therefore, in a γ decay, only one or two multipolarities are usually considered.

An excited nuclear state with an energy E_i, spin J_i and parity π_i can decay via the emission of a γ ray to a lower energetic level with an energy E_f , spin J_f and parity π_f. In absence of any external force, the total energy and the momentum have to be conserved:

$$\begin{aligned} E_i &= E_f + E_\gamma + T_R \\ \vec{0} &= \vec{p_\gamma} + \vec{p_R} \quad , \end{aligned} \tag{1.23}$$

where $\vec{p_R}$ is the momentum of the recoil and $T_R = \frac{p_R^2}{2M}$ its kinetic energy. Solving the above system of equations, the energy of the emitted photon is

$$E_\gamma = Mc^2 \left[-1 \pm \sqrt{1 + 2\frac{\Delta E}{Mc^2}} \right] \approx \Delta E - \frac{(\Delta E)^2}{2Mc^2} \quad , \tag{1.24}$$

where $\Delta E = E_i - E_f$ ranges between few keV to several MeV. Considering that the mass of the recoil nucleus is around 1 GeV per nucleon, in the majority of cases the recoil correction is negligible.

Since a γ ray is just a high energetic photon which is emitted from the nucleus, in addition to the energy also the angular momentum and the parity are conserved. Hence, the angular momentum of the γ ray ($L > 0$) has to satisfy the triangle inequality:

$$|J_i - J_f| \leq L \leq J_i + J_f \quad . \tag{1.25}$$

The change of parity for electric (EL) and magnetic (ML) character is given by

$$\begin{aligned} \Delta\pi(EL) &= (-1)^L \\ \Delta\pi(ML) &= (-1)^{L+1} \quad . \end{aligned} \tag{1.26}$$

The total transition probability from an excited level i to a level f is determined as

$$\lambda_{fi} = \frac{8\pi\,(L+1)}{\epsilon_0 \hbar L\,[(2L+1)!!]^2}\left(\frac{E_\gamma}{\hbar c}\right)^{2L+1} B(\varepsilon L; I_i \to I_f) \quad , \tag{1.27}$$

where L is the angular momentum carried by the photon, E_γ its energy, I_f and I_i the spin of the final and initial states respectively, σ represents the character of the transition, and $B(\varepsilon L; I_i \to I_f)$ a quantity called *reduced transition probability.* The reduced transition probability has different forms according to the character ε of the electromagnetic transition and it is defined as

$$B(\varepsilon L; I_i \to I_f) = \frac{1}{2I_i+1}\left|\langle f|\,\mathcal{O}(\varepsilon L)\,|i\rangle\right|^2 \quad . \tag{1.28}$$

The relation between transition probabilities and reduce matrix elements is summarised in Table 1.1.

$T(E1) = 1.587 \cdot 10^{15} E^3 B(E1)$	$T(M1) = 1.779 \cdot 10^{13} E^3 B(M1)$
$T(E2) = 1.223 \cdot 10^{9} E^5 B(E2)$	$T(M2) = 1.371 \cdot 10^{7} E^5 B(M2)$
$T(E3) = 5.689 \cdot 10^{2} E^7 B(E3)$	$T(M3) = 6.387 \cdot 10^{0} E^7 B(M3)$
$T(E4) = 1.649 \cdot 10^{-4} E^9 B(E4)$	$T(M4) = 1.889 \cdot 10^{-6} E^9 B(M4)$
$T(E5) = 3.451 \cdot 10^{-11} E^{11} B(E5)$	$T(M5) = 3.868 \cdot 10^{-13} E^{11} B(M5)$

Table 1.1.: Electromagnetic transition rates. The transition probabilities T are in s^{-1}, the energies E are in MeV, $B(EL)$ in $\mathrm{e}^2\mathrm{fm}^{2L}$ and $B(ML)$ in $\mu_N^2\mathrm{fm}^{2L-2}$.

Effective transition operators

As it was previously discussed, the reduction of the Hilbert space to a model space because of computational reasons leads to the construction and employment of effective interactions. For the same reasons, the bare transition operators cannot reproduce the correct results because important contributions to the transition matrix elements may have been lost in the truncation procedure.

Considering the wave functions $|a\rangle$ and $|b\rangle$ from the model space, the effective operators for the single-particle transition operators has to conserve the expectation value of the full Hilbert space case:

$$\left\langle a'\right|\mathcal{O}_{eff}\left|b'\right\rangle = \frac{\langle a|\,\mathcal{O}\,|b\rangle}{\sqrt{\langle a|a\rangle\,\langle b|b\rangle}} \quad . \tag{1.29}$$

After defining the operator $Q = 1 - P = 1 - \sum_{i\in M}|\psi_i\rangle\langle\psi_i|$, which projects off the model space M, the matrix element of Equation 1.29 can be expanded in series [61]:

$$\left\langle a'\right|\mathcal{O}_{eff}\left|b'\right\rangle = \left\langle a'\right|\left(\mathcal{O} + \mathcal{O}\frac{Q}{E_v - H_v^{(0)}}G + G\frac{Q}{E_v - H_v^{(0)}}\mathcal{O} + ...\right)\left|b'\right\rangle \quad , \tag{1.30}$$

where G is the reaction matrix, coming from the solution of the Bethe-Goldstone equation for the given residual interaction, while E_v and $H_v^{(0)}$ are respectivelly the energy and the unperturbed Hamiltonian rewritten in the valence space [62]. The first order of such equation contains the unperturbed valence energy denominators that consider all the possible particle-hole states, which must represent the excitation energy of the intermediate states with respect to the unperturbed valence states $|a'\rangle$ and $|b'\rangle$. Practically, because of the emission or absorption of a quantum gamma of character ε and momentum L, a core particle is excited into an unoccupied orbit and creates a particle-hole state; then this $p-h$ states later recombines in a scattering process with the single particle outside the core. A diagrammatic explanation of such a process is shown in Figure 1.12.

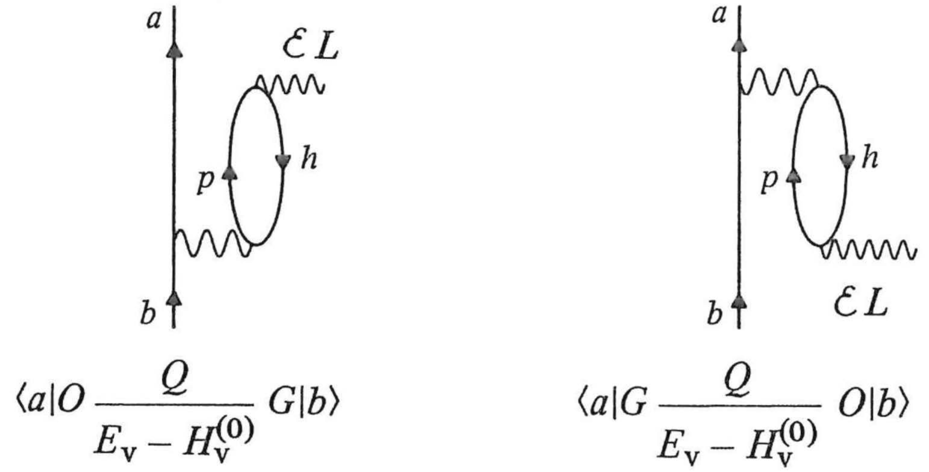
a
$\mathcal{E}L$
p
h
b
$\langle a|O \frac{Q}{E_V - H_V^{(0)}} G|b\rangle$
a
p
h
b
$\mathcal{E}L$
$\langle a|G \frac{Q}{E_V - H_V^{(0)}} O|b\rangle$

Figure 1.12.: Diagrams explaining the first-order expansion of the Equation 1.30: because of the emission or absorption of a quantum gamma of character ε and momentum L, a core particle is excited into an unoccupied orbit and creates a particle-hole state; then this $p-h$ states later recombines in a scattering process with the single particle outside the core. Figure adapted from Reference [61].

Thus for a given 2^L-pole transition of a nucleon from state Ψ_i to state Ψ_f, an *effective charge* can be introduced as the ratio between the first- and the zeroth-order reduced matrix elements (the latter always taken for a proton)

$$\Delta^{(1)} e(j_i, j_f, t_z) = \frac{\Delta \langle j_f, t_z | \mathcal{O}(\varepsilon L) | j_i, t_z \rangle}{\langle j_f, t_z = -1/2 | \mathcal{O}(\varepsilon L) | j_i, t_z = -1/2 \rangle} e \tag{1.31}$$

with

$$\Delta^{(1)} \langle j_f, t_z | \mathcal{O}(\varepsilon L) | j_i, t_z \rangle \equiv \langle j_f, t_z | \left(\mathcal{O}(\varepsilon L) \frac{Q}{E_v - H_v^{(0)}} G + G \frac{Q}{E_V - H_v^{(0)}} \mathcal{O}(\varepsilon L) \right) | j_i, t_z \rangle \quad . \tag{1.32}$$

For a neutron, bearing no electric charge, the zeroth-order matrix elements vanish. On the other hand, since the neutron can excite a proton particle-hole pair that recombines in an electric 2^L-pole transition a non-zero charge is associated to it. Similarly a proton particle-hole pair formed after absorption/emission of a γ-ray can be deexcited in a collision process with a neutron.

The effective charges are dependent on the multipolarity of the transition, on the initial and final states concerned and on the configuration space. In practice, the effective proton and neutron charges are introduced to account for polarization effects of the valence nucleons on the otherwise inert core of the shell-model calculation. The polarization charge, which is the difference between the effective and bare charge, is believed to arise from virtual excitations of isoscalar (IS) and isovector (IV) giant resonances of the nucleus [10, 63, 64]:

$$\begin{aligned}\epsilon_p &\equiv \Delta^{(1)}e(j_i, j_f, -1/2) = 1 + e_{pol} = 1 + e^{IS}_{pol} - e^{IV}_{pol} \\ \epsilon_n &\equiv \Delta^{(1)}e(j_i, j_f, 1/2) = e_{pol} = e^{IS}_{pol} + e^{IV}_{pol}\end{aligned} \tag{1.33}$$

where e^{IS}_{pol} and e^{IV}_{pol} represent the isoscalar and iscovector polarization charge, respectively. In the case of $E2$ transitions involving $N \approx Z$ stable nuclei, these charges are predicted to be $e^{IS}_{pol} \approx 0.5$ and $e^{IV}_{pol} \approx 0.32$ [10]. On the other hand, Hamamoto and collaborators [63] discussed the role of effective charges for nuclei far from stability: in nuclei $|N - Z| \gg 0$ the calculated IS Giant Quadrupole Resonance (GQR) carries an appreciable amount of the IV density due to the neutron/proton excess, while the calculated IV GQR carries very little IS density. It was also clearly seen by Hamamoto that the polarizabilities are small for nucleons with small binding energies and small orbital angular momenta, since those nucleons do not polarize the core nuclei efficiently. In Reference [65] was shown that, when the model space being used to describe the physics of a given nucleus does not consider all possible $0\hbar\omega$ excitations, the inclusion of the effective three-body forces is essential to understand quantitatively the experimentally observed transition rates. These often-ignored terms have not been explicitly treated in a full perturbative calculation so far. However, following the rigorous analysis of Reference [66], the effects can be assessed by explicitly considering the relevant particle-hole excitations from the core. Therefore when performing Large-Scale Shell-Model (LSSM) calculations it is very important to properly treat the effective many-body terms. In the work discussed in this thesis, as it will be discussed in Chapter 6, this treatment is an important point since one might consider calculations of the neutron-deficient Sn isotopes with a ^{100}Sn (or ^{90}Zr) core, i.e. without the proton and neutron (or neutron) $g_{9/2}$ orbital in the valence space. This calculations might demand effective three-body forces and two-body E2 operators to describe the experimental reduced transition probabilities $B(E2)$ values.

1.4.2. Internal conversion

In addition to the de-excitation of a nuclear level via the emission of a γ ray, internal conversion is another mechanism through which a nuclear excited state can decay. It was first observed by O. Hahn and L. Meitner [67] and the phenomenon was called "conversion of γ radiation". A few years later the physicist H.R. Hulme [68] gave the first correct theoretical interpretation of the process.

Internal conversion proceeds by the ejection of an atomic electron, due to the interaction between the electromagnetic field produced by the nucleus and the atomic electron. In this phenomenon, that seems not to depend from the nuclear structure, the electron wave function penetrates the nucleus and interacts with its electromagnetic field. For this reason it is obviously more probable that this mechanism involves the inner electrons. After the ejection of the atomic electron, a vacancy remains in its shell and it will be immediately refilled by the electrons from the upper shells: as effect of this cascade, X-rays and Auger electron emission takes place.

The involved atom shell depends on the multipole character of the field. However, the internal conversion rate can be altered by changing the chemical conditions of the atom because the transition is heavily dependent upon the electron configuration. From atomic physics, the chemical bonds involve the external electrons, whose contribution to the internal conversion rate becomes significant only for high order corrections. In fact, recent studies show that the internal conversion rate is modified by the ionization of the atom [69] but this effect decreases rapidly with the increasing atomic number Z [70]. For this reason the theoretical predictions of the conversion process usually consider the atom as a free and neutral system.

Internal conversion is caused by variations in the radial part of the electromagnetic potential, while the γ-ray emission is caused by transverse variations. For this reason this process competes with the γ-ray emission: the total electromagnetic decay probability λ_t has indeed two components, λ_γ arising from γ-ray emission and λ_e from internal conversion:

$$\lambda_t = \lambda_\gamma + \lambda_e = \lambda_\gamma \left(1 + \frac{\lambda_e}{\lambda_\gamma}\right) \equiv \lambda_\gamma \left(1 + \alpha\right) \quad . \tag{1.34}$$

When including both the processes in the decay probability, it is convenient to define the (total) internal conversion coefficient $\alpha \equiv \frac{\lambda_e}{\lambda_\gamma}$, which helps to compare the two ways of decay.

Since well known aspects of atomic physics are involved, it is possible to evaluate these coefficients theoretically: the main contribution, that is given by the inner electrons, can be calculated with extreme precision. On the other hand, as introduced before, the high order corrections, which are due to more external electrons, can strongly change with the boundary conditions. However, under the assumptions that the penetration of the electron wave function in the nucleus in negligible and that the ejected electron can be described as a free particle, an approximate nuclear-structure independent description of the internal conversion coefficient can be found:

$$\begin{aligned} \alpha(EL) &\approx \frac{Z^3}{n^3} \frac{L}{L+1} \left(\frac{e^2}{4\pi\epsilon_0 \hbar c}\right)^4 \left(\frac{2m_e c^2}{E_\gamma}\right)^{L+\frac{5}{2}} \\ \alpha(ML) &\approx \frac{Z^3}{n^3} \left(\frac{e^2}{4\pi\epsilon_0 \hbar c}\right)^4 \left(\frac{2m_e c^2}{E_\gamma}\right)^{L+\frac{3}{2}} \quad . \end{aligned} \tag{1.35}$$

The internal conversion coefficient increases with Z^3, with the angular momentum L and with the inverse of the transition energy (E_γ). The internal conversion coefficients are tabulated [71, 72].

1.4.3. Gamma-ray detection: interaction of radiation with matter

For γ-ray spectroscopic studies a complete absorption of the energy of the γ ray is most important. In nuclear physics the γ-ray energies, which are relevant for such studies, cover over 3 orders of magnitude ($\approx$ 10 keV - 10 MeV) and in this range the interaction of the electromagnetic radiation with matter can mainly take place through four mechanisms:

- Rayleigh scattering
- photoelectric effect
- Compton scattering
- pair production

The contribution of these phenomena to the total cross section depends not only on the atomic number Z of the detector material but also on the energy E_γ of the impinging γ ray. The absorption capabilities of the different mechanisms as a function of the γ-ray energy is presented for germanium detection material in Figure 1.13.

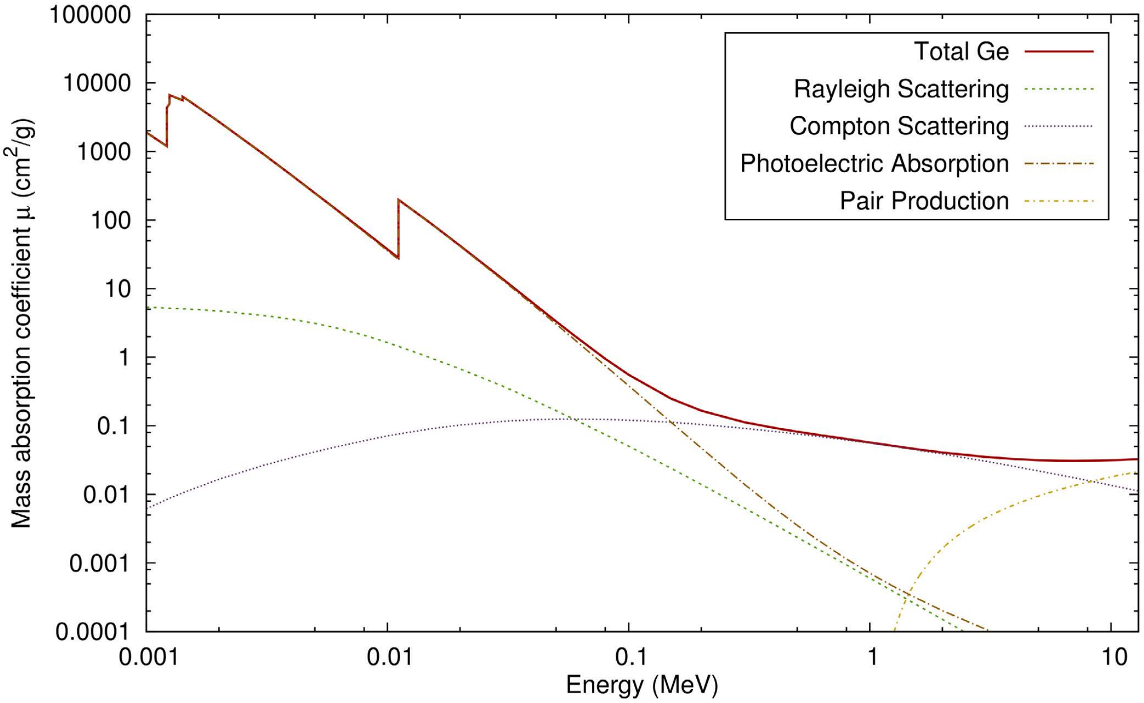

Figure 1.13.: Mass absorption coefficient of electromagnetic radiation in germanium ($Z = 32$) as a function of the γ-ray energy. The coloured lines represent the different interaction mechanisms. Data taken from Reference [73].

Due to the cross sections of the involved processes, a high atomic number Z of the detector material and a large volume is preferred to detect the γ rays. On one side, scintillation detectors, like $NaI(Tl)$, BGO or $LaBr_3$(Ce), have a high Z but their energy resolution is limited to a few percent. On the other side, semiconductor detectors, like germanium detectors, have a superior energy resolution but for γ-ray energies between 150 keV and 8 MeV the Compton effect is the predominant interaction (see Figure 1.13).

Rayleigh scattering

The Rayleigh scattering is the elastic scattering of electromagnetic radiation by particles much smaller than the wavelength of the radiation itself. Such a phenomenon results from the electric polarisability of the particles: the oscillating electric field of a light wave acts on the charges within a particle, causing them to move at the same frequency. Therefore, the particle becomes a small radiating dipole, whose radiation is seen as scattered light.

While the scattering probability depends on the atomic number of the particle[4] and on the unpolarised impinging-radiation wavelength, e. g.

$$\sigma \approx Z^2 \lambda^{-4} \quad , \tag{1.36}$$

the intensity of the emitted electromagnetic radiation is proportional to the sixth power of the particle's radius. For this reason, as can be deduced from Figure 1.13, the process is practically negligible at the atomic nucleus scale but it becomes more important when it involves atoms and molecules. Indeed, the process is known mainly because Rayleigh scattering of sunlight in the atmosphere causes the blue colour of the sky.

Photoelectric effect

The photoelectric effect is the emission of electrons or other free carriers when light is shone onto a material. With this phenomenon the bound atomic electron interacts electromagnetically with the γ ray and, after the absorption, the photoelectron appears with an energy given by

$$E_{e^-} = h\nu - E_b \quad , \tag{1.37}$$

where E_b represents the binding energy of the carrier in its original shell.

In addition to the photoelectron, the interaction also creates an ionized absorber atom with a vacancy in one of its bound shells. This vacancy is quickly filled through capture of a free electron from the medium and/or rearrangement of electrons from other shells of the atom. Therefore, one or more characteristic X-ray photons may also be generated. In some cases the emission of an Auger electron may take place and carry away the atomic excitation energy.

The photoelectric process in germanium is the predominant mode of interaction for low-energy γ rays (see Figure 1.13). This process is also enhanced for materials with a high atomic number and, even if no analytic expression exists for describing the photoelectric absorption per atom over all range of γ-ray energy E_γ, an empirical trend of the cross section is deduced to be

$$\sigma \approx \frac{Z^n}{E_\gamma^{3.5}} \quad , \tag{1.38}$$

---

[4] The Rayleigh scattering becomes important when the electromagnetic radiation impinges on atoms and molecules. For this reason, the scattering properties depends on an *effective* atomic number of the particle, as it is discussed in References [74, 75].

where the exponent n varies between 4 and 5 over the γ-ray energy region of interest.

In the low-energy region of Figure 1.13 discontinuities in the photoelectric absorption curve appear at γ-ray energies that correspond to the binding energies of electrons in the various shells of the absorber atom. In fact, for γ-ray energies slightly below the edge, the process is no longer possible and therefore the interaction probability drops.

Compton scattering

The interaction process of Compton scattering takes place between the incident γ ray and an electron of the absorbing material: the incoming γ ray is deflected through an angle θ with respect to its original direction, transferring part of its energy to the electron.

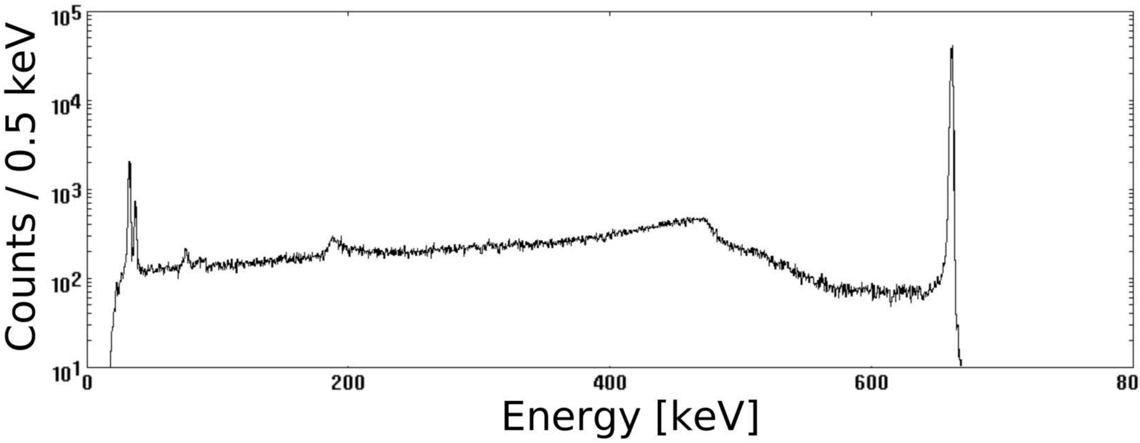

Figure 1.14.: Experimental γ-ray energy spectrum for ^{137}Cs radioactive source. The large peak at 662 keV is due to the γ ray emitted after the beta decay of the nucleus, while the little bump at around 480 keV is the *Compton edge* caused by the backward-scattered γ rays that escape from the germanium detector.

Due to the energy and momentum conservation, the transferred energy can vary from zero to a large fraction of γ-ray energy that is related to the scattering angle. The relation between the energy of the photon before ($h\nu$) and after ($h\nu'$) the scattering can be easily obtained from the conservation laws

$$h\nu' = \frac{h\nu}{1 + \dfrac{h\nu}{m_0c^2}(1 - cos\theta)} \quad , \tag{1.39}$$

where m_0c^2 is the rest-mass energy of the electron.

The probability of Compton scattering per atom of the absorber depends on the number of electrons available as scattering targets and therefore increases linearly with Z. The angular distribution of scattered γ rays is predicted by the Klein-Nishina formula [76]

$$\frac{d\sigma}{d\Omega} = Zr_0^2 \frac{1}{\left[1 + \frac{h\nu}{m_0c^2}\left(1 - cos\theta\right)\right]^2} \frac{1 + cos^2\theta}{2} \left[1 + \frac{\left(\frac{h\nu}{m_oc^2}\right)^2 (1 - cos\theta)^2}{(1 + cos^2\theta)\left[1 + \frac{h\nu}{m_0c^2}\left(1 - cos\theta\right)\right]}\right] , \tag{1.40}$$

where r_0 is the classical electron radius.

Considering a germanium detector, because of the finite volume of the crystal, a Compton scattered γ ray can exit the detector and hence only deposit part of its energy. The effect of this mechanism is the increasing of the background for energies lower than the so called *Compton edge*, which represents the limit when the γ ray is completely back-scattered ($\theta = \pi$). Figure 1.14, showing the γ-ray energy spectrum for ^{137}Cs radioactive source, is reported as an example of such phenomenon.

Pair production

For E_γ larger than twice the rest-mass energy of an electron, the process of pair production is energetically possible. As it is shown in Figure 1.13, the pair-production probability remains very low until the γ-ray energy approach several MeV: indeed in a germanium detector this process becomes predominant when $E_\gamma > 8$ MeV. In this interaction mechanism the γ ray is converted in an electron-positron pair, which has kinetic energy $E_k^{e\bar{e}} = E_\gamma - 1.022$ MeV. Because the positron will subsequently annihilate after slowing down in the absorbing medium, two annihilation photons are normally produced as secondary products of the interaction.

No simple expression exists for the probability of the pair production mechanism, but it has been experimentally seen that the magnitude varies approximately as the square of the material atomic number ($\sigma \approx Z^2$).

As it was the case for the Compton scattering, also the γ ray originated from the annihilation of the position can escape from the germanium detector. These events appear as a continuous background in the measured γ-ray spectrum or as additional peaks having the full energy minus 511 keV (single-escape peak) or 1022 keV (double-escape peak).

1.5. What is known along Z=50

Across the Segrè chart of nuclei, the tin isotopes have a privileged status. Besides containing the longest chain of isotopes in between two doubly magic nuclei, in this case ^{100}Sn and ^{132}Sn, accessible experimentally, the valley of stability crosses this chain in the middle. This allows systematic studies of basic nuclear properties from very neutron-deficient $N = Z$ to very neutron-rich nuclei.

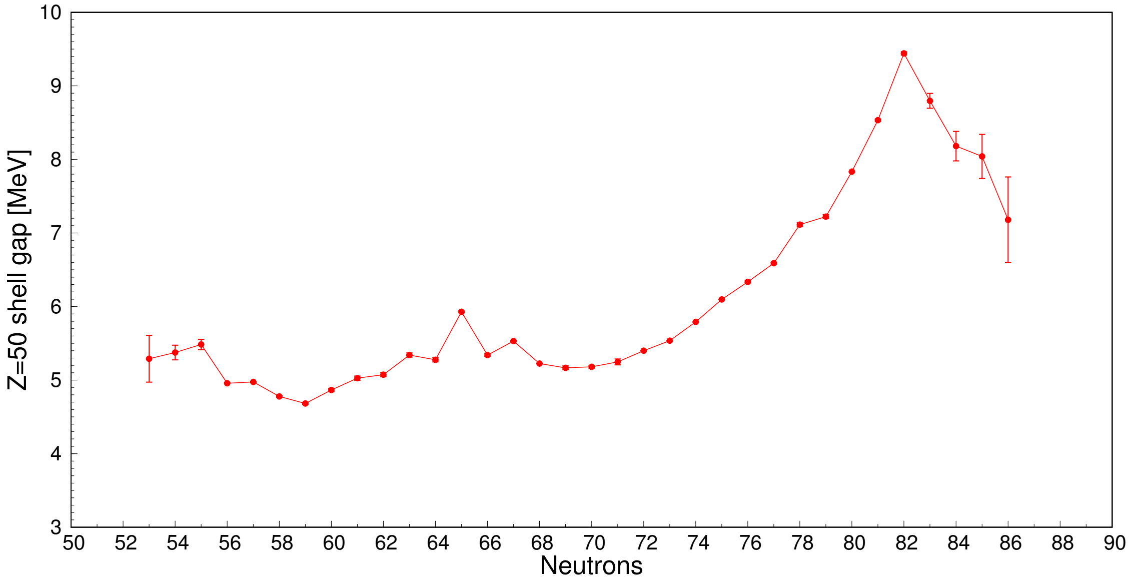

Figure 1.15.: Systematics of the $Z = 50$ proton shell gap as a function of the neutron number. The experimental values are taken from Reference [77].

Several studies have been performed in this region to examine the robustness of the proton shell closure when the $N = 50, 82$ magic numbers are approached. The magnitude of the proton gap is well known for neutron-rich nuclei beyond the end of the major shell and shows a maximum for ^{132}Sn [77, 78]. However, on the neutron-deficient side experimental information is more scarce and only indirect evidence for a good $Z = 50$ shell closure exists, e.g. the excitation energy of the core-excited isomer in ^{98}Cd [79] or the large Gamow-Teller strength observed in the β decay of ^{100}Sn [80]. The two works provide different and incompatible evaluation of the $Z = 50$ shell closure for ^{100}Sn: the first estimates a proton shell gap of ≈ 6.5 MeV, adopted value for the majority of the theoretical calculations, while the second gives a gap of ≈ 3 MeV. In Figure 1.15 the systematic of the directly-measured proton shell gap $Z = 50$ is shown as a function of the neutron number: the value of such shell gap has been defined as the difference $S_{2p}(Z = 50) - S_{2p}(Z = 52)$, where $S_{2p}(Z)$ represents the separation energy for extracting two protons from a nucleus with a given atomic number [77].

Complementary probes of the shell gap evolution can be obtained from the excitation energy E_x of the first 2^+ and 4^+ states and the reduced transition probability $B(E2; 2_1^+ \rightarrow 0_{g.s.}^+)$ of the neutron-deficient even-even Sn isotopes when ^{100}Sn is approached.

Excitation energy and seniority isomers

Figure 1.16 shows the systematics of the low-lying excited states for the even-even Sn nuclei for mass numbers between $A = 102$ and $A = 130$. The excitation energies of the low-lying excited states 2^+ and 4^+ of the tin isotopes between ^{100}Sn and ^{132}Sn seem rather constant. For neutron-deficient Sn isotopes with $A \leq 112$ the presence of the isomer 6^+ with lifetimes larger than 1 ns suggests the typical seniority for the $(g_{7/2})^{v=2}$ configuration. Similar consideration can be done for heavier Sn isotopes, whose 10^+ states have a long lifetime of the order of few μs: such state can also be identified as a seniority isomer arising from the neutron orbital $(h_{11/2})^{v=2}$. These two regions seem to be divided by a soft closed subshell at $N = 64$ [81].

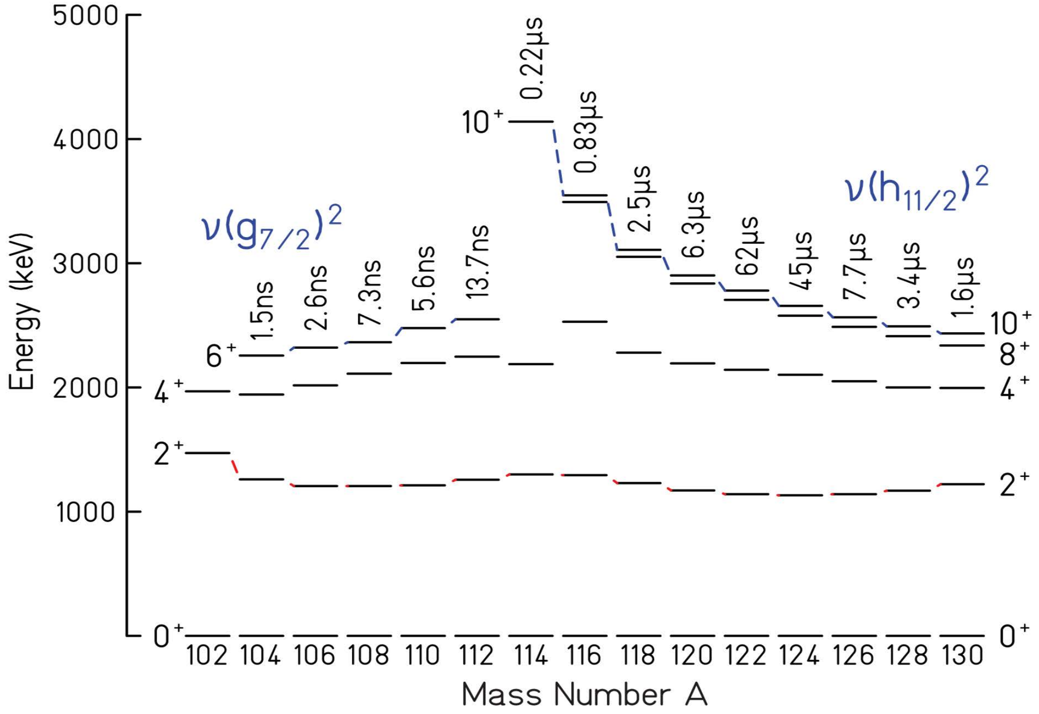
5000
4000
3000
2000
1000
Energy (keV)
ν(g7/2)2
ν(h11/2)2
1.5ns
2.6ns
7.3ns
5.6ns
13.7ns
0.22μs
0.83μs
2.5μs
6.3μs
62μs
45μs
7.7μs
3.4μs
1.6μs
10+
6+
4+
2+
0+
10+
8+
4+
2+
0+
102 104 106 108 110 112 114 116 118 120 122 124 126 128 130
Mass Number A

Figure 1.16.: Systematics for even-even Sn nuclei of mass numbers between $A = 102$ and $A = 130$ showing the partial level schemes up to the seniority isomers. For neutron-deficient Sn isotopes with $A \leq 112$ the presence of the 6^+ isomer with lifetimes larger than 1 ns suggests the typical seniority for the $(g_{7/2})^{v=2}$ configuration. For heavier Sn isotopes, whose 10^+ states have a long lifetime of the order of few μs, such state can also be identified as a seniority isomer arising from the neutron orbital $(h_{11/2})^{v=2}$. Levels of the same spin and positive parity are connected by dashed lines. Figure adapted from Reference [81].

Reduced transition probability

While the excitation energies of the 2^+_1 and 4^+_1 states are well known and rather constant, the $B(E2; 2^+ \rightarrow 0^+)$ transition strengths follow a kind of bell-shape behaviour. If a generalized seniority scheme is *naïvely* considered, the *a priori* expectation is an inverted parabola showing the maximum collectivity at mid-shell and smoothly decreasing towards the shell closures, reflecting the number of particles times the number of holes available within the major shell. This simplistic picture has been largely discussed among the nuclear physics community. Considering a single j shell in the seniority scheme frame work, the solution for the transition energies and for the transition operator matrix elements can be obtained analytically. The solution predicts constant $E_x(2^+)$ excitation energies and a parabolic pattern for the transition strengths. It has been shown that these key characteristics remain valid in the generalized seniority scheme as long as the orbits within the major shell are filled with the same rate, while for different level occupancies a shallow minimum for the $B(E2)$ values can be obtained at mid shell [82].

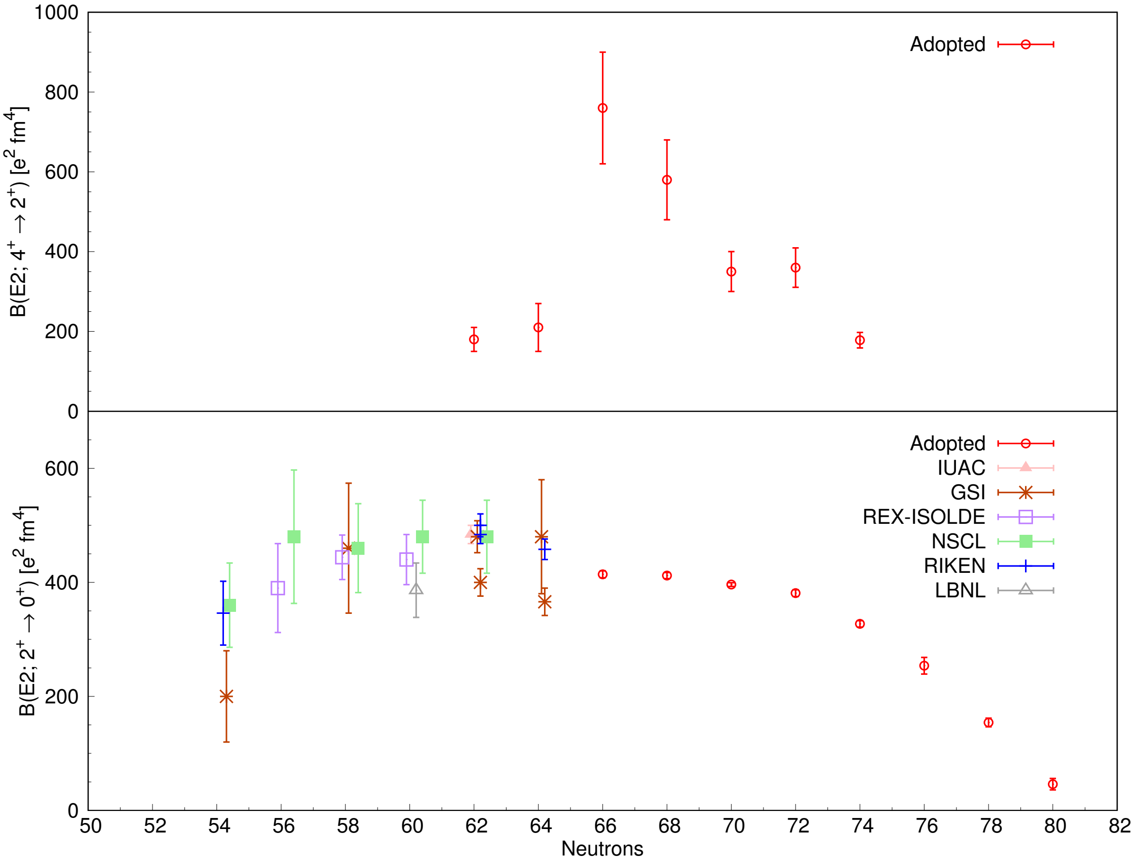

Figure 1.17.: Reduced transition probability $B(E2)$ systematics along the whole Sn isotopic chain for (top) $4^+ \rightarrow 2^+$ and (bottom) $2^+ \rightarrow 0^+$ transitions. The “adopted” results for the neutron-rich isotopes are taken from Reference [2], while for the neutron-deficient region the results are taken from References [81, 83–93]. The rapid change in the $B(E2)$ values at $N = 64$ seems to be related to the neutron subshell closure [81].

However, Figure 1.17 shows that such *naïve* prediction do not reproduce the experimental results. In fact, on one side for the neutron-rich Sn isotopes the reduced transition probability seems to follow the parabolic behaviour with the maximum at the mid shell [94, 95] (typical trend that one would expect for one-body even operator, such as the $B(E2)$) that is well described by Large-Scale Shell-Model (LSSM) calculations [83, 86]. On the other side for the neutron-deficient Sn isotopes the $B(E2; 2^+ \rightarrow 0^+)$ values [81, 83–87] seems to have a smoother trend that is almost constant for $106 \leq A \leq 112$. In addition, for such neutron-deficient region there is a lack of information on the $B(E2; 4^+ \rightarrow 2^+)$, while their values would help to make a more robust physical interpretation. Several theoretical interpretations and calculations have been performed during the last decades, but none of them is able to reproduce consistently the trend of the experimental results.

Despite fusion-evaporation reactions are appropriate for the population and the investigation of neutron-deficient nuclei, the presence of the 6^+ seniority isomers avoids the measurement of the reduced transition probability of the low-lying 2^+ and 4^+ states lifetimes. For this reason, up to date the region has been studied via Coulomb excitation measurements [81, 83–87], which allow a direct population of the low-lying states of interest. Obviously such measurement can be performed only in facilities which provides proton-rich radioactive beams, whose intensities ($10^2 - 10^8$ pps) are usually several orders of magnitude lower than stable beams ($10^9 - 10^{10}$ pps). Those experiments were performed or via safe (forward) Coulomb excitation or via relativistic Coulomb excitation measurements, which favour single-step processes.

1.5.1. Physical motivation of the experiment

In order to study the robustness of the proton shell closure and the origin of the flatter $B(E2; 2^+ \rightarrow 0^+)$ values when ^{100}Sn is approached, a more precise measurement of the reduced transition probabilities is crucial for the neutron-deficient Sn isotopes. Figure 1.17 shows that for neutron-deficient Sn isotopes only experimental $B(E2; 2^+ \rightarrow 0^+)$ values are present but they suffer from large experimental uncertainties, which make the physical interpretation difficult. Indeed, so far no theoretical calculation is capable to successfully describe the full Sn chain.

Extra constraints can be obtained from the measurement of the reduced transition probability for $4^+ \rightarrow 2^+$ transitions. In fact, while the wave functions describing the first 2^+ and 4^+ state are expected to be very similar, for the Sn isotopes the $4^+ \rightarrow 2^+$ transitions conserve seniority ($\Delta v = 0$) and $2^+ \rightarrow 0^+$ transitions do not ($\Delta v = 2$).

The experiment described in this thesis was performed in order to derive the reduced transition probabilities $B(E2; 2^+ \rightarrow 0^+)$ and $B(E2; 4^+ \rightarrow 2^+)$ in ^{106,108}Sn from the lifetime measurements of their low-lying excited states.

1.5.2. The experiment

A different method from that of Coulomb excitation and fusion-evaporation reactions was adopted to measure the lifetime of the low-lying states 2^+ and 4^+ in the neutron-deficient Sn isotopes. It was shown by Broda and collaborators [96, 97] that neutron-deficient nuclei close to the $N = Z = 50$ region can be populated via multi-nucleon transfer reactions. These reaction mechanism is usually adopted for investigating neutron-rich nuclei [54, 98] and allows the direct population of the low-lying yrast and near-yrast states (see Figure 1.9).

The experiment described in this thesis was devoted to the measurement of the reduced transition probability for ^{106,108}Sn by using the Recoil Distance Doppler-Shift (RDDS) method [99, 100]. The nuclei of interest were populated via a MNT reaction where a ^{106}Cd beam, provided by one separated-sector cyclotron of the GANIL facility (France) at the energy of 770 MeV and with an average intensity of $\approx 10^{10}$ pps, impinged onto a 0.715 mg/cm^2 thick ^{92}Mo target [101, 102]. For lifetime measurements the RDDS method was employed using the differential Cologne plunger, placing a 1.6 mg/cm^2 thick ^{24}Mg degrader after the target. More details on the optimisation of the experimental setup can be found in Appendix A.

The complete identification for the projectile-like products was obtained on an event-by-event basis using the VAMOS++ spectrometer. In coincidence with the magnetic spectrometer the γ rays were detected by eight AGATA Triple Clusters, placed at backward angles in a compact configuration. In addition, combining the reaction mechanism with a large angular acceptance magnetic spectrometer also allowed to control the feeding from higher-lying states via a gate on the Total Kinetic Energy Loss (TKEL) [98].

The experiment presented in this thesis is complementary to the Coulomb excitation experiments performed up to date in this region. Moreover, the performed experiment represents the very first lifetime measurement of the neutron-deficient Sn low-lying states and in particular the first estimation of the reduced transition probability for the $4^+ \rightarrow 2^+$ transitions.

2

Experimental Setup

In this chapter the experimental setup is described. After a brief description of the GANIL facility, the AGATA spectrometer and its working principle are presented. Afterwards, the VAMOS++ magnetic spectrometer follows with the description of all its detectors. Then the Cologne differential plunger device is also introduced.

2.1. The GANIL accelerator complex

In Caen (France) the Grand Accélérateur National d'Ions Lourds (GANIL) provides heavy ion beams for nuclear and atomic physics, astrophysics, material science and radiobiology studies. GANIL-SPIRAL is the largest accelerator complex in France and one of the largest facilities for heavy ions in Europe. The facility was jointly created and constructed by two research organizations, CEA/DSM and CNRS/IN2P3, which decided in August 1975 to build this laboratory in Caen. The first beam was delivered in November 1982, and the first experiment took place in January 1983. In the following years, the laboratory continuously developed and acquired a worldwide reputation in the field of nuclear physics. In particular, in 1984 the doubly achromatic LISE spectrometer was installed in GANIL for the study of of exotic nuclei, produced by the fragmentation of high-energy heavy-ion beams with thick light targets. With its spectrometer GANIL has been one of the very first facilities working on the production and investigation of radioactive ion beams. Then, in 1990 an upgrade of the accelerators was made. As a result, a wide spectrum of high intensity ion beams ranging from ^{12}C to ^{238}U accelerated up to 95 MeV/A was available. In 1995 GANIL received the status of a European Large Scale Facility for research. A major upgrade was achieved in 2001 with SPIRAL, with the addition of the Isotope Separation On Line (ISOL) technique for the production of secondary beams of light exotic ions and post-accelerated by a new cyclotron. GANIL is continuously evolving. A major step was the signature for the construction of SPIRAL2 in 2006 for the production of radioactive ion beams originating from the ^{238}U fission.

The production of stable and radioactive ion beams for nuclear physics studies represent the principal activity of GANIL. Using its 5 cyclotrons GANIL-SPIRAL is a truly multi-beam facility and different experiments can be simultaneously run in different experimental areas. In Figure 2.1 a schematic view of the facility is presented, showing the accelerators and the main devices installed in the different experimental halls.

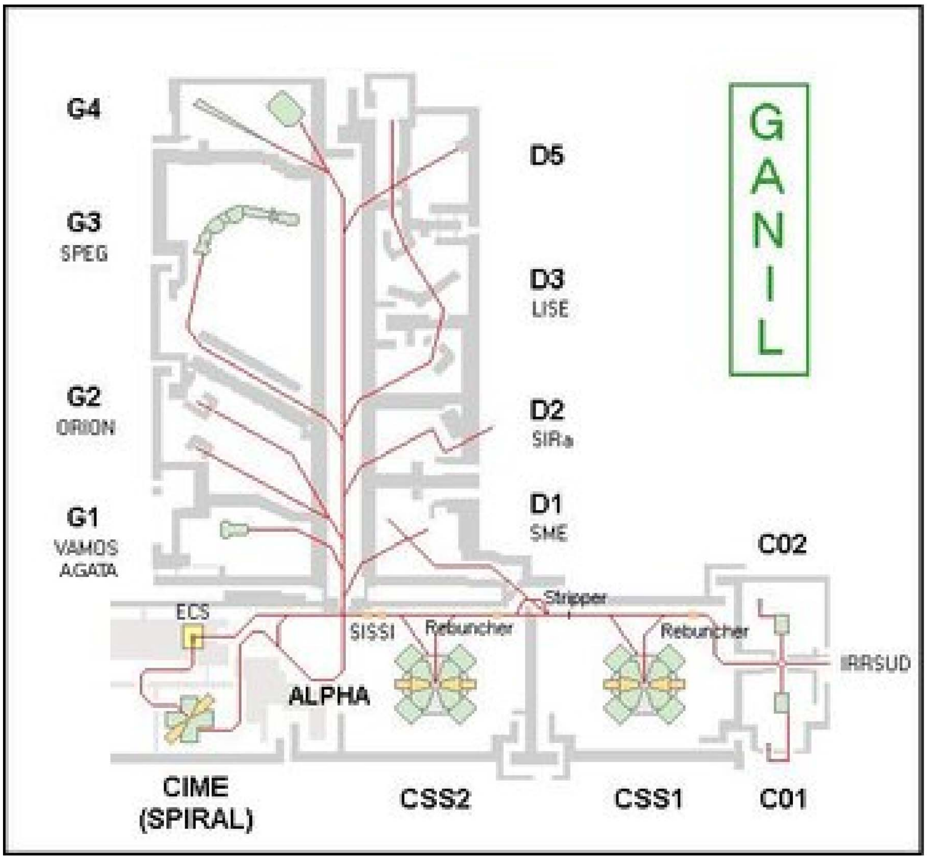
G4
D5
G
A
N
I
L
G3
SPEG
D3
LISE
G2
ORION
D2
SIRa
G1
VAMOS
AGATA
D1
SME
C02
Stripper
ECS
SISSI
Rebuncher
Rebuncher
IRRSUD
ALPHA
CIME
(SPIRAL)
CSS2
CSS1
C01

Figure 2.1.: Sketch of the GANIL facility. The beams coming from the 5 cyclotrons are distributed in the different experimental area. The experiment described in this work took place in the experimental hall G1, using the VAMOS-AGATA setup.

After extracting the ion of interest from the source, the cyclotron C0 pre-accelerates the beam to an energy ranging from 0.25 MeV to 1 MeV, depending on the charge state over mass ratio. Then the particles travel inside the CSS1 cyclotron and, after completing between 100 and 500 revolutions, their trajectory reachs the maximum radius of 3 m. During the experiment that will be discussed in this work, the ^{106}Cd beam was provided by the CSS1 at the energy of 770 MeV and delivered to the experimental hall G1, where the VAMOS magnetic spectrometer was coupled with AGATA.

2.2. AGATA spectrometer

One of the most powerful methods to study the structure of nuclei is the detection of γ rays, which are emitted by the de-excitation of the nuclei produced in the nuclear reaction. In order to measure such radiation, it is convenient to use a solid detection medium and in particular semiconductors, such as germanium: thanks to their low energy band gap (less than 4 eV at 300 K) and the consequent low carrier-generation energy ($\approx 2-3$ eV/pair), semiconductors can provide a very good energy resolution for detecting the γ rays. Thanks to this property and due to its relatively high atomic number, germanium is used for building efficient electromagnetic radiation detectors: in particular High-Purity Ge (HPGe) detectors are commonly employed for γ-ray spectroscopy. In order to reach a high detection efficiency, the solid angle coverage of the γ spectrometer should be as high as possible. However the distance between the target and the detector is limited by the presence of the reaction chamber, where complementary devices, such as the plunger (see section 4), can be placed. Another issue arise when the detectors are put too close to the chamber. Due to the large counting rate induced by intense stable beam, the signal of several γ rays impinging on one crystals are summed up which makes the spectroscopy difficult. In the energy range of the γ-ray transitions the Compton-scattering probability is significant and, considering the dimensions of typical HPGe detector, that is approximatively 8 cm cylinder, and the mean-free path of a γ ray inside germanium (≈ 2 cm at 1 MeV), the radiation can escape from the detector increasing the background. For this reason, the HPGe detectors are usually surrounded by other veto detectors in order to suppress the escaped Compton-scattered events and to improve the peak-to total (P/T) ratio. The presence of these veto detectors, called anti-Compton shields, limits the possible detecting active volume reducing significantly the solid angle and consequently the maximum efficiency of the full γ-ray array. Additionally, in the case of in-beam spectroscopy the uncertainty of the γ-ray position should be as small as possible in order to perform a good Doppler correction.

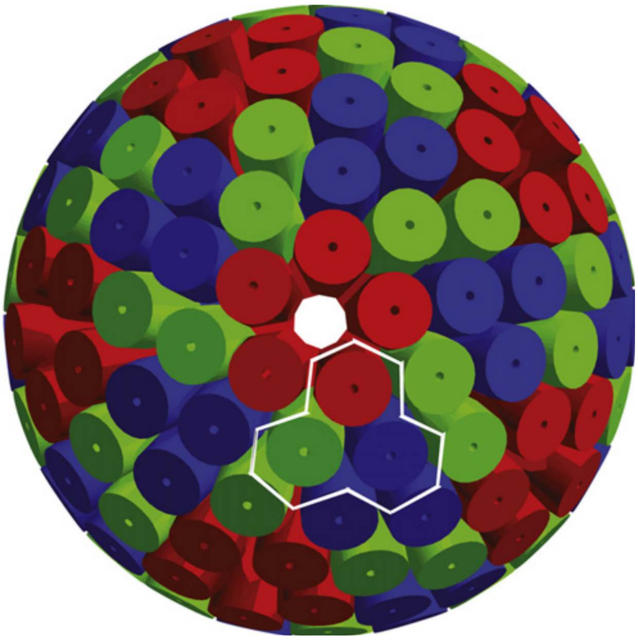

Figure 2.2.: Design of the geodesic geometry for the 4π solid angle coverage array. The white line represent a ATC detector, counting one (R,G,B) triplet of crystals. The figures is adapted from Reference [103].

In order to overcome these limitations, a new generation of HPGe detectors have been designed and developed. One of these new arrays is the Advange GAmma Tracking Array

(AGATA), European project supported by the funding of several agencies. The strength of the project is the segmentation of each detector, which allows first to determine the γ ray interaction position inside each crystal with the measured signal shapes and then to reconstruct the path of γ ray inside the array. The geodesic geometry shown in Figure 2.2 with 180 detectors has been chosen to maximise the active volume. Moreover, by employing the state-of-art of digital electronics and digital trigger systems, the maximum counting rate per detector is increased by one order of magnitude.

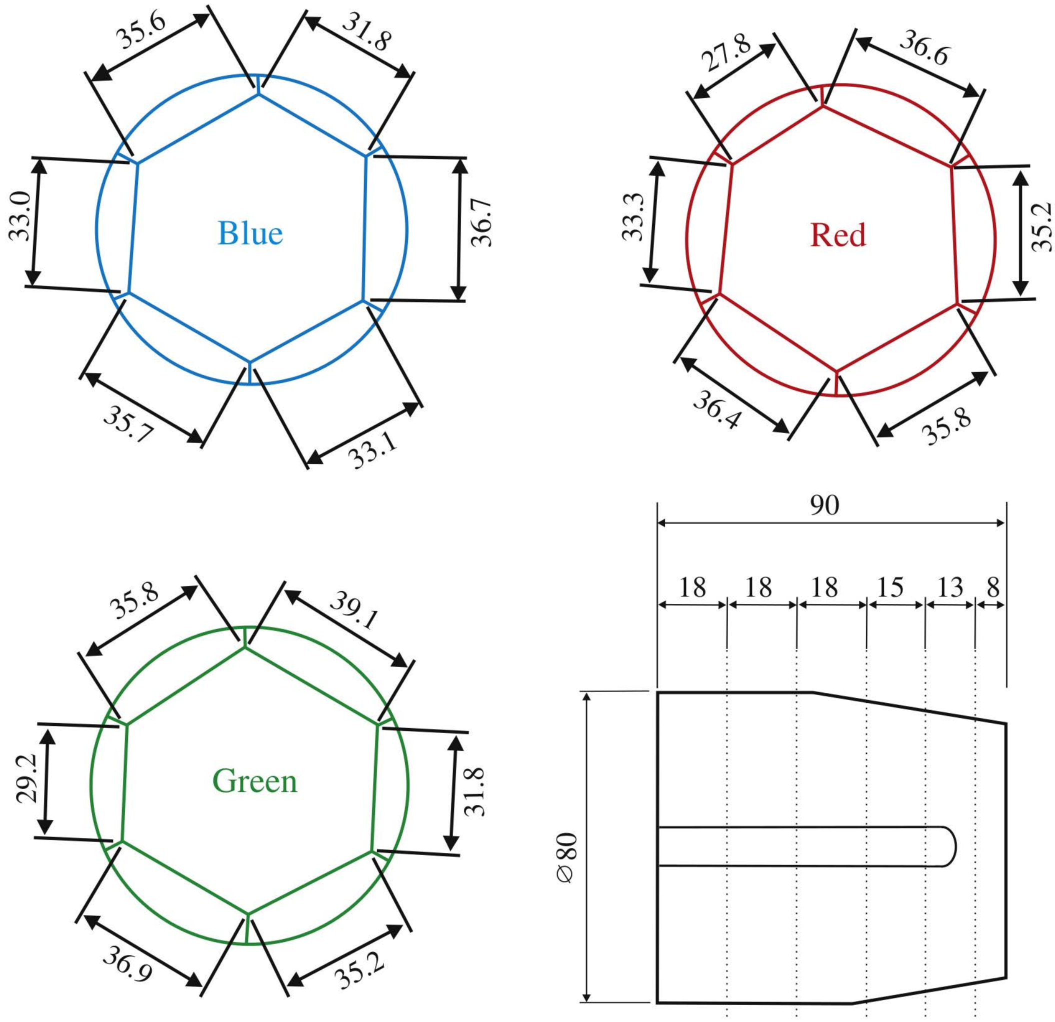

Figure 2.3.: AGATA technical drawings. Dimensions of the (R,G,B) types of the AGATA asymmetric crystals, composing an ATC detector. The figure is adapted from Reference [103].

The full AGATA array will be built out of 60 triple cluster (ATC), each of them composed by three asymmetric HPGe crystals. The technical drawing with the dimensions of the three different crystals is presented in Figure 2.3. Each crystal is a coaxial n-type HPGe, electrically segmented in 36 parts, as it is shown in the left panel of Figure 2.4. A cross talk of the level 10^{-3} between the segments has been observed, while the cross talk between the crystals is negligible [104]. Each segment has its own preamplifier, which is divided into a warm and a cold part, operating at cryogenic temperatures. These crystals are encapsulated in a sealed thin aluminium case, minimising the passive material between the crystals. On the right panel of Figure 2.4 a picture of an ATC is presented, showing the aluminium capsule and the cold and warm parts of the electronics.

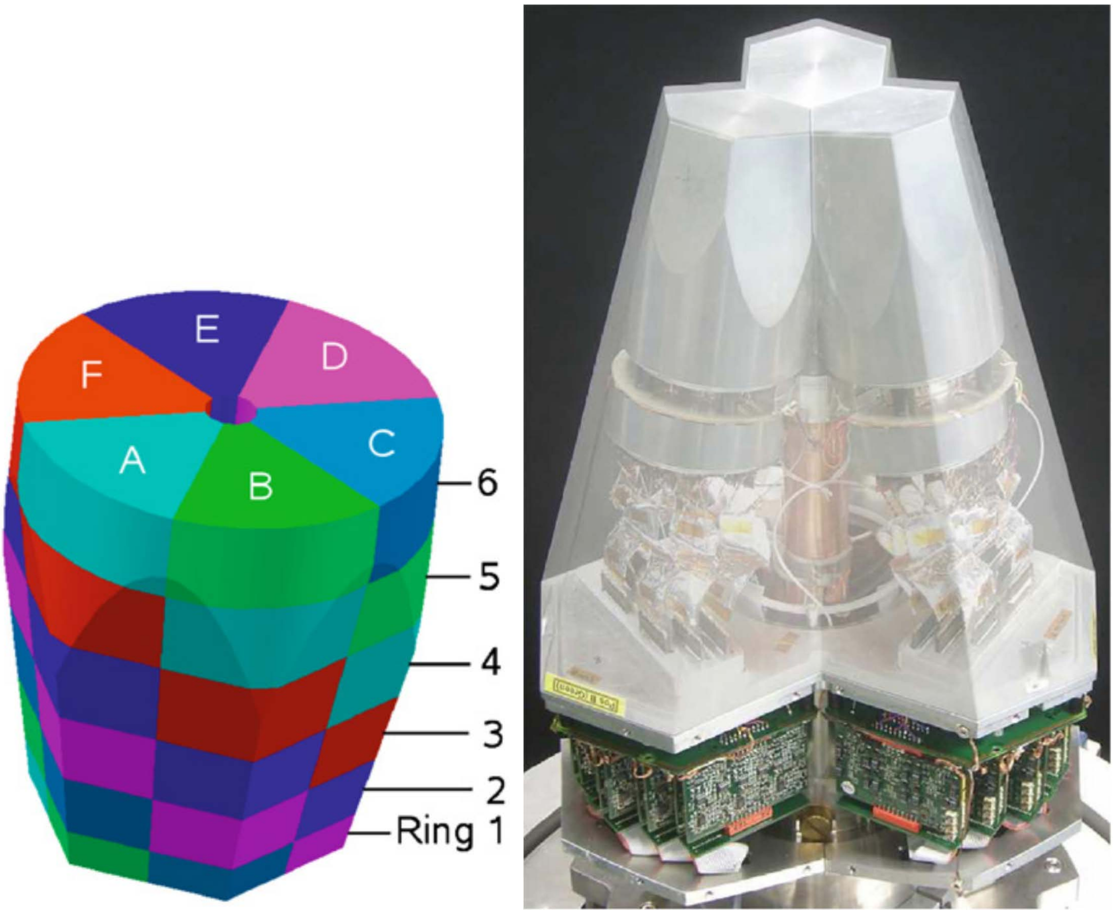

Figure 2.4.: AGATA triple cluster detectors. (left) Drawing of an AGATA crystal with its electrical segmentation into 36 segments, 6 rings of 6 segments each. (right) AGATA detector with graphically-edited transparent end cap, showing the three HPGe encapsulated crystals and their electronics. Figure taken from Reference [104].

For the experiment described in this thesis, 8 ATC detectors were mounted backward with respect to the fragments direction and the array was placed in a compact configuration in order to increase the overall γ-ray detection efficiency. In order to keep a good separation between the two components of a transition that are produced in the Recoil Distance Doppler-Shift (RDDS) method [100], the detector should not be placed too close to 90° degrees where the Doppler shift is minimum. Then, as a compromise between the requirements for larger efficiency and for the detector position, the array was placed at 18.5 cm from the target. A picture of the array surrounding the reaction chamber is shown in

Figure 2.5.

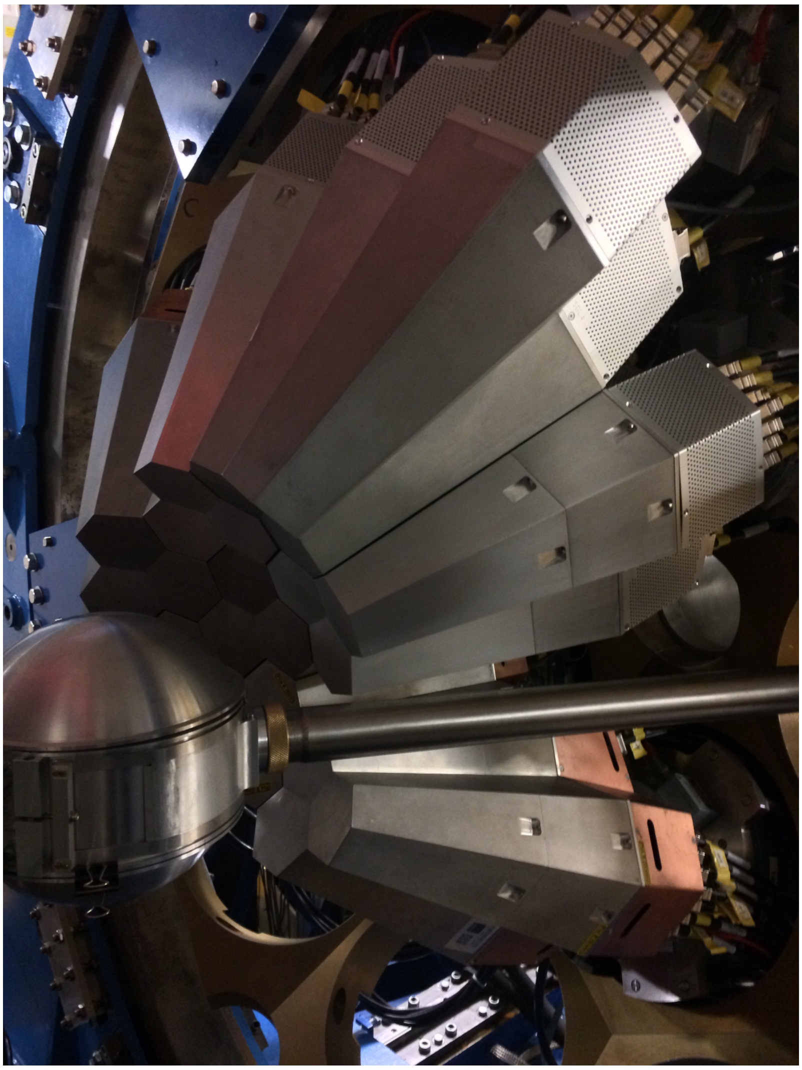

Figure 2.5.: During the experiment, the AGATA array was composed by 24 crystals and it was placed in compact configuration around the reaction chamber.

2.2.1. Pulse shape analysis

In a coaxial germanium detector, the shape of the charge collection signal as a function of the time depends on the distance between the position of the γ-ray interaction and the electrode which collects the charge. Indeed, the charge induced on the electrode by moving charge carriers (electrons and holes) in a coaxial germanium detector depends on the interaction position [105]. Consequently, the pulse shape analysis allows a radial determination of the position of the γ ray.

In the case of an electrically segmented detector, charges are induced also on the neighbouring electrodes, called mirror charges. In Figure 2.6 the central pad correspond to the segment where the γ ray interacted and created electron-hole pairs. This is called the segment with a *net-charge signal*. Moreover, the moving charges induce in the neighbouring electrodes other signals, called *transient signals*. As it is shown in the pads surrounding the central one of Figure 2.6, the transient signals have different shapes according to the position of the neighbour segments. The shape of net-charge and transient signals depends on the interaction position of the γ ray, so using those charge information a better position resolution can be achieved.

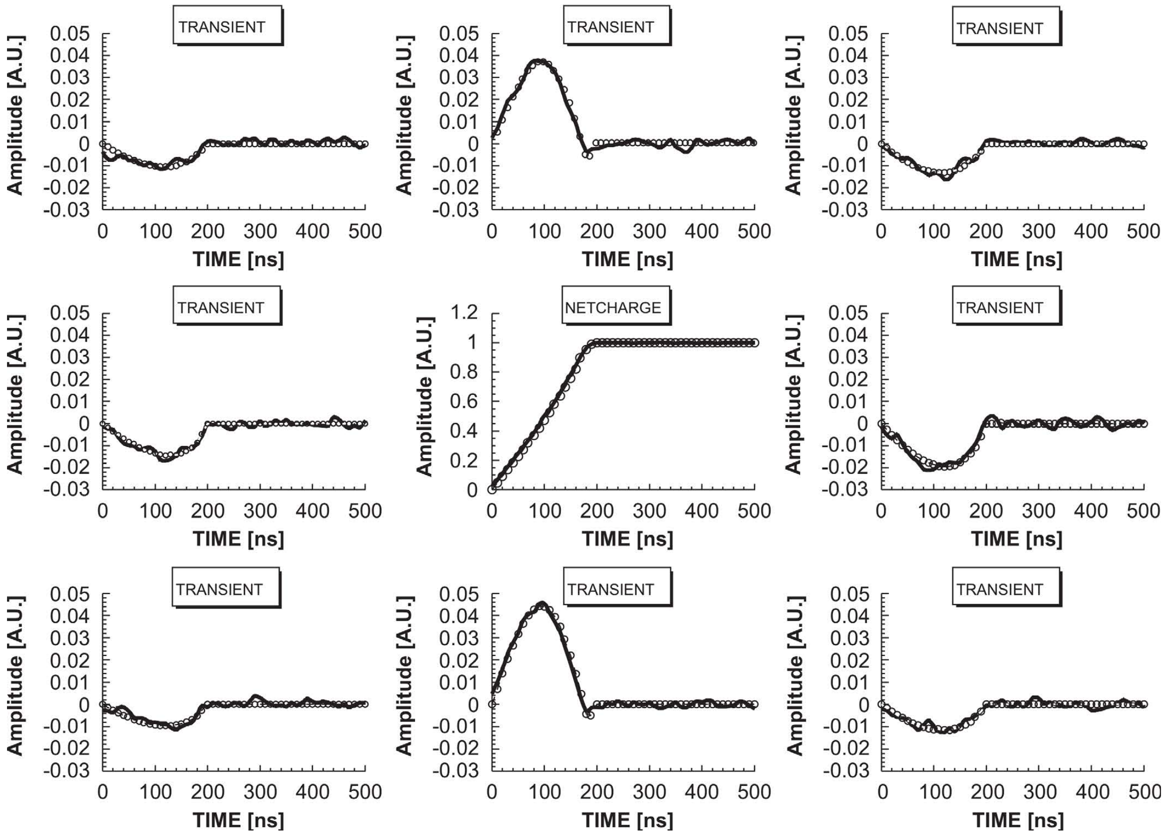

Figure 2.6.: Comparison between the simulated signal shape (circles) and the measured one (solid line), obtained with ^{137}Cs source. The signals displayed in the different panels are the net charge signal of the segment on which the measure is focused and the 8 transient signals given by its 8 neighbour segments. Figure taken from Reference [106].

For the determination of the interaction point which produces the measured signals, a base of reference signals is needed. In order to obtain the reference base signals, it is possible to scan each detector with a collimated source. Several scanning systems for the AGATA crystals have been constructed during the last decades [106–108], but nowadays the Pulse Shape Analysis (PSA) algorithm [109, 110] compares both the net and transient charges of each detector with a simulated-signal shape database. Figure 2.7 shows the time evolution of the shape of both net and transient signals as function of the interaction point inside a segment.

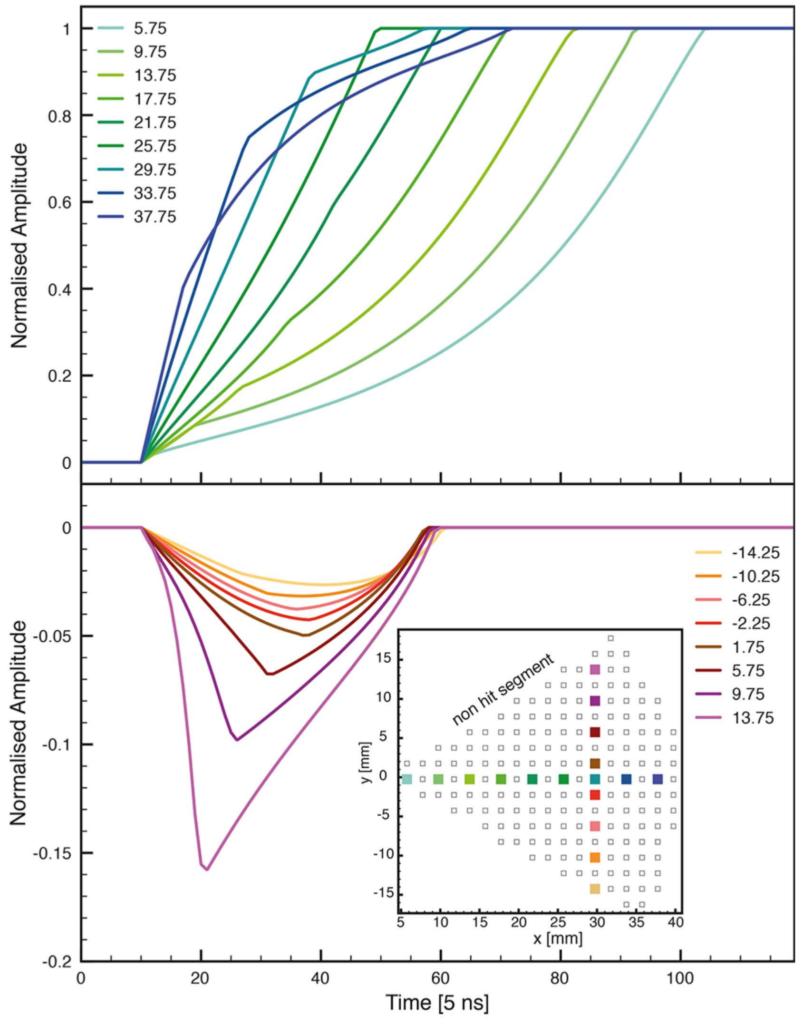

Figure 2.7.: Simulated traces for an AGATA detector: (top) the core signal for different radii and (bottom) the transient signals induced in a non-hit neighbouring segment. Colour code as indicated in the inset of the right graph. The slice is at 40.25 mm from the front of the detector. The figure is adapted from Reference [111].

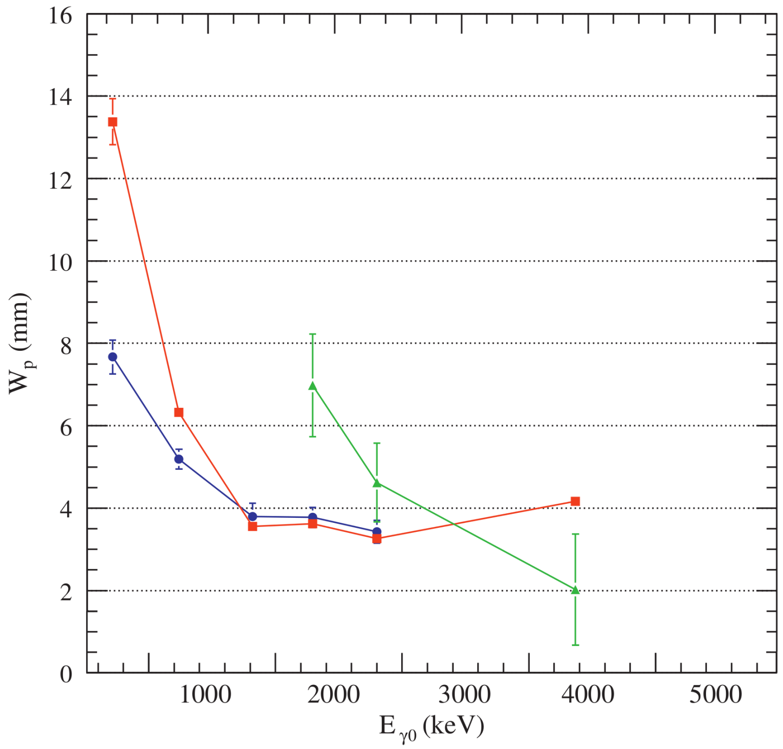

Figure 2.8.: Interaction position resolution (W_p) as function of the γ-ray energy for different interaction mechanisms: photoelectric effect (blue), Compton scattering (red) and pair production (green). The error bars are due to statistical errors only. The figure is adapted from Reference [112].

For this thesis the full grid search algorithm is used to identify the signal in the database with the best possible resolution, even if it is more time consuming than the adaptive algorithm [110]. Employing the full-grid Pulse Shape Analysis (PSA) algorithm, a 5 mm position resolution of the γ-ray interaction is achieved [109, 112]. In Figure 2.8 the interaction position resolution as function of the energy is shown for different interaction mechanism. The spatial resolution allows to determine precisely the angle of emission of the γ ray. Therefore, the AGATA array is very well suited for the Doppler correction of γ rays emitted in flight.

2.2.2. Tracking

The main task of γ-ray tracking is to identify the individual transitions of an event and to reconstruct their scattering sequence inside the detector using the energy and the spatial coordinates of the interaction points. In Figure 2.9 the characteristic features of γ-ray tracking are illustrated for the most relevant interaction mechanisms:

- Low-energy γ ray has a short mean free path and mainly interacts with matter via photoelectric absorption, transferring its energy to the electron into an isolated interaction point.

- Gamma rays with energies from a few hundred keV to some MeV are absorbed in the detector with a sequence of (a few) Compton scattering interactions and a final photoelectric effect. Such events are reconstructed using a figure of merit that quantifies how well the scattering angles determined from the position of the involved interaction points agree with the values obtained inserting the pertinent energies into the Compton scattering formula. The figure of merit is calculated for all permutations of the interaction points and the event is accepted if the merit of the best permutation is compatible with an empirically defined limit.

- Above the threshold energy of 1.022 MeV, pair production events become important. A strong signature of this mechanism is given by the fact that the first point of interaction collects the total γ-ray energy minus the mass needed to create the electron-positron pair, while the two annihilation photons generate their own clusters of interaction points in the vicinity of their interaction point.

The input for the tracking algorithms consists of energy and three-dimensional position for each interaction point (E_i, x_i, y_i, z_i). This information is provided from the PSA. A tracking algorithm is used to reconstruct the trajectories of the γ rays in order to determine their energy and direction. For the reconstruction of the γ-ray path a dedicated software procedure is used, considering the position uncertainty of the PSA and the possibility that not the total charge is collected. Currently, there are two different algorithms to perform tracking with AGATA, both are based on the forward tracking: the Orsay Forward Tracking (OFT) [113] and the MARS Gamma Tracking (MGT) [114].

The first step of the tracking algorithm is to group the interaction points in the crystal, deduced by the PSA, into clusters in the (θ, ϕ) plane, as it is shown in Figure 2.10. The angular coordinates (θ, ϕ) of all the interaction points are calculated at the beginning of the program and the interaction points are sorted according to increasing θ in order to make the cluster searching easier. Points are group in clusters according to their relative angular distance, which is adapted depending on the multiplicity of interaction points. For

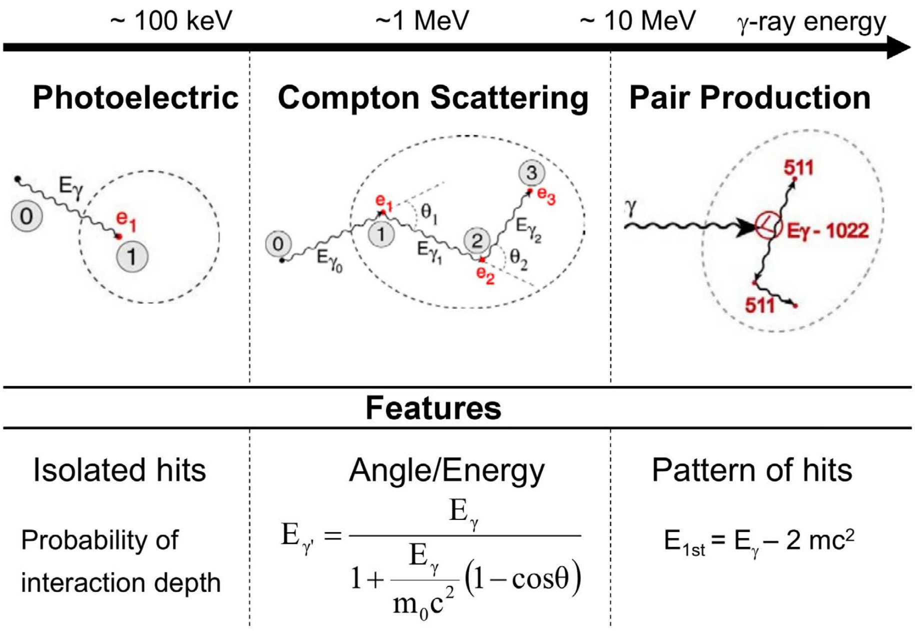
~ 100 keV
~1 MeV
~ 10 MeV
γ-ray energy
Photoelectric
Compton Scattering
Pair Production
0
1
Eγ
e1
0
1
2
3
Eγ0
Eγ1
Eγ2
e1
e2
e3
θ1
θ2
γ
511
511
Eγ - 1022
Features
Isolated hits
Probability of interaction depth
Angle/Energy
$E_{\gamma'} = \frac{E_\gamma}{1 + \frac{E_\gamma}{m_0 c^2}(1 - \cos\theta)}$
Pattern of hits
$E_{1st} = E_\gamma - 2\,mc^2$

Figure 2.9.: The relevant γ-ray interaction mechanisms in matter and the features exploited by the tracking algorithms. Figure taken from Reference [114].

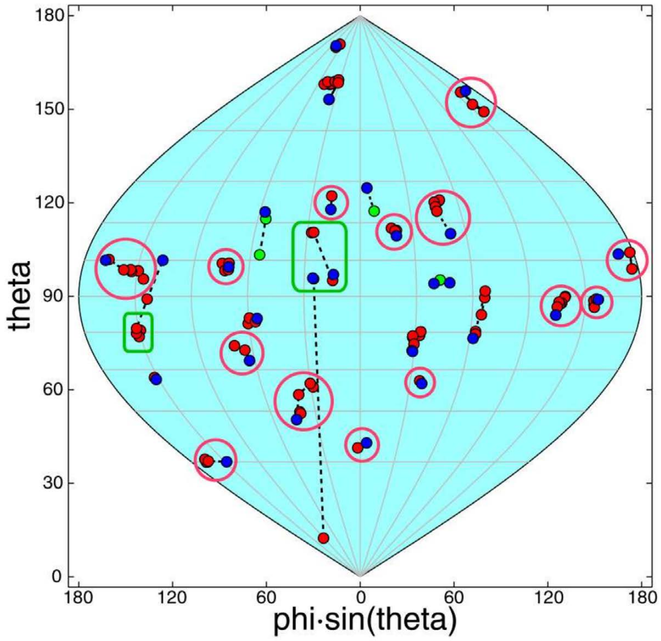

Figure 2.10.: Interaction positions and cluster identification in a 4π germanium shell as considered by the tracking algorithm. Figure taken form Reference [115].

each cluster and each permutation of the interaction points using the target position as the source of the γ ray, a figure of merit is calculated. In order to be further processed, single interaction points must be well isolated hits: in the OFT algorithm the closest interaction point must be physically at least 4 cm away. If this is the case, the figure of merit of the cluster is computed: the algorithm estimates the probability for the incident photon to travel the distance in germanium from the target position to the position of the interaction point and then to undergo a photoelectric interaction.

For this work the OFT algorithm was used in the identification of the γ-ray path inside the AGATA array. This algorithm depends on 3 empirical parameters that can be chosen in order to optimise the tracking performances in agreement with the goal of the experiment. In Chapter 3 the description of the parameters will be presented, while in Appendix B their optimisation will be discussed.

2.3. VAMOS spectrometer

The *VAriable MOde Spectrometer* (VAMOS) [116, 117] is a large acceptance ion spectrometer used to fully identify, providing both the atomic number Z and the mass A, the fragments produced in a heavy-ion induced reaction. It consist of two large aperture quadrupoles and a large magnetic dipole configured to operate in different ion optical modes. Depending upon the kinematics of the reaction, the operating mode of VAMOS can be varied to optimise different requirements. In the mass-dispersive mode operation, the spectrometer selects and separates the reaction products according to the momentum to charge ratio and their unique identification is achieved via event-by-event reconstruction of ion trajectories in the magnetic field. The main operational features of the spectrometer are listed in Table 2.1.

Horizontal acceptance	-125 mrad to +100 mrad
Vertical acceptance	±160 mrad
M/q resolution	≈0.6%
Maximum rigidity	1.6 Tm
Flight path lenght	≈ 760 cm

Table 2.1.: Optimal features of VAMOS for mass-dispersive mode operation

The large acceptance of the spectrometer induces significant image aberrations in the focal plane of the spectrometer. For this reason it is crucial to employ trajectory reconstruction to determine the particle momentum and scattering angle from the measured final coordinates. The unique identification of the reaction products is achieved by combining the reconstructed parameters, such as the magnetic rigidity (Bρ) and the path lenght (L), with measured quantities, such as time of flight (TOF), energy (E) and energy loss (ΔE). In order to obtain this information, the spectrometer counts also a dual position-sensitive Multi-Wire Proportional Counter (MWPC) entrace detector, a Multi-Wire Parallalel-Plate Avalanche Counter (MWPPAC) and two Drift Chambers (DC). Moreover, at the focal plane an Ionization Chamber (IC) is placed for the identification of the reaction recoils providing the atomic number. In order to increase the momentum acceptance of the spectrometer, the standard focal plane detectors were substituted with larger areas ones (1000×150 mm^2) [118]: with this upgrade of the apparatus the momentum acceptance increased from ≈ 11%

to ≈ 30% and the spectrometer name changed to VAMOS++. Despite the upgrade, in the following pages the spectrometer is going to be called VAMOS for clarity. In Figure 2.11 the schematic design of the VAMOS spectrometer is shown with its various detectors.

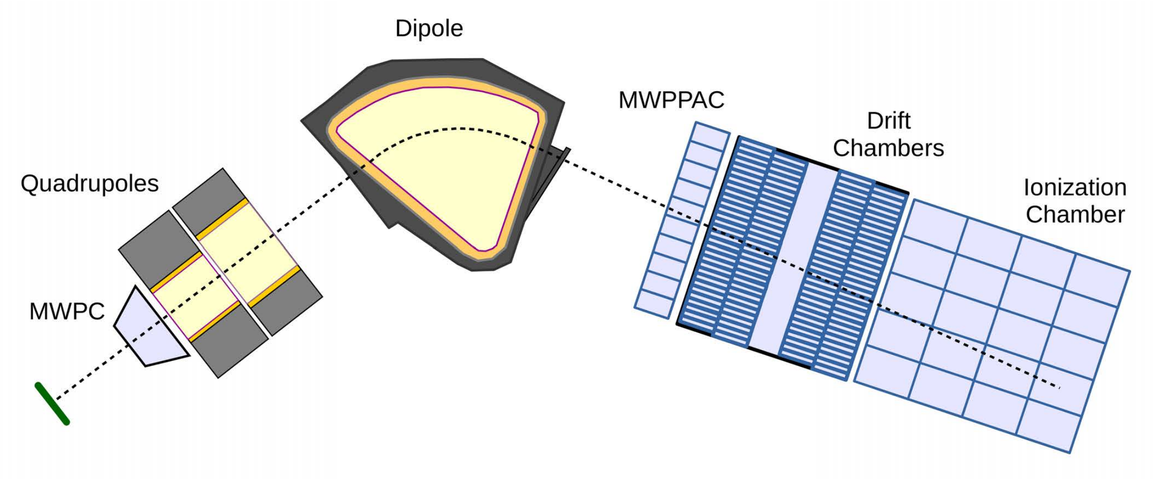

Figure 2.11.: Schematic drawing of VAMOS. At the entrance of the spectrometer the dual position sensitive MWPC measures the direction of the recoils. This detector together with a MWPPAC placed at the focal plane measures the TOF of the fragments. The recoil position and direction at the focal plane are provided by the two DC. Just after the DC an IC is placed to measure the energy loss and total kinetic energy of the reaction products, which allows the identification of their atomic number.

By coupling VAMOS with AGATA, the γ rays in coincidence with the recoils can be Doppler corrected event by event, thanks to the kinematic reconstruction of the recoil velocity vector. The ion identification procedure and the Doppler correction will be presented in Chapter 4.

2.3.1. Multi-wire entrance detector

One of the latest upgrades of the VAMOS spectrometer consists in its new entrance detector. The purpose of this detector is to provide the position of the recoil ions produced in the reaction, determining their direction with a sufficient angular resolution for Doppler correction. Placed between the reaction chamber and the entrance of VAMOS spectrometer, the new detector assembly consists of a pair of two position sensitive Multi-Wire Proportional Counter (MWPC) [119] in a common gas volume. A schematic view and pictures of the detector are presented in Figure 2.12, showing the distances between its components and the definition of the target-position angles (θ_V, ϕ_V).

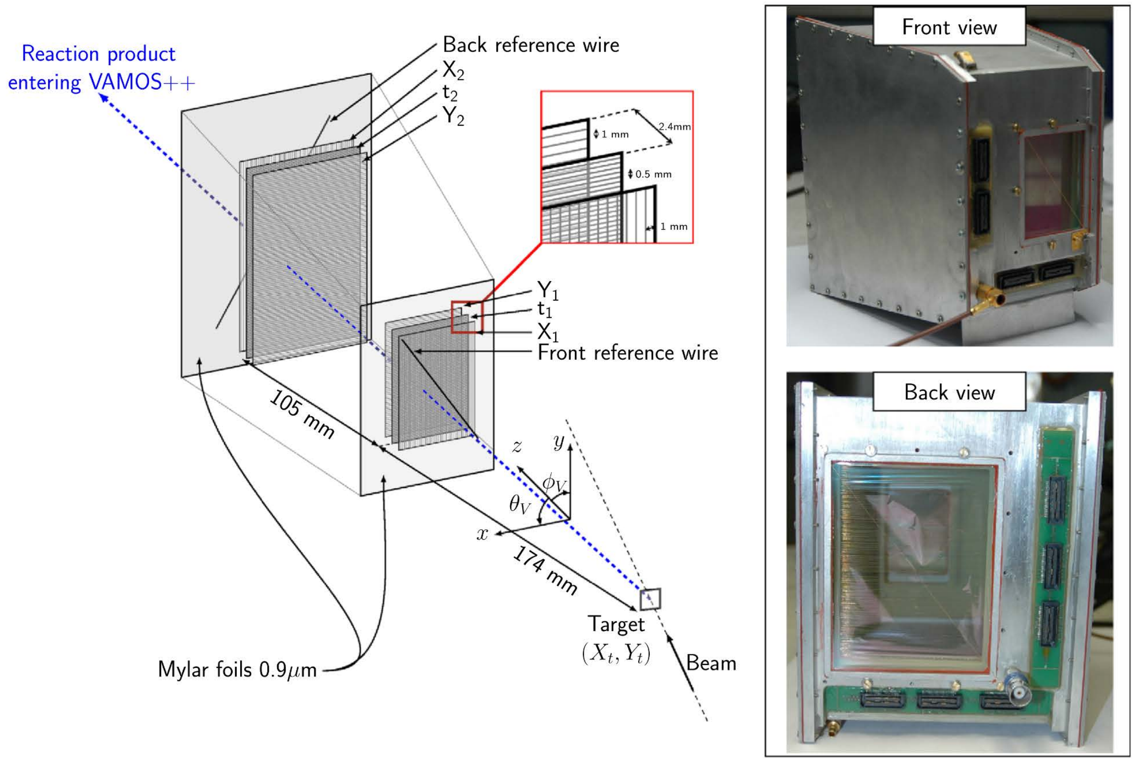
Reaction product entering VAMOS++
Back reference wire
X$_2$
t$_2$
Y$_2$
1 mm
2.4mm
0.5 mm
1 mm
Y$_1$
t$_1$
X$_1$
Front reference wire
105 mm
174 mm
z
y
x
ϕ_V
θ_V
Target
(X_t, Y_t)
Beam
Mylar foils 0.9μm
Front view
Back view

Figure 2.12.: (left) Schematic view of the dual position-sensitive multi-wire proportional counter (MWPC) placed as VAMOS entrance detector. In the inset the expansion of the three wire planes illustrating the wire plane orientation and spacings. (right) Front and back views of the detector assembly. Figure adapted from Reference [119].

The front and back MWPC have active areas of 40×61 mm^2 and 65×93 mm^2 respectively. Each detector is composed of three electrodes: a central cathode that provides a time signal ($t_{1,2}$) and two orthogonally oriented anodes wire planes ($X_{1,2}$, $Y_{1,2}$). For each MWPC the cathode is composed by gold plated tungsten wires with a diameter of 20 μm, separated by 0.5 mm. The X and Y anodes are composed of the same wires placed at a distance of 1.0 mm from each other. The distances between the wires was chosen to obtain the required avalanche amplification gain. However, during the experiment few wires of both front and back MWPCs were broken, so a correction in the evaluation of the target-position angles has been introduced and it will be discussed in Chapter 3. The nominal performances of the MWPC assembly are summarised in Table 2.2.

Time resolution	130(5) ps
Spatial resolution (front)	73(9) μm
Spatial resolution (back)	84(11) μm

Table 2.2.: Nominal performances of the MWPC detector.

The cathodes of the two MWPCs are separated by 105 mm and the detector assembly is placed 174 mm downstream from the target. The detector system is operated using isobutane C_4H_{10} with gas pressure ranging between 2 and 6 mbar. In particular, for the experiment the pressure was set to 6.0 mbar. The 0.9 μm thickness entrance and exit Mylar windows are isolating the gas volume from the surrounding vacuum. Even if the spacial resolution should improve the Doppler correction, the large gas volume together with the Mylar windows decrease the recoil velocity, introducing a systematic error in its estimation. The correction of this systematic error will be discussed in Chapter 4.

2.3.2. Focal plane detector setup

The focal plane detection system consist of three types of detectors: a Multi-Wire Parallel Plate Avalanche Counter (MWPPAC), a pair of two dimensional position-sensitive Drift Chambers (DC) and a multi-segmented Ionization Chamber (IC) [118, 120]. The schematic view of the focal plane detectors is presented in Figure 2.13, showing the distances between its components and the definition of the focal-plane angles (θ, ϕ).

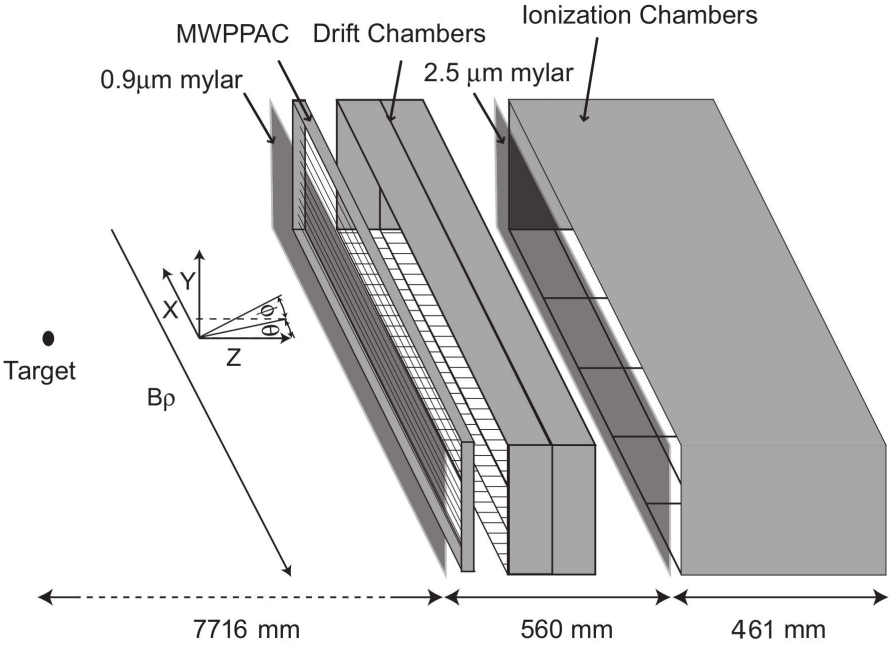

Figure 2.13.: Schematic view of the VAMOS focal plane detection system, indicating the direction for increasing values of the magnetic rigidity Bρ. The picture has been adapted from Reference [118].

Because of its fast timing properties and its high counting rate capabilities, the MWPPAC was chosen to measure the TOF, coupled with the MWPC entrance detector. The MWPPAC is composed of a central cathode and two anodes, each separated by 2.2 mm. The detector has an active area of 1000×150 mm^2 covered by vertical and horizontal gold-coated tungsten wires for the cathode and anode respectively. In order to reduce its capacitance, the cathode is segmented into 20 independent sections and it ensures a fast rise time of the signal. The detector is operated using isobutane C_4H_{10} and for the experiment the pressure was set to 6.0 mbar. A Mylar window of 0.9 μm isolates the beam line vacuum and it is supported by 100 μm diameter nylon wires placed every 50 mm. Because of the energy loss into the gas and the Mylar foil, a systematic error is introduced in the evaluation of the recoil velocity, as introduced for the MWPC detector. The discussion of this systematic error will be presented in Chapter 4.

The two DC measure the horizontal and vertical positions necessary to reconstruct the trajectories of the particles. Each DC has an active volume of $1000\times150\times100$ mm^3 and the cathode plane is made up of two rows with 160 pads. To improve the measurement of the position in between the pads, the two cathode rows are shifted by 3.2 mm. The detector is operated using isobutane C_4H_{10} and for the experiment the pressure was set to 6.0 mbar. During the trajectory reconstruction, described below, the event is validated by the tracking algorithm if there is a signal in at least two not-consecutive rows. This condition allows to measure with enough precision the direction of the ions, crucial in the tracking.

The IC has an active volume of $1000\times150\times460$ mm^3 and it is filled with CF_4 gas. During the experiment the detector was operating with a pressure of 55 mbar. The IC is made of four segments along the direction of the particle (row A/B/C/D), each of which is further segmented into five pads. Because of the analogical electronics that cannot support high counting rates, during the experiment the rate of validated events was limited to 4.5 kHz in order to avoid pile up. A Mylar foil with a thickness of 2.5 μm separates the DC and IC gas volumes. This foil is supported by 32 vertical nylon wires to avoid any deformation arising from the different operating pressure of the DC and IC. Despite the presence of the nylon wires, the different pressure of the two gasses has the effect of bending the Mylar foil, introducing a systematic error in the recoil ions energy loss. The treatment of the aberrations due to this systematic error will be discussed in Chapter 4.

2.3.3. Event reconstruction

With the information provided by all the detectors described above, the trajectories of the recoils are reconstructed via software in order to determine the momentum and scattering angles of the detected particles [121, 122]. The reconstruction method used in VAMOS is based on two independent steps: trajectory simulations and reconstruction algorithms [120].

The modelling of ion trajectories in an optical system is generally realized by two approaches. The first approach relies on a transfer map calculation which relates the initial coordinates to the final coordinates of a trajectory. The corresponding transfer map may be represented with a Taylor series of given order computed for some predefined optical object. However, because of the complexity of the quadrupoles that can introduce field correction up to fifth order, predefined standard models cannot be used with the VAMOS spectrometer for the tracking of the recoils. Then, a precise computation of trajectories can only be done with very accurate field models: the trajectories in VAMOS are reconstructed by using the field maps obtained during the magnet design and then integrating the Newton-Lorenz equation for individual particles. The accurate description of the VAMOS spectrometer is simulated by tracing a set of 20000 trajectories covering the full acceptance and storing their initial (d, x_i, θ_i, y_i, ϕ_i) and final coordinates (x_f, θ_f, y_f, ϕ_f, l). For a given trajectory the parameters x and y corresponds to the two transverse distances from the reference trajectory, θ and ϕ refers to the inclination angle in horizontal and vertical planes. The parameter $d = (p - p_0)/p_0$ defines the relative momentum deviation from the reference one and l is the difference in path length between the given and the reference path. In the experiment discussed in this work the trajectory of reference was the beam and its magnetic rigidity was set to 0.89 Tm in order to make the trajectory central.

The reconstruction algorithm uses a numerical procedure that calculates a polynomial relationship between the four final parameters (x_f, θ_f, y_f, ϕ_f), provided by the two DCs, and the initial parameters:

$$\begin{aligned}
\delta &= F_1^N(x_f, \theta_f, y_f, \phi_f) \\
\theta_i &= F_2^N(x_f, \theta_f, y_f, \phi_f) \\
\phi_i &= F_3^N(x_f, \theta_f, y_f, \phi_f) \\
l &= F_4^N(x_f, \theta_f, y_f, \phi_f) \quad .
\end{aligned} \tag{2.1}$$

For each detected particle, the reconstructed parameters are expressed as a set of N-order polynomial functions, presented in Equation 2.1. The coefficients are determined off-line by fitting the polynomials with the computed trajectories, described before. In order to reduce the complexity of the problem, it is possible to decompose the full acceptance of the spectrometer into N smaller bins and use a set of piece-wise lower order polynomials locally.

Between these extracted initial conditions, only the momentum and path information are usually necessary because the recoil target-position angles are directly measured by the MWPC entrance detector. On the other hand, because of the presence of broken wires in both the MWPCs, the reconstructed angles have been used in the already-introduced correction, related to the energy loss inside the entrance-detector gas volume, and it will be discussed in Chapter 3.

2.4. Differential plunger device

Since the goal of the experiment was to measure the lifetime of the low-lying states of nuclei close to ^{100}Sn, a differential plunger device was employed and placed inside the reaction chamber. The plunger allows to control the distance between the target and another foil, called degrader, that has the role of decreasing the recoils velocity after the reaction. This device, designed and constructed in Cologne, is used for direct lifetime measurement via Recoil Distance Doppler-Shift (RDDS) method [100], that will be described in Chapter 4.

In the case of deep-inelastic reactions, the direction of the recoils differs from the beam axis and it has to be taken into account in the design of the device. As a consequence, the plunger should be mounted in order to make its symmetry axis coincide with the entrance axis of the magnetic spectrometer. For the experiment discussed in this thesis, the VAMOS spectrometer was placed at the grazing angle of the reaction, so at an angle $\theta = 25°$ with respect to the beam line (see Appendix A).

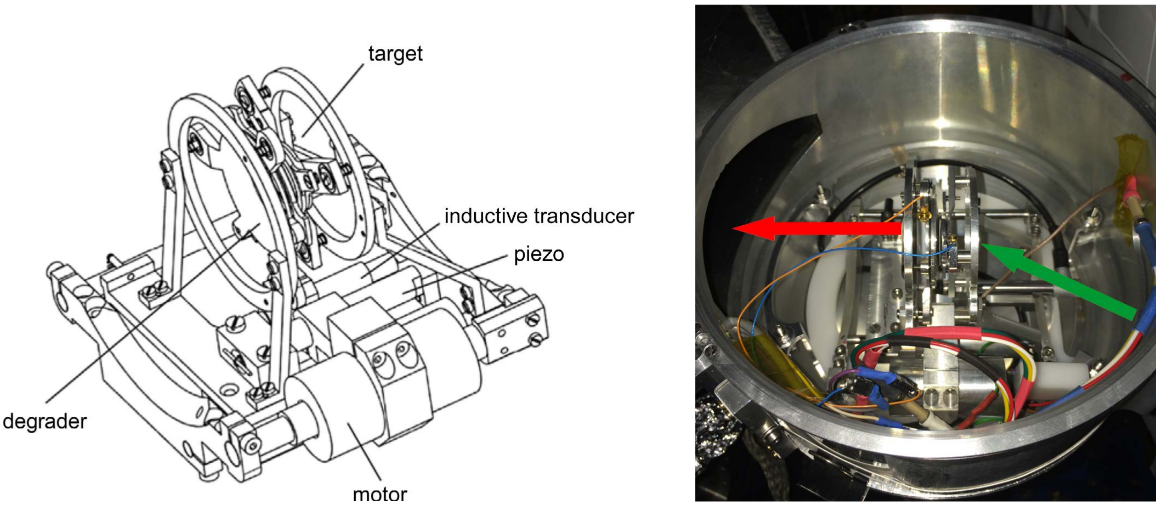

Figure 2.14.: Cologne plunger for deep-inelastic reactions: (left) design and (right) installation inside the reaction chamber. The green and red arrows represent the beam and recoils direction, respectively. The scheme on the left is taken from Reference [100].

Because of the tilted plunger axis with respect to the beam, all needed plunger components like the motor, the distance measuring systems and the mechanics which guarantee a smooth and precise linear movement of the degrader have to be placed in a rotating structure inside the target chamber. The plunger mechanics were built with as little material as possible to avoid γ-ray absorption. For large movements, such as the change of target-degrader distances, the motor used is an Inchworm piezoelectric linear motor with a maximum travel distance of 1 cm. The target-degrader separations are measured by two inductive transducers which cover the distance range from contact to 5 mm. Moreover, the plunger is equipped with a piezoelectric crystal stage needed for small movements, in particular for the piezoelectric feedback system whose sensitivity is better than 1 μm. Because of the very fast variations and the measured target-degrader capacitance, this feedback system cannot compensate the fast vibrations: the system can only compensate slow changes of the target-degrader separation, for example the deformation of target and degrader due to heating up caused by the impinging beam. Anyway, during the experiment the actual target-degrader separation is monitored permanently by measuring the capacitance between the two foils. This allows to estimate the distance fluctuation with respect to the nominal position, as it will discussed in Chapter 3. A schematic design and the installation inside the reaction chamber is presented in Figure 2.14.

As introduced before, the plunger device uses the RDDS method for direct lifetime measurements: after the reaction takes place in the thin target, the excited nucleus leaves the target with a velocity β_S. Then, as it is shown in Figure 2.15 it loses energy inside the degrader material, decreasing its velocity down to the velocity β_U which is directly measured event by event with the VAMOS spectrometer and then used for correcting the Doppler shift.

Because of the two different velocities of the fragments, for every γ-ray transition two components are present: the energy of the γ rays emitted after the degrader would be properly Doppler corrected, while the energy would be shifted at lower values for those emitted between the target and the degrader. For each γ-ray transition, the ratio between the area of the two components depends on the fragment TOF from the target to the degrader, that is obviously a function of the absolute distance d between the foils:

$$TOF = \frac{d}{v} = \frac{d}{\beta_S c} \quad . \tag{2.2}$$

Since the plunger gives information on the degrader position with respect to an internal reference, the absolute distance between the foils is obtained by evaluating the plunger zero offset, which will be discussed in both Chapter 3 and Chapter 4. The energy difference ΔE between the two components can be determined from the Doppler correction formula and for the velocities observed in the experiment it can be approximated as

$$\frac{\Delta E}{E_0} \approx \Delta\beta \; cos\theta \quad , \tag{2.3}$$

where E_0 is the energy of the emitted γ-ray depopulating the level of interest which is observed at rest, $\Delta\beta$ is the difference between the velocities β_S and β_U and θ is the angle between the recoil direction and the emitted γ-rays, that can be determined thanks to the position sensitivity of both VAMOS and AGATA.

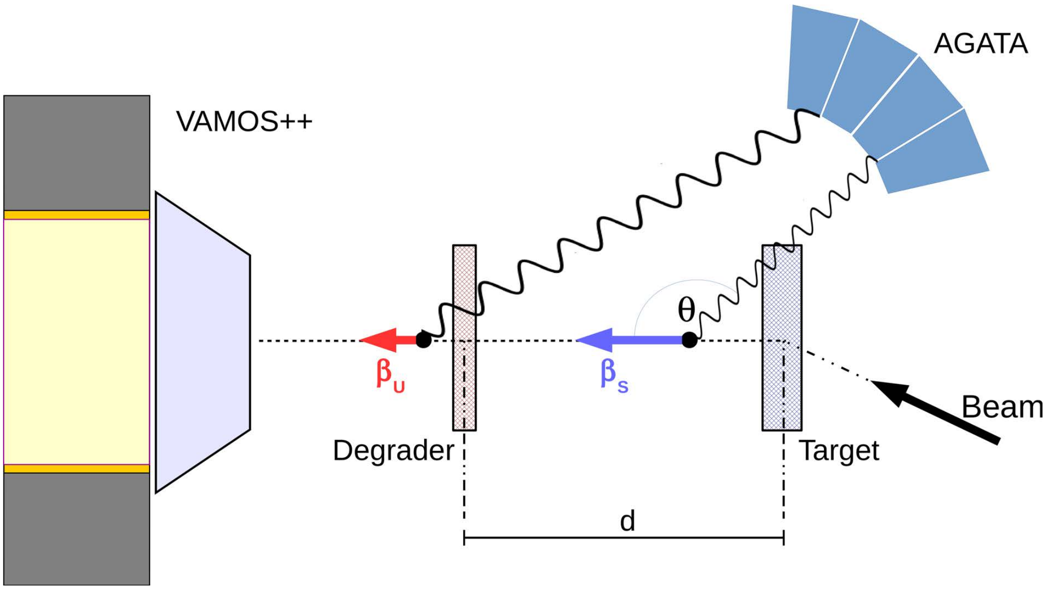

Figure 2.15.: Recoil Distance Doppler-Shift method. After the reaction, the excited nucleus leaves the target with a velocity β_S. The fragment loses energy inside the degrader material, decreasing its velocity down to the velocity β_U, that is directly measured by the magnetic spectrometer and then used for correcting the Doppler shift. Because of the two different velocities of the fragments, for every γ-ray transition two components are present: the energy of the γ rays emitted after the degrader would be properly Doppler corrected, while the energy would be shifted at lower values for those emitted before the degrader.

Having a good energy separation between the two components is a crucial requirement for lifetime measurements with RDDS method. Obviously, the energy difference ΔE depends on the energy loss by the fragments inside the degrader material and it increases with increasing degrader thickness. In Appendix A the optimisation of the reaction will be discussed, in particular by defining the degrader material and thickness as required by the experiment.

3

Presorting and Calibration

The described experiment was devoted to the lifetime measurement of low-lying excited states in ^{106,108}Sn. The nuclei of interest were populated via a MNT reaction where a ^{106}Cd beam impinged onto a ^{92}Mo target. For lifetime measurements via RDDS method the differential Cologne plunger was employed, placing a ^{24}Mg degrader after the target. The complete identification for the reaction products was obtained by using the VAMOS spectrometer, while the γ rays emitted in coincidence by the recoils were detected by the AGATA HPGe detector array.

This chapter presents the presorting of the data and the calibration of the detectors described in Chapter 2: the AGATA spectrometer, the VAMOS magnetic spectrometer and the plunger device.

3.1. AGATA spectrometer

The analysis of the AGATA data starts from the digitalized traces of segments and core signals for each of the crystals. Contrary to traditional arrays, which have analogue read out, AGATA allows for various corrections to the signals that improve its performances. These corrections are listed in the following. By comparing the signal of all the segments with the ones given by the core, the cross-talk correction can be applied. Moreover, if one unstable or broken segment is present in one crystal, its signal can be restored. Then, the position and energy of each interaction is deduced via a pulse shape analysis. From the information about the interaction points, a software correction of the signals can be applied in case of neutron damage of the crystal lattice. Finally, the obtained hits in the detector volume are passed to the tracking algorithm, which provides a list of the reconstructed rays. Due to the conceptual difference with a traditional γ-ray array, the procedure of the calibration and the data analysis is very peculiar and is described in detail in the following sections.

3.1.1. Energy calibration

The energy calibration impacts on the quality of the final spectrum. A precise energy calibration will provide a good energy resolution when all the crystals are summed up.

In our case this is crucial to clearly separate the two components of a γ-ray transition, caused by RDDS method. On the other hand, a good energy calibration is necessary in order to obtain a good performance of the γ-ray tracking algorithm as well. In Chapter 2 the characteristic features of γ-ray tracking were illustrated and it was underlined that the interaction mechanism of γ rays with matter depends on the energy of the radiation.

Each AGATA crystal is segmented into 36 outer contacts (segments) with a common core contact. The preamplifier of the central core contact has two different gain outputs. The energy calibration has to be done for each channel. Therefore, for the AGATA detectors involved in the present experiment, $(36 + 1 + 1) \times 24 = 912$ channels are present.

The energy calibration was performed by placing a strong ^{152}Eu source in front of AGATA. In each spectrum the 10 most intense transitions were used for calibrating each segment in an energy range up to 1408 keV. Because of the large number of channels, the calibration was obtained via automatic fit, thanks to the program *Recal* [123], by using a linear function fixing the offset to zero. Whenever the energy difference between the position of the calibrated peak and the nominal position was more than a certain value, the procedure was redone manually. Having in minds the goal of the experiment, the automatic calibration was considered satisfying if the energy difference was lower than 0.4 keV for the 1408 keV transition in ^{152}Eu.

The calibration coefficients were applied to all the energy channels as well as to scale the recorded traces used for the PSA.

3.1.2. Cross-talk correction

In segmented detectors electric cross-talk effects are observed [124, 125]: the sum of all segments energy is shifted to lower values and this effect increases with the segment multiplicity. Its origin can be explained by a capacitive coupling between the core and the segments via the bulk of germanium material [103].

Thus, in addition to a good energy calibration, a cross-talk correction has to be applied to AGATA to improve the energy resolution [124]. With the same dataset used for the energy calibration, the crosstalk correction coefficients were obtained by sorting the energies recorded in the segments with respect to the numbers of firing segments and deducing the shift from the nominal energy of the most intense transitions of the ^{152}Eu source. The derived matrices are used for the correction of the measured energies and the restoration of the baseline. The inverse of the correction matrix is folded to the calculated signal bases to include crosstalk effects in the pulse shape analysis.

3.1.3. Dead and unstable segments

Some of the AGATA detectors may have some problematic segments, that have been classified as *lost*, *broken* or *unstable* segments. If in one crystal there is only one segment having any of these issues, the performances of such detector can be recovered; on the other hand, if this procedure cannot be applied, the crystal can be removed with little impact on the PSA algorithm. An easy way to check the status of the detectors is to compare the energy measured by the core with respect to the segments energy. After the energy calibration of the detectors has been applied, the software *xTalkSort* [126], used also for the previously mentioned cross-talk correction, produces matrices showing the relation between the energy measured by the central contact (CC) with the energy of the segments and with the sum of all the segments (SSg). In the case of a problematic crystal, three different situations can be identified from these CC-SG matrices:

- In case of a **broken** segment, the net charge is not collected (e.g. due to a broken cable between the segment and the pre-amplifier). The cumulating charge flows to the neighbouring segments where it is collected. For this reason the neighbour-segments matrices and the SSg matrix present a second structure at lower core energy. Examples of this behaviour is shown in Figure 3.1 and Figure 3.3.

- In case of a **lost** segment, even if the net charge is collected, there is no information inside the data flow and a possible explanation is a faulty connection between the crystal pre-amplifier and the digitizer.

- In case of an **unstable** segment the energy signal is present inside the data flow, but the energy shifts with time. For this case, in the matrix of the problematic segment (and consequently the SSg matrix as well) there are two similar structures caused by the different gains. Such a behaviour is clearly presented in Figure 3.2.

In the experiment discussed in this thesis, three crystals presented such problems: 03A, 10C and 12B.

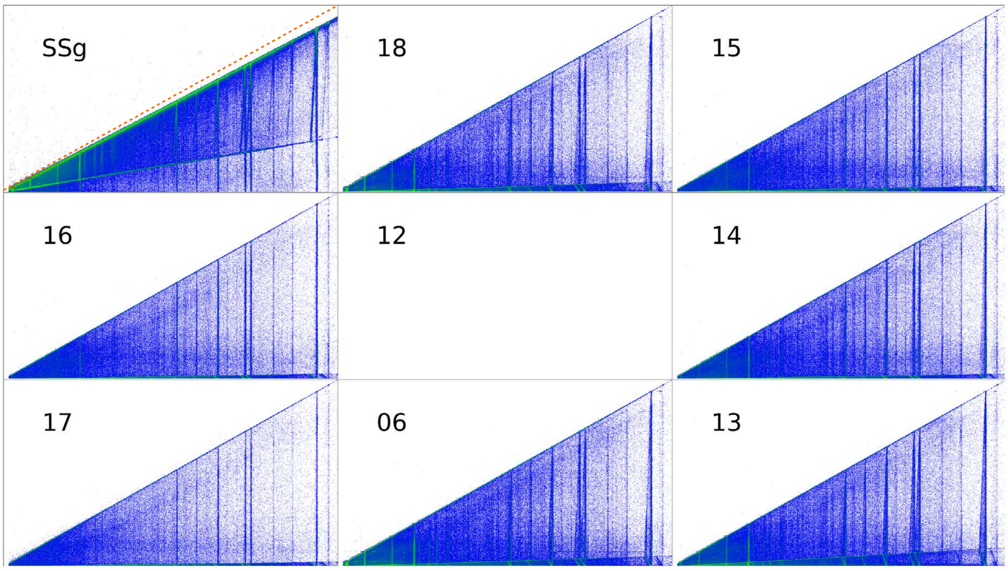

Figure 3.1.: Central contact energy as function of the segment and of the summed segments (SSg) energy for crystal 03A. This crystal has segment 12 (central pad) which is broken, so its charge is collected by the neighbouring segments (border pads). In addition, the SSg matrix (top-left pad) shows that the energy of the summed segments is lower than the CC energy (orange dashed line): indeed this HPGe has segment 02 that is lost.

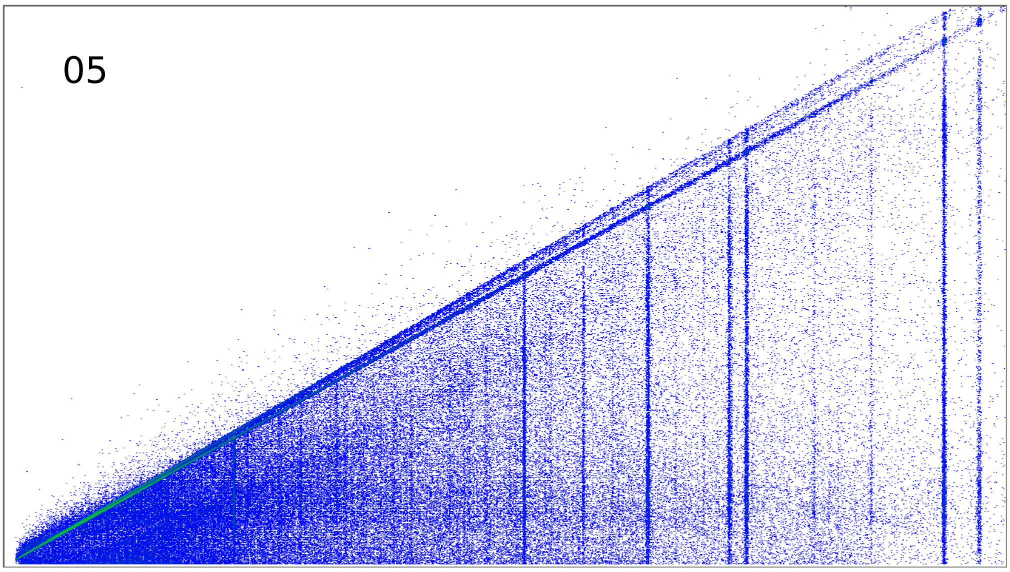

Figure 3.2.: Central contact energy as function of the energy of segment 05 for crystal 10C. Having a variable gain, this segment is unstable.

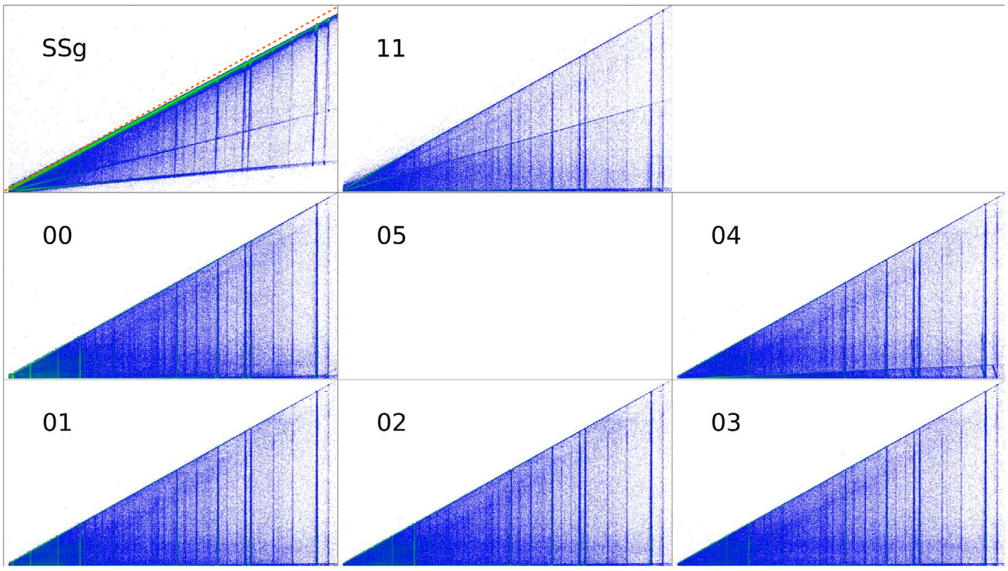

Figure 3.3.: Central contact energy as function of the segment and of the summed segments (SSg) energy for crystal 12B. This crystal has segment 05 (central pad) which is broken, so its charge is collected by the neighbouring segments (border pads). In addition to that, segment 11 (central-top pad), which is one of the neighbouring, has unstable gain as it can be identified by the presence of three different structures. The comparison between the central contact and sum energy of the segments (top-left pad) shows the presence of the two issues: the several structures reveal the presence of a broken segment, while the unstable one entails the SSg energy to be lower than the CC energy (orange dashed line).

As it is shown in Figure 3.1, crystal 03A presented two problems at the same time: on one side segment 02 was lost, so its information was not inside the data flow; while on the other side segment 12 was broken, so the cumulating charges were collected by the neighbouring segments. In the present version of the procedure, it was possible to correct only segment 12: the effect of this partial correction is that in the spectrum of the restored segment, "ghost" peaks, caused by the other segment firing, appear.

Then, crystal 10C had segment 05 that was unstable, as it is shown in Figure 3.2 where the change of gain is clearly visible. Considering the presence of only one problematic segment, the easy way to solve the issue was to remove it from the data flow and then to restore the information considering it as a broken one.

Crystal 12B had a different behaviour. In fact, it had both a broken (05) and an unstable (11) segment, as presented in Figure 3.3. Unfortunately, the unstable segment was a neighbour of the broken one and therefore in its CC-SG matrix three different structures are clearly visible. Also in this case, only one of the two problematic segment could be restored, and therefore segment 05 was chosen because of its very frontal position.

3.1.4. Time alignment

The time of a γ-ray hit is measured with respect to a reference given in AGATA by the crystal trigger. The AGATA system is triggered with a leading edge discriminator on the central contact of the crystal. A leading edge is used instead of a constant fraction discriminator (CFD) in order to be more sensitive to low-energy events. As a consequence, an energy dependence of the triggering time may be observed (walk effect).

In practice, all the segments and core signals are digitalised and recorded for each trigger. Each recorded pulse shape, or signal trace, consists of 100 samples: 40 before and 60 after the triggering point. Thus, the pulse shape provides a 1 μs snapshot of the charge collection inside the crystal. The time of a segment net charge (or of the core) with respect to the triggering point is obtained with a digital CFD applied on the recorded signal trace.

The PSA algorithm determines the position of the interaction of the γ ray comparing the pulse shapes of the net-charge and transient signals with a database. Inside the database, known interaction positions are assigned to a set of pulse shapes. The PSA comparison is reliable if the time of all the segments are aligned to the core time. This time alignment is the first time calibration step performed on the data-set.

The leading-edge timing of the net-charge segment is different from the one of the central contact, the "real" γ-ray time being in between. Therefore, a new time reference, called *TZero*, is chosen as the sum of the net charge time and the core time. This time provides a better resolution than the one determined by the leading-edge on the core signal. Nevertheless, this required a precise time calibration of the net-charge segment signals, i.e. the time alignment introduced before is crucial for a good time resolution.

In order to obtain the best result, determining the most accurate interaction position, the PSA algorithm tries different time shifts of the traces around the *TZero* time reference. As a consequence, this time reference can slightly shift depending on the crystal PSA database. Hence, the crystal time references are aligned to each other after the PSA algorithm. This time alignment is the second time calibration step.

The last time calibration step occurs at the global level where all the crystal data are put together. In the case of N detectors, a time dispersion matrix $M_{N\times N}$ is built with all pair detectors time. The matrix element of index $(i,\, j)$ is defined as

$$M(i,j) = TZero_i - TZero_j \quad . \tag{3.1}$$

A set of N time coefficients is obtained minimizing their time dispersion inside the matrix $M_{N\times N}$.

3.1.5. Pulse shape analysis

The hit position in a crystal is determined by the PSA algorithm and it depends on both energy calibration of the traces and on the *TZero* alignment of the traces. In principle, the distribution of the hits inside a crystal should be uniform. Nevertheless, it is not possible to fully suppress grouping of the hits inside the crystal. This is not due to a physical phenomenon, since there is no reason for a γ ray to interact more at some given positions inside a crystal, but it is due to misinterpretation of the PSA algorithm. This misleading assignment of the interaction position is under investigation within the AGATA collaboration.

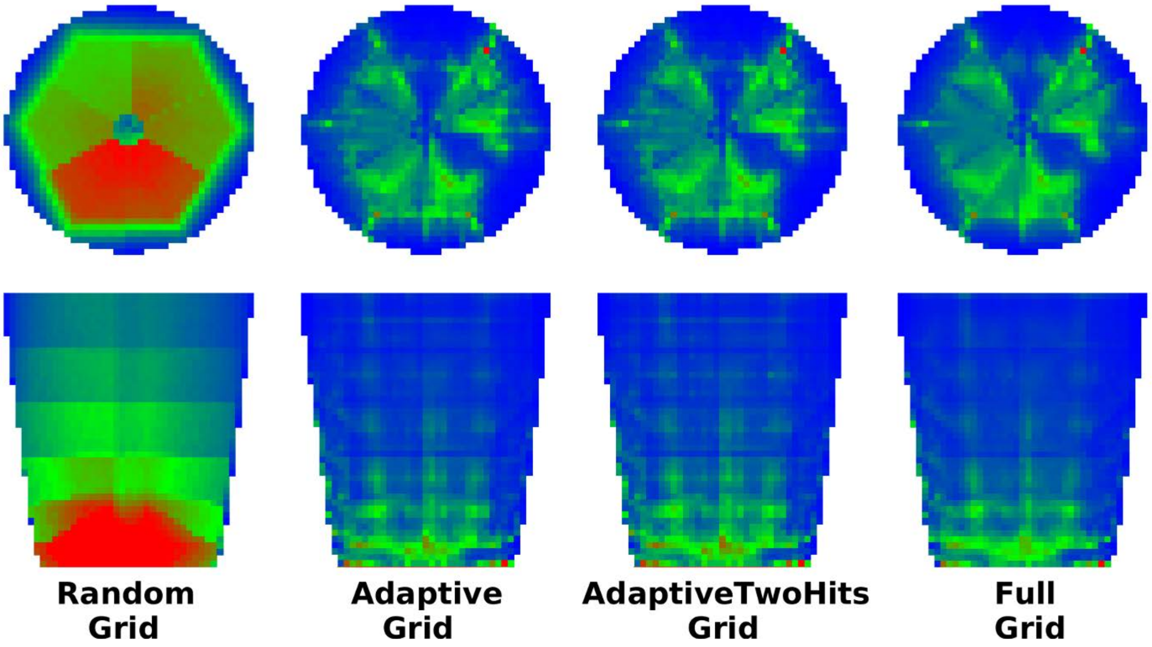

Figure 3.4.: Comparison between different PSA grid search for the crystal 00C: hit pattern projection on xy-plane (top) and xz-plane (bottom). For *Random* grid the interaction position is a random point inside the firing segment. For *Adaptive* [110] and *AdaptiveTwoHits* grids the algorithm stops searching the interaction point, as soon as a minimum of χ^2 is found; moreover *AdaptiveTwoHits* accepts the contemporaneous presence of two hits in the same segment. For *Full* grid the interaction point is search inside the whole database.

As introduced in Chapter 2, for this thesis the full grid search algorithm is used to identify the signal in the database with the best possible resolution, even if it is more time consuming than the adaptive algorithms. Employing the full-grid PSA algorithm, a 5 mm position resolution of the γ-ray interaction point is achieved [109, 112]. In fact, while the adaptive algorithms stops the search searching the interaction point, as soon as a minimum (even if local) of χ^2 is found, for the full grid algorithm the interaction point is searched inside the whole database. In Figure 3.4 the hit pattern for different grid search algorithms is presented.

3.1.6. Neutron damage correction

The interaction of fast neutrons in the germanium crystals induces lattice defects, which act as efficient charge carrier traps [127, 128]. Therefore, the efficiency of the charge collection is reduced due to these defects. The principal consequence of these dislocations, called Frenkel defects [129], is to increase the number of hole trapping in the detectors. Indeed the holes are more influenced by these defects, because during the charge collection they are slower than the electrons. This effect can be observed as a tail on the left side of the full-energy peak, i.e. on the lower energy part of the γ-ray peak. In Figure 3.5 the effect of the neutron damages on the γ-ray detection energy is shown for AGATA crystal 12C.

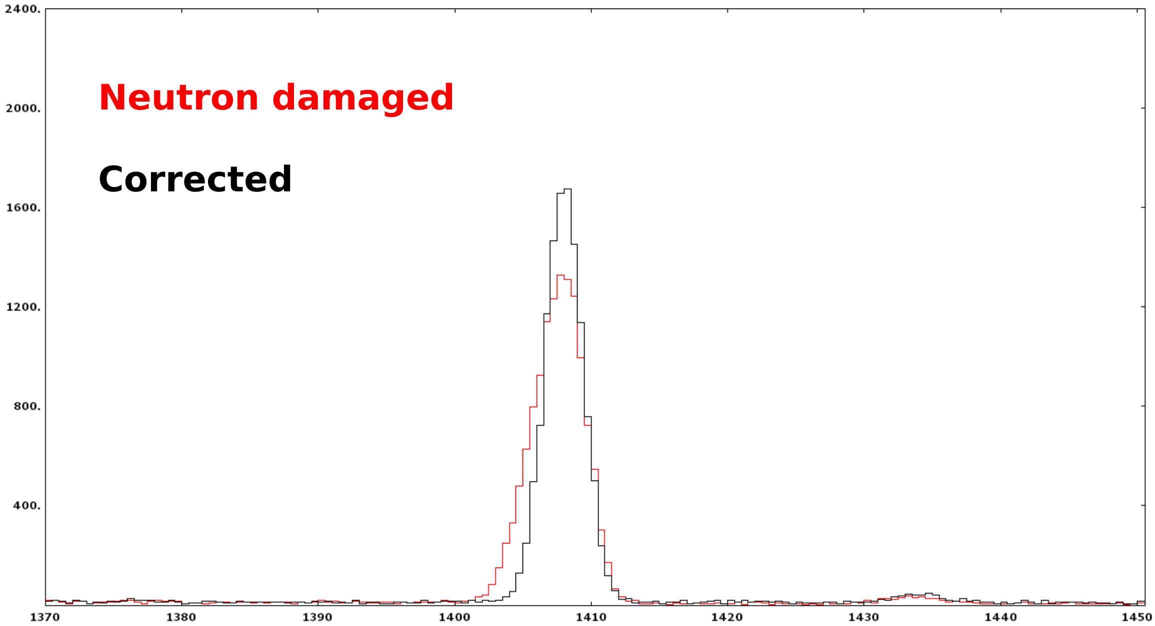

Figure 3.5.: Neutron damage correction of crystal 12C: the 1408 keV peak of ^{152}Eu, before (red) and after (black) the correction. Neutron damage induces defects inside the crystal lattice of the germanium detector, reducing the charge collection efficiency. These defects causes the presence of a tail on the lower energy part of the γ-ray peak.

The segments of the AGATA crystals are more sensitive to the hole trapping than the core contact [130]. In order to correct the “energy loss” due to the trapping, from the shape of the signals the mean-free path of both electrons and holes is estimated via software for each segment of all the crystals. Then, when the path differs from the nominal value inside germanium material, the shape of the signal is corrected. In case the detector is really damaged and the correction is not enough, another simple solution to recover the good energy resolution of the AGATA detectors is normalising the sum energy of all segments to the energy measured in the core contact, which is less effected by the neutron damage.

Crystal	FWHM (keV) before	FWHM (keV) after	Relative gain
03B	3.803	3.682	3.2 %
04B	4.233	3.826	9.6 %
04C	4.010	3.505	12.6 %
10C	3.569	3.512	1.6 %
12A	3.949	3.420	13.4 %
12C	4.240	3.349	21.0 %
13A	3.843	3.809	0.9 %

Table 3.1.: Comparison between the FWHM of the sum energy of all the segments before and after the neutron damage correction, measured at 1408 keV peak of ^{152}Eu. Only those detectors that needed the correction are reported in the table.

3.1.7. Tracking

In Chapter 2 it was underlined that the AGATA array power comes not only from its good position resolution but also from its tracking capabilities. In this thesis the OFT algorithm was used for the identification of the γ-ray path inside the AGATA array. This algorithm depends on three empirical parameters that can be chosen in order to change the tracking performances in agreement with the goal of the experiment [101, 102, 131].

- SigmaTheta: effective position resolution of the interaction points. It is used to assess the goodness of the comparison of the angles from the positions and the angles from deposited energies, given a sequence of interaction points.

- MinProbSing: in addition to the position requirement mentioned before, the minimum probability for accepting single interaction clusters defines a threshold for the calculated figure of merit. This probability is obtained by multiplying the probability to travel a given depth in Ge times the probability to undergo a photoelectric interaction for the energy of interest. This probability has the effect of an energy threshold above which, in fact, events are rejected as background.

- MinProbTrack: the acceptance level of multiple-interaction clusters is defined by the minimum probability threshold for the figure of merit.

The value of these three parameters was optimised in order to maximise at the same time both Peak-to-Total ratio (P/T) and the efficiency. For such optimisation, ^{152}Eu and ^{60}Co sources were used to test efficiently the tracking for both low and high energy. Anyway, considering that the transitions of interest have an energy ranging between 900 and 1300 keV, it was chosen to improve as much as possible the tracking capabilities for the 1332 keV transition of ^{60}Co source. Because of the large number of parameters and conditions to has to be taken into account during the procedure, all the graphs related to the optimisation are reported in Appendix B. The final values for the OFT tracking parameter are summarised in the following table.

SigmaTheta	1.20 mm
MinProbSing	2.0 %
MinProbTrack	5.0 %

Table 3.2.: The OFT algorithm depends on 3 empirical parameters that can be chosen following the requirements of the experiment: the reported values are optimised for the 1332 keV transition of the ^{60}Co source.

Efficiency calibration

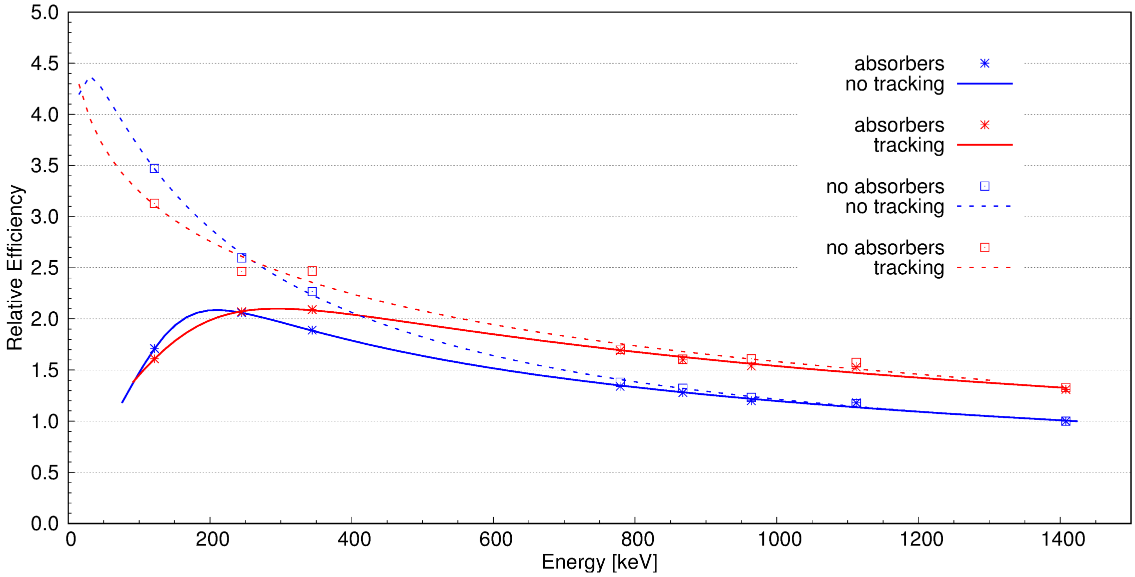

Figure 3.6.: AGATA relative efficiency as function of γ-ray energy without (blue) and with (red) tracking, measured with ^{152}Eu. In order to reduce the X-rays coming mostly from the beam and the target, 5 mm thick Cu absorbers were placed in front of the detectors. The comparison between the relative efficiency without (squares) and with (stars) the absorbers shows a decrease at energies below 400 keV. The efficiency curve without the tracking has been normalised to 1 for the 1408 keV transition energy. Taken from References [101, 131].

As result of the optimisation, in Figure 3.6 the comparison between the AGATA relative efficiency measured with a ^{152}Eu source is shown with and without tracking. In the energy region of low-lying transitions of the Sn isotopes (600-1200 keV), the tracking increases the efficiency up to 30%. On the other hand, for energies lower than 200 keV the efficiency is dropping when applying the tracking: as it is discussed in Appendix B, while rejecting bad events for improving P/T, also good ones are discarded because of the tracking parameters[1]. Moreover, during the experiment 5 mm thick Cu absorbers were placed in front of the detectors in order to reduce the X-rays coming mostly from the beam and the target.

The AGATA detecting efficiency is an important factor in the definition of the decay curve, as it will be discussed in Chapter 4. Thus, in order to be able to estimate the value of the efficiency along the whole energy range, the points reported in Figure 3.6 were fitted with different functions [132]. Because of the presence of the absorbers, the typical functions are not able to reproduce the experimental trend. For this reason, the data were then fitted with the function adopted in the *Radware* software [133], where low- and high-energy efficiency are considered separately. The function used for the fit is

$$\epsilon_\gamma(E_\gamma) = exp\left(\left[\left(A + B\frac{E_\gamma}{100\ keV}\right)^{-G} + \left(D + E\frac{E_\gamma}{1\ MeV} + F\left(\frac{E_\gamma}{1\ MeV}\right)^2\right)^{-G}\right]^{-\frac{1}{G}}\right) \quad , \tag{3.2}$$

where the constants A,B,D,E,F,G are free parameters.

3.2. VAMOS spectrometer

As introduced in Chapter 2, the VAMOS spectrometer identifies the atomic number (Z), mass (A) and charge state (q) of the reaction fragment entering it. Thanks to the MWPC entrance detector and to the fragments-trajectory reconstruction, the spectrometer also provides the velocity vector of the ions. Combining the information provided by the entrance detector and the focal plane system, the time of flight, the total energy and the energy loss can be measured. Afterwards, the calibrated energy and the ion velocity can be used to deduce the charge and the mass of the ion.

As a first step of the ion identification, the individual detector systems of the VAMOS spectrometer are calibrated. The measured information is used in a second step to identify the ion, procedure that will be presented in Chapter 4. Moreover, empirical corrections are applied to improve the mass resolution.

3.2.1. Ionization chamber

For the measurement of the energy and the energy loss of the ions, a good energy calibration and alignment among the 20 pads is necessary. For the analysis of this experiment the alignment coefficients from a previous experiment were used: the calibration coefficients seemed to work quite well for the central-trajectories pads, while small misalignments appeared for neighbouring pads. However, before matching the gains for each pad and then setting the thresholds, the time dependence of the ion energy loss inside the IC was corrected.

---

[1] In ^{152}Eu the 121 keV de-excitation is emitted in coincidence with both 244 keV and 1408 keV γ rays. These photons are emitted in similar direction. Because of the 4 cm proximity criterion, these low-energy γ rays will most likely not be considered as a single interaction points.

Time alignment: gas pressure-temperature dependence

Inside the IC the CF_4 gas flows constantly in order to avoid the presence of impurities that can worsen the energy resolution of the IC.

Despite this renewal of the gas, a time dependence of the fragments energy loss inside the gas was observed, as it is shown Figure 3.7. This trend was explained as the dependence of the gas pressure with the external temperature: during the day the warmer experimental hall caused the gas pressure to increase and consequently the fragments energy loss as well, while during the night the cooler external temperature entailed the opposite trend. This periodical fluctuations, which in some cases went upto 10%, introduced a systematic error in the evaluation of the recoil energy, deteriorating the atomic number resolution.

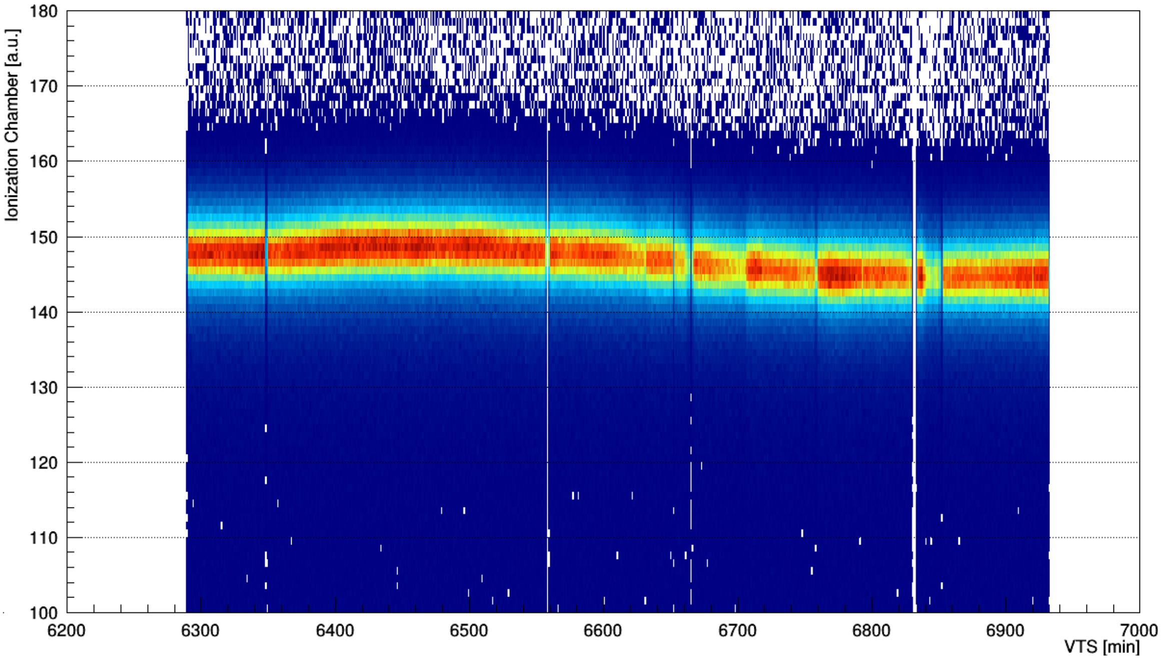

Figure 3.7.: Energy loss in IC-pad 02 (row A) as function of the validated time-stamp (VTS). Due to the gas pressure changing with the external temperature, the variation of ion energy loss can be observed.

These fluctuation were corrected via software during the analysis: per each pad the change of gas pressure was compensated with the introduction of a time-dependent gain. This time-dependent gain changed every minute. For the very first pads (row A and row B) it was chosen to move the high intensity peak (see Figure 3.8) always at the same position. Because of the absence of a reference point, for the last pads (row C and row D) it was decided to match the time-dependent gain in order to shift at the same position the points whose signal amplitude was 30% of the maximum.

Thresholds and gain matching

Once the shape of the spectrum of each pad was stable in time, two thresholds were set to make a veto on the bad events. The ADCs used for digitising the signals of the pads automatically remove the pedestal, whose information should not appear in the data flow. Despite this rejection, in a few cases some "events" related to the pedestal were still visible in the spectra and therefore low-energy individual thresholds were set per each pad. In order to reject pile up and to reduce possible contaminations in the element identification, high-energy thresholds were set as well. As example, in Figure 3.8 the rejection areas are shown for the central pad spectra.

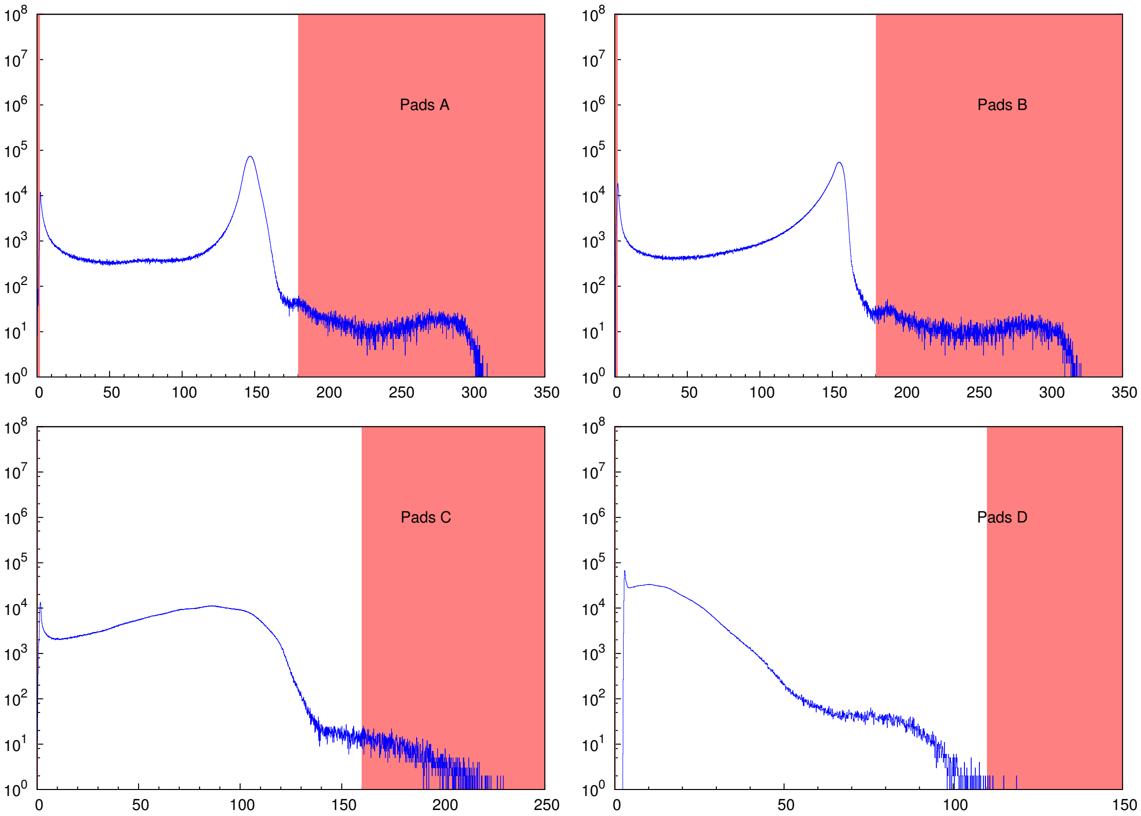

Figure 3.8.: Spectra of the central pads for the four different rows in the IC. The red area represents the events rejected in order to exclude pile up.

In the previously described time correction, the gain was matched in order to scale the IC-pad spectra to arbitrary positions. Thus, the misalignments between the pads became more important, as it is shown in Figure 3.9 (left), so a gain matching was mandatory. Because the energy calibration seemed to work quite well for the central-trajectories pads, the gain of the other IC pads was changed in order to obtain a continuous trend for each row. The effect of this adjustment can be seen in Figure 3.9 (right).

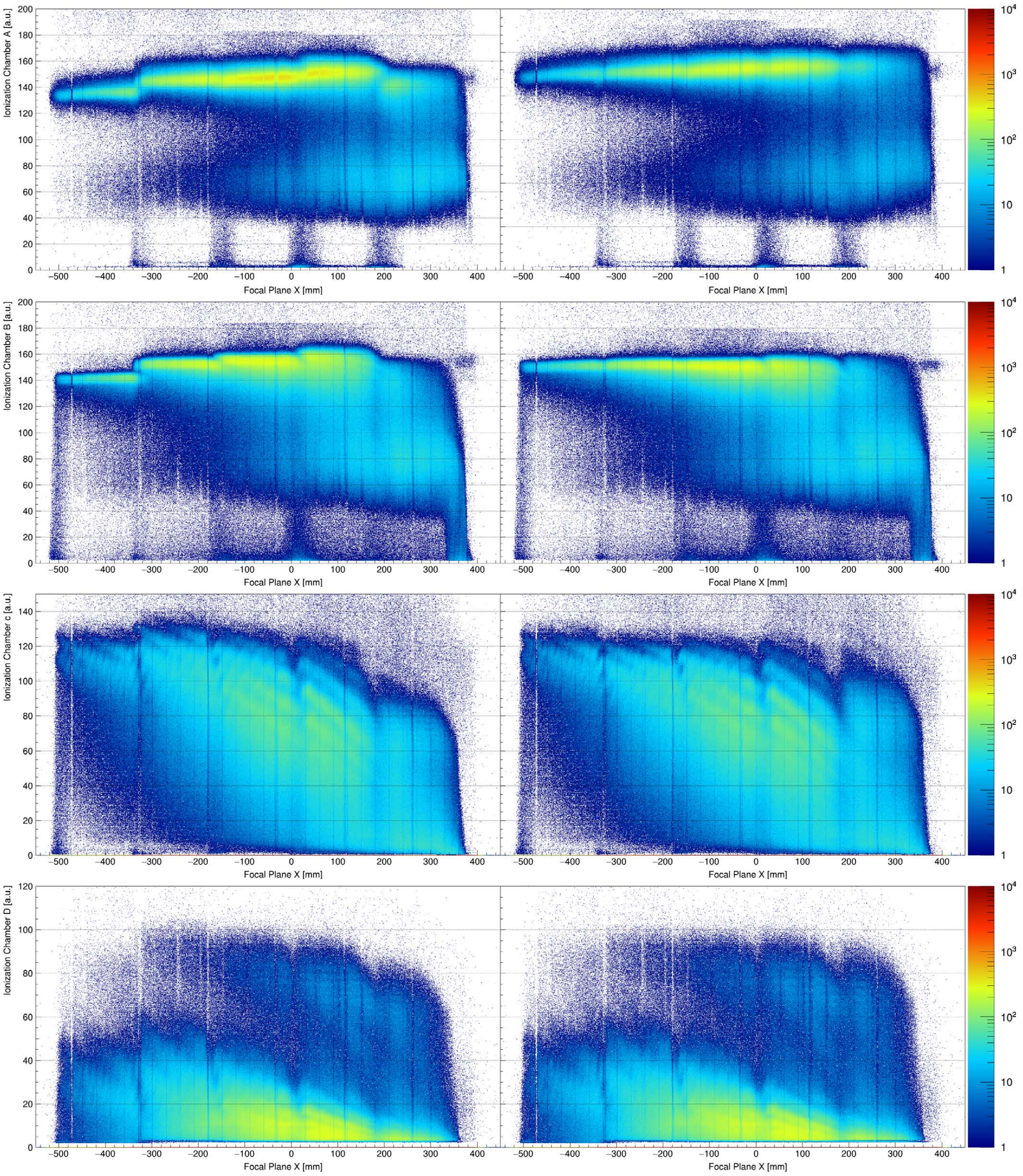

Figure 3.9.: IC signals as function of the horizontal focal plane position: (left) raw signals after the time-alignment correction where also the lower and upper thresholds have been applied, (right) the signals after the gain matching.

Trajectory requirement

Once the described corrections and the gain matching were applied, it was possible to define the gates for the Z identification. In fact, by plotting the energy loss ΔE_{AB} in the first two IC rows as a function of the total kinetic energy E_{TOT} (see Figure 3.10), defined structures appear, in agreement with the well known Bethe-Bloch formula [134].

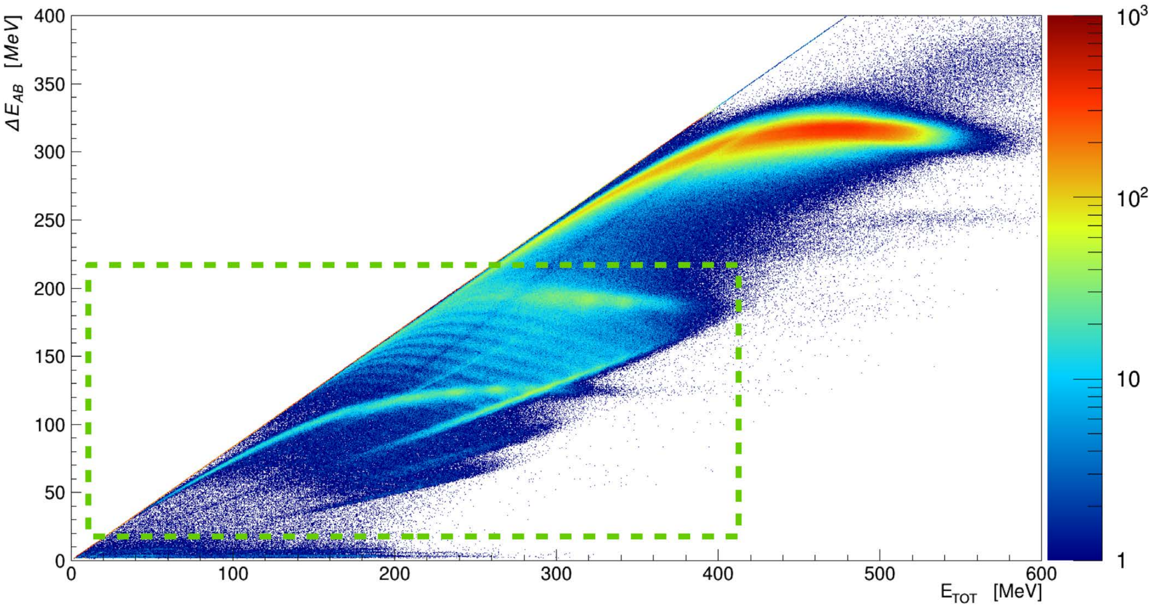

Figure 3.10.: Energy loss ΔE_{AB} in the first two IC rows as function of the total energy loss E_{TOT} (calibrated IC signal summed up the four rows). From the matrix the atomic number of the fragment will be defined. In the green-dashed rectangle a second structure is clearly visible and it is due to those events where the signal is missing from line A or line B.

However, in Figure 3.10 it is clearly visible the presence at low energies of a secondary structure due to not-correlated signals in the IC pads. Indeed, this second structure was mainly caused by the first two rows of the IC not firing at the passage of the ions: even if there was a valid signal coming from rows C and D, from time to time the pads of one of the first two IC lines did not provide a valid signal. In order to avoid contaminations due to the wrong identification coming from this second structure, an extra requirement of the ion trajectory inside the IC was added in the analysis: the signal of one IC pad is considered valid only if the previous rows fire as well. This condition can be easily described with logic symbols as

$$\begin{aligned}
row_A &= row_A \times (row_A > 0) \\
row_B &= row_B \times (row_A > 0 \ \ \&\& \ \ row_B > 0) \\
row_C &= row_C \times (row_B > 0 \ \ \&\& \ \ row_C > 0) \\
row_D &= row_D \times (row_C > 0 \ \ \&\& \ \ row_D > 0) \ \ .
\end{aligned} \tag{3.3}$$

Thanks to the requirement of this extra condition for the IC, the second structure disappeared and the Z gates in the ΔE-E_{TOT} matrix could be defined. The identification of the chemical elements will be discussed in Chapter 4.

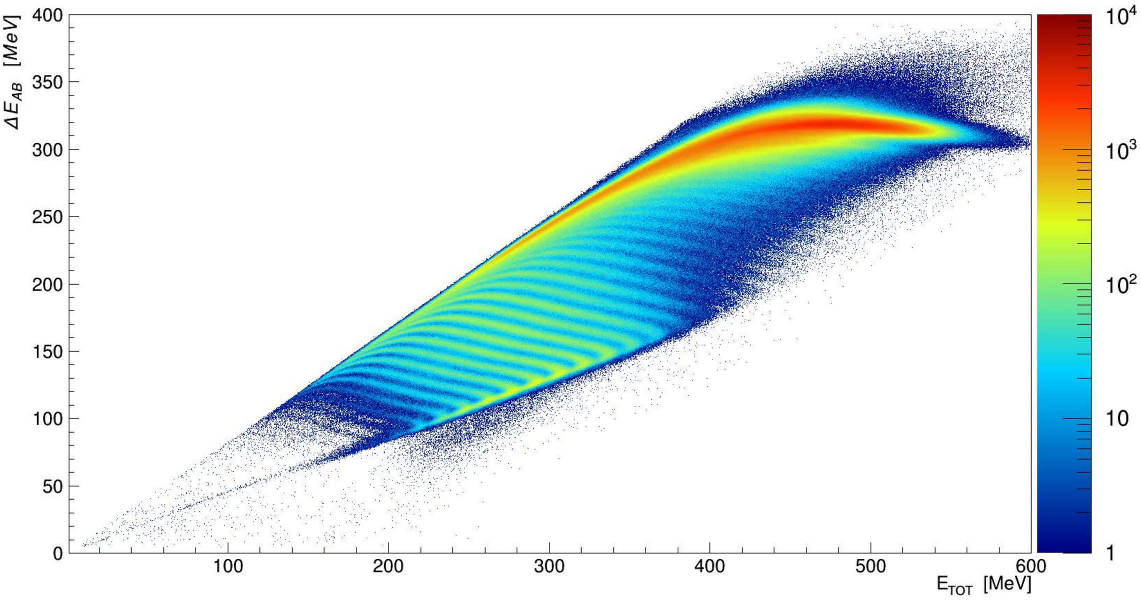

Figure 3.11.: Energy loss in the first two IC rows ΔE_{AB} as function of the total energy loss E_{TOT} (calibrated IC signal summed up the four rows), after requiring the trajectory conditions of Equation 3.3.

3.2.2. Drift chambers

As introduced in Chapter 2, the role of the Drift Chamber is crucial for the trajectory reconstruction of the ions flying into the magnetic spectrometer. In fact, thanks to these detectors, it is possible to directly measure the coordinates (x_f, θ_f, y_f, ϕ_f) which are the starting point for the tracking of the fragments path. The extrapolation of the focal plane coordinates is presented in Figure 3.13.

The event is considered valid only if at least two non-consecutive DC rows fire. Once this condition is satisfied, the ion position inside the DC row is estimated taking the firing channel having the maximum signal. Obviously a misalignment of the channels gain would create a systematic error in the reconstruction of the fragment trajectories. That was the case for the experiment discussed in this thesis, as it is shown in Figure 3.12 (left). Thus, for the 160 channels of all the 4 DC the gain matching was mandatory. Because of the large number of channels to take into account, an automatic procedure was developed in order to obtain a continuous charge distribution in each DC row. The result of this procedure can be seen in 3.12 (right).

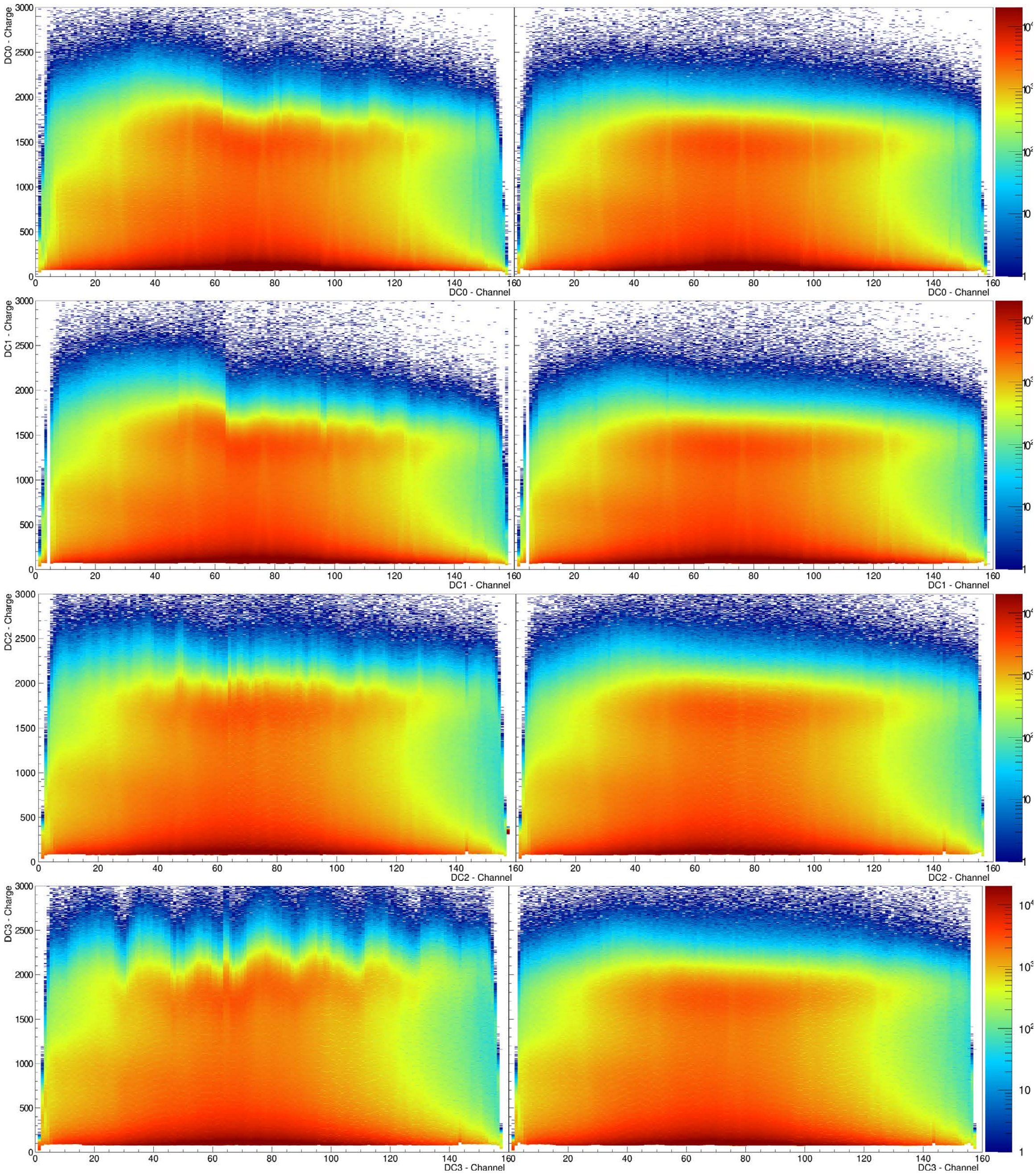

Figure 3.12.: DC signals as function of each channel: (left) raw signals and (right) the signals after the gain matching. The fragments trajectory is reconstructed if at least two non-consecutive rows fire.

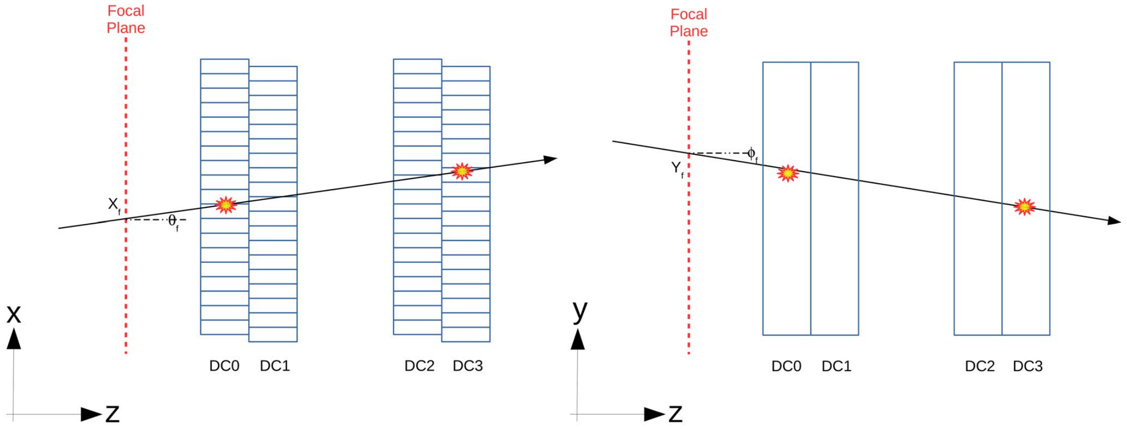

Figure 3.13.: Schematic drawing of the drift chambers (DC) along the xz- (left) and yz-plane, showing trajectory requirement and focal plane coordinates reconstruction. The event is considered valid only if at least two non-consecutive DC rows fire. Then the focal plane position (x_f,y_f), the inclination angles in horizontal (θ_f) and vertical planes (ϕ_f) are extrapolated considering a straight trajectory of the ion.

Once the gain matching was done for all the channels and the focal plane coordinates were measured, the trajectory of the ions was reconstructed, obtaining the magnetic rigidity $B\rho$ and the length of the trajectories. By knowing the length of the trajectory from the target to the focal plane position ($Path$), the coordinates at both the focal plane and the target (x_i, θ_i, y_i, ϕ_i) position, the distance between the detectors measuring the TOF of the beam-like fragments was calculated as

$$D = Path - \frac{17.40}{cos(\phi_i)\ cos(\theta_i)} + \frac{764.52 - 760.00}{cos(\phi_f)\ cos(\theta_f)} \quad , \tag{3.4}$$

where 17.40 cm and 4.52 cm represent the target-start and focal plane-stop distances, respectively. As it is shown in the formula, the distance is a function of both the initial and final angles and this dependence would cause aberrations which required empirical corrections, that will be described in Chapter 4.

3.2.3. Multi-wire entrance detector

The two position-sensitive MWPCs were mounted at the entrance of VAMOS in order to directly measure the initial position of the ions, that is essential to apply an event-by-event Doppler correction (see Chapter 4).

However, as it is shown in Figure 3.14, during the experiment several wires in both the detectors were broken. Because of signal absence in one or both of the detectors, the original tracking code rejected up to ≈80% of good events. In order to avoid losing these data, the trajectory reconstruction code was modified:

- when both the MWPCs had a valid signals, the initial angles were calculated taking into account the horizontal and vertical positions provided by the two detectors

- in case one of the signals coming from one of the detectors is missing, the initial angles were estimated considering the reaction taking place exactly at the centre of the target position
- in the unlucky situation when the entrance detector did not provide valid position signals, the initial coordinates of the particles were taken from the trajectory reconstruction

From the comparison of the Doppler-corrected γ-ray energy spectra of ^{60}Ni (see Chapter 4.2) obtained before and after such trajectory-reconstruction procedure, the statistics was successfully recovered without worsening the energy resolution.

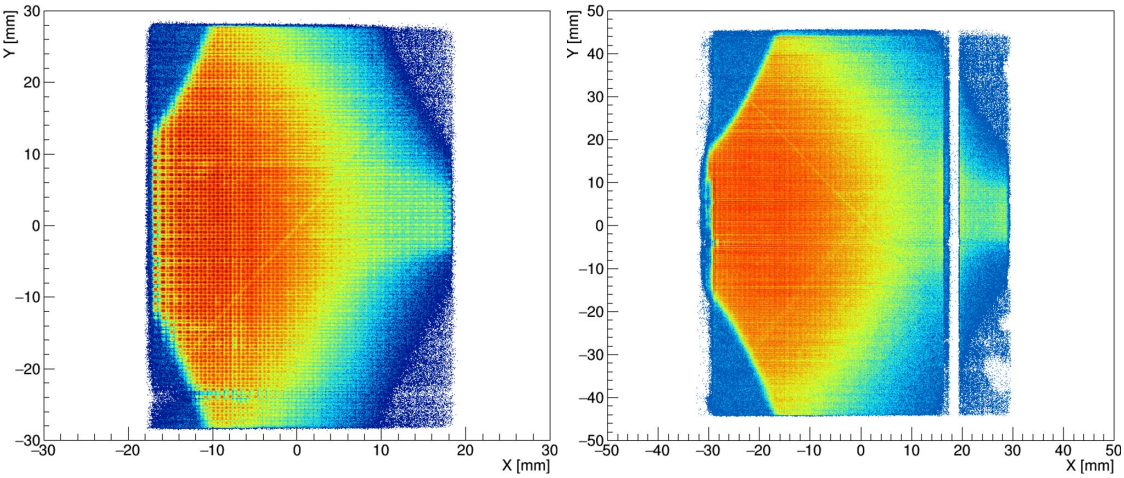

Figure 3.14.: Hit pattern of the first (left) and second (right) MWPC entrance detectors.

3.2.4. Multi-wire focal plane

The MWPPAC detector provides a timing signal used for the TOF construction of the ions, which entered in the VAMOS spectrometer and then reached the focal plane. As it is described in Chapter 2, the detector is segmented into 20 independent sections in order to obtain a fast rise time of the signal. However the signal of each section may be affected by an offset, causing a misalignment between the sections of the detector. Such misalignment introduces a systematic error in the evaluation of the particles TOF and then in the mass identification.

Because of its crucial importance for the ion identification, for the various sections alignment the mass number over the charge state (A/q) ratio was used. Indeed, the ratio directly depends on the results of the reconstruction ($B\rho$ and D) and in first approximation is proportional to the TOF:

$$\frac{A}{q} = \frac{B\rho c}{3.105 D\gamma} TOF \quad . \tag{3.5}$$

Thus, an offset was added to the TOF measured by each MWPPAC section in order to align the A/q, obtaining horizontal straight lines along the x focal plane position.

Despite this alignment, small fluctuations of the mass to charge ratio were present along the horizontal focal plane position. Then, a manual offset was added millimetre-by-millimetre

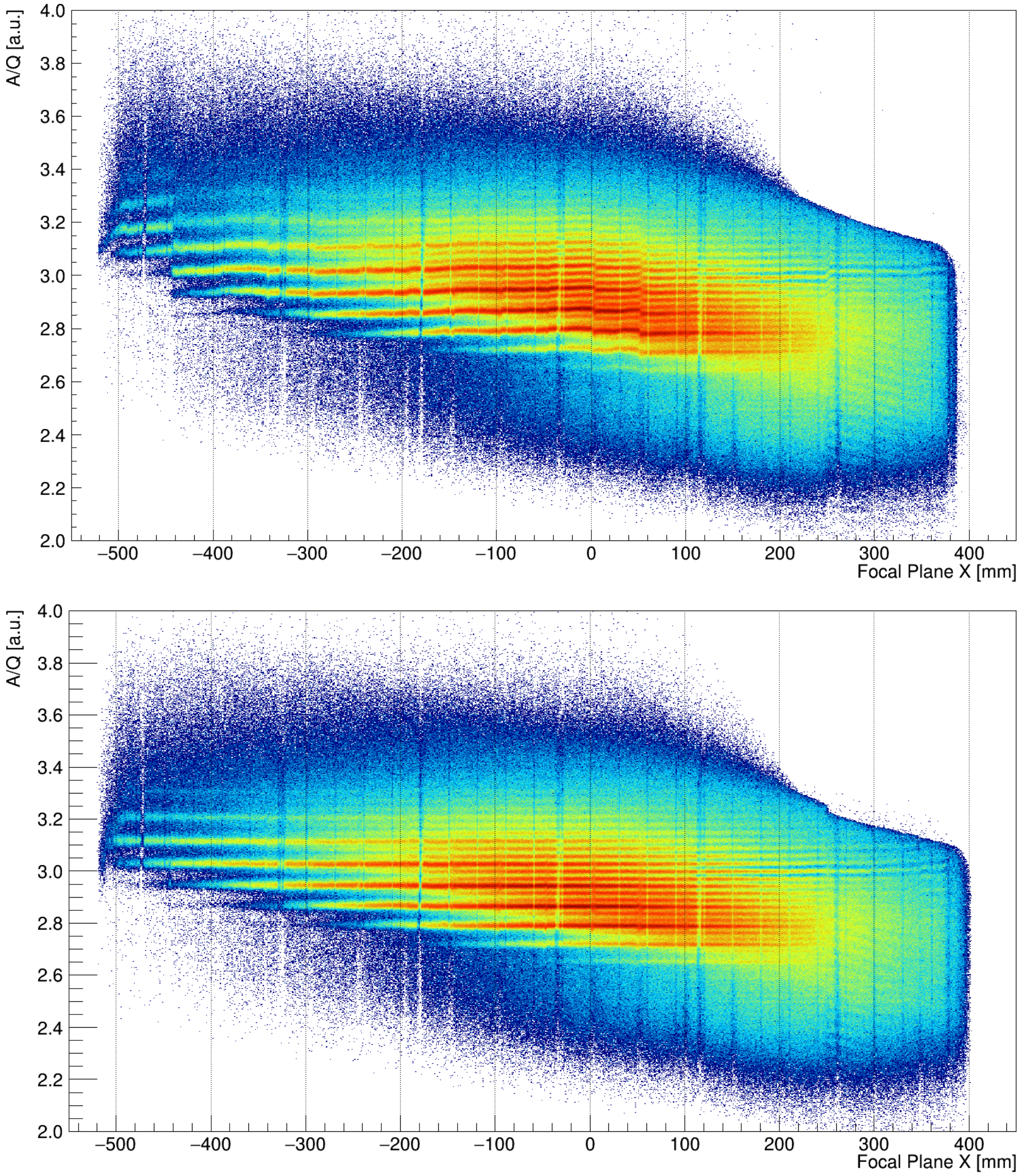

Figure 3.15.: Time alignment of the MWPPAC: per each pad of this focal plane detector an offset is added to the measured TOF. In order to be more sensitive in the procedure, the time alignment was done looking at the mass number over charge state (A/q) ratio as function of the focal plane horizontal position. The two graphs represent the A/q ratio before (top) and after (bottom) the alignment.

to A/q in order to avoid this oscillation, improving the mass resolution of the fragments identification. In Figure 3.15 the A/q versus the horizontal focal plane position is shown before and after the alignment of the 20 sections.

In the two graphs is also possible to see the presence of a different structure for a focal plane horizontal position larger than 200 mm. This effect is due to: this effect was caused by the trajectory-reconstruction algorithm which is not able to calculate at the same time the trajectories for both transfer and fission fragments. Unfortunately, this limit of the algorithm caused the presence of those oblique lines, introducing a mismatch in particular in the fission-fragments mass identification, as it will be discussed in Chapter 4.

Empirical corrections

During the analysis empirical corrections were performed in order to remove aberrations, which introduced dependences between the variables. The most important aberration is caused by the estimation of the distance D between the entrance detector and the MWPPAC at the focal-plane: Equation 3.4 shows that this variable is indirectly obtained from the $Path$ of the reaction products inside VAMOS, initial and final angles. Such dependence propagates in particular to the ion velocity

$$\beta \equiv \frac{1}{c}\frac{D(\theta_i, \phi_i, \theta_f, \phi_f)}{TOF} \quad . \tag{3.6}$$

The latter is used for the calculation of many other variables, such as the A/q ratio (Equation 3.5) and then the charge state (Equation 4.3), which are affected by the discussed relation with the initial and final angles. These dependences do not have any physical meaning, so an empirical correction was performed: the effects of the distance $D(\theta_i, \phi_i, \theta_f, \phi_f)$ were balanced by introducing the same relation in the TOF. From the practical point of view, for each MWPPAC section the TOF was multiplied by a polynomial function $p_{n_i}(i)$ of the $i-$th angle, e. g.

$$TOF(\theta_i, \phi_i, \theta_f, \phi_f) \equiv TOF \times p_{n_1}(\theta_i) \times p_{n_2}(\phi_i) \times p_{n_3}(\theta_f) \times p_{n_4}(\phi_f) \quad , \tag{3.7}$$

until the A/q ratio was independent from the other variables. The result of such aberration correction was shown in Figure 3.15.

3.3. Plunger device

In Chapter 2 the RDDS method for lifetime measurement, which employs a plunger device, was introduced. For this experimental procedure there are mainly two method for extracting the lifetime of an excited state: the Decay-Curve Method (DCM) and the Differential Decay-Curve Method (DDCM). In this thesis both methods were used for extracting the lifetimes of different excited states of interest. In Chapter 4 both experimental procedures will be discussed in detail. For the moment it is important to underline the main difference between the two methods: while on one side with DDCM just the relative distance between two points is considered, on the other side the DCM depends on the absolute target-degrader distance. However, as it was introduced in Chapter 2, the plunger device gives information on the degrader position with respect to an internal reference. Thus, the evaluation of the plunger zero offset was checked in order to obtain the absolute distances.

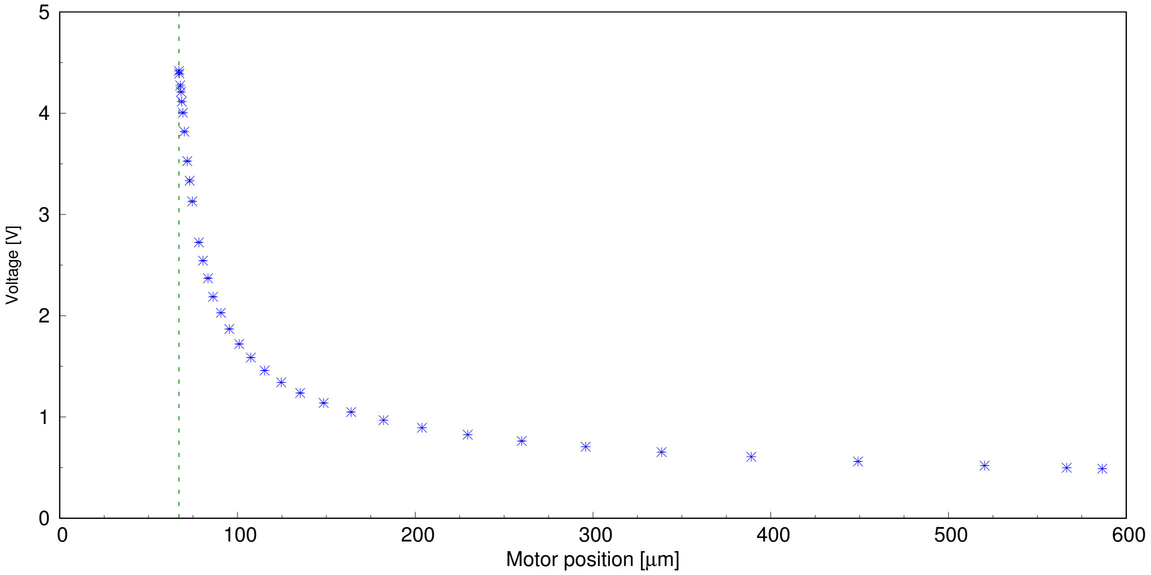

Figure 3.16.: Amplitude of the induced tension signal as function of the motor positions. In order to calibrate the feedback system of the plunger, the calibration procedure was repeated ranging from the contact point (green-dashed line) up to the sensitivity limit of the device.

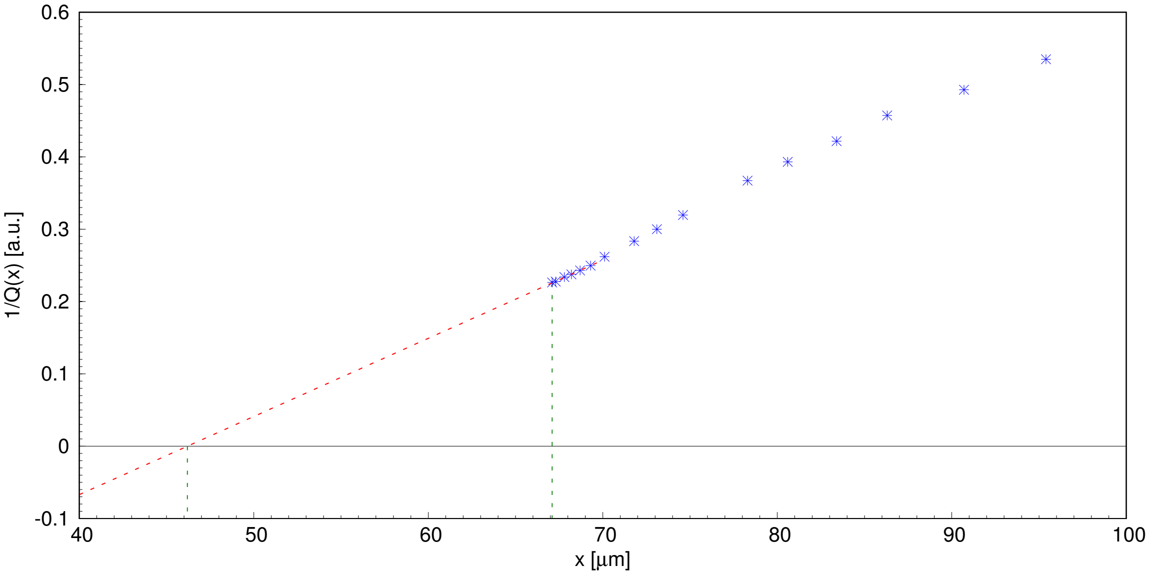

Figure 3.17.: Inverse of the induced charge as function of the motor positions. For small target-degrader separation the trend is linear, so the position of the contact point ($1/Q(x) = 0$) can be extrapolated with a linear fit (red line). The plunger zero offset is given by the distance between the extrapolated and the measured contact point positions (green lines). Figure taken from Reference [101].

First of all the device was calibrated with the capacitance method [135]: while decreasing the foils separation down to the contact point and sending a pulsed tension signal V through the plunger, the induced charge is measured. The procedure was repeated for several motor positions x in order to calibrate the feedback system, as presented in Figure 3.16.

In the case of two planar foils with area A, the induced charge $Q(x)$ as function of the distance x goes as the inverse of the separation between the foils, as described by

$$Q(x) = C(x)V = \epsilon_0 \epsilon_r \frac{A}{x} V \quad , \tag{3.8}$$

where ϵ_0 and ϵ_r are the dielectric constant in vacuum and the relative permittivity, respectively. This asymptotic trend is real for small target-degrader distance. Thus, by plotting the inverse of the induced charge as function of the motor positions, it is possible to estimate the position of the contact point ($1/Q(x) = 0$), as it is shown in Figure 3.17.

From the difference between the estimated contact point and the measured one, the plunger zero offset can be obtained. The estimated value was 20.9 ± 1.2 μm. In Table 3.3 the target-degrader distances are summarised together with their errors. For each distance the total error has two contributions: the systematic error due to the plunger zero offset and the statistical error caused by the fluctuation of the foils during the experiment.

Absolute position	Statistical error	Total error
30.9	0.326	1.24
35.9	0.820	1.45
40.9	0.391	1.26
50.9	0.249	1.23
170.9	0.440	1.29
320.9	0.848	1.47
520.9	1.446	1.88

Table 3.3.: Nominal plunger positions and absolute target-degrader distances with their errors. The statistical error is the root mean square of the fluctuation of the foils separation with respect to the nominal position. The total error has the contributions from the statistical error and the systematic error.

Then, in order to check the presence of other systematic errors, the lifetime of the 2_1^+ state of the ^{106}Cd beam was measured via both DCM and DDCM [101]. The result of the comparison will be presented in Chapter 5.

4

Experimental Data Analysis

This chapter presents the analysis of the data performed after the calibration of the detectors, described in the previous chapter. In particular, the attention will be focused on the complete identification of reaction products, providing their atomic number, charge state and atomic mass. In addition to this, the discussion on the empirical correction devoted to improve the ion identification will be presented. Then, the Doppler correction will be discussed, considering a refined version obtained by optimising the AGATA position and by correcting the measured ion energy for the energy loss inside VAMOS. After that the reconstruction of the Q-value of the reaction, crucial tool for controlling the feeding from higher-lying states, will be shown. In order to better understand the Q-value distribution and the possible consequences for the lifetime measurement, a qualitative interpretation of the resulting identification will be discussed. Because the beam energy was $\approx 70\%$ above the Coulomb barrier, Deep-Inelastic Collisions (DIC) were in competition with the MNT reactions: the beam-like ions were obtained by the reaction ^{106}Cd+^{92}Mo, while the nuclei in the Ni region were mostly produced in the ^{106}Cd+^{24}Mg reaction. At the end, the Recoil Distance Doppler-Shift (RDDS) method, already introduced in Section 2.4, will be carefully presented, focusing the attention on the two main techniques that were used to extract the lifetime of an excited state: the Decay-Curve Method (DCM) and Differential Decay-Curve Method (DDCM).

4.1. Ion identification

During the experiment, the data were collected by requiring the coincidence condition that at least one γ ray and one particle had to be detected by AGATA and VAMOS spectrometers, respectively, within a time window of 2 μs. However, given this time window was much larger than the time between consecutive beam bunches, delivered by the cyclotron with a period of ≈ 110 ns, a more restrictive condition was necessary in order to avoid the random coincidences between γ rays and identified particles. This time condition was set on the difference between the timestamp of AGATA ($TStrack$) and the one of VAMOS (VTS), in order to select only one bunch. In addition to that, an extra requirement on the TOF was then set in order to avoid the random coincidence. In the following, all the discussed results will include such coincidence conditions, that are presented in the 2D particle-γ matrix of

Figure 4.1.

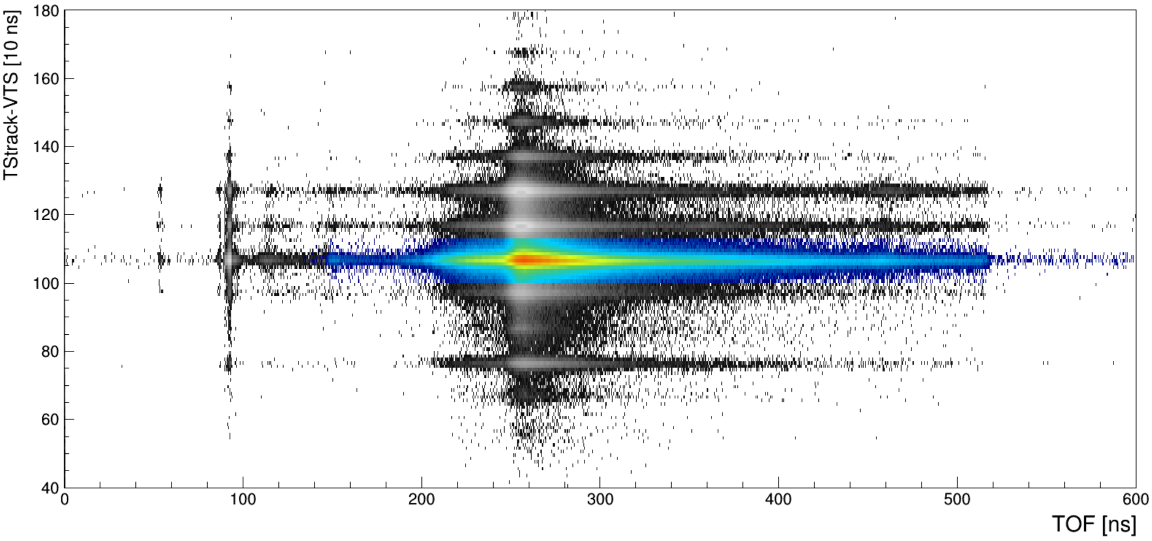

Figure 4.1.: Difference between the timestamp of AGATA ($TStrack$) and the VAMOS one (VTS) as a function of the ions TOF, showing all the events when a particle and a γ ray were detected in coincidence. In the timestamp difference it is possible to distinguish between the different bunches of the beam, delivered by the cyclotron with a period of ≈110 ns. In order to exclude random coincidences, a time condition (coloured in the plot) was set.

As introduced in Section 2.3, VAMOS provides the complete identification of the reaction products passing into the spectrometer, giving event-by-event information such as the atomic number (Z), the atomic mass (A) and the charge state (q). After the calibration and the corrections applied to the data coming from the IC, the Z-identification of the ions was performed. Then, by combining the information related to the ions total energy together with the direct TOF measurement, the charge state of the fragments was defined. Finally, the atomic mass was easily extracted.

In addition to that, thanks to the MWPC entrance detector and to the ions-trajectory reconstruction, the spectrometer also provides the ions velocity vector. This information is crucial for performing an accurate even-by-event Doppler correction for those γ rays emitted in coincidence with the identified reaction products.

4.1.1. Atomic number identification

After the gain matching, the time correction of the IC signals and the validation conditions of Equation 3.3, the gate for the atomic number identification were set. In fact, ions lose energy inside the IC gas according to the Bethe-Bloch formula [105], whose trend is proportional to the atomic number of the flying fragment [136]

$$\left\langle \frac{dE}{dx} \right\rangle \propto Z^2 \quad . \tag{4.1}$$

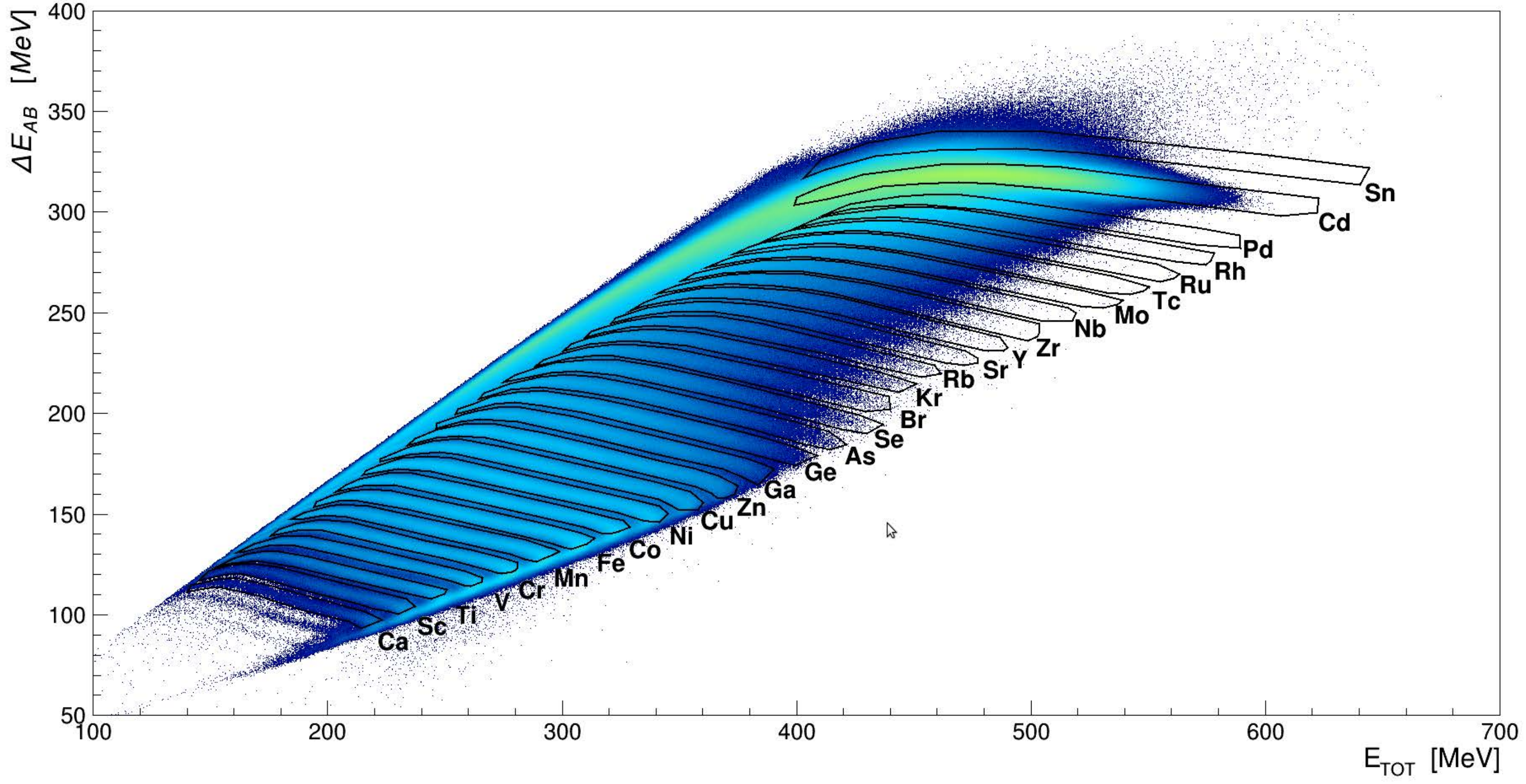

Figure 4.2.: Energy loss in the first two IC rows (ΔE_{AB}) as function of the total energy loss E_{TOT}, showing the gates on the atomic number for all the identified ions. In the experiment the ^{106}Cd beam at the energy of 770 MeV impinged onto ^{92}Mo target, while ^{24}Mg foil was used as a degrader for the RDDS method. The beam-like ions were obtained by the reaction ^{106}Cd+^{92}Mo, while the nuclei in the Ni region were mostly produced in the ^{106}Cd+^{24}Mg reaction.

In Figure 4.2 all the gates used for the Z identification of the fragments are shown. The identified channels were mainly due to two different reactions: on one side the beam-like ions were primarily populated via multi-nucleon transfer and deep-inelastic reactions, while on the other side the lighter nuclei were obtained via the fusion-fission reaction of the beam interacting with the degrader material.

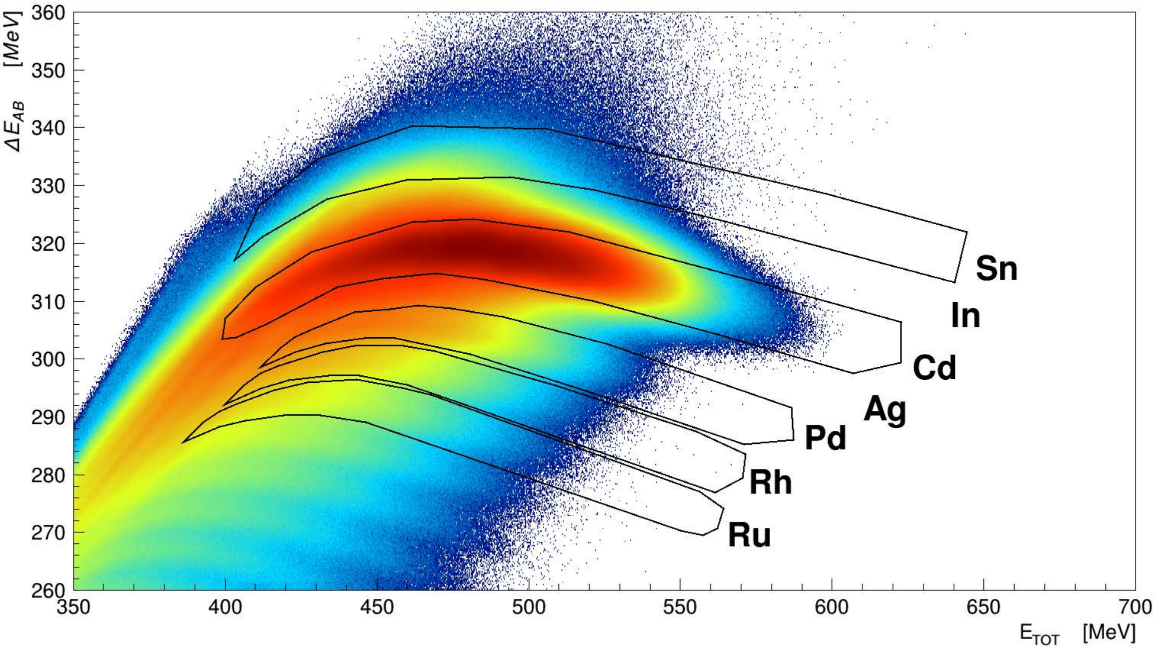

Figure 4.3.: Energy loss in the first two IC rows (ΔE_{AB}) as function of the total energy loss E_{TOT}, focusing the attention on the beam-like fragments. The Z resolution was at the limit for the nuclei in this region. Especially difficult was the selection of the atomic number close to the overwhelming inelastic channels (i.e. $\pm 1p$ channels).

Focusing the attention in the beam-like channels, in the $\Delta E - E$ matrix of Figure 4.3 the separation between the channels is not well defined. As mentioned in Chapter 2, experimental details, such as the beam energy, were optimised in order to identify the beam-like fragments without increasing too much the excitation energy of the reaction products. However, while passing through the spectrometer, the energy loss of the reaction products was larger than planned due to the change of the entrance detector to the described new dual position-sensitive MWPC [119]. Unfortunately, increasing the beam energy would lead to a smaller grazing angle but, because of mechanical constraints due to the coupling of the two spectrometers [137], it would not allow to put AGATA in the compact configuration (see Appendix A), resulting in a lower γ-ray detection efficiency. Obviously, during the analysis this low Z-resolution resulted in several problems, such as heavy contaminations due to the inelastic-scattered beam (for example any identification of the $\pm 1p$ channels is completely impossible because they are overwhelmed by the ^{106}Cd events). Indeed, because of this second issue, the Z-gate identification of the channel of interest was systematically changed in order to maximise the statistics in the Sn spectra and reduce at the same time the contamination from the beam.

4.1.2. Charge state identification

By summing the energy loss inside each IC row the ion total energy E_{TOT} can be obtained. In first approximation, E_{TOT} can be considered equal to the kinetic energy E_k, which can be calculated from the TOF measurement. From this assumption a "temporary mass" M_{temp} can be estimated:

$$E_{TOT} = E_k = (\gamma - 1)\, M_{temp} c^2 \quad , \tag{4.2}$$

where γ is the Lorentz factor. Considering that the A/q ratio is given by the kinematic information (see Equation 3.5), the charge state q of the reaction products can be easily obtained as

$$q = \frac{M_{temp}}{A/q} = \frac{E_{TOT}}{(\gamma - 1)\, A/q} \quad . \tag{4.3}$$

As described in Section 3.2, during the analysis a time dependence correction had been introduced for the IC signal in order to get rid of the pressure fluctuation caused by the variation of the gas temperature. Despite such correction, minor but still non-negligible fluctuations were observed in the charge state, as it is shown in Figure 4.4. In order to remove the time dependence of the charge state, the same procedure described for the IC signals was performed also to this variable: a minute-by-minute correction was applied in order to move the centroid of the different charge states to the proper value.

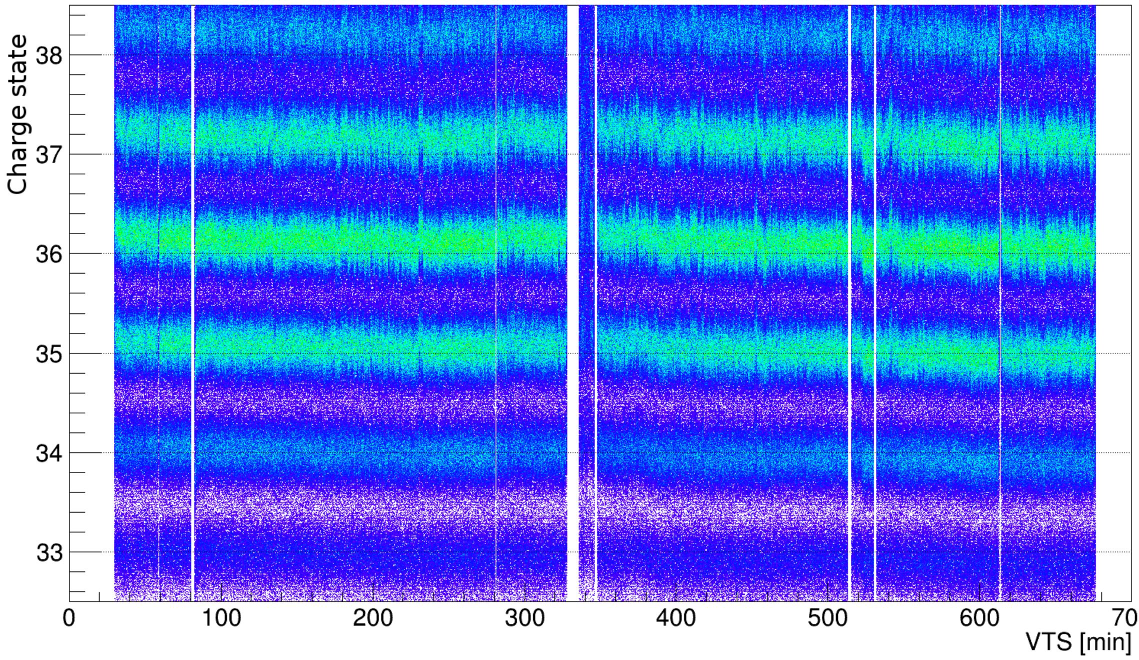

Figure 4.4.: Charge states as function of the validated time-stamp (VTS). Even after correcting the energy loss fluctuations in the ionization chamber, the same time correction has to be set directly to the charge state.

After applying the time and the empirical corrections (the latter will be explained in the following), for each identified element, gates on q were set in order to reduce possible contaminations. In fact, considering the procedure to extract the charge-state information, the problems affecting the A/q ratio (see Figure 3.15) influenced the charge-state variable as well. Such problem was caused by the trajectory-reconstruction algorithm which is not able to calculate at the same time the trajectories for both transfer and fission fragments [138]. This issue affects mainly the fission-fragments identification. However, in order to validate the experimental charge state assignation, the measured charge state was compared with different codes [139–142] for the inelastic-scattered beam in order to check the experimental method. In Figure 4.5 the normalised charge-state yields for the identified ^{106}Cd are reproduced by the most recent formulas [140, 142]; the negligible mismatch with the calculated values for the higher charge states can be explained by the acceptance of the VAMOS magnetic rigidity [118], which may cause a cut-off.

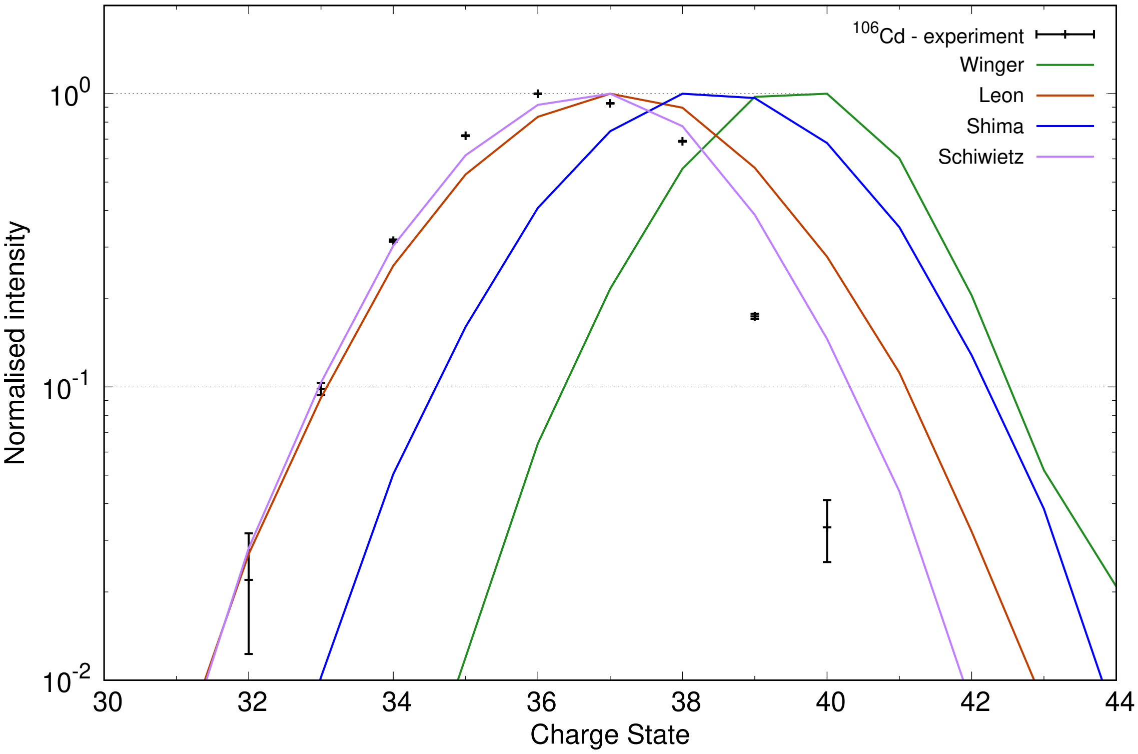

Figure 4.5.: Normalised yields of the charge states for the identified ^{106}Cd. The experimental values are compared with different empirical formulas: (green) Winger [139], (brown) Leon [140], (blue) Shima [141] and (purple) Schiwietz [142]. The empirical predictions were calculated by using LISE++ [143–146], considering the reaction products at focal plane. Measured and calculated yields are normalised setting the maximum value equal to 1.

Empirical corrections

In addition to the corrections mentioned in Section 3.2, other empirical corrections were introduced during the analysis in order to solve the presence of systematic errors caused by technical development of the detectors.

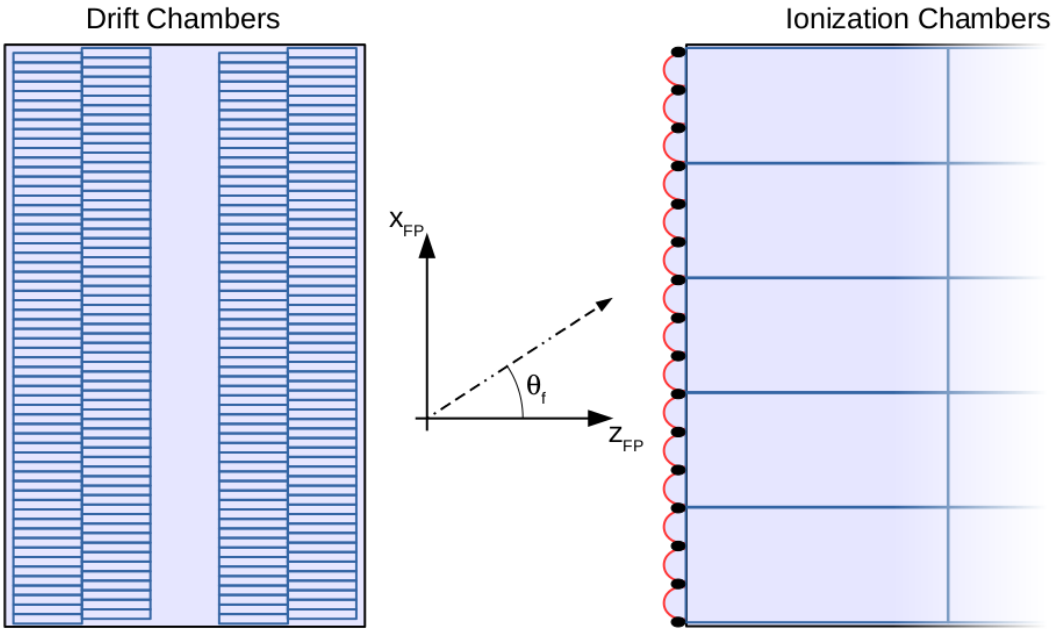

Figure 4.6.: Schematic draw of the focal-plane detection system along the xz-plane, showing in particular the IC Mylar window (red line) which is supported by the vertical nylon wires (black dots). Despite the presence of the wires, the Mylar foil is bent because of the different operating pressure of the DC and IC. By knowing the horizontal angle at the focal plane (see Figure 2.13), the reaction products energy loss can be corrected.

One of these corrections involve the IC of VAMOS: a 2.5 μm Mylar foil is placed in front of the detector and it is supported by 32 vertical nylon wires. However, despite the presence of the wires, the window was bent because of the gas pressure in the chamber, as it is shown schematically in Figure 4.6. The bumps between the wires introduced a systematic error which affected mainly the energy loss in the first rows, because the ions had to travel through a gas volume of different thicknesses. Because of such deformations of the Mylar window, the variation on the measured total energy was estimated to be $\delta E/E \approx 2-10\%$. The horizontal position of the wires x_{wire} can be easily defined as

$$x_{wire} = x_{FP} + 473.0\ tan(\theta_f) \quad , \tag{4.4}$$

where 473.0 is the distance in millimetres between the focal-plane and the Mylar window position. Then, the energy loss in the first (ΔE_A) and second (ΔE_B) IC row can be fixed by multiplying the calibrated signals for a polynomial function of x_{wire}, as in analogy with the previously-described aberrations:

$$\begin{aligned} \Delta E_A &= \Delta E_A \times p_{n_A}(x_{wire}) \\ \Delta E_B &= \Delta E_B \times p_{n_B}(x_{wire}) \quad . \end{aligned} \tag{4.5}$$

Finally, in order to perform a more precise correction of the total energy loss, the procedure was redone by observing the trend of the charge state $q \propto E_{TOT}$ as a function of the horizontal position at the IC entrance. Thanks to this empirical correction, the charge state resolution $\delta q/q$ improved by almost 20%.

4.1.3. Atomic mass identification

Once the charge gates were defined for each element, the atomic mass can be easily obtained by multiplying the A/Q ratio for the charge state. However, in order to improve the resolution of the mass spectra, a calibration was performed: after gating on each charge state and obtaining the peaks position by having fitted the A/q spectrum with a multi-Gaussian function, the *effective charge state* q_{eff} and the *mass offset* M_{off} were extracted from the linear fit

$$M = A/q \times q_{eff} + M_{off} \quad . \tag{4.6}$$

Unfortunately, despite the gates set for both atomic number and charge state, in the A/q spectra background events were still visible. Thus, before performing the extraction of A, per each charge state an extra condition was set to the A/q spectra in order to reject the unwanted events and reduce the presence of such background. In left panels of Figure 4.7 the A/q spectra and the gates, used to cut the unwanted background events, are presented per each charge state of the palladium ($Z = 46$) channel.

Thanks to the calibration and the refining conditions, the mass resolution reached in the analysis was $A/\Delta A \approx 170$. Then, by looking at the mass spectrum as a function of the horizontal position at the focal plane, 2D gates were set for the definition of the atomic-mass number and for reducing the possible contaminations between consecutive channels. As example of such required condition, in the right-top panel of Figure 4.7 the 2D gates are showed for the palladium isotopes. Then, the comparison between the calibrated mass spectrum of palladium isotopes and the set gates is presented in right-bottom panel of Figure 4.7.

4.1.4. Yields of beam-like recoils

The procedure for obtaining the mass distribution is done for all the atomic numbers. Therefore, in this way the yield for all the beam-like recoils produced in the reaction was obtained. From this yields the cross section can be extracted for each channel, after a detailed estimation of the response function of the VAMOS spectrometer[1].

For all the isotopes, the yields measured in this experiment are shown in Figure 4.8. In this figure two different regions can be clearly identified:

---

[1] For the relative cross section, the study of the response function of the spectrometer is sufficient. For the absolute cross section, instead, a normalization to a reference point (e.g. elastic channel, already known measurement, theoretical prediction, etc.) is also necessary.

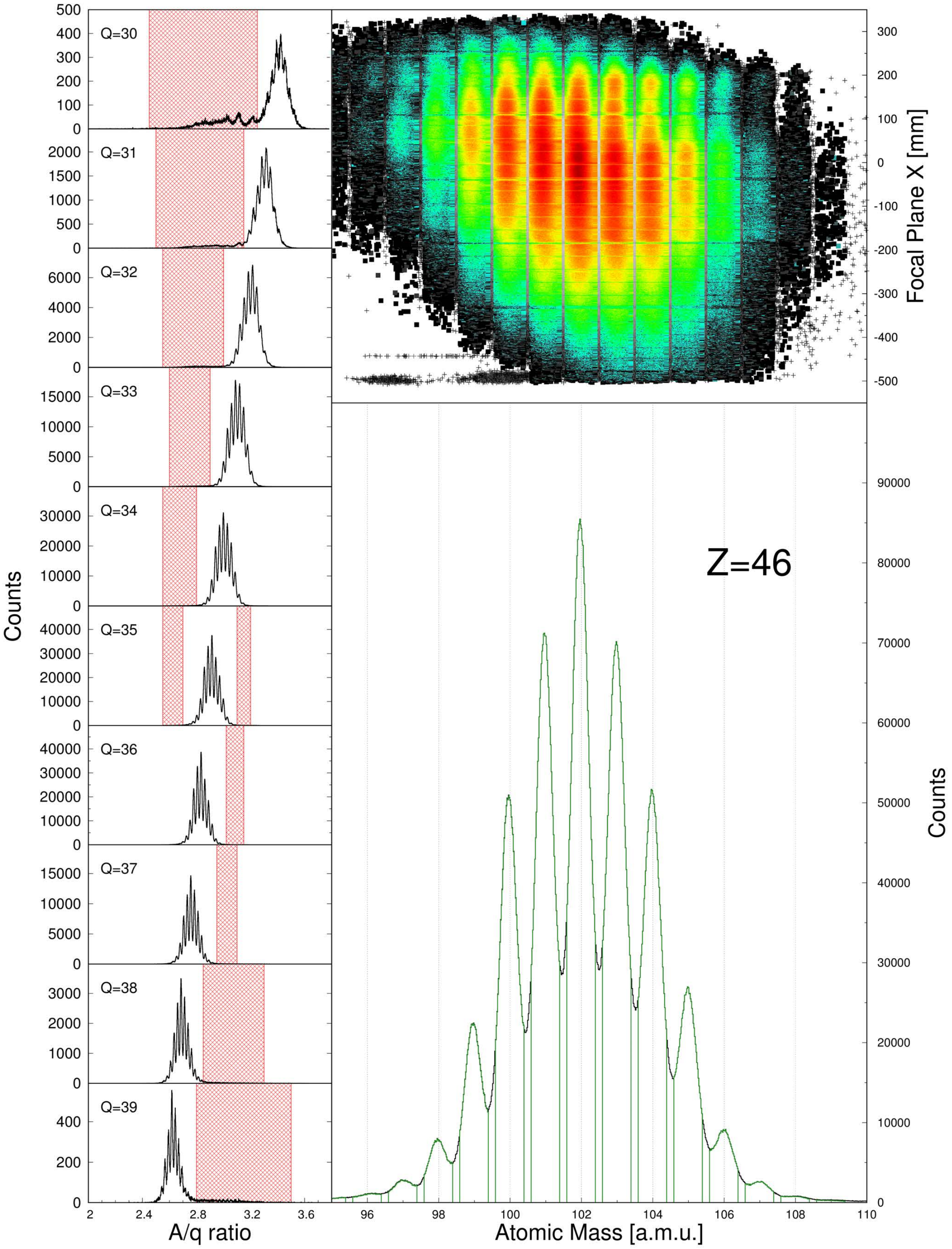

Figure 4.7.: Atomic mass identification for the gate on $Z = 46$. (left) A/q spectra for the different charge states, showing in red the events that were rejected for reducing the background. (right-top) Calibrated mass as a function of the focal-plane horizontal position. The coloured region represents the 2D gates, while the grey-scale points are the rejected events. (right-bottom) Calibrated mass spectrum, showing in green the gates that were defined for the different atomic mass numbers.

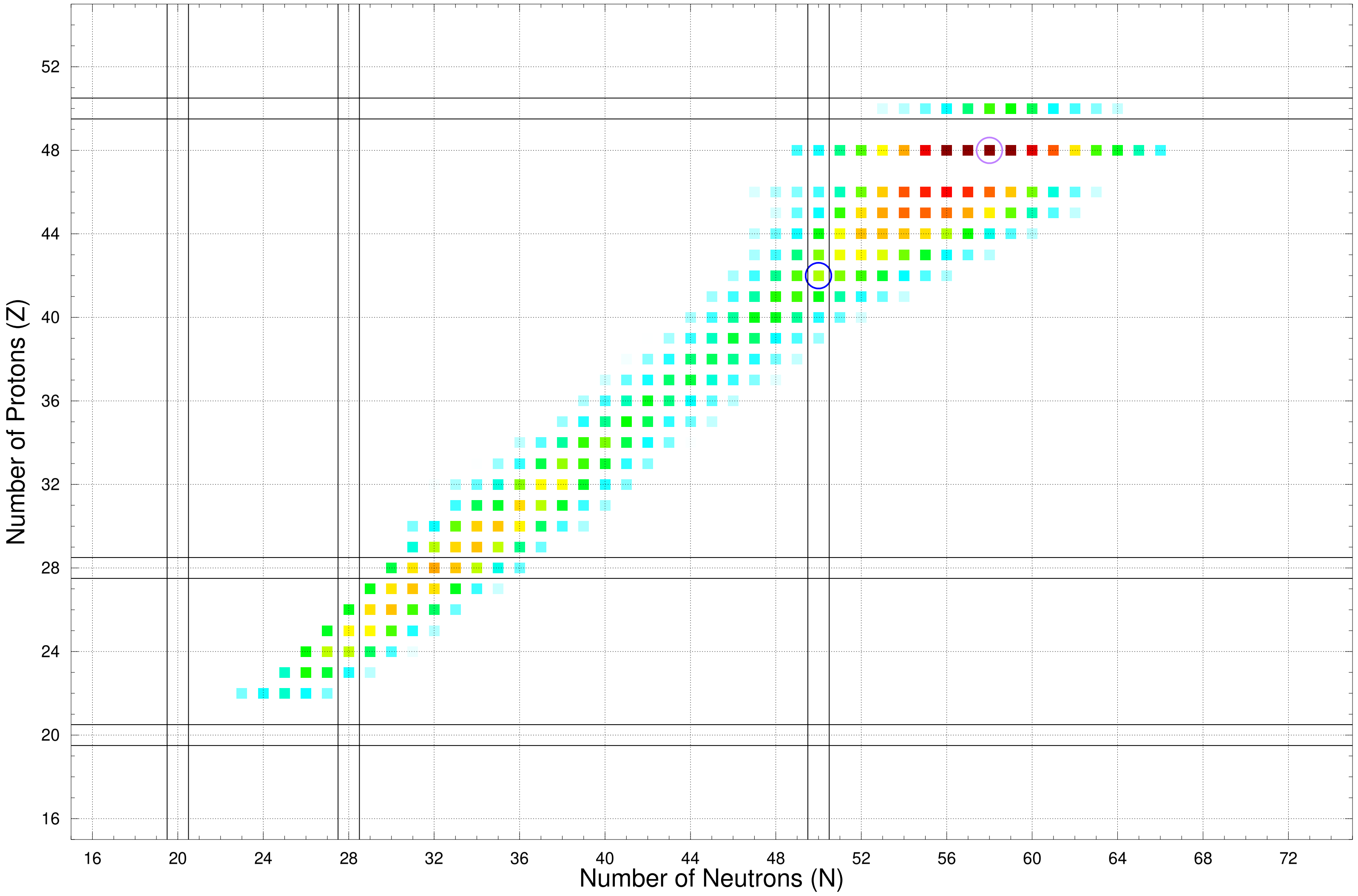

Figure 4.8.: Yields of the nuclei, identified by the VAMOS spectrometer in coincidence with AGATA, as a function of their proton and neutron numbers. The beam-like ions were obtained by the reaction of the ^{106}Cd beam with the ^{92}Mo target, while the nuclei in the Ni region were mostly produced by the ^{106}Cd impinging onto the ^{24}Mg degrader. The position of the beam and target nuclei are highlighted by the purple and blue circles, respectively.

- close to $Z \approx 28$ the nuclei were populated via the fusion-fission reaction of the beam with the degrader material;
- the beam-like products ($Z \approx 48$) were produced mainly via MNT reactions close to the ^{106}Cd and via deep-inelastic collisions (DIC) for more exotic channels.

The latter region, in fact, is too extended to be populated only via MNT reaction: for example, in the figure the yields of the ^{100}Mo ($-6p$ channel) and ^{112}Cd ($+6n$ channel), whose cross section should be negligible according to the GRAZING code [147] (see Figure 4.11), are of the same order of magnitude than the $+2p$ channel. This can be due to the combination of two facts: on one side, the contamination of the inelastic-scattered beam which overwhelms the nearby channels; on the other side, the presence of DIC components, as the beam energy was $\approx 70\%$ above the Coulomb barrier.

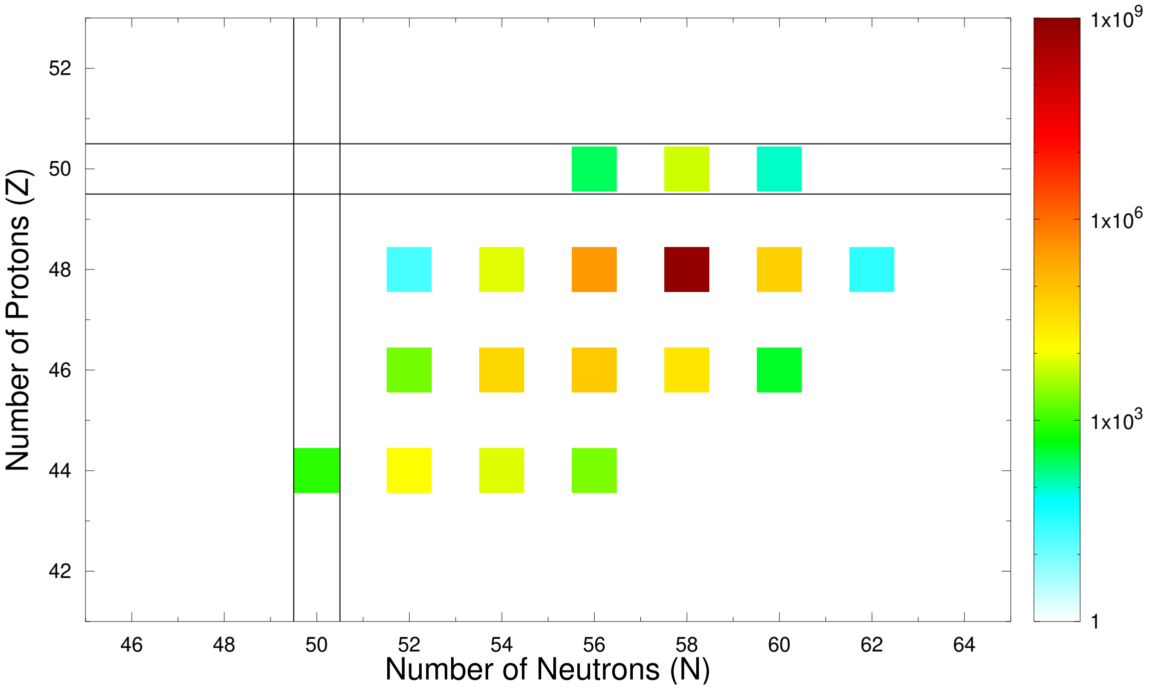

Figure 4.9.: Yields of the even-even beam-like nuclei as a function of their proton and neutron numbers. The yields were estimated from the efficiency-corrected peak area of the $2^+ \rightarrow 0^+_{g.s.}$ transition.

In order to better depict the yield of the various isotopes in the $Z \approx 48$ region of interest, from the Doppler-corrected spectra the peak area of the $2^+_1 \rightarrow 0^+_{g.s.}$ transition was measured in all the even-even beam-like products and it has been plotted in Figure 4.9. This plot overcomes the problem in the uncertainty of the Z gates or in the contamination from the inelastic-scattered beam events. Indeed Figure 4.9 show the presence of two different behaviours of the identified beam-like ions: on one side Pd ($Z = 46$) and Ru ($Z = 44$) isotopic chains have a symmetric distribution, which is typical for deep-inelastic processes[2]

---

[2] Another contribution to this symmetric trend can be due to the re-distribution of the primary fragments because of evaporation process [149].

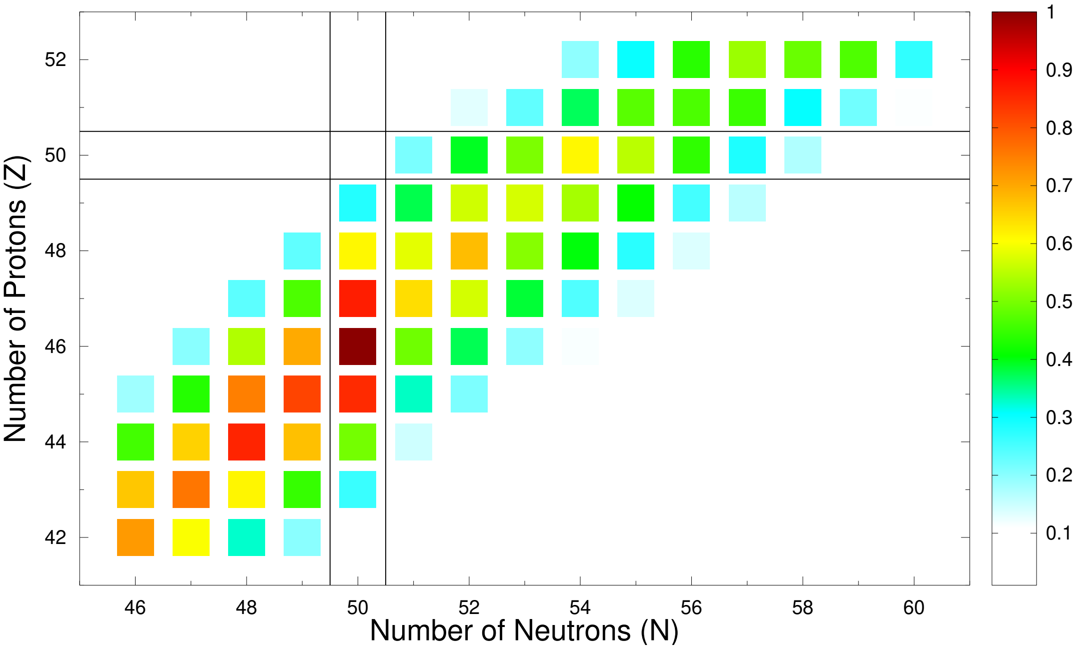

Figure 4.10.: Normalised yield of the fusion-fission reaction of the ^{106}Cd beam with the ^{92}Mo target, calculated by the reaction code GEF [148]. In the simulation the compound nucleus ^{198}Th with the excitation energy $E_x = 120$ MeV were considered and secondary processes like particle evaporation were also added. In the graph the highest yield is normalised to 1.

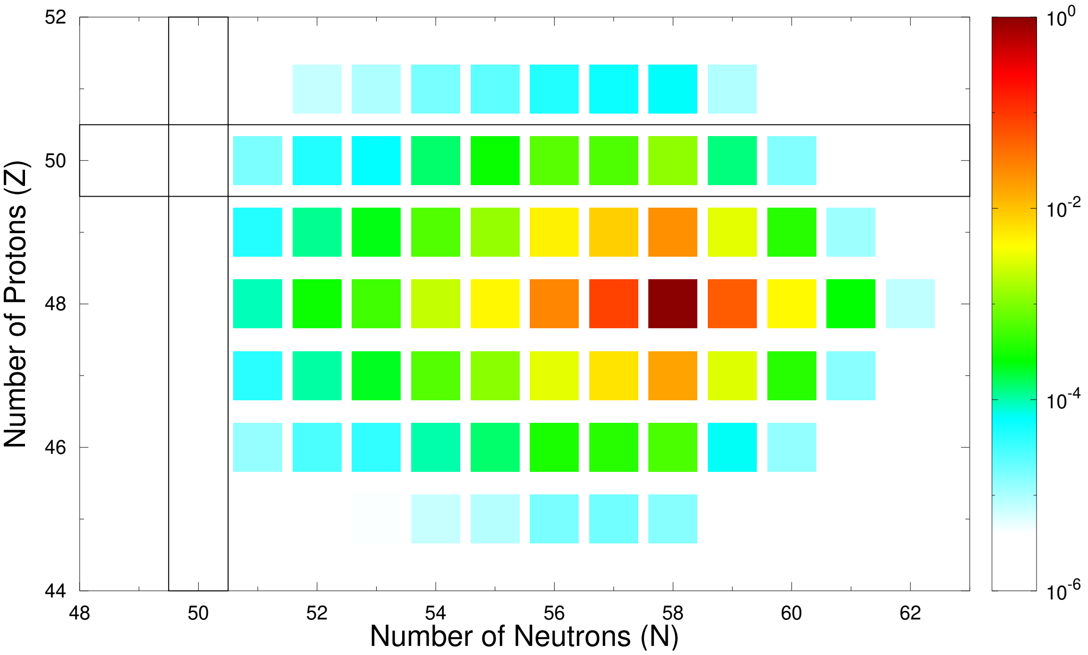

Figure 4.11.: Normalised yield of the MNT reaction of the ^{106}Cd beam impinging onto the ^{92}Mo target at the energy of 770 MeV. The calculation, performed with the reaction code GRAZING [147], was also considering secondary processes, such as particle evaporation. In the graph the highest yield is normalised to 1.

[48]; while on the other side cadmium ($Z = 48$) and tin ($Z = 50$) chains have a more asymmetric distribution expanding to more neutron-deficient nuclei, which is a fingerprint of MNT reactions [48] due to the Q-value (see Chapter 1). These results confirm that the channels of interest were populated mainly via MNT reactions.

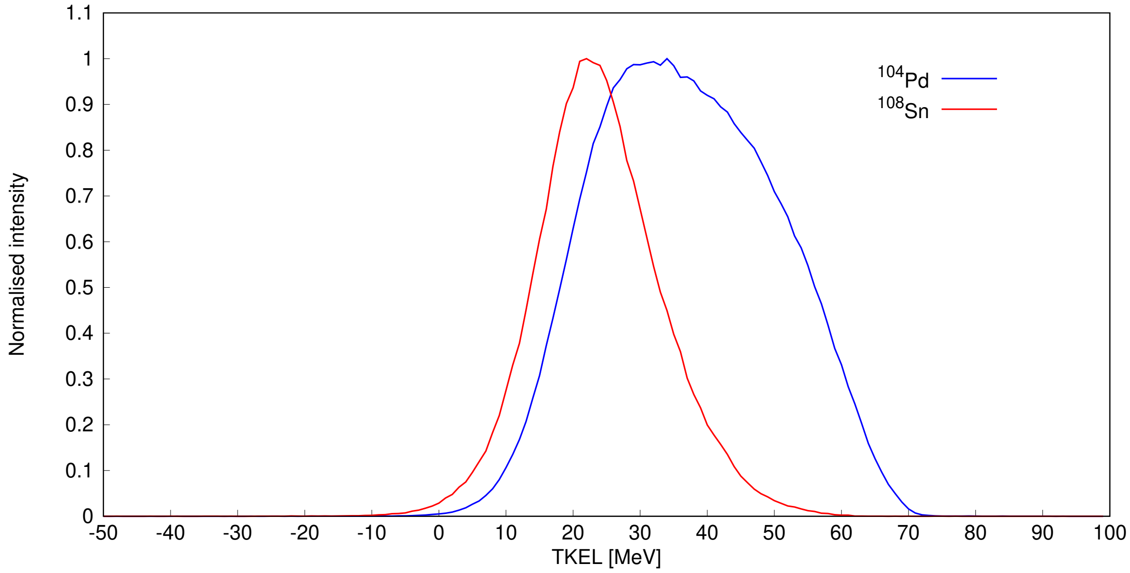

Figure 4.12.: Total Kinetic Energy Loss (TKEL) distribution, obtained by gating on ^{108}Sn (red) and ^{104}Pd (blue). The two nuclei were populated via different reaction mechanisms and this affected the distribution of the TKEL. The distributions are normalised by scaling their maximum value to 1.

The understanding of the reaction mechanisms populating the identified beam-like ions is crucial for choosing the proper method of analysis. In fact, while Q-value method has been widely used with MNT reactions [98, 150], DIC make such analysis more complicated: in this second case, the Q-value distribution is broader than the MNT one, so the control of the feeding from high-energy states becomes less precise. During the analysis, this effect was seen while measuring the lifetime of low-lying states in nuclei with $Z \leq 46$. In these nuclei, where the statistics is not sufficient to use the coincidence method, the Q-value gate cannot "simplify" their level scheme by reducing the direct feeding of the states. However, as it will be discussed in Section 5.2, the Q-value method works for lifetime measurement in Sn isotopes. The difference between the two cases can be seen in Figure 4.12, where the Total Kinetic Energy Loss (TKEL) distribution is shown for ^{104}Pd and ^{108}Sn.

In order to get a qualitative idea of the reaction mechanisms populating the beam-like ions, the fusion-fission reaction of the ^{106}Cd beam with the ^{92}Mo target material was simulated via the reaction code GEF [148]. In fact, considering that during the experiment the beam energy was about 70% larger than the Coulomb barrier, it is reasonable to think that the beam-like fragments with $Z \leq 46$ were produced via fusion-fission reaction. The channels populated in the fission of the compound nucleus ^{198}Th at the excitation energy $E_x = 120$ MeV were calculated including also secondary processes, such as particles evaporation. The result can be observed in Figure 4.10, where the normalised yields of the fission fragments are presented: along the isotopic chains the distribution is quite symmetric, while the yields drop quite rapidly as the atomic number increases for $Z > 46$. Such trend is completely different with respect to what is predicted by the GRAZING reaction code [147] for MNT reaction: Figure 4.11, in fact, shows that the normalised yields decrease exponentially with the increasing transferred nucleons, relatively to the ^{106}Cd beam. Obviously these two calculations give just a qualitative idea about the reaction mechanisms, because other important factors, such as the response of the VAMOS spectrometer, are not included in the predictions.

4.2. Doppler correction

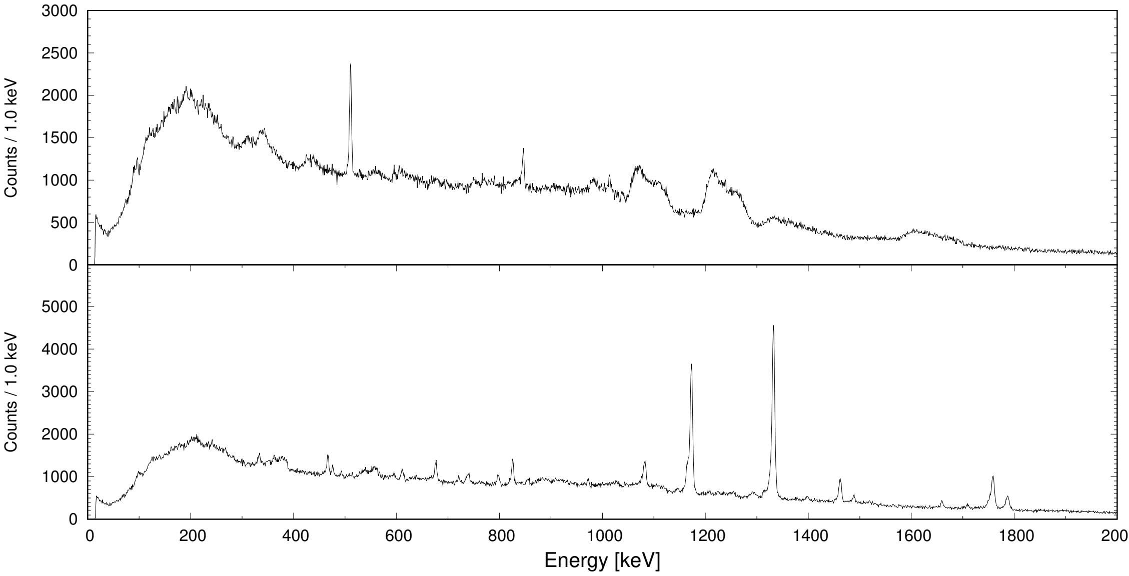

Figure 4.13.: Gamma-ray energy spectrum for ^{60}Ni before (top) and after (bottom) performing the Doppler correction. The FWHM of the 1332 keV peak is 5.3 keV, which is just ≈ 30% higher than what had been obtained with radioactive sources.

The emitted γ rays were detected in coincidence with the particles identified in VAMOS. Thus, two different cases can be distinguished: on one side the excited ions emitted the electromagnetic radiation while resting because implanted in the reaction chamber or stopped inside the target material; on the other side the VAMOS-identified ions emitted γ rays in flight. For this second situation the detected energy was affected by the Doppler shift, which depends on the particle velocity ($\beta \approx 11\%$) and the angle θ between the emitted γ-ray and the direction of the particle. The relationship between the real γ-ray transition energy $E_{\gamma 0}$ in the centre-of-mass frame and the detected energy E_γ is

$$E_\gamma = E_{\gamma 0} \frac{\sqrt{1-\beta^2}}{1-\beta\ cos\theta} \quad . \tag{4.7}$$

By combining the information of the first interaction point in the AGATA detectors, provided by the γ-ray tracking algorithm, with the recoil velocity vector determined by VAMOS, the Doppler correction of the emitted γ rays can be performed on an event-by-event basis.

The TOF of the reaction fragments flying inside VAMOS was measured between the MWPPAC and the MWPC. Between such detectors the ions had to fly through passive materials losing kinetic energy [151]. Thus, a correction for the energy loss was introduced in order to obtain the proper ion velocity that should be used in Equation 4.7.

In addition, in order to get a more precise estimation of the γ-particle angle the effective target-AGATA distance was evaluated. In fact, during the setting of the experimental apparatus, there could be a shift of the plunger device or of the AGATA spectrometer. This offset might be up to a few millimetres and therefore will degrade the energy resolution after the Doppler correction.

In Figure 4.13 the effect of the Doppler correction can be observed for the nucleus ^{60}Ni: after the optimisation, the FWHM at 1332 keV was 5.3 keV [101, 102]. By gating on this nucleus, produced via the fusion-fission reaction of ^{106}Cd on ^{24}Mg, the quality of the Doppler correction can be checked and directly compared to the resolution obtained with a ^{60}Co source. Thanks to the unique capabilities of AGATA and VAMOS, it was possible to obtain an in-beam energy resolution just $\approx$ 30% higher than what had been obtained with radioactive γ-sources. A good energy resolution is crucial to clearly separate the two components of the γ-ray transitions when using the RDDS method.

4.2.1. Energy loss inside VAMOS

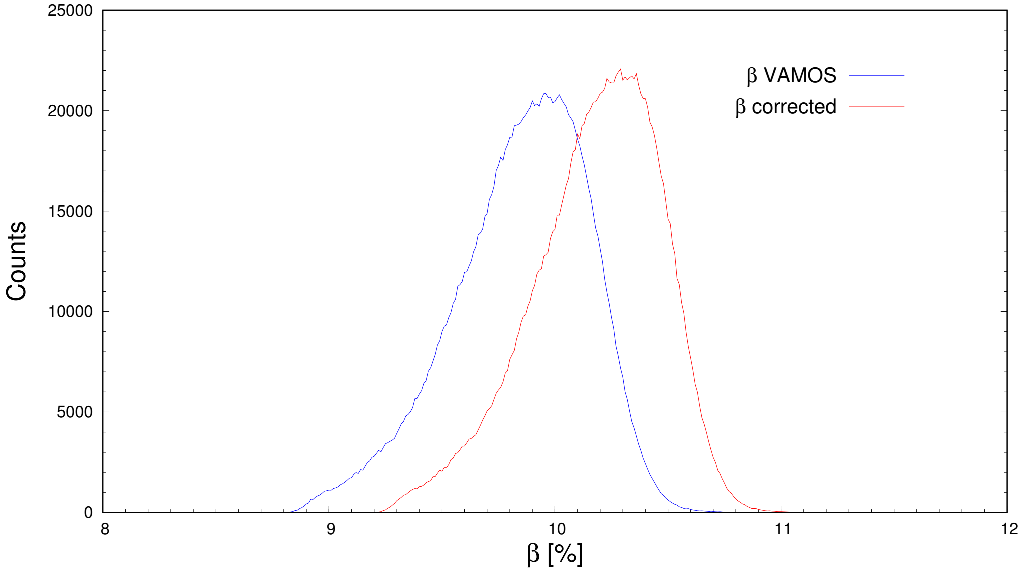

Figure 4.14.: Comparison between the reaction fragments velocity (blue) directly measured by VAMOS and (red) the energy-loss corrected one for the ^{106}Cd after the reaction. Because of the energy loss in such materials, the velocity that should be used for the Doppler correction is $\Delta\beta/\beta \approx 4\%$ larger than what was measured by the VAMOS spectrometer.

While flying inside the VAMOS spectrometer, the reaction products passed through the MWPC (two Mylar foils and almost 10 cm of gas) and into the MWPPAC (one Mylar foil), slowing down.

The energy loss was estimated with the RangeLibC++ [152], whose database includes also isobutane and Mylar as stopping materials. From the trajectory reconstruction in VAMOS the correction was performed event-by-event by considering the effective path inside the detectors and the pressure of the gas volume. In Figure 4.14 the velocity distribution of ^{106}Cd ions is shown before and after the correction; because of the energy loss in the materials, the velocity that should be used for the Doppler correction is $\Delta\beta/\beta \approx 4\%$ larger than what was measured by the VAMOS spectrometer.

4.2.2. AGATA position

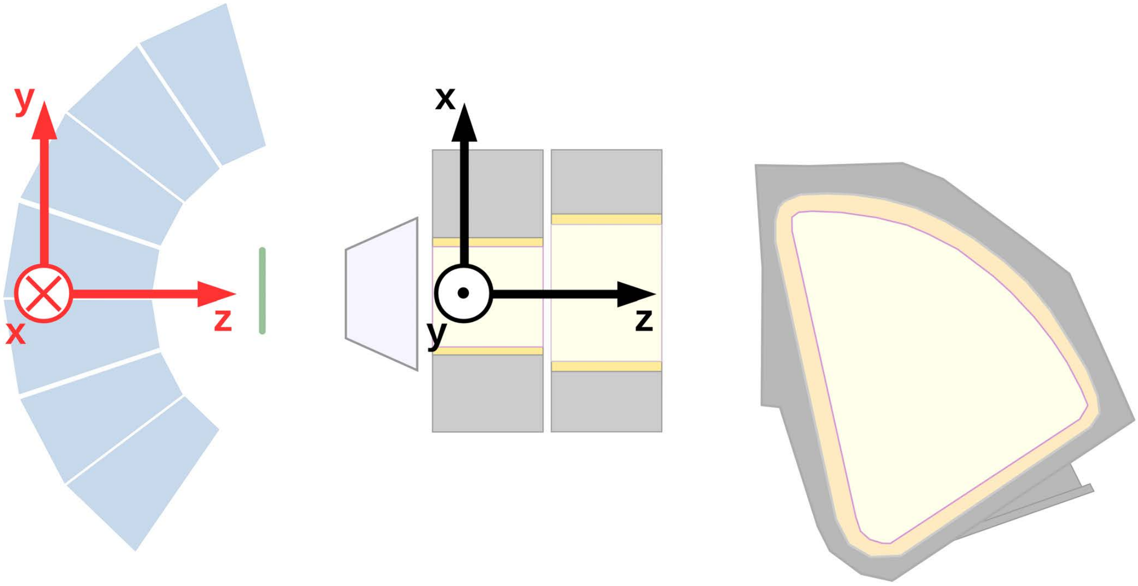

Figure 4.15.: Schematic drawing of the experimental setup, showing the AGATA (red) and VAMOS (black) frames of reference.

In Equation 4.7 the other important factor for the Doppler correction is the angle θ between the emitted γ ray and the velocity vector $\vec{\beta}$ of the particle. In order to calculate properly the γ-particle angle, the two positions had to be given in the same frame of reference and then the relative position of the two spectrometers had to be taken into account. For simplicity, the VAMOS frame of reference was chosen for the coordinate-axis directions and the target position was set as origin. Thus, the particle $\vec{x}_p$ and $\vec{x}_\gamma$ directions are given by

$$\vec{r}_p = \begin{pmatrix} 174.0\ tan\theta_i \\ 174.0\ tan\phi_i \\ 174.0 \end{pmatrix} \qquad \vec{r}_\gamma = \begin{pmatrix} y_{AGATA} \\ -x_{AGATA} \\ z_{AGATA} + 50.0 \end{pmatrix} \quad , \tag{4.8}$$

where 174.0 is the distance in millimetres of the entrance detector from the target position (see Figure 2.12), 50.0 is the offset in millimetres for the established compact position of

AGATA (see Section 2.2), while θ_i and ϕ_i are respectively the horizontal and vertical angles measured by the MWPC.

The coordinates given in Equation 4.8 takes into account the nominal position of the detectors. However, in order to improve the Doppler correction, the effective position of the experimental setup had to be estimated. To perform this, three possible conditions were checked during the analysis:

- translation of the target along the z-axis
- rotation of AGATA along the z-axis
- translation of AGATA along the z-axis

In order to control such roto-translations, the coordinates of Equation 4.8 were modified by introducing a parameter (e.g. offset on the z-coordinate, a rotation angle) and then the effect of the Doppler correction as a function of the parameter was studied. For example, in Figure 4.16 the Doppler-corrected γ-ray energy of ^{60}Ni is investigated as a function of the AGATA position along the z-axis. The value of the parameter, which determines the effective position, was obtained by maximising the amplitude and minimizing the FWHM of the two peaks at 1173 keV and 1332 keV. From such procedure it resulted that there was an offset in the z-coordinate of $\vec{r}_\gamma$: the AGATA spectrometer was placed 3.5 mm farther from the target.

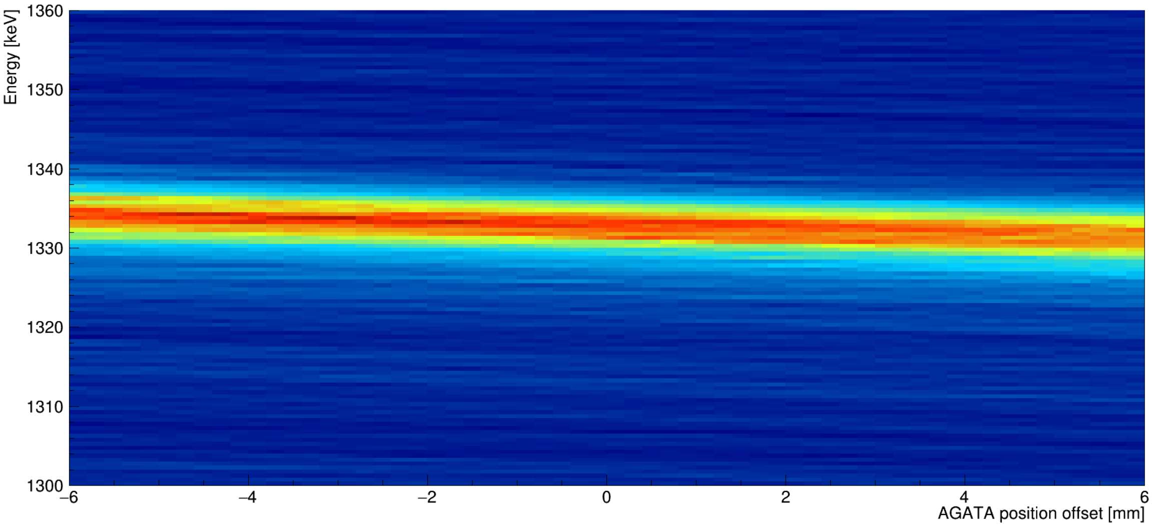

Figure 4.16.: Doppler-corrected γ-ray energy of ^{60}Ni as a function of the offset along the z-axis to the set position of AGATA. The optimal value of the offset is obtained by maximising the amplitude and improving the energy resolution of the peak at 1332 keV. From the procedure it results that the offset is −3.5 mm.

4.3. Reconstructed Q-value

The simultaneous measurement of the angle and of the energy of the reaction fragments entering in VAMOS enables the measurement of the Q-value of the reaction under the assumption of a binary reaction without particle evaporation[3]. For the reconstruction it was assumed, that the reaction occurs in the centre of the target. The energy of the beam ion at the centre of the target (E_{reac}) was calculated by subtracting the energy loss, estimated by RangeLibC++ [152]. The same procedure was done to calculate the energy of the detected reaction products (E_{bl}) at the centre of the target. The Q-value of the reaction was obtained by using the non-relativistic formula [153]

$$Q = \frac{m_{tl} + m_{bl}}{m_{tl}} E_{bl} - \frac{m_{tl} - m_b}{m_{tl}} E_{reac} - \frac{2}{m_{tl}} \sqrt{m_b \; m_{bl} \; E_{reac} \; E_{bl}} \; cos\theta_{bl} \quad , \qquad (4.9)$$

where m_t , m_{tl} and m_{bl} are the target, the target-like and beam-like masses respectively, E_{bl} is the detected energy of the beam-like fragments, while θ_{bl} is the angle of the beam-like ion with respect to the beam direction.

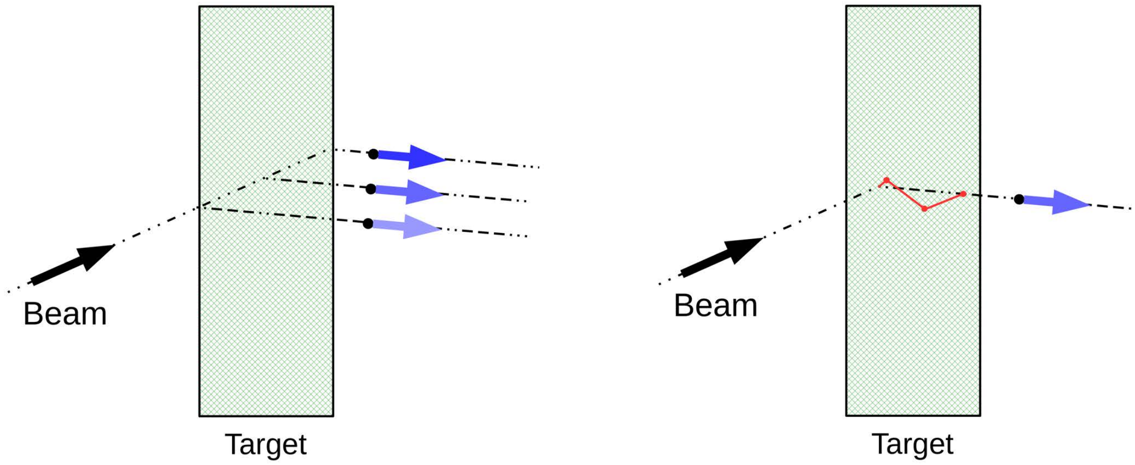

Figure 4.17.: The major contribution to the Q-value uncertainty is given by the energy loss inside the target. (left) According to the position where the reaction takes place inside the target, the beam and the fragment lose energy differently. Then, considering that usually the reaction point in the target is unknown, the Q-value can be calculated under certain assumption: in the analysis, the reactions were supposed to take place in the middle of the target. (right) Inside the target both beam and reaction-fragment will straggle within the target.

As it is deeply discussed in Appendix A, there are several uncertainties of the reconstructed Q-value. The major contribution to the uncertainty is the thickness 0.715 mg/cm^2 of the target and hence the different energy loss of the ions in the target, depending on the position where the reaction took place. The energy loss of an ion in matter depends on its mass, atomic charge number and energy (see Figure 4.17). Even though the energy loss of the recoil is calculated for the identified ion, the difference of energy loss between the beam ion is higher for the transfer channels. Especially for the transfer of many protons this effect is important.

---

[3] In the text the reconstructed Q-value is also called Total Kinetic Energy Loss (TKEL). This is due to the fact that there is a relation between the two variable ($Q = -TKEL$), so a gate on the first automatically identifies a gate on the second.

The straggling and the unknown position of the beam spot on the target increases the uncertainty of the reconstructed Q-value. By combining all these effects, an uncertainty of around 20 MeV can be expected, as it can be deduced from Figure A.2.

The Q-value is a powerful tool which allows to control the feeding from higher-lying states [98]. In order to check its implementation, the lifetimes of low-lying states in ^{104}Cd were extracted (see Chapter 5).

4.4. Recoil distance Doppler-shift method

The Recoil Distance Doppler-Shift (RDDS) [100] method is a well established technique for the determination of picosecond lifetimes of excited nuclear states. The technique is based on the extrapolation of the lifetime by observing the intensity of both shifted $I_s(x)$ and unshifted $I_u(x)$ components of a γ-ray transition as a function of the target-degrader distance x. Such components are due to the different Doppler shift, caused by the slowing down of the reaction products after passing through the degrader material (see Figure 2.15).

The ratio between the intensity of the two components depends on the time of flight between the target and the degrader. In particular two ratios can be defined, the *decay curve* $R(x)$ and the *flight curve* $F(x)$:

$$\begin{aligned} R(x) &= \frac{I_u(x)}{I_u(x)+I_s(x)} \\ F(x) &= \frac{I_s(x)}{I_u(x)+I_s(x)} \quad . \end{aligned} \tag{4.10}$$

According to such definition, the two ratios are related functions and they can be easily written as $R(x) = 1 - F(x)$[4].

4.4.1. Decay-curve method

The decay curve $R(x)$ is commonly used for the lifetime determination. In fact, for the simple case of one unique level deexciting, the decay curve presents an exponential trend:

$$R(x) = n(0)e^{-\dfrac{t}{\tau}} = n(0)e^{-\dfrac{x}{\beta_s c\tau}} \quad , \tag{4.11}$$

where τ is the lifetime of the level, $n(0)$ is the initial level population and c is the speed of light.

---

[4] Instead of the sum $I_u(x) + I_s(x)$, other normalizations (e.g. number of ions) can be used in the analysis and they usually entail that the two ratios become mathematically independent.

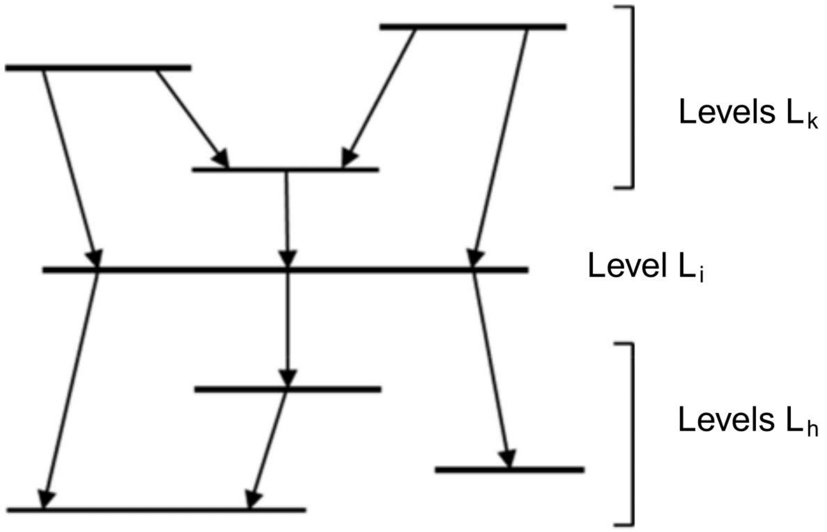

Figure 4.18.: Representation of a possible level-feeding pattern: the levels k populate the level of interest i, which deexcites via transitions to the levels h. Taken from Reference [100].

In real cases however, when more levels are involved creating a complicated level-feeding pattern (see Figure 4.18), the analysis of a lifetime measurement is basically done by solving the corresponding system of differential equations. Following the notation used in Figure 4.18, the differential equation for the level of interest L_i reads

$$\frac{d}{dt} n_i(t) = -\lambda_i \; n_i(t) + \sum_{k=i+1}^{N} \lambda_k \; n_k(t) \; b_{ki} \quad , \tag{4.12}$$

where $n_i(t)$ and $n_k(t)$ are the number of nuclei in the levels i and k at the time t, the quantity b_{ki} are the branching ratios from the level k to the level i and $\lambda_j = 1/\tau_j$ is the decay constant of the j-th state (j lays between i and k). In the simple case of a decay chain when every state has just one feeder ($b_{ki} = 1$), the solution of the differential equation is given by the *Bateman equation* [154]

$$n_i(t) = \sum_{k=1}^{i} \left[n_k(0) \times \left(\prod_{j=k}^{i-1} \lambda_j \right) \times \left(\sum_{j=k}^{i} \frac{e^{-\lambda_j t}}{\prod_{p=k,p\neq j}^{i} (\lambda_p - \lambda_j)} \right) \right] \quad . \tag{4.13}$$

Otherwise, in the more general case the solution of Equation 4.12 with respect to the decay curve $R_i(t)$ can be written as [100]

$$R_i(t) = P_i e^{-\lambda_i t} + \sum_{k=i+1}^{N} M_{ki} \left[\frac{\lambda_i}{\lambda_k} e^{-\lambda_k t} - e^{-\lambda_i t} \right] \quad , \tag{4.14}$$

where P_i denotes the direct feeding intensity of the level i. The coefficients M_{ki} are defined as

$$M_{ki}\left(\frac{\lambda_i}{\lambda_k}-1\right)=b_{ki}P_k-b_{ki}\sum_{m=k+1}^{N}M_{mk}+\sum_{m=i+1}^{N}M_{km}b_{mi}\frac{\lambda_m}{\lambda_i} \tag{4.15}$$

and represent the ratio of the decay constants of Equation 4.13.

Coincidence measurement

A great progress in the field of lifetime measurements was achieved when the step from γ-ray singles plunger measurements to $\gamma\gamma$-coincidence measurements was made. The main motivation to perform coincidence plunger measurements was to overcome the problems concerning the feeding from states above the one of interest [155]. In order to take into account the discrete feeding, many experimental values, such as feeding intensities and lifetimes of the feeders, have to be determined which can be problematic in some cases. Even higher difficulties are associated with the unobserved feeding, which normally introduces large uncertainties.

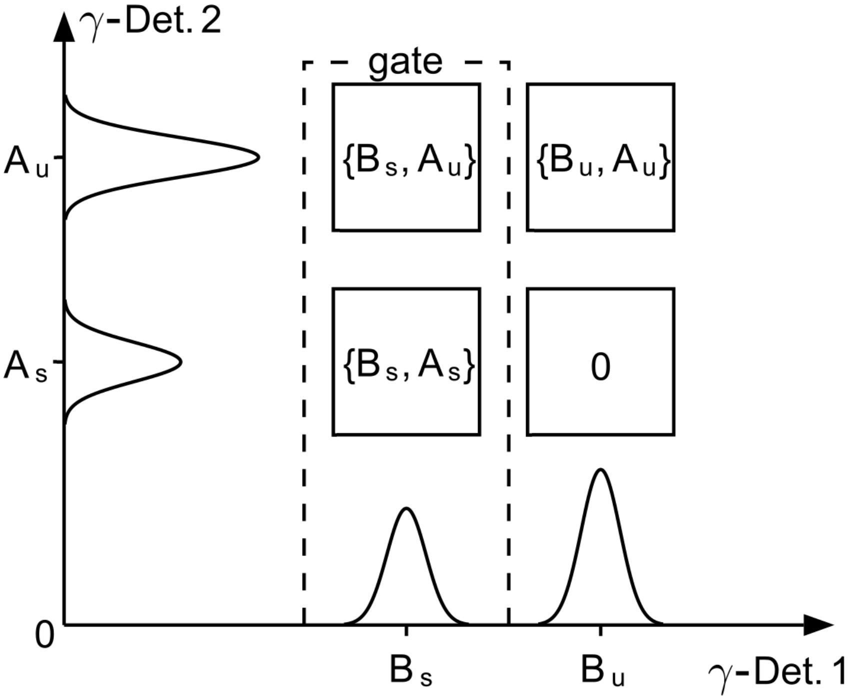

Figure 4.19.: Schematic drawing explaining the basics of the coincidence method. By gating on the shifted component of the feeder B, the transition of interest A would have both shifted and unshifted components; on the other hand, by gating on B_u, all the A-transition γ rays would be emitted after the degrader. Adapted from Reference [100].

By gating on one of the feeding transitions L_k of the level of interest, the side-feeding is eliminated and only the feeding via the selected transition B is relevant for the determination of the level lifetime τ. A more simple interpretation of the method is that, by selecting the transition B, only the population due to such feeding is investigated. In particular, as it is summarised in Figure 4.19, by gating on the shifted component (B_s) of the feeder B, the transition of interest A would have both shifted and unshifted components; on the other hand, by gating on unshifted component B_u, all the A-transition γ rays would be emitted after the degrader.

4.4.2. Differential decay-curve method

The Differential Decay-Curve Method (DDCM) [99, 100, 156] is an alternative analysis procedure for lifetime measurements with RDDS data. With respect to the standard analysis this method entails several advantages:

- there are no assumptions on the shape of the curve $R(t)$ (see Equation 4.10)
- only relative target-degrader distances, which can be measured with high precision without the estimation of the plunger zero offset (see Section 3.3), are required
- in each case there is a certain target-degrader distance range where the data points are sensitive to the corresponding lifetime

With such method, the lifetime of a state can be easily obtained as

$$\tau_i(t) = \frac{1}{\lambda_i} = -\frac{R_i(t) - \sum_k b_{ki}\alpha_{ki}R_k(t)}{\dfrac{d}{dt}R_i(t)} \quad , \tag{4.16}$$

where the factor of proportionality $\alpha_{ki} = \dfrac{\omega_k(\Theta)\ \epsilon_k(E_\gamma)}{\omega_i(\Theta)\ \epsilon_i(E_\gamma)}$ is determined by the detector efficiency $\epsilon_j(E_\gamma)$ and the angular distribution $\omega_j(\Theta)$ of the electromagnetic radiation.

In the equation the denominator is the derivative of the function $R_i(t)$. Assuming similar errors for numerator and denominator for all flight times, the error of the lifetime gets large for small denominator values, that is for small slopes of the $R_i(t)$ curve. This is used for the definition of the sensitive region, which has its limits at those flight times where the slope of the $R_i(t)$ curve is at the half of the maximum value.

Following Equation 4.16, for each value of the flight time t one value for the lifetime can be determined. Since the lifetime of a state is a constant, the function $\tau_i(t)$ must be a constant as well. Thus, deviations from a constant value most likely indicate the presence of a systematic error.

Coincidence measurements

Analogous to the DCM, coincidence measurements can be performed also with DDCM in order to get rid of the presence of side-feeding transitions. In fact, as it is shown in Figure 4.19, after gating on the component feeding transition B, the Equation 4.16 becomes

$$\tau(t) = \frac{A_u^{B_s}(t)}{\dfrac{d}{dt}A_s^{B_s}(t)} \quad , \tag{4.17}$$

where $A_s^{B_s}(t)$ and $A_u^{B_s}(t)$ are the coincidence intensities of the shifted and unshifted components of the transition of interest, respectively.

Also in this case, it is extremely important to fit a smooth curve to the data points, especially in the sensitive region. In principle, the curve must be monotonically increasing with exactly one inflection point, which has to be inside the sensitive region.

5

Results from Lifetime Measurements

After performing the complete identification of the reaction fragments and optimising the Doppler correction for the γ rays emitted in flight, the validity of the experimental method can be tested. The plunger zero offset (see Section 3.3) was tested by measuring the lifetime of the first 2^+ state of ^{106}Cd with the coincidence method, in order to ensure that the reaction occurred between the ^{106}Cd beam and the ^{92}Mo target. The implementation of the reconstructed Q-value was also checked by measuring the lifetime of the low-lying states of ^{104}Cd. The Q-value gate avoids the inclusion of systematic errors caused by the beam excitation on the ^{24}Mg degrader. In this chapter the lifetime measurement of the first 2^+ and 4^+ states in ^{106,108}Sn, which were the goal of the experiment, will be presented. In particular an additional and detailed discussion is focused on the different methods to get the lifetime of these states with the lower error bars for the ^{108}Sn case. At the end of the chapter, the feasibility of measuring lifetimes in the identified odd-mass Sn isotopes, ^{107,109}Sn, is discussed.

5.1. Cadmium isotopic chain

Thanks to the large statistics and well known lifetimes of the low-lying states along the whole isotopic Cd chain, the low-lying excited states of Cd are used as benchmark of the experimental method and analysis.

As described in Section 3.3, the plunger device was first calibrated in order to have the correspondence between the induced tension of the feed-back system and the motor position (see Figure 3.16), then the zero offset was extrapolated in order to obtain the absolute distances between the target and degrader foils (see Table 3.3). By observing the γ rays emitted by the ^{106}Cd beam, the evaluation of the plunger zero offset was checked by extracting the lifetime of the 2^+ state via both DCM and DDCM [101]. In fact, as mentioned in Chapter 4, the first method depends on the absolute target-degrader distances while the second only on the relative distances.

In addition, the reconstructed Q-value, introduced in Chapter 4, was also used to control the feeding from higher-lying states [98] and to simplify the decay model, which should be taken into account for the lifetime of a given state. In order to check the implementation of such a powerful tool, the lifetimes of low-lying states in ^{104}Cd were extracted.

5.1.1. ^{106}Cd

The excited states of the ^{106}Cd projectile are the most strongly populated in the experiment. In Figure 5.1 the Doppler-corrected γ-ray energy spectrum gated on ^{106}Cd shows that mostly the low-lying states of both ^{106}Cd and ^{92}Mo were populated in the reaction. From the transitions identified in the single γ-ray energy spectrum and by observing the coincidences thanks to the prompt $\gamma - \gamma$ matrix of Figure 5.2, a partial level scheme of ^{106}Cd can be deduced. Indeed, by observing carefully the $\gamma - \gamma$ matrix, the $2_1^+ \rightarrow 0_{g.s.}^+$ transition is in coincidence not only with the $4_1^+ \rightarrow 2_1^+$ transition but also with many others. The presence of all these transitions feeding the first 2^+ state makes the measurement of its lifetime via single γ rays really complicated. For this reason, the coincidence method was used by gating on the shifted component of the $4_1^+ \rightarrow 2_1^+$ transition, the largest feeder, in order to extract the lifetime of the 2_1^+ state from the resulting decay curve. Moreover, gating on the shifted peak of the feeding transition ensures that the reaction took place at the target position and that both shifted and unshifted components of the transition of interest would be present. This avoid also the systematic error due to the possible excitation of the beam ions on the degrader material.

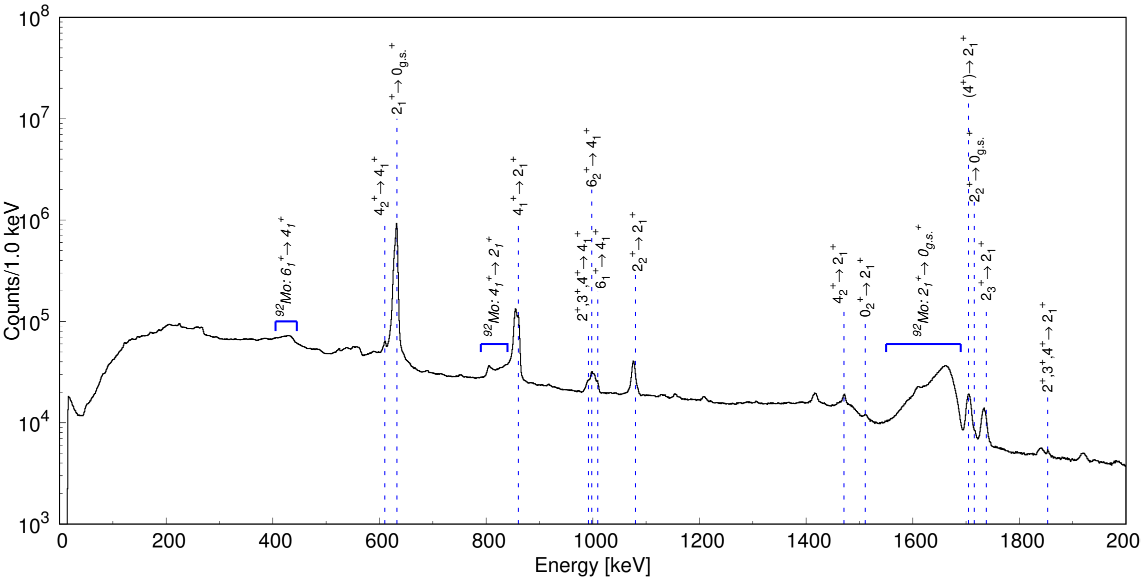

Figure 5.1.: Doppler-corrected γ-ray energy spectrum, obtained gating on ^{106}Cd, for all the plunger distances. The most intense transitions of both ^{106}Cd and ^{92}Mo are identified and labelled.

By using the DCM, which depends on the absolute target-degrader distances (see Table 3.3), a lifetime of 10.7(4) ps is obtained for the 2^+ state. Figure 5.3 (left) shows the decay curve, obtained by fitting the normalised area of the $2_1^+ \rightarrow 0_{g.s.}^+$ unshifted component as a function of the distances between the foils. Then, the DDCM, which depends only on the relative distance between the points, has been applied: as presented in Figure 5.3 (right), after averaging the obtained values of the lifetime in the sensitivity region of the method [99, 100], the lifetime of the 2^+ state results to be 10.4(2) ps.

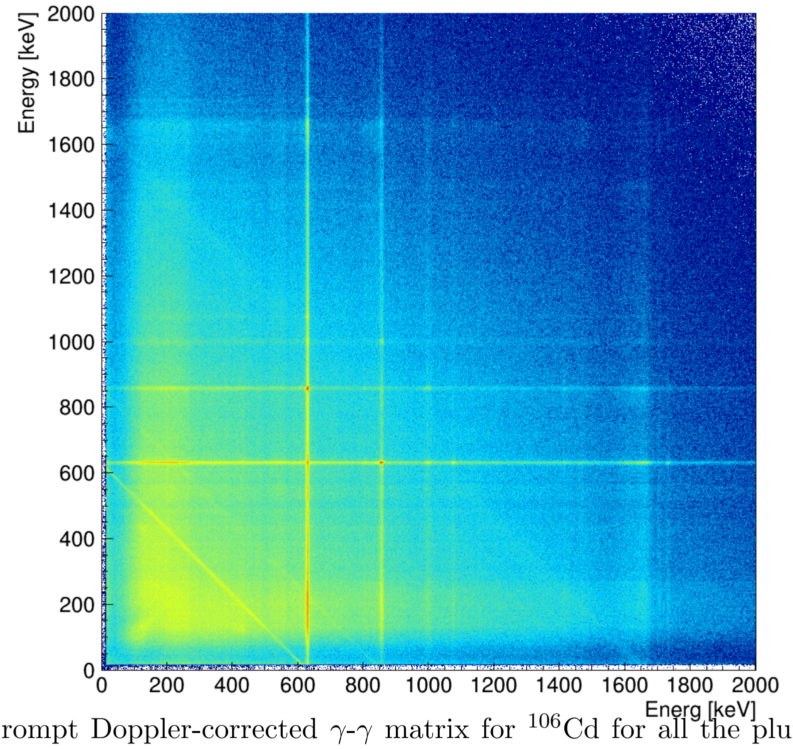

Figure 5.2.: Prompt Doppler-corrected γ-γ matrix for ^{106}Cd for all the plunger distances. By gating on a certain transition it is possible to observe the γ rays detected inside a coincidence time window of 6 ns and then determine the partial level scheme of the populated nuclei.

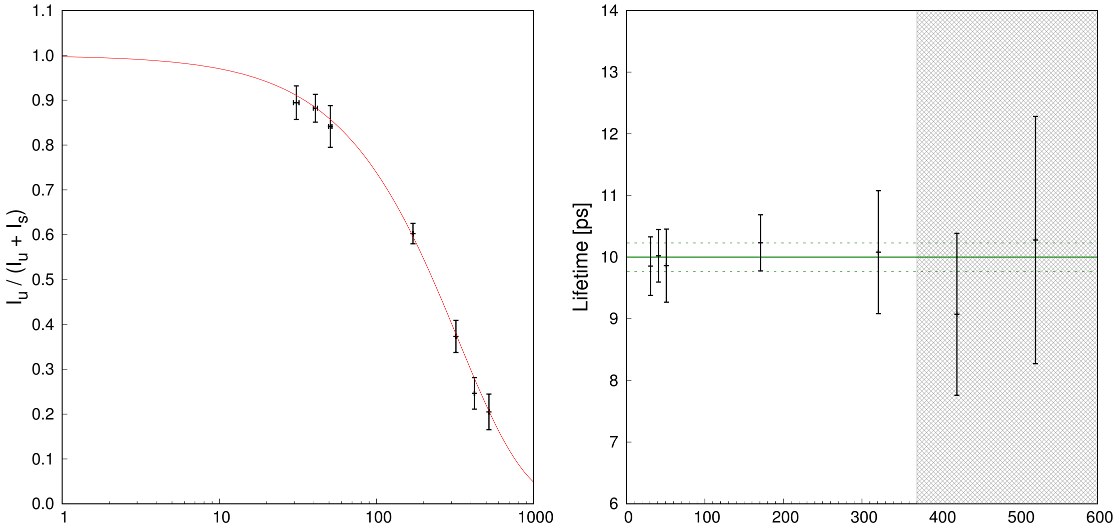

Figure 5.3.: Lifetime measurement of the ^{106}Cd first 2^+ state via the coincidence procedure, performed by gating on the shifted component of the $4_1^+ \rightarrow 2_1^+$ transition. (left) Normalised area as function of the target-degrader distances for the $2_1^+ \rightarrow 0_{g.s.}^+$ transition, showing (red line) the fitting function used for the Decay Curve Method. (right) Lifetime of the 2^+ state as function of the target-degrader distances, obtained via the Differential Decay Curve Method: the solid line represents the average value, the dashed lines are the corresponding error bars and the grey area marks the region outside the sensitivity of DDCM. The final results are summarized for the two methods in Table 5.1.

The lifetime of the first 2^+ state of ^{106}Cd was then obtained with two different methods, which provided exactly the same result: this fact confirms that the previously estimated value of the plunger zero offset is correct. Moreover, the result is perfectly in agreement also with previous measurements reported in bibliography [157], which further supports the validity of the experimental method. The comparison between the experimental results and the one adopted in the literature is summarized in Table 5.1:

Literature value	DCM	DDCM
10.5 (1)	10.7 (4)	10.4 (2)

Table 5.1.: Lifetime of the 2_1^+ state of ^{106}Cd: the results obtained via the DCM and DDCM are compared to the literature adopted value [157].

5.1.2. ^{104}Cd

Once confirmed the calibration for the plunger distances, another variable that is important for the lifetime measurement has to be checked: the reconstructed Q-value. Because the statistics of ^{106}Cd do not allow to perform the test with the coincidence procedure, avoiding in this way the systematic error caused by the beam excitation on the degrader[1], the lifetime measurement of excited states in ^{104}Cd was used to validate the Q-value gating procedure.

The ^{104}Cd nuclei were populated mostly through the transfer of 2 neutrons from the beam to the target. In Figure 5.4 the spectrum shows that states with spin up to $10\hbar$ were populated in the yrast band, but also γ-ray transitions belonging to side bands with both positive and negative parity can be identified. From these identified γ-ray transitions the level scheme of ^{104}Cd was reconstructed.

As introduced before, a Q-value gate allows to control the feeding from the higher-energy transition. On the other hand, such extra condition has to be a compromise between the simplification of the decay model and the statistics in the transitions of interest. However, keeping in mind that the Q-value has an intrinsic resolution due to the energy loss in the target (see Appendix A) of few MeV and considering the complexity of the level scheme reported in Figure 5.4, for the test it was decided to "suppress" the transitions that are above the first 4^+ state. Thus, the $Q > -14$ MeV was set and the resulting γ-ray spectra are shown in Figure 5.5

---

[1] Even if it is difficult to estimate the systematic error, it seems that its contribution is negligible because of the ^{24}Mg foil thickness. In fact, when performing the Q-value test with the ^{106}Cd data, the measured lifetime is 10.6(8) ps, which is perfectly in agreement with the results reported in Table 5.1.

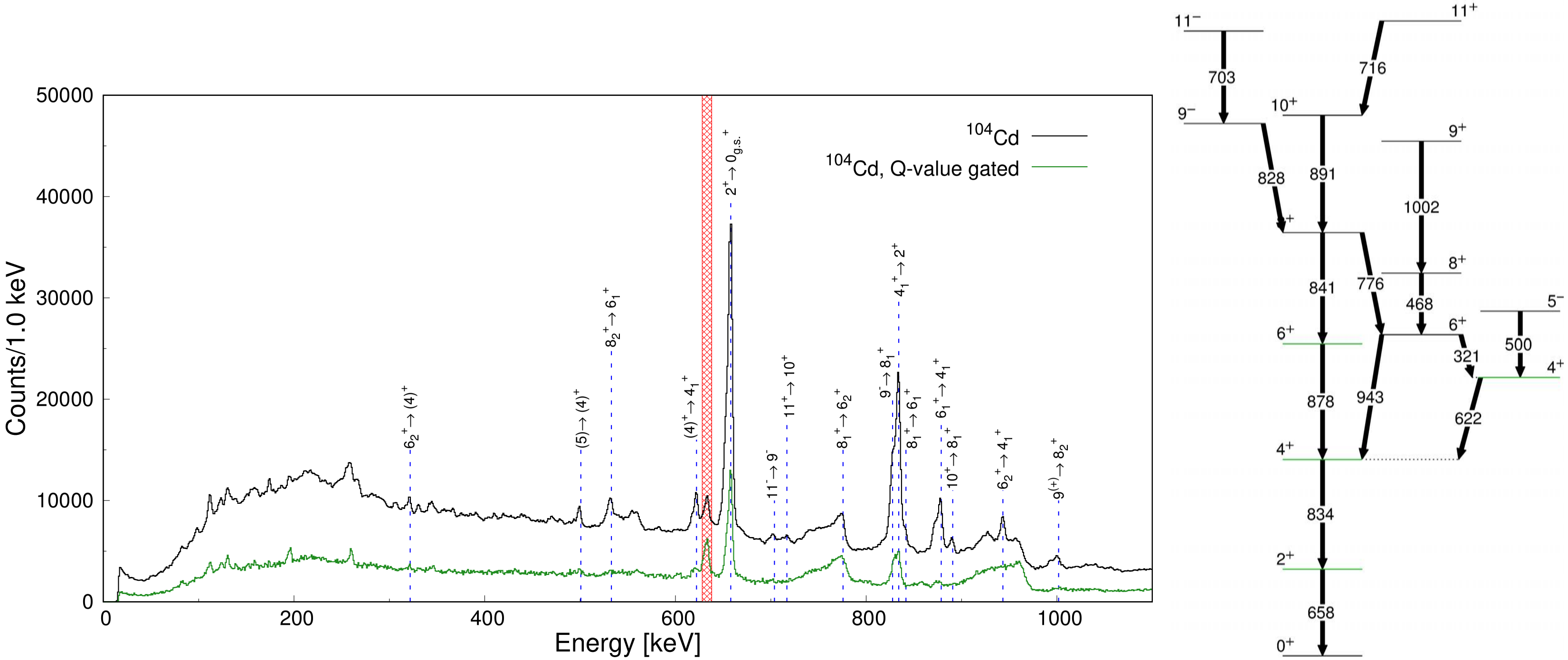

Figure 5.4.: (left) Doppler-corrected γ-ray energy spectrum gated on ^{104}Cd for all the plunger distances. The spectrum is compared with the one obtained by gating on the Q-value (green). For graphical reasons, the statistics of the Q-value gated spectrum is multiplied by a factor 5. Despite the clear mass identification, contamination (red) from the inelastic-scattered ^{106}Cd beam is still present. All the identified transitions of the beam-like ion are shown and (right) reported in the level scheme of the ^{104}Cd.

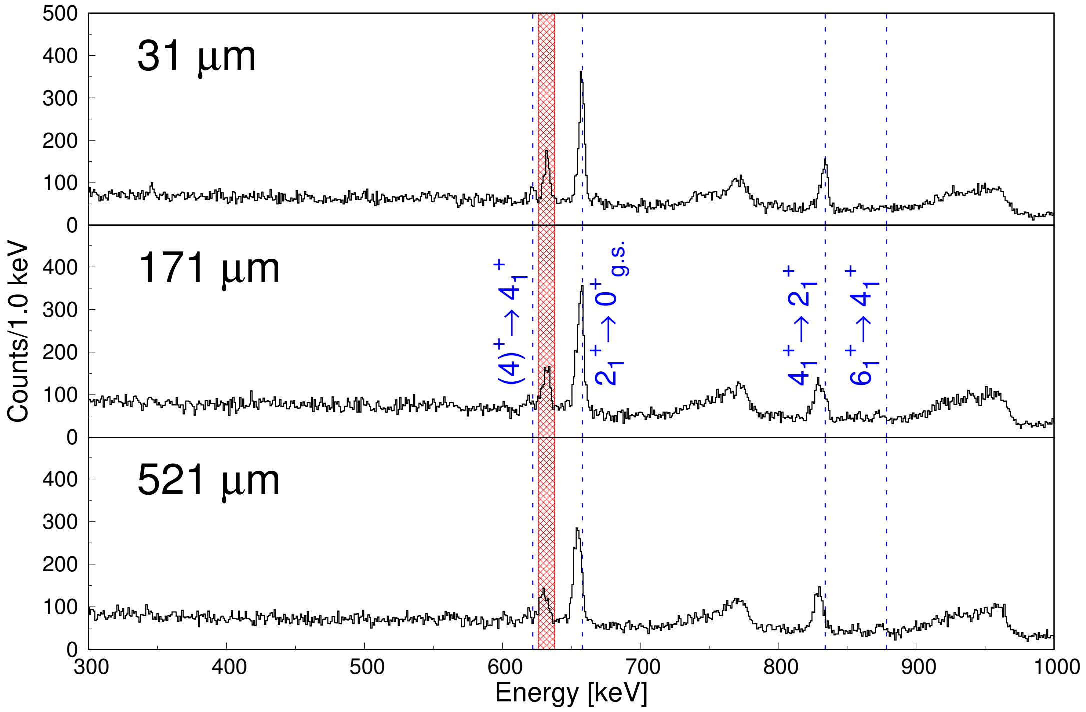

Figure 5.5.: Doppler-corrected γ-ray energy spectrum for ^{104}Cd, gating on the Q-value for reducing the feeding from high-spin transitions (see text). For the three distances the lowest-lying transitions are shown (blue): the feeding from the states above the 4^+ state is practically negligible. Despite of the additional constraint on the reconstructed Q-value, there are still ^{106}Cd contaminations (red).

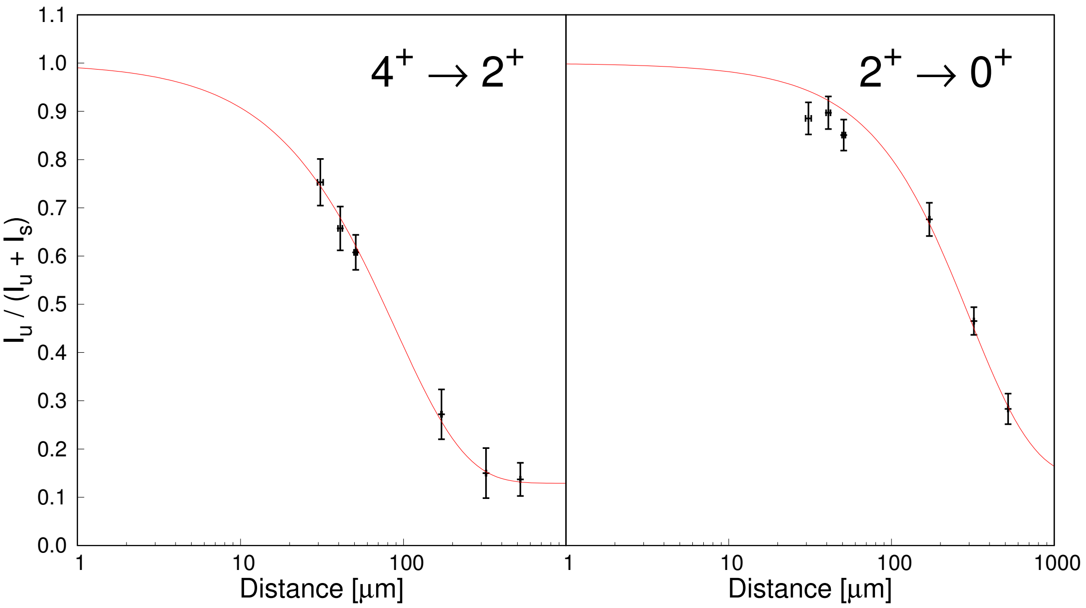

Figure 5.6.: Normalised unshifted area as function of the target-degrader distance for (left) $4_1^+ \to 2_1^+$ and (right) $2_1^+ \to 0^+_{g.s.}$, showing (red line) the fitting function used for the Decay Curve Method. The area is normalised to the sum of shifted and unshifted areas. The obtained lifetimes are $\tau_{eff}(4^+) = 3.0(3)$ ps and $\tau(2^+) = 8.0(5)$ ps.

By observing the decay curves of Figure 5.6 and the γ-ray spectrum of Figure 5.5, it is clear that the 4_1^+ state has some feeders, due to the $(4)^+ \rightarrow 4_1^+$ and $6_1^+ \rightarrow 4_1^+$ transitions. For this reason the lifetime of the 4^+ state $\tau_{eff}(4^+) = 3.0(3)$ ps is larger than what is reported in literature $\tau(4^+) = 1.5(5)$ ps [158]. However, since the goal was to measure the lifetime of 2^+ state, the measured $\tau_{eff}(4^+)$ was considered as an effective lifetime. In this way, the lifetime of the first 2^+ state could be measured: the result is perfectly in agreement with previous measurements and the error bar is even smaller than the values reported in literature. In Table 5.2 the results obtained for ^{104}Cd are summarised:

State	τ [ps]	τ [ps] literature
2_1^+	8.0 (5)	9 (3) ^{a} 8.5 (12) ^{b}
4_1^+	3.0 (3)	< 6 ^{a} 1.5 (5) ^{b}

Table 5.2.: Comparison between the measured lifetime of both 2_1^+ and 4_1^+ states in ^{104}Cd with results reported in literature. Results ^{a} are taken from [159] and ^{b} come from [158].

5.2. Tin isotopic chain

As introduced before and also extensively described in Appendix A, the experimental setup was optimised in order to populate and select ^{108}Sn. Because of the steep change of the reaction Q-value (see Table A.2) and according to the Q-value considerations (see Equation 1.19), for the most neutron-deficient Sn isotopes the cross-section decreases abruptly, as expected for many nucleon transfers. For this reason only the $^{106-109}$Sn cases will be discussed.

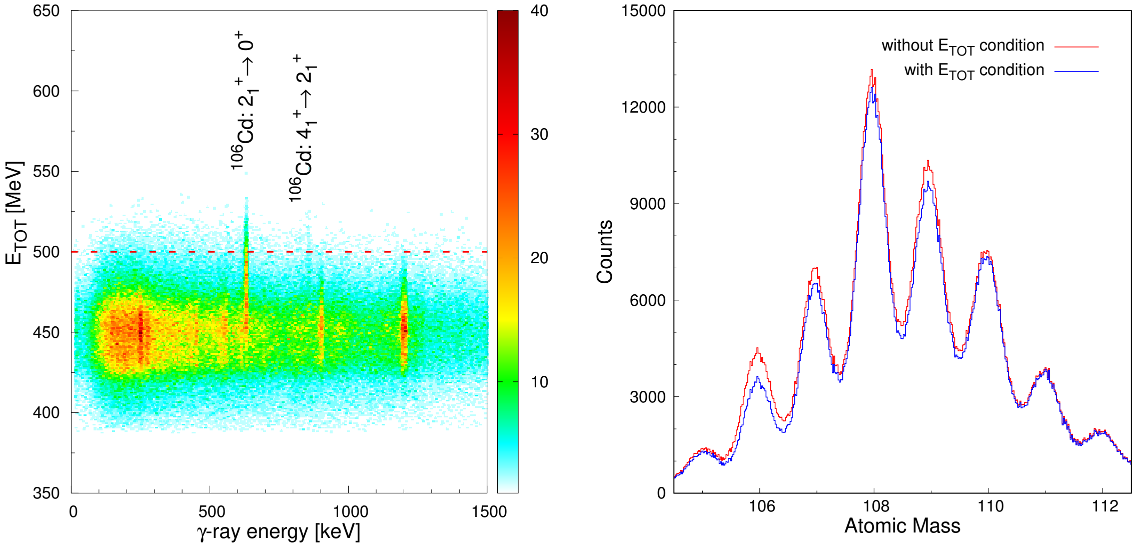

Figure 5.7.: Inelastic-scattered beam contamination in the Sn isotopic chain. (left) Fragments total energy (E_{TOT}) as function of the γ-ray Doppler-corrected energy, requiring the $Z = 50$ identification: the $2^+ \to 0^+$ transition of ^{106}Cd indicates that is possible to reduce the contamination by requiring the condition (dashed red line) $E_{TOT} < 500$MeV. (right) Mass spectrum of the Sn isotopic chain with (blue) and without (red) the condition for reducing the ^{106}Cd contamination: the peaks related to ^{106,109}Sn have a sensible reduction, while the rest of the statistics remains practically untouched.

An additional problem, which limits the study of the Sn isotopic chain, is given by the contamination of the inelastic-scattered beam. In fact, Section 4.1 shows that the kinetic energy of the fragments at the entrance of the IC was not sufficient to have a clear identification in Z (see Figure 4.3): the channels from $-1p$ to $+2p$ are overwhelmed by inelastic-scattered beam events.

In order to reduce such contamination in the channels of interest without losing statistics, a gate on the measured total energy of the fragments was set. In Figure 5.7 (left) the relation between the γ-ray energy spectra and the fragments total energy is shown: by requiring the condition $E_{TOT} < 500$ MeV, it is possible to reduce the contamination of both the $2^+ \to 0^+$ and $4^+ \to 2^+$ transitions of ^{106}Cd, without rejecting events related to the Sn channels. Then, in Figure 5.7 (right) the effect of such a condition in the Sn isotopic chain mass spectrum is presented: the peaks related to ^{106,109}Sn have a sensible reduction[2], while the rest of the statistics remains practically untouched.

In the followings the results of the $^{106-109}$Sn nuclei are presented, with the above condition ($E_{TOT} < 500$ MeV) applied.

5.2.1. ^{108}Sn

The ^{108}Sn nucleus represents the most populated isotope of the whole isotopic chain. In Figure 5.8 the spectrum shows that states with spin up to $10\hbar$ were populated during the experiment and from the observed γ-ray transitions the level scheme of ^{108}Sn is reported. One notices immediately that the transition de-exciting of the 8^+ state can make the lifetime measurement of the 2^+ state difficult: in fact the unshifted component of the $8^+ \to 6^+$ transition has exactly the energy of the shifted component of the $2^+ \to 0^+$ transition. Thus, in order to correctly extract the lifetime of the 2^+ state a gate on the reconstructed Q-value is mandatory.

As it was previously tested for the ^{104}Cd case, the Q-value gate allows to control the feeding from the higher-energy transitions. In particular, for ^{108}Sn it was possible to suppress all the transitions above the 6^+ isomeric state: in fact only the peaks belonging to the $6^+ \to 4^+$, $4^+ \to 2^+$ and $2^+ \to 0^+$ transitions are still visible in the γ-ray energy spectrum when the condition $Q > -21$ MeV is required. In Figure 5.9 the Q-value gated γ-ray spectra of ^{108}Sn are presented for each target-degrader distance, showing the evolution of the shifted and unshifted components of the $4^+ \to 2^+$ and $2^+ \to 0^+$ transitions.

From these gated spectra the direct feeding to the low-lying 2^+, 4^+ and 6^+ states could be determined: this procedure is crucial for extracting the lifetime of these states via DCM, because it helps introducing some constraints to the fitting function parameters. The direct feeding parameters after the Q-value gate are summarised in Table 5.3.

	Measured feeding
$N_{6,0}$	$(11 \pm 4)\%$
$N_{4,0}$	$(27 \pm 5)\%$
$N_{2,0}$	$(62 \pm 5)\%$

Table 5.3.: Direct feeding measured from the γ-ray spectra of Figure 5.9.

Thanks to the Q-value gate, in order to extract the lifetimes just a three-step decay-chain model can be used, considering the de-excitation of 6^+, 4^+ and 2^+ states. The 6^+ state is an isomer with $\tau(6^+) = 10.5(6)$ ns [160, 161] and therefore its contribution to the decay curves is constant over all the distances. Via the DCM the lifetimes of first the 4^+ and later the 2^+ states are extracted with an error below 15%: $\tau(4^+) = 3.6(5)$ ps and $\tau(2^+) = 0.76(8)$ ps. The lifetime of the 2^+ state is perfectly in agreement with the literature adopted one $\tau(2^+) = 0.69(17)$ ps [2], extrapolated from Coulomb excitation measurements [2, 83, 84]. The normalised unshifted area as a function of the plunger distances and the fitting curves are presented for the $4^+ \to 2^+$ (left) and $2^+ \to 0^+$ (right) transitions in Figure 5.10.

---

[2] In experiments involving magnetic spectrometers like VAMOS, it has been empirically observed that the A/q ratio has a distribution peaked around 3. Because of this, the beam contamination was affecting the channels with mass $106 + 3 \times m$ where m is an integer value

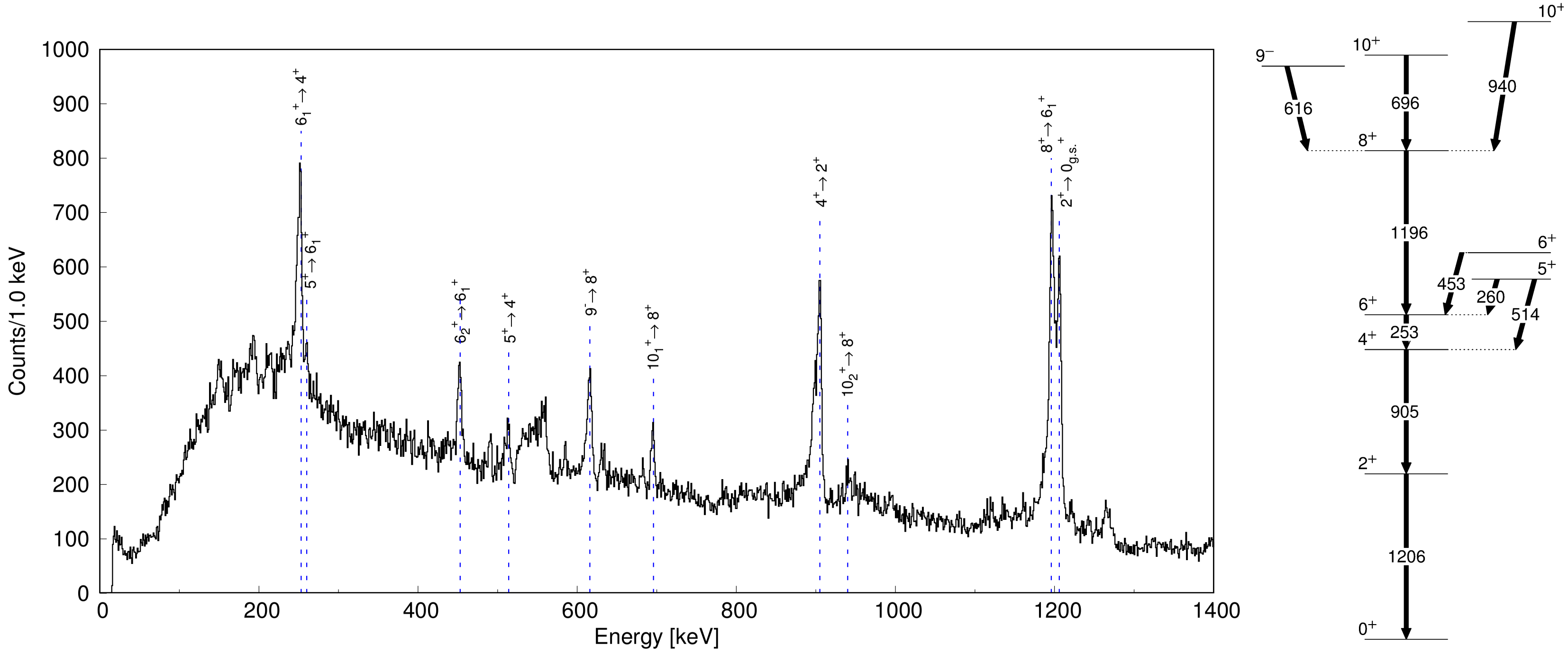

Figure 5.8.: (left) Doppler-corrected γ-ray energy spectrum in coincidence with ^{108}Sn, summed for all the plunger distances. All the identified transitions are reported in the level scheme of ^{108}Sn (right).

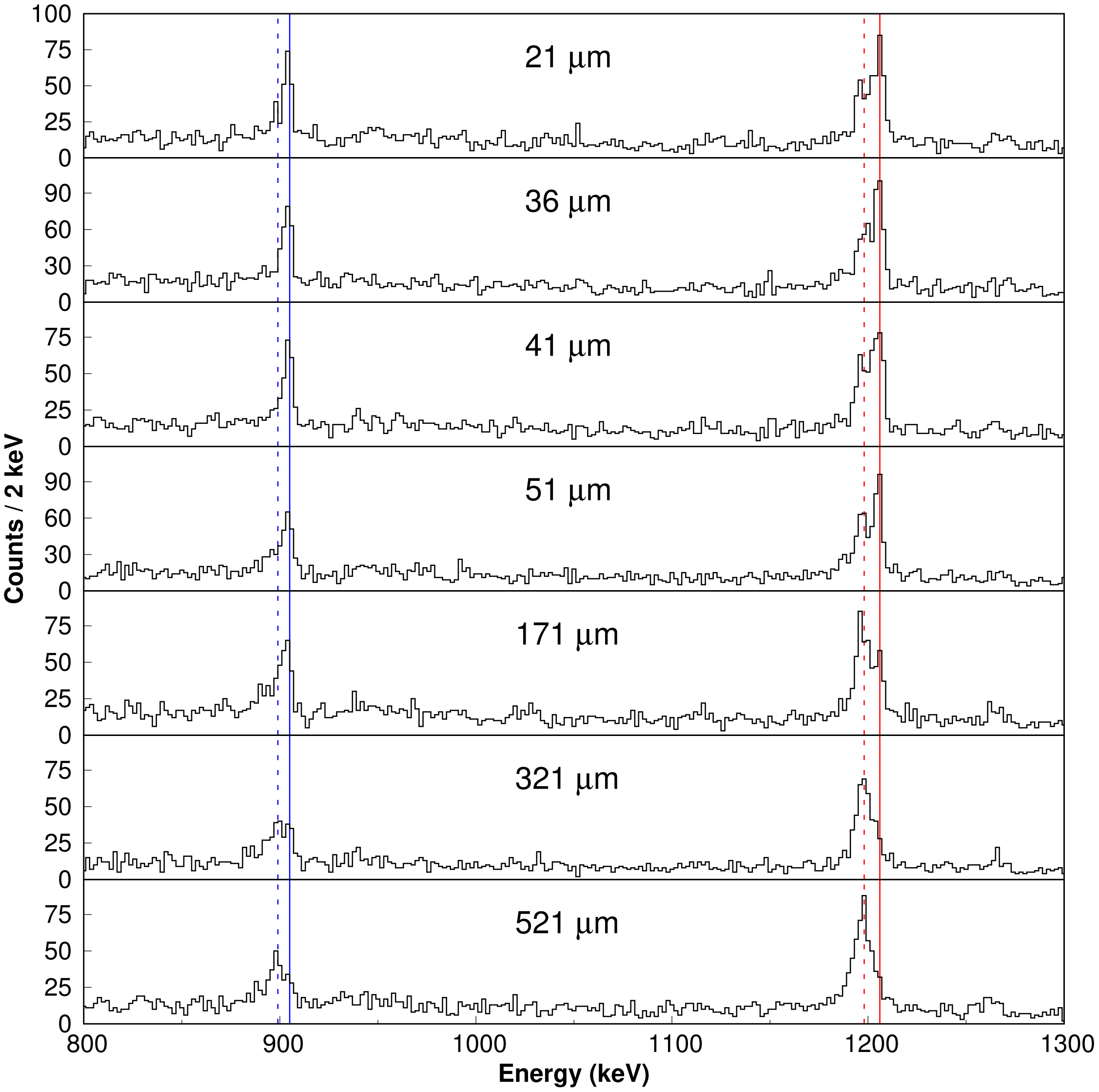

Figure 5.9.: Doppler-corrected γ-ray energy spectrum for ^{108}Sn, after gating on the Q-value to reduce the feeding from high-spin states (see text). For each plunger distance the $4^+ \rightarrow 2^+$ (blue lines show the centroids) and $2^+ \rightarrow 0^+$ (red lines show the centroids) transitions are shown, presenting for both of them the shifted (dashed) and unshifted (solid) components.

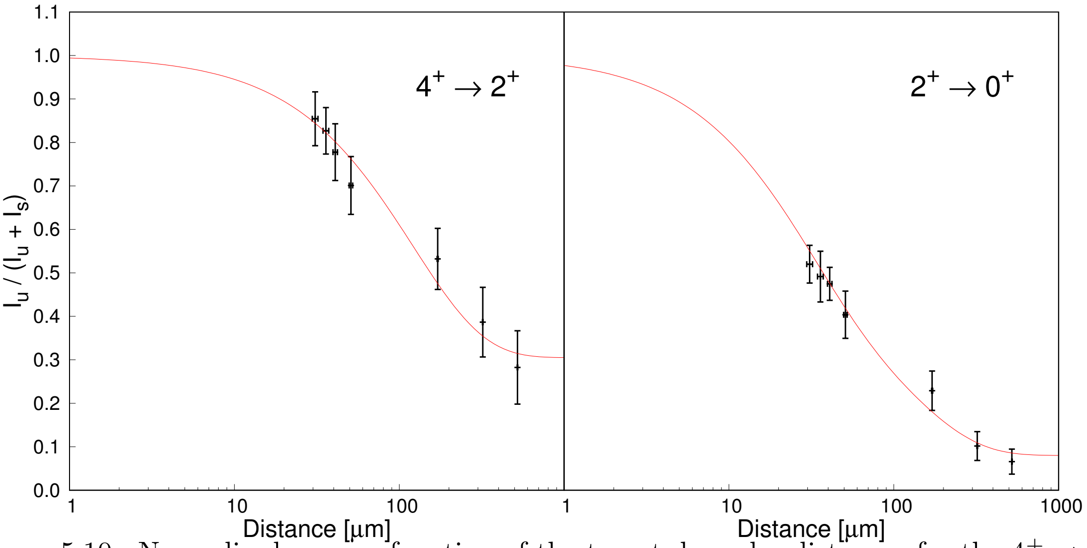

Figure 5.10.: Normalised area as function of the target-degrader distances for the $4^+ \rightarrow 2^+$ (left) and $2^+ \rightarrow 0^+$ (right) transitions, obtained from the spectra of Figure 5.9. The lifetimes $\tau(4^+) = 3.6(5)$ ps and $\tau(2^+) = 0.76(8)$ ps are extracted from the fitting curve (solid red) via the Decay Curve Method (DCM).

In the following other methods to derive the lifetime of the first 2^+ and 4^+ states in the ^{108}Sn with the goal to reduce the error will be described.

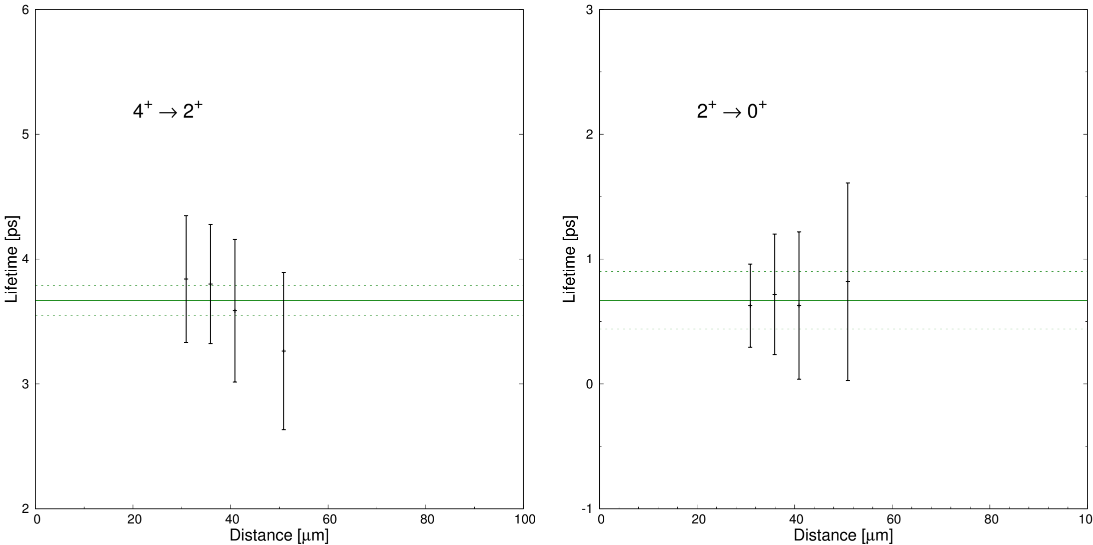

Figure 5.11.: Lifetime measurement of the first (left) 4^+ and (right) 2^+ state in ^{108}Sn as function of the target-degrader distance, obtained via the Differential Decay Curve Method: the solid line represents the fitting function, while the dashed ones are the error bars. The lifetimes result to be $\tau(4^+) = 3.67(12)$ and $\tau(2^+) = 0.7(2)$ ps. In the graphs the points in the method sensitive region are shown.

The first attempt consisted in measuring the lifetime of the states via DCM, using a "combined χ^2" function: in fact, as the lifetime of the 4^+ state is a common parameter in both the decay curve fitting functions of Figure 5.10, a combined function can be defined in order to minimize the χ^2 both for the lifetime of 4^+ and 2^+ states simultaneously. With this method, while the fitting conditions for the 2^+ state remain the same, the number of points taken into account for the lifetime estimation of 4^+ state is doubled. Despite the expectations, this procedure gives larger errors for the states lifetimes: $\tau(4^+) = 4.1(10)$ ps and $\tau(2^+) = 0.76(10)$ ps.

The second attempt consisted in the extrapolation of the lifetimes via the DDCM. Because of the statistics, the adopted method was different from what was used for ^{106}Cd: in fact, instead of the coincidence procedure, the measurement was performed with the single-γ one. As explained in Section 4.4 and summarized in Equation 4.16, in this method the contribution of the feeders to the state of interest has to be subtracted. This introduces two problems which may prevent the measurement: on one side the area of the 6^+ state cannot be estimated; on the other side, because of the error propagation, the method becomes less precise as the number of feeders increases. A possible solution for the 6^+ area issue comes from the fitting functions, used in the measurement via DCM: in that procedure, in fact, the value of the offset gives information on the direct feeding to the 6^+ state, which corresponds to $(9 \pm 2)\%$. Using this evaluation of the peak area of the $6^+ \rightarrow 4^+$ transition, the weighted average of the points in Figure 5.11 gives a lifetimes of the two states of interest: $\tau(4^+) = 3.67(12)$ and $\tau(2^+) = 0.7(2)$ ps, which are perfectly in agreement with what was obtained via DCM. However the lifetime of 2^+ state has a larger error than the one obtained via DCM.

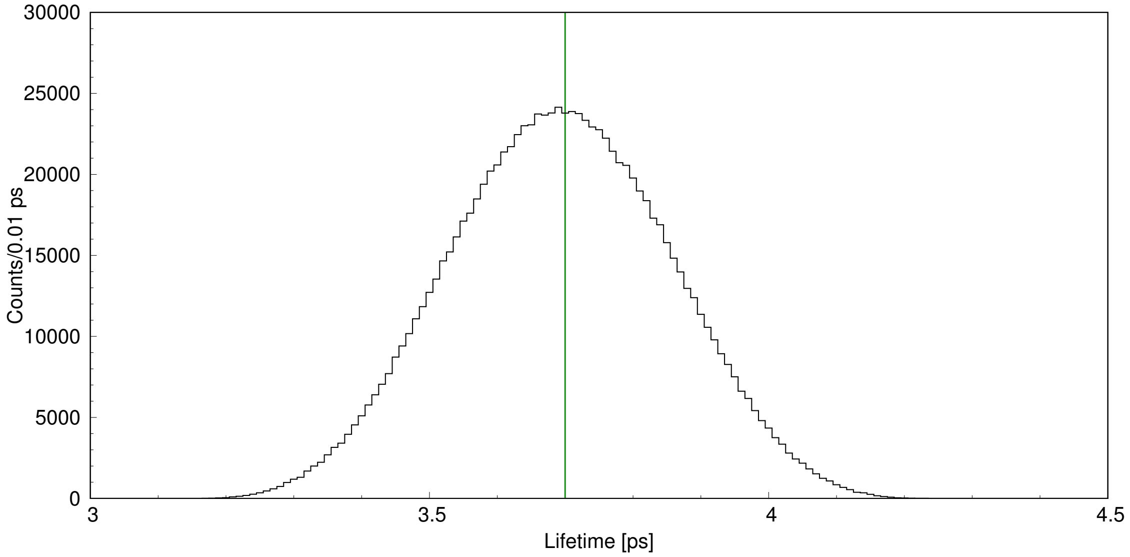

Figure 5.12.: Distribution of the 4^+ state lifetime, obtained simulating the peak area of the 6^+ isomeric state and then performing the measurement via DDCM. The green solid line represent the mean value of the distribution. The resulting lifetime is $\tau(4^+) = 3.7(2)$ ps.

After having verified the limits of the method, additional work was done for improving the analysis of the lifetime of the 4^+ state in order to make the procedure more robust. In fact, a possible objection about the described steps of the analysis concerns the evaluation of the peak area of the $6^+ \rightarrow 4^+$ transition: from the offset of the DCM fitting function just an average value of the peak area can be extracted. For this reason, instead of subtracting the constant offset, the measurement was performed via DDCM, introducing the fluctuations around the estimated average value. Per each point the peak area of the $6^+ \rightarrow 4^+$ transition was taken randomly from a uniform distribution in the range from 5 to 13, determined by considering 2σ from the average value. Then, the effect of such parameter on the analysis was investigated through a Monte-Carlo simulation. From the distribution of the lifetime, which is shown in Figure 5.12, the final result can be obtained $\tau(4^+) = 3.7(2)$ ps where the error is given by the FWHM of the distribution.

All the described methods yield compatible values of the 2^+ and 4^+ states lifetime. The values adopted from now are $\tau(2^+) = 0.76(8)$ ps and $\tau(4^+) = 3.7(2)$ ps, which represent the most precise and robust estimation of the lifetimes.

5.2.2. ^{106}Sn

The ^{106}Sn nucleus represents the lightest Sn isotope with enough statistics to allow to performing lifetime measurements. Despite the large contaminations from the ^{106}Cd beam and In isotopes, the spectrum in Figure 5.13 shows clearly that only the yrast states up to the 10^+ of ^{106}Sn were populated. As in many other neutron-deficient even-even Sn isotopes, the 6^+ state is a seniority isomer with a lifetime of $\tau(6^+) = 3.8(6)$ ns [162–164].

Thanks to the fact that only the yrast states up to the 10^+ were populated and to the presence of the 6^+ isomer, for the low-spin states lifetime determination a procedure similar to the one adopted for ^{108}Sn can be adopted, by considering only the 2^+, 4^+ and 6^+ states. From the γ-ray spectrum of Figure 5.13 the direct feeding to the low-lying states could be determined. The direct feeding parameters are given in Table 5.4.

	Measured feeding
$N_{6,0}$	$(15 \pm 9)\%$
$N_{4,0}$	$(37 \pm 7)\%$
$N_{2,0}$	$(48 \pm 7)\%$

Table 5.4.: Direct feeding measured from the γ-ray spectra of Figure 5.13.

Unfortunately the statistics of the $4^+ \rightarrow 2^+$ transition peak are not sufficient for directly extracting the lifetime of 4^+ state. Thus, after constraining the range of the feeding parameters, the lifetimes of the two lower states are extracted only from the decay curve of the 2^+ state, presented in Figure 5.14. The obtained lifetimes are $\tau(4^+) = 5.2(39)$ ps and $\tau(2^+) = 1.3(7)$ ps.

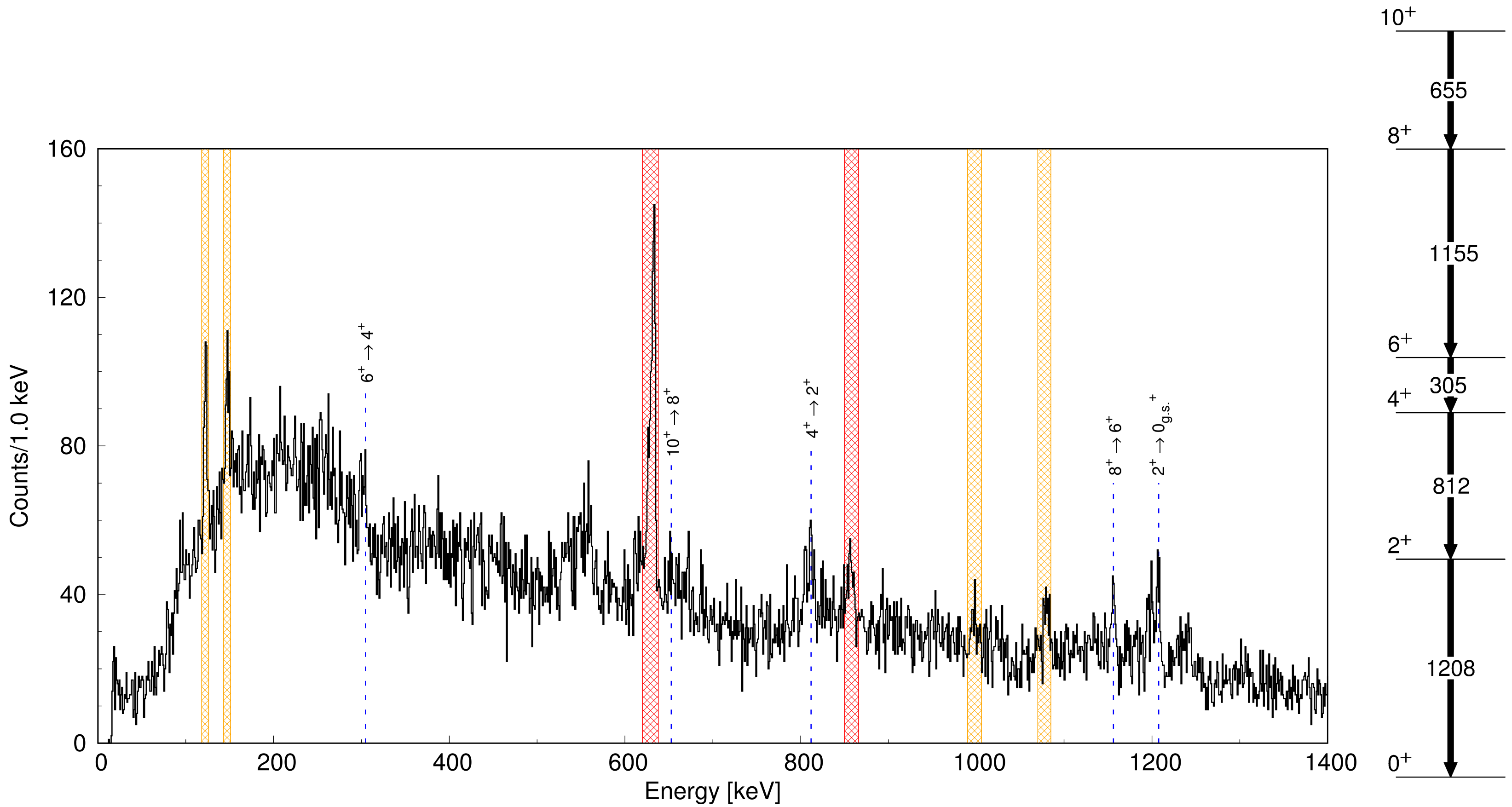

Figure 5.13.: (left) Doppler-corrected γ-ray energy spectrum for ^{106}Sn for all the plunger distances. Despite the constraint on the fragments total energy (E_{TOT}), contaminations from the inelastic-scattered ^{106}Cd beam (red) and In isotopes (orange) are still present. All the identified transitions belonging to ^{106}Sn are shown and reported in the level scheme (right).

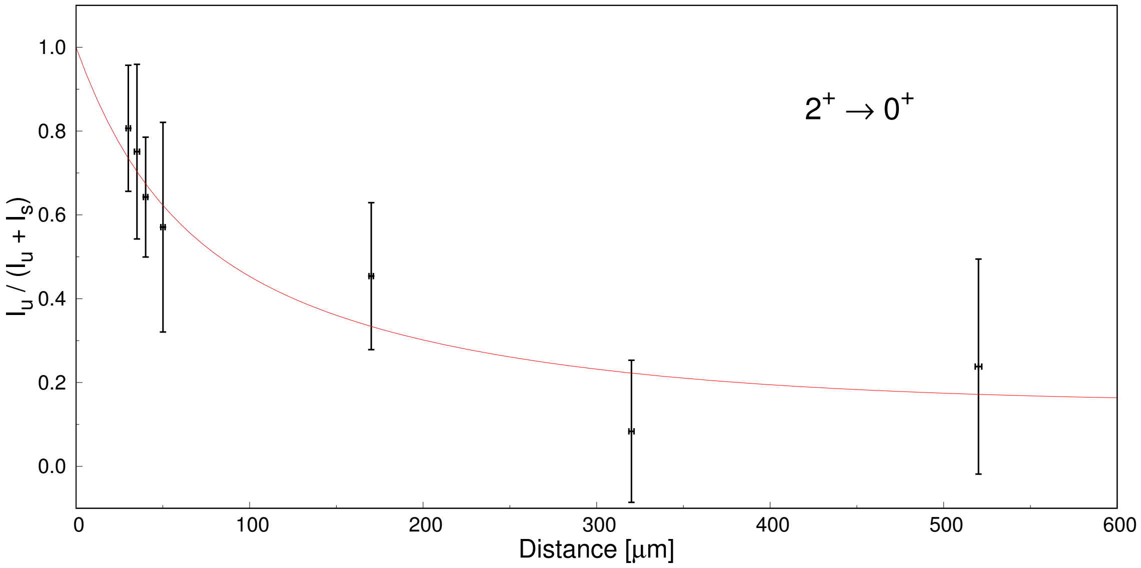

Figure 5.14.: Normalised area as function of the target-degrader distances for the $2^+ \rightarrow 0^+$ transition. The lifetimes $\tau(4^+) = 5.2(39)$ ps and $\tau(2^+) = 1.3(7)$ ps are extracted from the fitting curve (solid red) via the Decay Curve Method (DCM).

5.2.3. Odd-mass Sn

In addition to the even-even Sn isotopes just described, also the ^{107,109}Sn nuclei were populated with sufficient statistics to perform lifetime measurements.

These odd-mass Sn have structure similar to the one of the even Sn isotopes. Indeed, the two main bands, identified in the level schemes of ^{107}Sn and ^{109}Sn, can be explained as the coupling of the unpaired neutron from either the $2d_{5/2}$ or $1g_{7/2}$ orbits to the ^{106,108}Sn core, respectively. Several γ-ray spectroscopic studies were performed in the past to derive the complex level schemes of ^{107}Sn [165, 166] and ^{109}Sn [167–170] isotopes. Figure 5.15 and Figure 5.16 show the known level scheme for ^{107}Sn and ^{109}Sn, respectively.

Because of the presence at low spin of two bands, based on the coupling of a $g_{7/2}$ and $g_{5/2}$ neutron to the core, the γ-ray transitions in the two bands have very similar energy. Considering also that for each transition there are both the shifted and unshifted components, the lifetime measurement of any state is practically impossible via RDDS method. In fact, in both the spectra of Figure 5.17 and Figure 5.18 most of the peaks correspond to more than one γ-ray transition. From the observed γ-ray transitions, the ^{107}Sn states were populated up to the excitation energy $E_x \approx 4$ MeV, while the states of ^{109}Sn were populated until $E_x \approx 6$ MeV.

Concluding, even if the statistics are sufficient to extract the lifetimes, for the odd-mass ^{107,109}Sn isotopes the fact that too many transitions have similar energy makes the lifetime determination unfeasible, even by using the Q-value gate method.

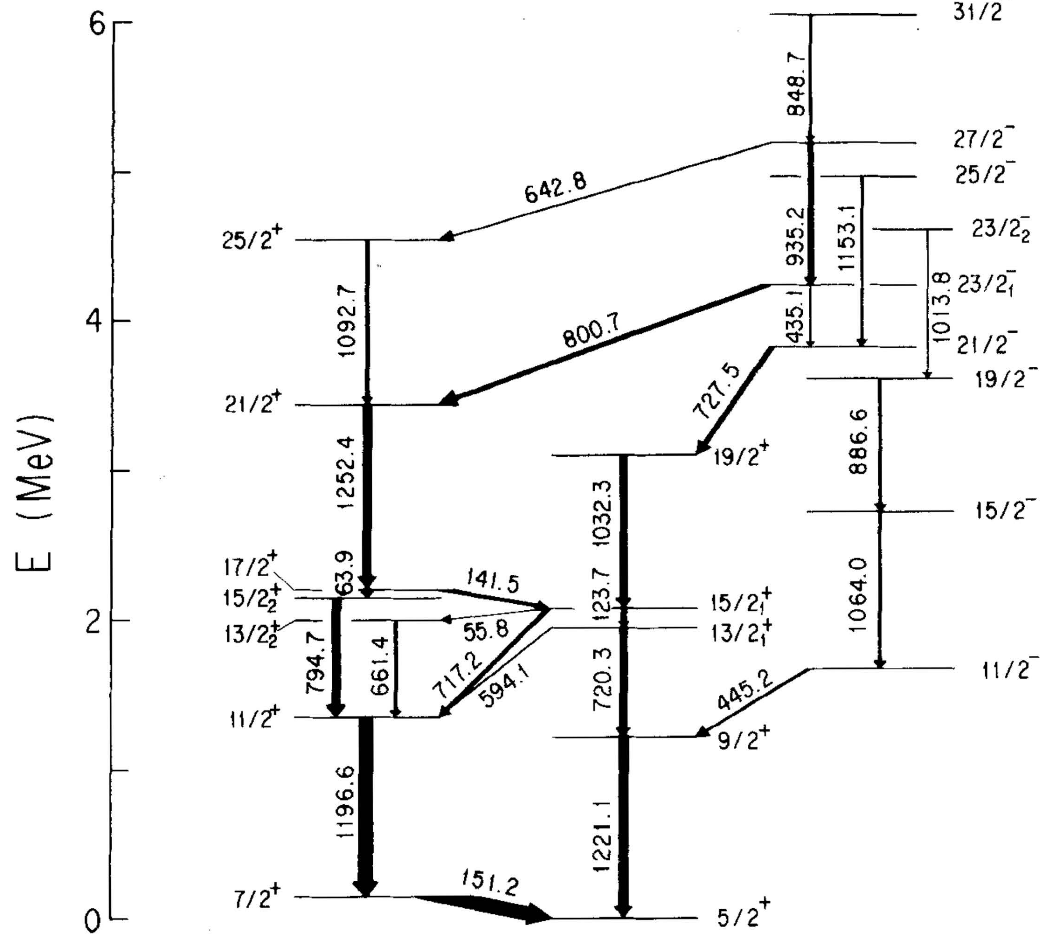
E (MeV)
0
2
4
6
31/2⁻
27/2⁻
25/2⁻
23/2₂⁻
23/2₁⁻
21/2⁻
19/2⁻
15/2⁻
11/2⁻
25/2⁺
21/2⁺
17/2⁺
15/2₂⁺
13/2₂⁺
11/2⁺
7/2⁺
19/2⁺
15/2₁⁺
13/2₁⁺
9/2⁺
5/2⁺
848.7
642.8
935.2
1153.1
1013.8
435.1
800.7
1092.7
727.5
1252.4
1032.3
886.6
63.9
141.5
123.7
55.8
1064.0
794.7
661.4
717.2
594.1
720.3
445.2
1196.6
1221.1
151.2

Figure 5.15.: Level scheme of the ^{107}Sn reported by Ishii *et al.* in Reference [166], showing the neutron-coupled and the negative parity bands.

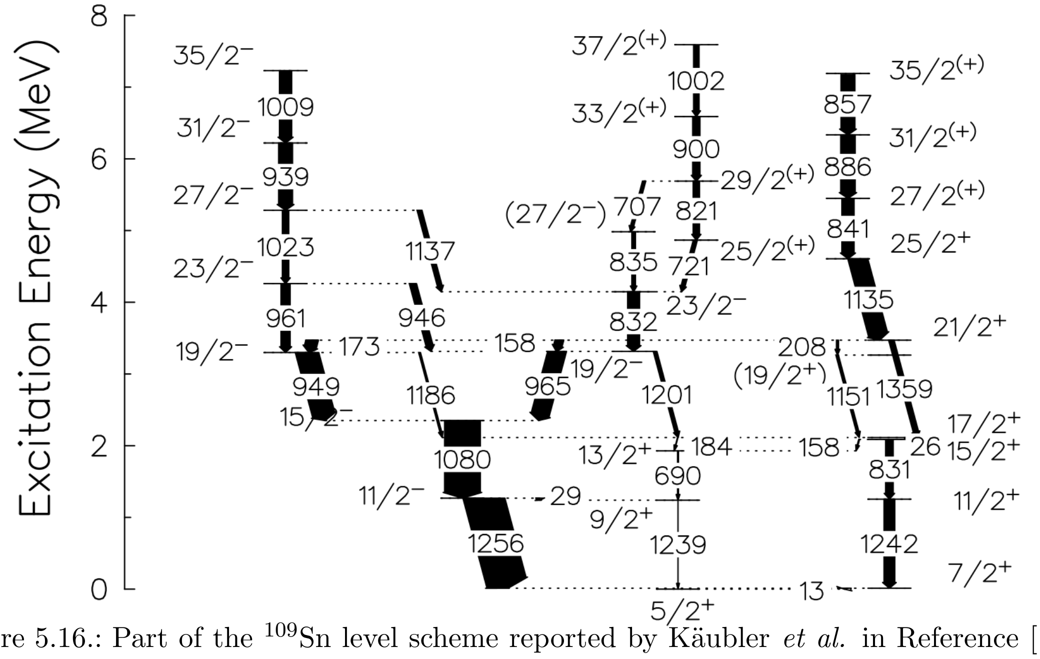
Excitation Energy (MeV)
0
2
4
6
8
35/2⁻
31/2⁻
27/2⁻
23/2⁻
19/2⁻
15/2⁻
1009
939
1023
961
949
173
1137
946
1186
158
965
1080
11/2⁻
29
1256
37/2(+)
1002
33/2(+)
900
29/2(+)
(27/2⁻)
707
821
835
721
25/2(+)
832
23/2⁻
19/2⁻
1201
13/2⁺
184
690
9/2⁺
1239
5/2⁺
208
(19/2⁺)
1151
158
13
35/2(+)
857
31/2(+)
886
27/2(+)
841
25/2⁺
1135
21/2⁺
1359
17/2⁺
26
15/2⁺
831
11/2⁺
1242
7/2⁺

Figure 5.16.: Part of the ^{109}Sn level scheme reported by Käubler *et al.* in Reference [169], showing the high-spin structures of 5 different bands.

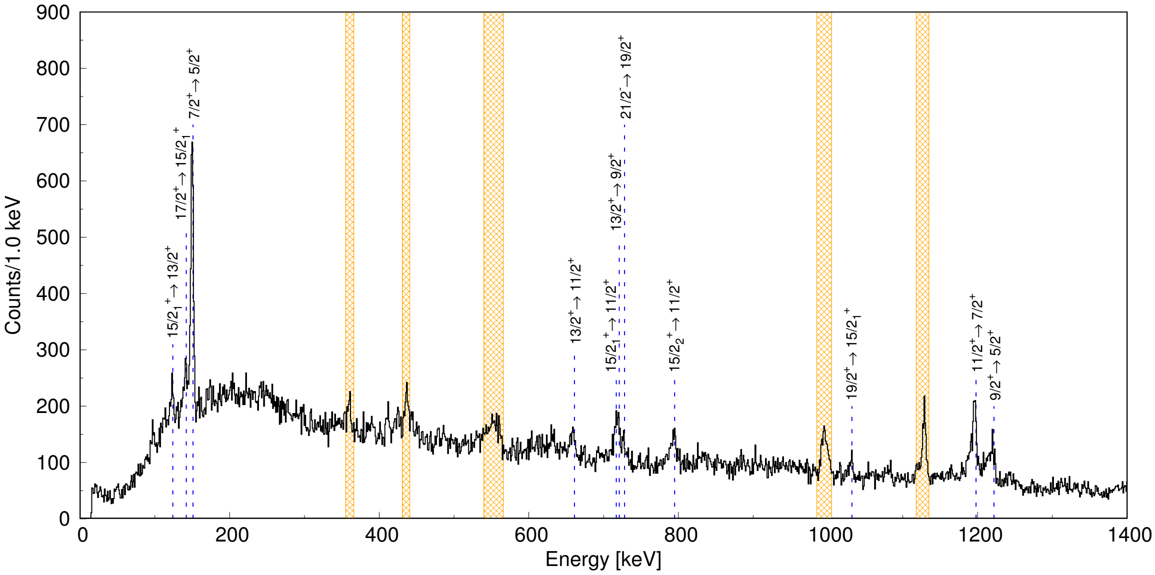

Figure 5.17.: Doppler-corrected γ-ray energy spectrum for ^{107}Sn, summing up all the statistics. No contamination from ^{106}Cd beam are present, but several peaks due to ^{107}In transitions (orange) are observed. When the assignment was possible, the identified transitions of the beam-like ion are shown.

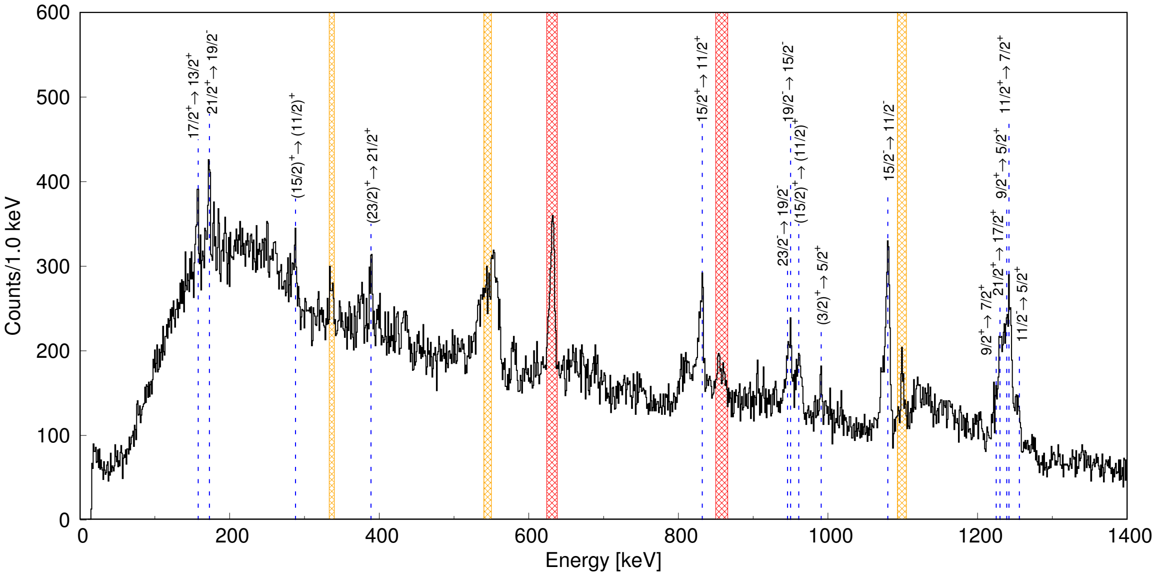

Figure 5.18.: Doppler-corrected γ-ray energy spectrum for ^{109}Sn, summing up all the statistics. Despite the constraint on the fragments total energy (E_{TOT}), contamination (red) from the inelastic-scattered ^{106}Cd beam is still present; in addition also contamination (orange) from ^{109}In are visible. When the assignment was possible, the identified transitions of the beam-like ion are shown.

6

Theoretical Interpretation

In the previous chapters the experimental method has been discussed, which allowed to extract the lifetimes of the 2^+ and 4^+ states in ^{106,108}Sn. The reduced transition probabilities have been deduced and, in this chapter, they are compared to previous experimental values, obtained by Coulomb excitation measurements. The $B(E2)$ values are also compared with the theoretical results, obtained from the state-of-the-art Large-Scale Shell-Model (LSSM) calculations, performed in collaboration with the theoretical group from the Institut Pluridisciplinaire Hubert Curien (IPHC, France).

6.1. B(E2) systematics along the Sn isotopic chain

The measurement of the reduced transition probabilities $B(E2; 2^+ \to 0^+)$ along the Sn isotopic chain has attracted a large interest: indeed, the information on the low-lying states in the neutron-deficient Sn isotopes can shed light on the evolution of "magicity" of the proton shell closure $Z = 50$. However, because of the presence of the seniority isomers, typical fingerprint of semi-magic nuclei, the investigation of transition strength, such as $B(E2; 2^+ \to 0^+)$, in neutron-deficient even-even tin isotopes has been mainly performed via Coulomb excitation measurements [81, 83–93]. The present result represents *de facto* the first direct lifetime measurement for the low-lying states 2^+ and 4^+ in the neutron-deficient Sn region. Furthermore, the data allowed to estimate the reduced transition probabilities $B(E2; 4^+ \to 2^+)$, that was never measured before for such neutron-deficient nuclei. In Figure 6.1, the systematics of the $B(E2)$ values for both $4^+ \to 2^+$ and $2^+ \to 0^+$ transitions are presented, which include also the results obtained in this thesis.

The lifetime of the first 2^+ state of ^{108}Sn corresponds to a reduced transition probability that is perfectly in agreement with all the previous Coulomb excitation measurements [81, 83, 84, 86]. This new result has an error of $\approx 10\%$, which makes it one of the most precise measurements if compared to the previous values. In addition, thanks to the different analysis procedures that were used and improved, for the same nucleus the $B(E2; 4^+ \to 2^+)$ is extracted with an error of $\approx 5\%$. Remarkable are also the results of ^{106}Sn: while the large error on the lifetime of the 4^+ state makes any clear conclusion on the evolution of the $B(E2; 4^+ \to 2^+)$ difficult, the $B(E2; 2^+ \to 0^+_{g.s.})$ suggests that this quantity is decreasing when going towards ^{100}Sn. In Table 6.1 the new and the previously-measured values of the reduced transition probabilities for the $4^+ \rightarrow 2^+$ and $2^+ \rightarrow 0^+$ transitions in ^{106,108}Sn are summarised[1].

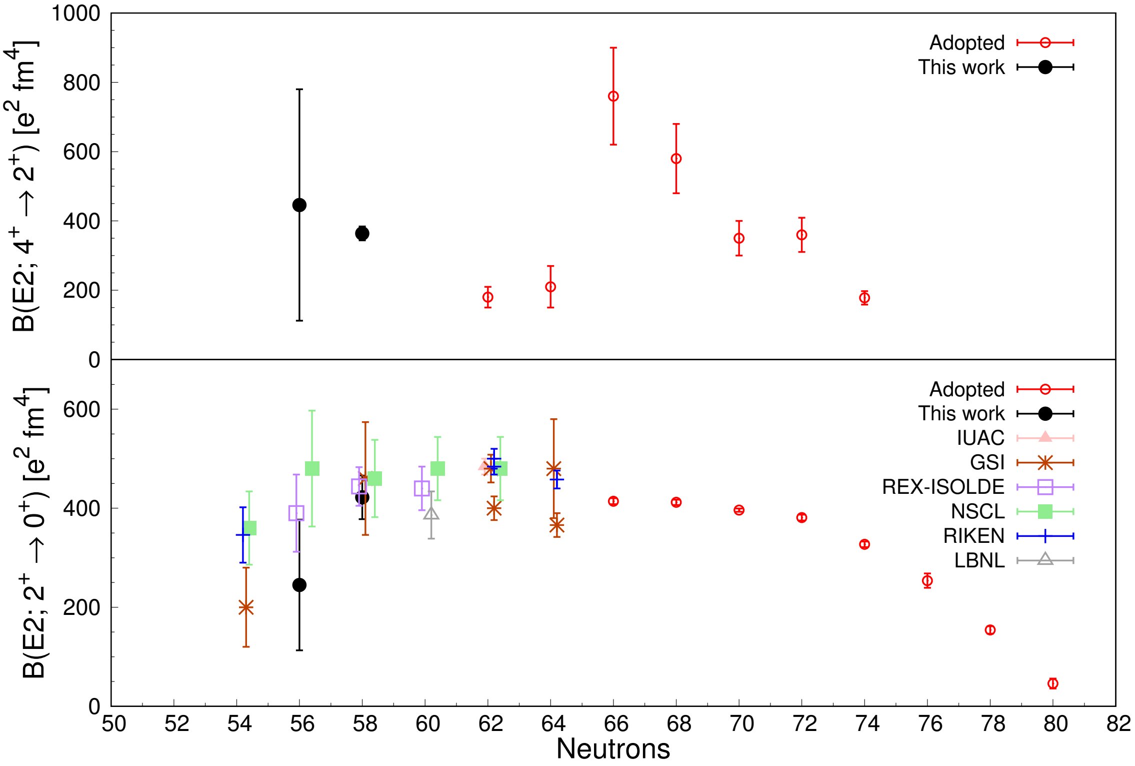

Figure 6.1.: Reduced transition probability $B(E2)$ systematics along the Sn isotopic chain for (top) $4^+ \rightarrow 2^+$ and (bottom) $2^+ \rightarrow 0^+$ transitions. The results discussed in this thesis (black dots) are compared with previous experiments. The "adopted" results for the neutron-rich isotopes are taken from Reference [2], while for the neutron-deficient region the results are taken from References [81, 83–93].

	^{106}Sn		^{108}Sn	
	$2^+ \rightarrow 0^+$	$4^+ \rightarrow 2^+$	$2^+ \rightarrow 0^+$	$4^+ \rightarrow 2^+$
Coulex at GSI	-	-	464 (114)	-
Coulex at NSCL	480 (117)	-	460 (78)	-
Coulex at ISOLDE	390 (78)	-	444 (38)	-
This work	245 (132)	446 (334)	422 (44)	364 (20)

Table 6.1.: Reduced transition probabilities for the low-lying $2^+ \rightarrow 0^+$ and $4^+ \rightarrow 2^+$ transitions of ^{106,108}Sn. The values, extracted from the lifetimes measured in this work, are shown together with those obtained via Coulomb excitation measurement [81, 83, 84, 86]. The results are reported in $e^2 fm^4$.

---

[1] The GSI value [83] of ^{108}Sn was recently corrected by the work of Kumar and collaborators [81], who changed the $B(E2; 2^+ \rightarrow 0^+)$ from 460 (114) to 464 (114) $e^2 fm^4$. Therefore, in the following the more recent value will be adopted.

6.2. Proton excitation across the Z=50 shell closure

For the neutron-rich tin isotopes the magnitude of the proton gap was directly extracted from the separation energy S_{2p}, experimentally measured for Sn and Te isotopes [77, 78], showing a maximum of ≈ 9 MeV for ^{132}Sn (see Figure 1.15). On the neutron-deficient side, however, only indirect evidence of the size of the $Z = 50$ shell closure exists, e.g. the excitation energy of the core-excited isomer in ^{98}Cd[2] [79] or the large Gamow-Teller strength observed in the β decay of ^{100}Sn [80]. The proton shell closure for ^{100}Sn has been estimated from the Effective Single Particle Energies (ESPE), which include only the monopole term of the nuclear interaction, and it was found to be ≈ 6.5 MeV, which is the value adopted in the majority of the theoretical calculations (see Figure 6.3).

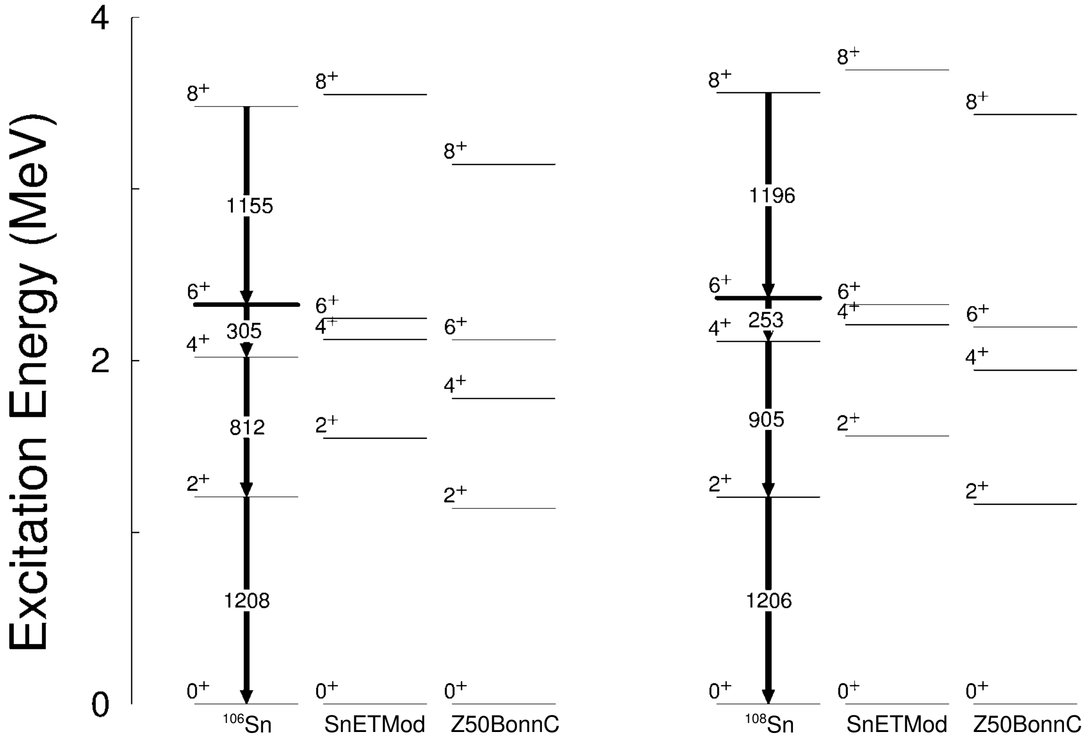

Figure 6.2.: Comparison between the experimental low-lying states in ^{106,108}Sn with LSSM calculations, obtained with SnETMod [171] and Z50BonnC [172] interactions. In the calculations, ^{100}Sn was defined as core and the neutrons model space consisted of the $1d_{5/2}$, $0g_{7/2}$, $1d_{3/2}$, $2s_{1/2}$ and $0h_{11/2}$ orbitals.

The structure of the Sn isotopes can be calculated by considering a ^{100}Sn core. As an example, in Figure 6.2 the yrast band up to the 8^+ state in ^{106,108}Sn is compared with LSSM calculations, obtained by using the SnETMod [171] and Z50BonnC [172] interactions. For both neutrons and protons the $d_{5/2}$, $g_{7/2}$, $d_{3/2}$, $s_{1/2}$ and $h_{11/2}$ orbitals were included in the valence space[3]. On one side, the agreement between the experimental and the calculated level scheme is quite good, especially with the Z50BonnC interaction. However, when computing the transition probabilities, one realizes that the use of the standard effective charges gives an underestimation of the $B(E2)$ values. In fact, by comparing the values reported in Table 6.1 with those obtained via LSSM calculations (Table 6.2), it is clear that the neutron excitation alone is not able to reproduce the experimental results: while the $B(E2; 4^+ \rightarrow 2^+)$ cannot be reproduced at all, reasonable values of the $B(E2; 2^+ \rightarrow 0^+)$ can be obtained by using a neutron effective charge $e_\nu = 1.3e$. Such large value of the neutron effective charge comes from the fact the proton $g_{9/2}$ shell is closed and there is a missing part of the $0\hbar\omega$ major shell to the $E2$ quadrupole operator [173].

---

[2] In the work of Blazhev and collaborators the neutron shell gap of ^{100}Sn has been estimated from the 12^+ isomer of ^{98}Cd. Then, taking into account the isospin symmetry of the nuclear interaction, the proton shell gap was considered equal to the neutron one.

	^{106}Sn		^{108}Sn	
	$2^+ \rightarrow 0^+$	$4^+ \rightarrow 2^+$	$2^+ \rightarrow 0^+$	$4^+ \rightarrow 2^+$
SnETMod ($e_\nu = 0.5e$)	55	13	65	1
SnETMod ($e_\nu = 1.3e$)	368	90	438	8
Z50BonnC ($e_\nu = 0.5e$)	60	2	76	2
Z50BonnC ($e_\nu = 1.3e$)	409	16	513	15

Table 6.2.: Reduced transition probabilities for the low-lying $2^+ \rightarrow 0^+$ and $4^+ \rightarrow 2^+$ transitions in ^{106,108}Sn, calculated with the SnETMod [171] and Z50BonnC [172] interactions. In the calculations, the core was ^{100}Sn and the neutrons model space consisted of $g_{7/2}dsh_{11/2}$ orbitals. The results are given in units of e^2fm^4.

The main reason of such mismatch between experimental and calculated values of the transition strength is due to the lack of proton-core correlations. The quadrupole correlations between orbitals near the Fermi surface are larger when $\Delta L = 2$ and $\Delta J = 2$ [174]. This is indeed the case under discussion, since the orbitals $g_{9/2}$ and $d_{5/2}$ are involved for the neutron-deficient Sn isotopes (see Figure 1.3). Therefore, the role of particle-hole excitations across the $Z = 50$ proton gap becomes important to explain the physics involved and the large $E2$ polarization. Figure 6.3 shows the evolution of the proton ESPE, obtained considering the $g_{9/2}$, $d_{5/2}$, $g_{7/2}$, $d_{3/2}$ and $s_{1/2}$ proton orbitals and the $d_{5/2}$, $g_{7/2}$, $d_{3/2}$, $s_{1/2}$ and $h_{11/2}$ neutron orbitals as model space [83]: the effective shell gap $Z = 50$ reaches the maximum values at the neutron magic numbers $N = 50, 82$.

As example of the crucial role of particle-hole excitations across the $Z = 50$ proton gap, in the work of Banu and collaborators [83], based on the Coulomb excitation measurement of ^{108}Sn, the experimental results are compared with a LSSM calculations considering a ^{90}Zr core, with $g_{9/2}$, $d_{5/2}$, $g_{7/2}$, $d_{3/2}$ and $s_{1/2}$ proton orbitals and $d_{5/2}$, $g_{7/2}$, $d_{3/2}$, $s_{1/2}$ and $h_{11/2}$ neutron orbitals as model space[4]. For such closed-shell core, the effective interaction [79, 83] is isospin independent (proton and neutron shell gaps have the same energy), but it was phenomenologically adjusted in order to reproduce the structure of the Sn isotopes and of the $N = 82$ isotones. The calculation allows up to $4p - 4h$ proton excitations and the effective charges are set to the pure-isoscalar values $e_\pi = 1.5e$ and $e_\nu = 0.5e$. Because in this model space the m-scheme dimension would be excessively large, the coupled code

---

[3] For simplicity in the following the model space will be defined as $g_{7/2}dsh_{11/2}$.

[4] For simplicity in the following the proton and neutron valence spaces will be called $\pi(g, d, s)$ and $\nu(g_{7/2}, d, s, h_{11/2})$, respectively.

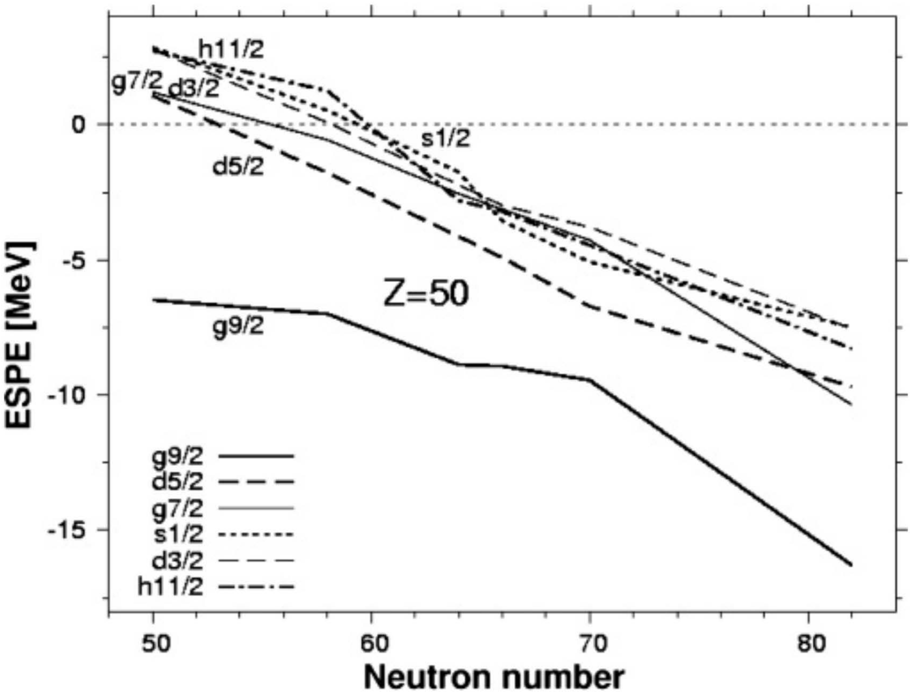

Figure 6.3.: Calculated proton Effective Single-Particle Energies (ESPE) as a function of the neutron number. The LSSM predictions were obtained considering the ^{90}Zr closed-shell core (see text). Figure taken from Reference [83].

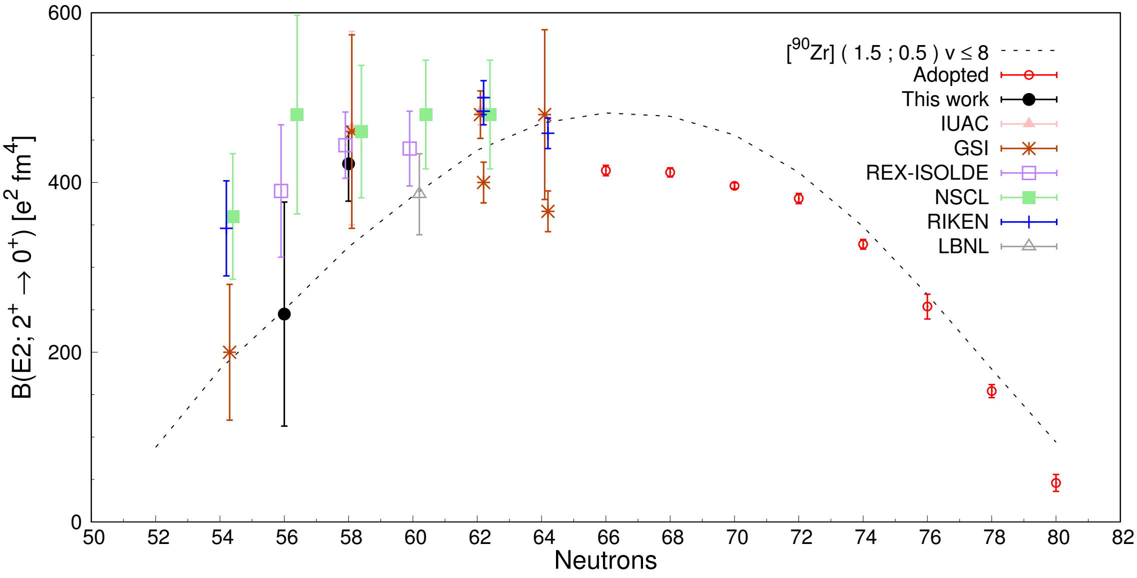

Figure 6.4.: Comparison of the measured $B(E2; 2^+ \rightarrow 0^+)$ values with LSSM predictions, considering ^{90}Zr as closed-shell core (see text). The results discussed in this thesis (black dots) are compared with previous experiments: the "adopted" results for the neutron-rich isotopes are taken from Reference [2], while for the neutron-deficient region the results are taken from References [81, 83–93]. The LSSM predictions are taken from Reference [83].

NATHAN [34] is used, which allows for a seniority truncation. Convergence was obtained for seniority $v = 8$. In Figure 6.4 the comparison between the described LSSM predictions and the experimental values of the reduced transition probabilities is shown for the whole Sn isotopic chain. While in the case of the ^{100}Sn core (see Table 6.2) very large neutron effective charge was necessary to reproduce the $B(E2; 2^+ \rightarrow 0^+)$ values, the pure-isoscalar effective-charges values are sufficient if proton excitations across the $Z = 50$ shell closure is considered.

Despite the inclusion of the proton-core excitations, the experimentally observed asymmetry of the $B(E2)$ systematics cannot be reproduced. This suggests to further investigate the role of proton-core excitations and also other features of the theoretical predictions, such as the effect of seniority truncation or of the core polarization as a function of the neutron number. Indeed, so far all the previous theoretical calculations have used pure-isoscalar effective-charge values $e_\pi = 1.5e$ and $e_\nu = 0.5e$.

6.3. Effect of seniority in LSSM calculations

Thanks to the results obtained in the present experiment, it is possible to theoretically investigate the trend of the reduced transition probabilities for the $4^+ \rightarrow 2^+$ ($\Delta v = 0$) and $2^+ \rightarrow 0^+$ ($\Delta v = 2$) transitions. Thus, new LSSM calculations have been performed in order to reproduce the trend of the experimental values. In such calculation a ^{80}Zr core has been adopted and the matrix elements were fitted on the same experimental observables used for the interaction of the work of Banu and collaborators [173]. As a model space, the $\pi(g, d, s)$ and $g_{9/2}$, $d_{5/2}$, $g_{7/2}$, $d_{3/2}$, $s_{1/2}$ and $h_{11/2}$ neutron orbitals have been considered[5]. Because of the large dimensions of the model space, the neutron orbital $0g_{9/2}$ has been "frozen", avoiding excitation across the $N = 50$ shell gap, the proton excitations have been limited up to $4p-4h$ and the neutron occupation of orbit $0h_{11/2}$ has been also restricted up to 4. In order to check the effects of the seniority truncation, the calculations have been performed in two cases: on one side the seniority is limited up to 8, as in the work of Banu and collaborators [83]; while on the other side no truncations have been applied to the seniority. Then, in the second case, the calculations have been performed for three different sets of effective charges:

- pure-isoscalar effective-charges ($e_\pi = 1.5e; e_\nu = 0.5e$), in order to compare the results with those obtained with the ^{90}Zr core
- ($e_\pi = 1.4e; e_\nu = 0.6e$), in order to introduce a small isovector component ($e^{IV}_{pol} = 0.1e$) in the nuclear interaction
- ($e_\pi = 1.3e; e_\nu = 0.7e$), in order to introduce a small isovector component ($e^{IV}_{pol} = 0.2e$); these values are taken from the work of Blazhev and collaborators [79], who studied the excitation energy of the core-excited isomer in ^{98}Cd and estimated the neutron shell gap for $Z = 50$ (the proton shell gap of ^{100}Sn was then deduced by considering the isospin symmetry of the nuclear interaction)

Because of the different required configurations and of the large dimensions of the valence space, these new calculations are time demanding and therefore the calculations along the whole Sn isotopic chain are still on going. For the moment, results are available for the neutron-deficient nuclei up to ^{110}Sn. In Figure 6.5 the comparison between the experimental $B(E2)$ values and the LSSM calculations is presented for the $^{104-110}$Sn isotopes.

---

[5] For simplicity in the following the neutron valence space will be called $\nu(g, d, s, h_{11/2})$.

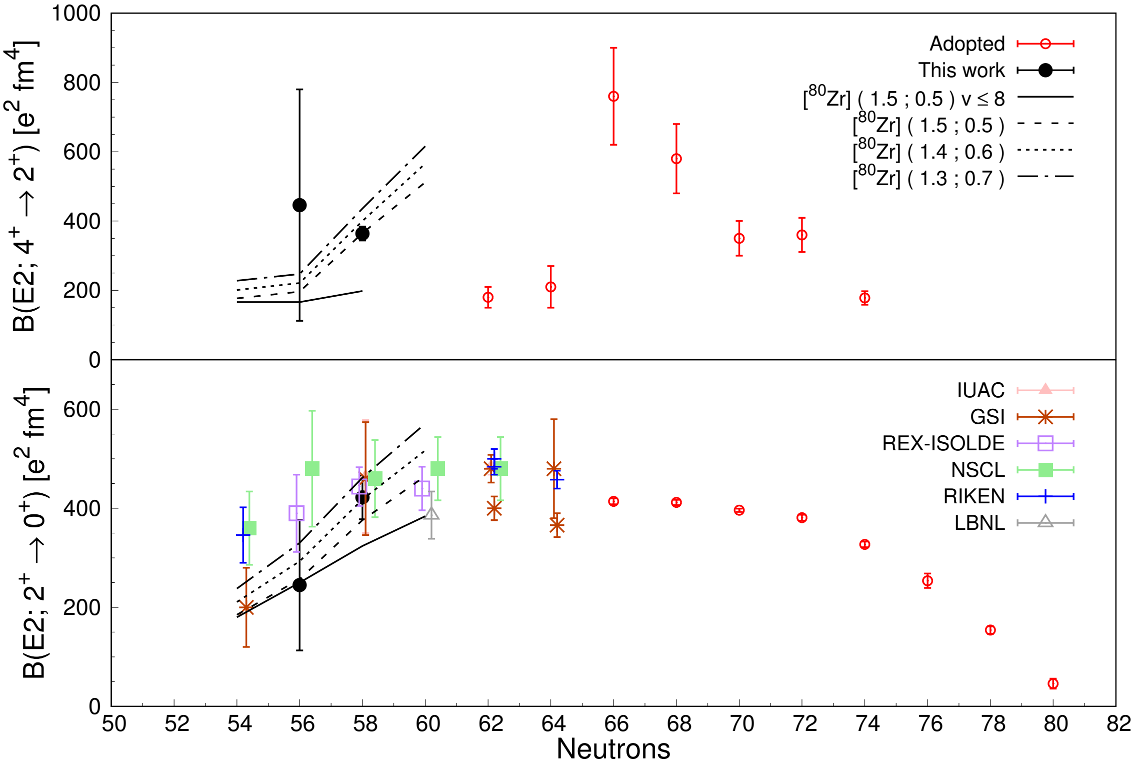

Figure 6.5.: Experimental $B(E2)$ values for the $4^+ \rightarrow 2^+$ and $2^+ \rightarrow 0^+$ transitions together with LSSM predictions, considering a ^{80}Zr closed-shell core (see text). The results discussed in this thesis (black dots) are compared with previous experiments: the "adopted" results for the neutron-rich isotopes are taken from Reference [2], while for the neutron-deficient region the results are taken from References [81, 83–93]. The different lines represent the LSSM calculations: the solid line represents the $B(E2)$ prediction obtained from the seniority truncation $v \leq 8$, while the dashed lines are the theoretical results where no seniority truncation has been considered and three different sets of effective charges are used.

6.3.1. Seniority-truncated predictions

The $B(E2; 2^+ \rightarrow 0^+)$ values, obtained with the new LSSM calculations, based on a ^{80}Zr core with the neutron orbital $g_{9/2}$ "frozen" and a seniority truncation $v \leq 8$, correspond so far to the theoretical values obtained by Banu and collaborators [83] using the ^{90}Zr core (see Figure 6.4). The reduced transition probabilities of the $4^+ \rightarrow 2^+$ transitions are clearly underestimated with the seniority truncation (see Figure 6.5). On the contrary, the predictions of the LSSM calculations with no restrictions on the seniority agree better with the experimental results. This can be clearly seen by looking at the $B(E2; 4^+ \rightarrow 2^+)$ value of ^{108}Sn.

The wave functions of the 0^+, 2^+ and 4^+ states in ^{106,108}Sn isotopes can be described as a linear combination of the eigenvectors related to a certain value of the seniority v. Indeed, for semi-magic nuclei, as the Sn isotopes, the seniority represents a "good" quantum number [3]. In particular, the wave functions of the ^{106}Sn nucleus can be written as

$$\begin{aligned}
\left|0^+\right\rangle &\approx \sqrt{68\%}\left|v=0\right\rangle + \sqrt{0\%}\left|v=2\right\rangle + \sqrt{27\%}\left|v=4\right\rangle + \sqrt{2\%}\left|v=6\right\rangle + \sqrt{3\%}\left|v=8\right\rangle \\
\left|2^+\right\rangle &\approx \sqrt{0\%}\left|v=0\right\rangle + \sqrt{71\%}\left|v=2\right\rangle + \sqrt{8\%}\left|v=4\right\rangle + \sqrt{19\%}\left|v=6\right\rangle + \sqrt{2\%}\left|v=8\right\rangle \\
\left|4^+\right\rangle &\approx \sqrt{0\%}\left|v=0\right\rangle + \sqrt{62\%}\left|v=2\right\rangle + \sqrt{18\%}\left|v=4\right\rangle + \sqrt{17\%}\left|v=6\right\rangle + \sqrt{3\%}\left|v=8\right\rangle \quad ,
\end{aligned} \tag{6.1}$$

while for the ^{108}Sn they become

$$\begin{aligned}
\left|0^+\right\rangle &\approx \sqrt{62\%}\left|v=0\right\rangle + \sqrt{0\%}\left|v=2\right\rangle + \sqrt{32\%}\left|v=4\right\rangle + \sqrt{2\%}\left|v=6\right\rangle + \sqrt{4\%}\left|v=8\right\rangle \\
\left|2^+\right\rangle &\approx \sqrt{0\%}\left|v=0\right\rangle + \sqrt{70\%}\left|v=2\right\rangle + \sqrt{7\%}\left|v=4\right\rangle + \sqrt{21\%}\left|v=6\right\rangle + \sqrt{2\%}\left|v=8\right\rangle \\
\left|4^+\right\rangle &\approx \sqrt{0\%}\left|v=0\right\rangle + \sqrt{59\%}\left|v=2\right\rangle + \sqrt{18\%}\left|v=4\right\rangle + \sqrt{19\%}\left|v=6\right\rangle + \sqrt{4\%}\left|v=8\right\rangle \quad .
\end{aligned} \tag{6.2}$$

For both Sn isotopes, the wave functions describing the ground state are composed by $\approx 60\%$ of configurations with seniority $v = 0$, as it is expected from a "textbook" seniority description. On the other hand, important contributions are present from configurations with seniority $v \geq 4$ that suggest a more complex and fragmented wave function. The complete absence of terms with seniority $v = 2$ is due to the parity and spin composition rules: two unpaired nucleons with different spin cannot be coupled to total spin equal to $0\hbar$. Regarding the wave functions of the 2^+ and 4^+ states, the main contribution is given by $v = 2$ configurations, as it is expected from the seniority description. Then, the terms with seniority $v \geq 4$ become more and more significant with increasing spin. Another important feature of the wave functions, obtained with a $v \leq 8$ truncation, is that the contribution of the highest possible seniority is just $2 - 4\%$. Therefore, a *naïve* estimation of the $v > 8$ components in the full seniority calculations entails that such terms would be around 1%. However, as it is shown in Figure 6.5, their contribution is sufficient to drastically change the trend of the reduced transition probabilities, especially for the $4^+ \rightarrow 2^+$ transition in ^{108}Sn.

These results indicate the complexity of the wave functions describing the excited states of nuclei in the $N = Z = 50$ region: despite the proximity to the doubly-magic ^{100}Sn, already the ground state has a really fragmented wave function, that is far from the usual textbook examples where the nucleons occupy the orbitals with the lowest single particle energy.

6.4. Theoretical results and discussion

The results obtained in this thesis, namely the lifetimes of the 2^+ and 4^+ states in the neutron-deficient ^{106,108}Sn isotopes, has provided new data to further test the nucleon-nucleon interaction in the region around $N = Z = 50$. From the comparison between the experimentally deduced transition probabilities $B(E2; 2^+ \rightarrow 0^+)$ and $B(E2; 4^+ \rightarrow 2^+)$ with

LSSM calculations (see Figure 6.5) one can make two major observations that improve our understanding of this so far badly comprehended region close to ^{100}Sn. However, before discussing our two main conclusions, one should keep in mind the following statements:

- the wave functions of the 2^+ and 4^+ states are very fragmented. Indeed, the largest configuration contribution goes from around 20% (14%) of the ground state down to 9% (4%) of the first 4^+ state in ^{106}Sn (^{108}Sn). This means that for neutron-deficient Sn isotopes the *naïve* description of the 2^+ and 4^+ excited states as $(g_{7/2})^{v=2}$ configurations is far from being a reliable description.

- the inclusion of proton excitation across the $Z = 50$ is crucial to define the physics case. In fact, for ^{106}Sn the probability of having the proton $g_{9/2}$ fully-occupied is $\approx 60\%$ and it decreases down to 50% for ^{108}Sn.

The first conclusion of this thesis is related to the kink observed experimentally and theoretically in the $B(E2; 2^+ \to 0^+)$ values, when going from $N = 56$ to $N = 58$. Although our experimental $B(E2; 2^+ \to 0^+)$ value for the ^{106}Sn presents a large experimental uncertainty, it shows a downturn with respect to ^{108}Sn. The kink observed in our experimental $B(E2; 2^+ \to 0^+)$ values when passing from ^{106}Sn to the ^{108}Sn is nicely reproduced by the LSSM calculations when no seniority truncation is considered. Indeed, when comparing the theoretical $B(E2; 2^+ \to 0^+)$ values, obtained with the same valence space but with a seniority truncation $v \leq 8$, and with the non-seniority truncated calculations, the first has a smooth behaviour of the $B(E2)$ values while the second presents a step-like behaviour. Differences in the truncated and non-truncated $B(E2; 2^+ \to 0^+)$ calculations start to appear for $N \geq 58$, since more neutron valence particles are available to contribute to larger seniority components of the wave function. The drastic change of trend in the reduced transition probabilities is even more evident for the $B(E2; 4^+ \to 2^+)$, where the theoretical calculations show an evident jump when passing from ^{106}Sn to ^{108}Sn. It is clear that the experimental $B(E2; 4^+ \to 2^+)$ for ^{108}Sn can only be reproduced if no truncation is considered. For the ^{106}Sn, the difference among the theoretical calculations with or without seniority truncation is less evident, due to the reason just discussed above; therefore, even if our experimental value presents large uncertainties, it cannot be decisive to discriminate between the two calculations. The effects of the truncation can be evidently seen in the Figure 6.6, that shows the expected values of the occupation numbers for the adopted model space. It is observed in this plot that by including higher orders of seniority, the proton excitation across the $Z = 50$ shell gap becomes more important with the consequent decrease of the population of the $g_{9/2}$ orbital (increase of the orbitals $g_{7/2}$-$d_{3/2}$). Instead, for the neutrons, there is a reduction of the population of the $h_{11/2}$ orbital in case of no seniority truncation, while the occupation of both $g_{7/2}$ and $d_{3/2}$ orbitals increases. These variations in the occupation numbers entails a larger contribution to the quadrupole correlations, which causes an increment of the reduced transition probabilities $B(E2)$.

Summarising, the very-first measurement of the $B(E2; 4^+ \to 2^+)$ value in Sn is crucial to conclude that seniority truncated wave functions do not contain all the physics necessary to describe the neutron-deficient Sn nuclei. This remarkable result questions the validity of the previous attempts of reproducing the experimental trend of the $B(E2; 2^+ \to 0^+)$ in a consistent way, via theoretical LSSM calculations considering the seniority truncation. The full non-seniority truncated calculations also show a step-like behaviour on the $B(E2)$

values as a function of the neutrons number, something not predicted until now.

Regarding the trend of the reduced transition probabilities, obtained with non-truncated LSSM calculations, a few words can be spent about the slight overestimation of the theoretical predictions for ^{110}Sn with respect to the experimental data. This suggests that, when increasing the number of valence neutrons, the definition of the valence space inside a major shell could be too restrictive. Despite the $\nu(g, d, s, h_{11/2})$ valence space contains all the $0\hbar\omega$ excitations, for the presented theoretical calculations the truncation on the neutron occupancy of the $h_{11/2}$ orbit is still too restrictive. Keeping in mind that the $h_{11/2}$ orbit does not provide quadrupole correlations, the limitation on its occupancy entails that the other orbitals population has to increase. However, as discussed previously, the quadrupole correlation between the remaining orbitals is really strong ($\Delta L = 2$ and $\Delta J = 2$) and therefore a small variation on the neutron occupancy can cause a large deviation on the $B(E2)$ values. The influence of the truncation on the $h_{11/2}$ occupancy would become more and more important as the neutron number increases. On the other hand, in the previous section it was shown that the contribution of the valence neutrons to the $B(E2)$ values is really limited, because most of the quadrupole correlations are provided by the proton-core correlations. The same comment can be extended also to the proton valence space, which is not including $h_{11/2}$ orbital. In fact, the "reduced" valence space can cause an overestimation of the population in those proton orbitals, which largely contribute to the quadrupole correlations. Unfortunately, while the possible population of the proton $h_{11/2}$ orbital can be *naïvely* estimated to be around 10^{-3} particles, by observing the occupation numbers presented in Figure 6.6, the contribution of the $h_{11/2}$ orbitals to the reduced transition probabilities $B(E2)$ cannot be easily evaluated.

The second important observation when comparing our experimental data with theory is related to the effective charges used in the calculations. The valence space contains all the $0\hbar\omega$ excitations and the quasi $SU(3)$ partners $g_{9/2}$ and $d_{5/2}$ that holds the dominant quadrupole strength [30] in this valence space. In the LSSM calculations the neutrons in the $g_{9/2}$ have been blocked, having observed that for the most neutron deficient Sn isotopes the neutrons in such an orbital do not contribute to the $B(E2)$ values. Therefore, in this valence space one expects that the renormalised interaction takes into account the excitations from the core that leads to standard effective charges $e_\nu = 0.5e$ and $e_\pi = 1.5e$ for neutrons and protons, respectively, that will remain constant in the valence space [11]. However, from our data it has been observed that, to get a better agreement with experiment, effective charges different to these standard ones ($e_\nu = 0.5e$ and $e_\pi = 1.5e$, i.e $e^{IS}_{pol} = 0.5e$, $e^{IV}_{pol} = 0e$) have to be invoked. It seems that the best effective charges that reproduce the experimental data are $e_\nu = 0.6e$ and $e_\pi = 1.4e$ that imply the following isoscalar and isovector polarisation charges $e^{IS}_{pol} = 0.5e$ and $e^{IV}_{pol} = 0.1e$, respectively. Similar value of the effective charges was discussed in Reference [79]. One might ask what is the origin of this small isovector contribution to the effective charges. On one hand, one has to note that in the calculations only up to $4p - 4h$ excitation from the $g_{9/2}$ proton core are allowed, in addition to the fact that the $h_{11/2}$ intruder orbital in the neutron valence space has been included in the calculations. This could imply a small departure from the canonical effective charges. However, more importantly, Hamamoto and collaborators [63] showed that for nuclei far away from the valley of stability the IS GQR carries also an appreciable amount of the IV density due to the neutron (proton) excess, while the calculated IV GQR carries very little IS density. Alongside the discussion of Hamamoto, Du Rietz and colleagues [64] observed also that

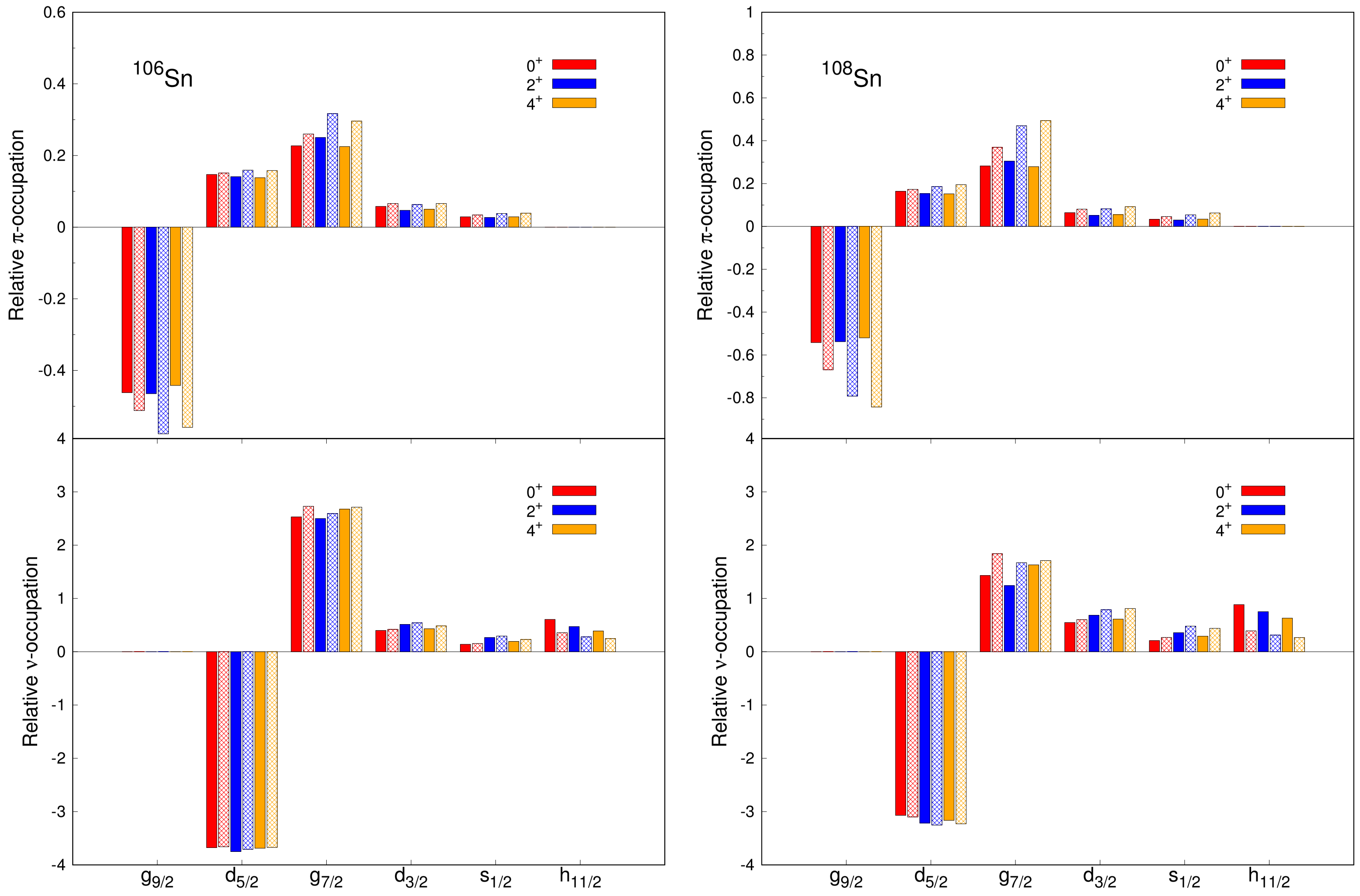

Figure 6.6.: Relative occupation numbers of protons (top) and neutrons (bottom) for the 0^+, 2^+ and 4^+ states of ^{106,108}Sn, given with respect to the occupation numbers of ^{106}Sn (left), i.e. $\pi : (g_{9/2})^{10}(d_{5/2})^0(g_{7/2})^0(d_{3/2})^0(s_{1/2})^0$, $\nu : (g_{9/2})^{10}(d_{5/2})^6(g_{7/2})^0(d_{3/2})^0(s_{1/2})^0(h_{11/2})^0$, and to the ones of ^{108}Sn (right), i.e. $\pi : (g_{9/2})^{10}(d_{5/2})^0(g_{7/2})^0(d_{3/2})^0(s_{1/2})^0$, $\nu : (g_{9/2})^{10}(d_{5/2})^6(g_{7/2})^2(d_{3/2})^0(s_{1/2})^0(h_{11/2})^0$. The theoretical predictions are given by the LSSM calculations, considering a ^{80}Zr core. The hatched colors represents the full-seniority predictions, while the solid ones are given by the truncated seniority calculation.

in the mirror nuclei ^{51}Fe-^{51}Mn effective charges with a considerable isovector polarisation charge were necessary in order to describe the experimental transition probabilities.
These two effects, the partial truncation of the $0\hbar\omega$ valence space and the possibility to have an isovector component in the effective charges for neutron-deficient nuclei, could explain the observation that non-canonical effective charges are needed in the neutron deficient Sn region in order to explain the trend observed experimentally in the $B(E2; 2^+ \rightarrow 0^+)$. *Ad pleniorem scientiam*, this question deserves further experimental and theoretical efforts.

In conclusion, the work presented in this thesis has underlined the importance of the transition strengths for the understanding of the degrees of freedom necessary to describe properly the nuclei in this region. While the energy of the excited states can be reproduced even considering a ^{100}Sn core (see Figure 6.2), basic nuclear properties, such as the reduced transition probabilities, are more sensitive to the even small components of the wave function. Indeed our results of the $B(E2; 2^+ \rightarrow 0^+)$ values, but especially the $B(E2; 4^+ \rightarrow 2^+)$ for ^{108}Sn clearly show that high seniority components of the wave functions are of extreme importance to define the transition probabilities in this region. Actually the bell shape like behaviour of the $B(E2; 2^+ \rightarrow 0^+)$ in all previous LSSM calculations does not hold any more, and a kink is clearly seen experimentally and theoretically in the $B(E2)$ values when passing from ^{106}Sn ($N = 56$) to ^{108}Sn ($N = 58$). Another important conclusion from our data is related to the compatibility of our experimental $B(E2)$ values with a small isovector component in the effective charges when all the $0\hbar\omega$ excitations in the valence space have been taken into account, but with some truncations in the proton $g_{9/2}$ and neutron $h_{11/2}$ orbitals. A systematic experimental and theoretical study in this region would shed light on the isoscalar and isovector polarization of the core when far away from the stability.

7

Conclusions and Further Perspectives

Transition probabilities, especially $B(E2)$ values, give valuable insights into the nature of nuclear interaction and its evolution with respect to the neutron (N) and proton (Z) numbers; in fact, they are an indicator of the appearing/disappearing of a shell closure or of the presence of areas of deformation. In the neutron-deficient Sn region several studies have been performed to examine the evolution of the $B(E2; 2^+ \to 0^+)$ values as a function of the neutron number, that, when approaching $N = 50$, can help to elucidate the robustness of the proton shell closure in the vicinity of ^{100}Sn. Before this work the reduced transition probabilities have been measured via both safe and relativistic Coulomb excitation measurements. However, because of the difficulties in producing such neutron-deficient nuclei close to the proton drip line, the experimental values suffer from large uncertainties which make the physical interpretation challenging. In addition, despite the theoretical progress describing the atomic nucleus during the last decades, so far it has not been possible to reproduce consistently the trend of the experimental reduced transition probabilities $B(E2; 2^+ \to 0^+)$ in the full Sn chain.

7.1. Conclusions

As mentioned in the introduction, the tin isotopes have a privileged status because they form the longest chain in between two doubly magic nuclei, ^{100}Sn and ^{132}Sn, accessible experimentally. This allows systematic studies of basic nuclear properties from very neutron-deficient $N = Z$ to very neutron-rich nuclei. Since the transition probabilities give particularly valuable insights into the nature of the nuclear interaction, the multipole correlations should be deeply investigated in order to shed light on the nuclear structure in the vicinity of both proton and neutron drip lines.

In order to measure the $B(E2)$ transition strengths in neutron-deficient Sn nuclei, in this thesis a different experimental approach was used with respect to Coulomb excitation, namely Multi-Nucleon Transfer (MNT) reactions, which are a powerful tool for studying low-lying states. More specifically, the lifetimes of both 2_1^+ and 4_1^+ excited states were measured via Recoil Distance Doppler-Shift (RDDS) method in ^{106}Sn and ^{108}Sn. Such results represent the very first direct lifetime measurement of low-lying states in the neutron-deficient Sn region. The experiment discussed in the thesis proves that the combination of

MNT reactions with the RDDS method is an alternative method to obtain precise estimation of the reduce transition probabilities in this region.

From a theoretical point of view it is well known that, despite the proximity to the doubly-magic ^{100}Sn, already the ground state of the investigated Sn isotopes has a fragmented wave function, that is far from the usual textbook examples where the nucleons occupy the orbitals with lowest single particle energy. This means that for neutron-deficient Sn isotopes the naïve description of the 2^+ and 4^+ excited states as $(g_{7/2})^{v=2}$ seniority configurations is not correct. In fact, the experimental reduced transition probabilities cannot be reproduced by the simplistic parabolic trend, typical for one-body even operator such as the $\mathcal{O}(E2)$, as one might expect from the seniority scheme conservation.

Thanks to the lifetime measurement of both 4^+ states in ^{106,108}Sn, it was possible for the first time to determine the $B(E2;4^+ \to 2^+)$ values. From the comparison of this second remarkable result with Large-Scale Shell-Model (LSSM) calculations, the validity of previous theoretical discussions has been questioned. In fact, while the energy of the excited states can be reproduced within the LSSM calculation framework by even considering a ^{100}Sn core, the experimental $B(E2;4^+ \to 2^+)$ values have showed to be really sensitive to the form of the wave function: in fact, in addition to the proton excitation across the $Z = 50$ shell gap, such reduced transition probabilities can be reproduced only by avoiding any seniority truncation. This fact is exceptional because until now all the previous theoretical interpretations have been based on seniority-truncated calculations and they have not been able to reproduce consistently the trend of the experimental $B(E2;2^+ \to 0^+)$ values.

In addition, the theoretical calculations have highlighted the presence of an isovector contribution to the effective charges arising from the polarization of the core. Other experimental and theoretical studies have already observed and predicted that nuclei in the neutron-deficient region might present a significant isovector contribution to the effective charges. However the origin of such polarization is still under discussion and deserves further experimental and theoretical efforts. In fact, on one hand, despite the valence space contained all the $0\hbar\omega$ excitations, the truncation on the $g_{9/2}$ orbitals and the inclusion of the neutron $h_{11/2}$ could imply a departure from the canonical effective charges.

7.2. Future perspectives

The limited combination of stable beams and targets, that one can use in nuclear physics research, restricts the study of nuclei far from the stability valley. However, in the last decades new experimental apparatus have allowed to increase the detection efficiency and/or the selectivity, permitting to investigate more and more exotic species. One example is the state-of-the-art HPGe detector AGATA, whose employment was crucial for the success of the present experiment, and in the near future will move to the Laboratori Nazionali di Legnaro (Legnaro, Italy). There, the coupling of the 2π solid-angle coverage of AGATA detectors with other ancillary detectors, such as magnetic spectrometer (PRISMA [175–177]), charged-particle detectors (EUCLIDES [178], SPIDER [179], TRACE [180], etc.) and neutron detectors (Neutron Wall [181], NEDA [182]) will provide to the physicists unprecedented opportunities in the study of exotic nuclei, even by using stable beams.

Contemporaneously with the arrival of AGATA at Legnaro, the first physics campaign employing radioactive beams will start with the SPES [184–186] project (see Figure 7.1).

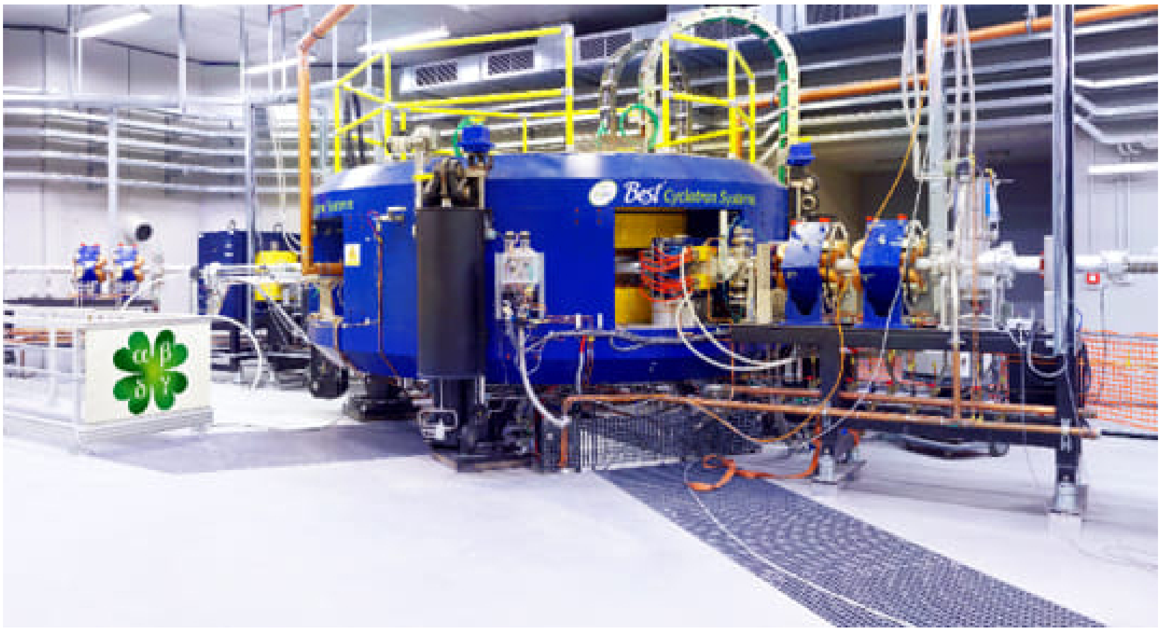

Figure 7.1.: P70 proton cyclotron at the Laboratori Nazionali di Legnaro for the SPES project. The primary proton beam will be accelerated up to the energy of 70 MeV and impinge onto a uranium carbide target, producing several exotic species via proton-induced fission; then, the radioactive nuclei will be reaccelerated by the ALPI super-conductive radio-frequency linear accelerator up to an energy of about 10 MeV/A, to be delivered to the experimental apparata. Taken from Reference [183].

Thanks to the unique capabilities of the new generation detectors and the employment of radioactive beams, many doors will be opened for the investigation of the nuclear structure far from the stability valley. Besides the Laboratori Nazionali di Legnaro, in Europe other radioactive-ion beams facilities exist or are being built, such as HIE-ISOLDE [187, 188] at CERN, SPIRAL2 [189–191] at GANIL and the future FAIR facility [192] at GSI (Darmstadt, Germany). This global trend of investing so much effort in the development of new facilities and new generation experimental setups will pave the way to study new exotic species, that will help in a better understanding the nature of the nuclear interaction.

In addition, as multi-nucleon transfer reactions have been shown to be powerful tools for investigating both neutron-rich and neutron-deficient nuclei, experiments similar to the one discussed in this thesis can be performed in order to study in detail the nucleon-nucleon interaction further away from the valley of stability towards the neutron and proton drip lines. As an example of these new opportunities, Figure 7.2 reports different GRAZING calculations for the production cross section of target-like recoils in multi-nucleon transfer reactions where ^{A}Rb beams impinge onto ^{208}Pb target at the energy $\approx 20\%$ above the Coulomb barrier [193]. The calculations were performed for four different cases: neutron-deficient unstable ^{76}Rb beam, ^{87}Rb stable beam and neutron-rich unstable ^{94,98}Rb beams. In this figure it can be seen that, when using neutron-rich beams, more neutron-rich species

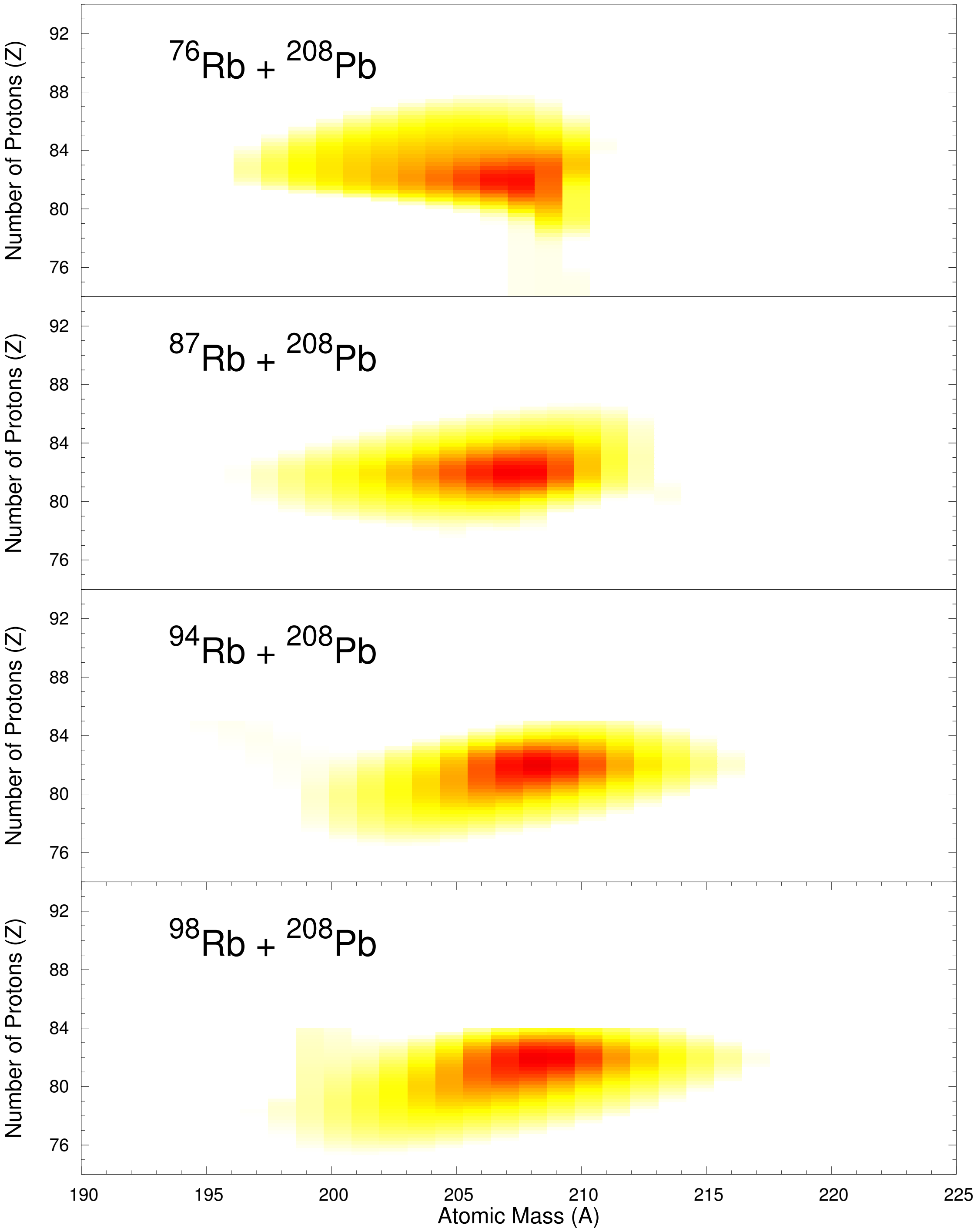

Figure 7.2.: GRAZING code calculations for the production cross sections of target-like nuclei in multi-nucleon transfer reactions as a function of transferred protons and neutrons. The results refer to the collision of Rb isotopes on ^{208}Pb at energies about 20% above the nominal Coulomb barrier. The panels correspond to the heavy binary partner in the reactions: from the top they are ^{76}Rb+^{208}Pb, ^{87}Rb+^{208}Pb, ^{94}Rb+^{208}Pb and ^{98}Rb+^{208}Pb. Taken from Reference [193].

in the region of ^{208}Pb are accessible. Thus, the combination of this reaction mechanism together with the high-intensity radioactive beam and state-of-the-art experimental apparata will push the research to explore new regions of the Segrè chart, that have been not accessible up to now.

A

Optimisation of the Experiment

The aim of the experiment described in this work is to study the $^{106-108}$Sn isotopes via a multi-nucleon transfer reaction, populating these nuclei through $+2p-2n$ and $+2p$ channels, respectively[1]. In order to reach the final goal of the experiment, the setup was carefully optimised. Thus, the beam-target combination was optimised for the present lifetime measurement by choosing a ^{106}Cd beam and a ^{92}Mo target, that will yield the best rates for the nuclei of interest and will allow a good identification of the produced nuclei. The optimisation of the experimental apparatus, such as target and degrader material, beam energy and VAMOS setup, has been made by taking into account several features:

- The energy of the beam-like fragments had to be sufficient to reach the VAMOS focal plane and to allow the identification. In particular, numerical simulations show that the recoils energy should be larger than 3.7 MeV/A at the entrance of the ionization chamber in order to obtain a good resolution of Z.
- The goal of the experiment was to study the low-lying states below an isomer, therefore the beam energy had to be kept as low as possible to limit the feeding of the high-spin states. This request puts an upper limit on excitation energy and consequently on the beam energy.
- The velocity difference, due to the energy loss of the recoils in the degrader, had to be enough to separate the two components of each transition and in particular those of interest. Increasing the degrader thickness, the energy loss would be larger but, on the other hand, also the velocity spread and the parasitic counting rates would increase as well.
- For both AGATA and VAMOS the parasitic counting rate had to be reduced as much as possible. This puts a constraint on the degrader material: taking into account the angular acceptance of VAMOS and the kinematics of the reaction of the beam with the degrader, the fragments should not reach the focal plane.

Some of the listed requests enter in conflict with others, limiting the possible target-degrader materials and the energy of the beam. It is clear that the conditions depend on several parameters all related together, thus the optimisation procedure was repeated several times in order to find the best possible combination of beam, target and degrader. Table A.1 summarises the results coming from the calculations and simulations presented and discussed in the next sections.

---

[1] In the text the reaction channels are defined with respect to the beam, which is the heavy partner.

Beam	^{106}Cd
	770 MeV
Target	^{92}Mo
	0.715 mg/cm^2
Degrader	^{24}Mg
	1.6 mg/cm^2

Table A.1.: The experimental setup was optimised to populate ^{108}Sn isotopes, which correspond to the $+2p-2n$ channels of the proposed multi-nucleon transfer reaction: the beam, target and degrader combination was carefully chosen after simulations.

A.1. Target: material and thickness

In order to maximise the kinetic energy of the beam-like recoils, an inverse-kinematic reaction was chosen. Indeed, for a fixed projectile-target combination and for a defined centre of mass energy $E_i^{c.m.}$, the beam-like reaction products would have more energy than in the case of direct kinematics, because of the transferred momentum during the collision. In Figure A.1 the comparison between the inverse and direct kinematics is presented for the projectile-target combination reported in Table A.1 and for a fixed $E_i^{c.m.}$: the calculations clearly show that in inverse kinematics the ^{108}Sn fragments have the energy that is ≈100 MeV higher than the direct reaction.

Material

In order to build a thin self-supporting target, there are just few possible materials that are lighter than ^{106}Cd: before the alignment with the degrader in the plunger, the material of the target should be enough resistant to support the stretching process. For these reasons, the possible selection was reduced to three metals: ^{58}Ni, ^{90}Zr and ^{92}Mo.

	^{58}Ni	^{90}Zr	^{92}Mo
$+2p$	-4.7 MeV	-5.9 MeV	-3.1 MeV
$+2p-2n$	-7.9 MeV	-13 MeV	-8.1 MeV

Table A.2.: Ground-state to ground-state Q-value for multi-nucleon transfer reaction, populating the $+2p$ and $+2p-2n$ channels that correspond to ^{108}Sn and ^{106}Sn, respectively. The values are reported for the different target-material options.

The choice of the target material was done in order to maximize the cross section of the

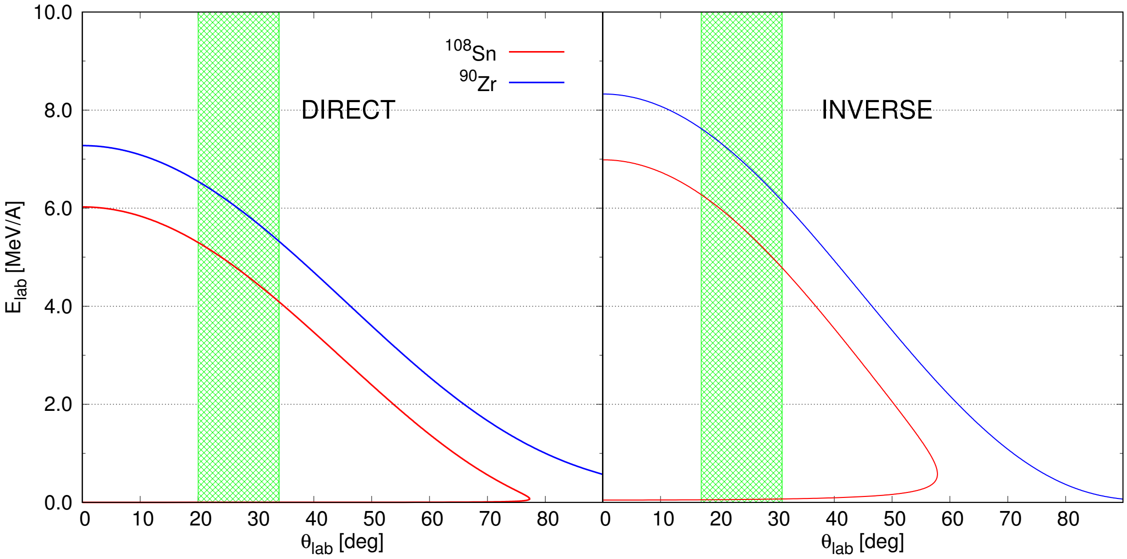

Figure A.1.: Comparison between (left) direct and (right) inverse kinematics for ^{106}Cd+^{92}Mo, fixing $E_i^{c.m.} = 351.5$ MeV. Both ^{108}Sn (red) and its binary partner ^{90}Zr (blue) fly in the direction of the spectrometer. However, for inverse kinematics the ^{108}Sn fragments have the energy that is ≈100 MeV higher than the one produced in the direct reaction, providing a better identification at the ionization chamber. The VAMOS angular acceptance is highlighted in green, placing the spectrometer at the grazing angle.

reaction. As introduced in Chapter 1, Equation 1.19 showed that multi-nucleon transfer cross-section has a cut-off that is proportional to exponential of the difference between the ground-state Q-value Q_{gg} and the optimum Q-value Q_{opt} [194, 195]. In Table A.2 the Q_{gg} is reported for the different target-material options and for the two channels of interest. In first approximation [196, 197] the optimum Q-value, described by Equation 1.20, can be estimated as

$$Q_{opt} = \frac{Z_{pl}Z_{tl} - Z_pZ_t}{Z_pZ_t} E_i^{c.m.} \quad , \tag{A.1}$$

where Z_i is the proton number of *i-th* particle, while *pl*, *tl*, *p* and *t* denote for projectile-like, target-like, projectile and target respectively. The Q_{opt} was calculated for the minimum beam energy E_i that should be sufficient to make the channels of interest reach the IC with 3.7 MeV/A. In Table A.3 the calculated values of the optimum Q-value are summarised for the different target-material options and for the Sn channel.

^{58}Ni	^{90}Zr	^{92}Mo
−8.3 MeV	−3.4 MeV	−2.9 MeV

Table A.3.: Optimum Q-value for different target material, estimated via Equation A.1.

From the comparison between the results reported in the two tables, the ^{58}Ni and ^{92}Mo would be a better target material for populating the channels of interest. In fact the smallest Q-value difference is only 0.2 MeV for both ^{58}Ni and ^{92}Mo in populating ^{106}Sn and ^{108}Sn, respectively. Moreover, according to GRAZING [147] calculation, the integrated cross section of the reaction for the two different targets is the very similar.

Because of some mechanical constraints due to the coupling of the two spectrometer, the relative position of AGATA and VAMOS and their configurations were limited [137]. Considering the minimum beam energy that allows the Sn fragments to reach the IC, the grazing angles with ^{58}Ni and ^{92}Mo target are 17° and 25°, respectively. However, for the grazing angle of ^{106}Cd+^{58}Ni reaction, it was not possible to set AGATA in compact configuration and it would have consequently meant a decrease of the overall γ-ray detection efficiency: from simulations, the efficiency lost was estimated to be 28%. Thus, ^{92}Mo was chosen as target material.

Thickness

Once the target material was defined, its thickness was to be discussed: while on one side a thicker target entails a larger production of the ions of interest, on the other side it causes a worsening of the Q-value experimental resolution.

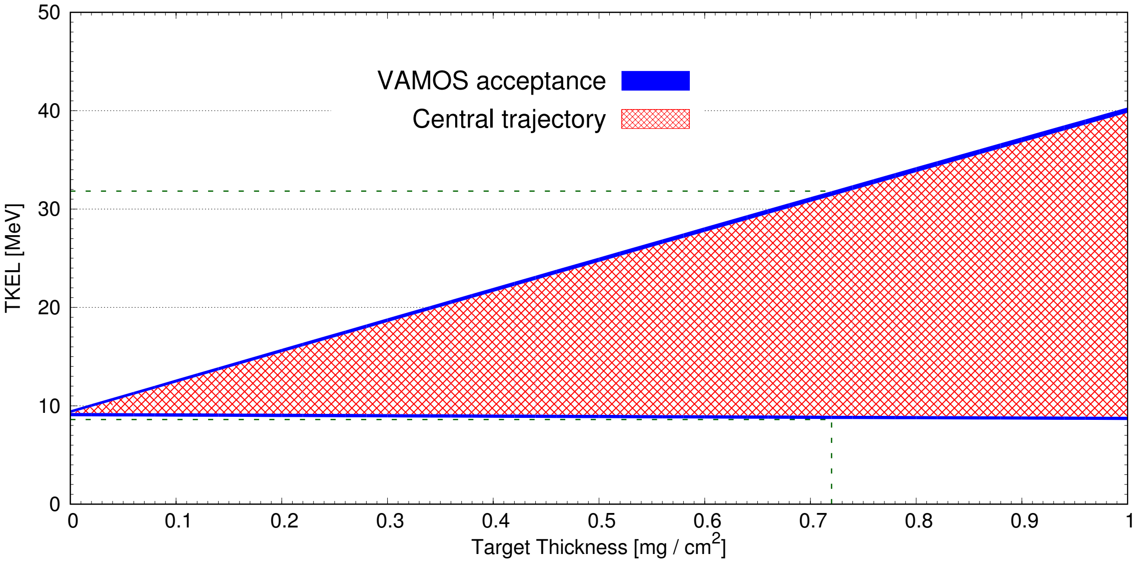

Figure A.2.: Total Kinetic Energy Loss (TKEL) as function of the target thickness, simulated for the central trajectory (red) and taking into account the VAMOS angular acceptance (blue). The TKEL dispersion is estimated considering the difference between the maximum and minimum values. The green dashed lines represent the chosen thickness for the experiment.

In the channel of interest there are transitions with similar energies with respect to the aim of the experiment, thus a good Q-value resolution is a key point to control the feeding from higher-lying states [98]. For this reason the target thickness was optimised by focusing the attention on the Q-value resolution.

In Chapter 4 the Q-value reconstruction of the reaction is deeply discussed. For this discussion the Q-value was calculated with Equation 4.9, that is written as [153]

$$Q = \frac{m_{tl} + m_{bl}}{m_{tl}} E_{bl} - \frac{m_{tl} - m_b}{m_{tl}} E_{reac} - \frac{2}{m_{tl}} \sqrt{m_b \, m_{bl} \, E_{reac} \, E_{bl}} \; cos\theta_{bl} \quad , \tag{A.2}$$

where m_t, m_{tl} and m_{bl} are the target, the target-like and beam-like masses respectively, E_{bl} is the detected energy of the beam-like fragments, E_{reac} is the beam energy at the reaction point, while θ_{bl} is the angle of the beam-like ion with respect to the beam direction.

In order to estimate the Q-value resolution as function of the target thickness, the Total Kinetic Energy Loss (TKEL= $-Q$) was calculated with Equation 4.9 for a beam energy of 750 MeV by simulating the reaction taking place at the beginning, at the centre and at the end of the target with RangeLibC++ [152]. In Figure A.2 the result of the simulation is shown: in red only the central trajectory was take into account, while in blue all the possible trajectories in agreement with the VAMOS acceptance.

As introduced before, the dispersion increases with the target thickness. Thus, the thickness had to be a compromise between the statistics and the possible selectivity, which is useful to control the feeding from higher-lying states. For this reason the target thickness was chosen to be around 0.7 mg/cm^2.

A.2. Degrader: material and thickness

As introduced in Chapter 2, in RDDS method the degrader reduces the velocity of the recoils and it allows to have for each γ-ray transition two components, whose areas are related to the lifetime of the state. Thus, the choice of both material and thickness has to maximise the energy separation between the two components, while reducing as much as possible the rates due to the reactions between the ^{106}Cd beam and the degrader. These two constraints are in conflict: a thicker degrader would increase the separation between the γ-ray transition components, but at the same time would increase the number of reactions in the degrader and emitted γ rays.

Material

For the same reason as for the target optimisation, the degrader material should be lighter than the beam in order to reduce the parasitic counting rate. On one side, for a fixed energy loss of the beam-like fragments, lighter materials entail thicker foils with a larger number of atoms (causing higher rate of beam-degrader interactions) [198]. On the other, the VAMOS spectrometer would stop most of the degrader-like reaction products because of their very different magnetic rigidity with respect to the channels of interest. Thus, even with a large number of emitted γ rays, those event would be rejected by requiring a particle-γ coincidence condition, because of the Bρ acceptance of VAMOS.

Moreover, in order to obtain a planar surface and to allow the capacitance feedback of the plunger, the degrader material should be stretchable and preferably metallic. Obviously the Coulomb-excitation lines of the material should be far from the transitions of interest in order to avoid superposition of the γ-ray peaks. Thus, the possible selection was reduced to four metals: ^{24}Mg, ^{45}Sc, ^{93}Nb and ^{92}Mo.

However, during lifetime experiments via RDDS method the target and degrader material should be obviously different in order to avoid the reaction of interest to take place on the

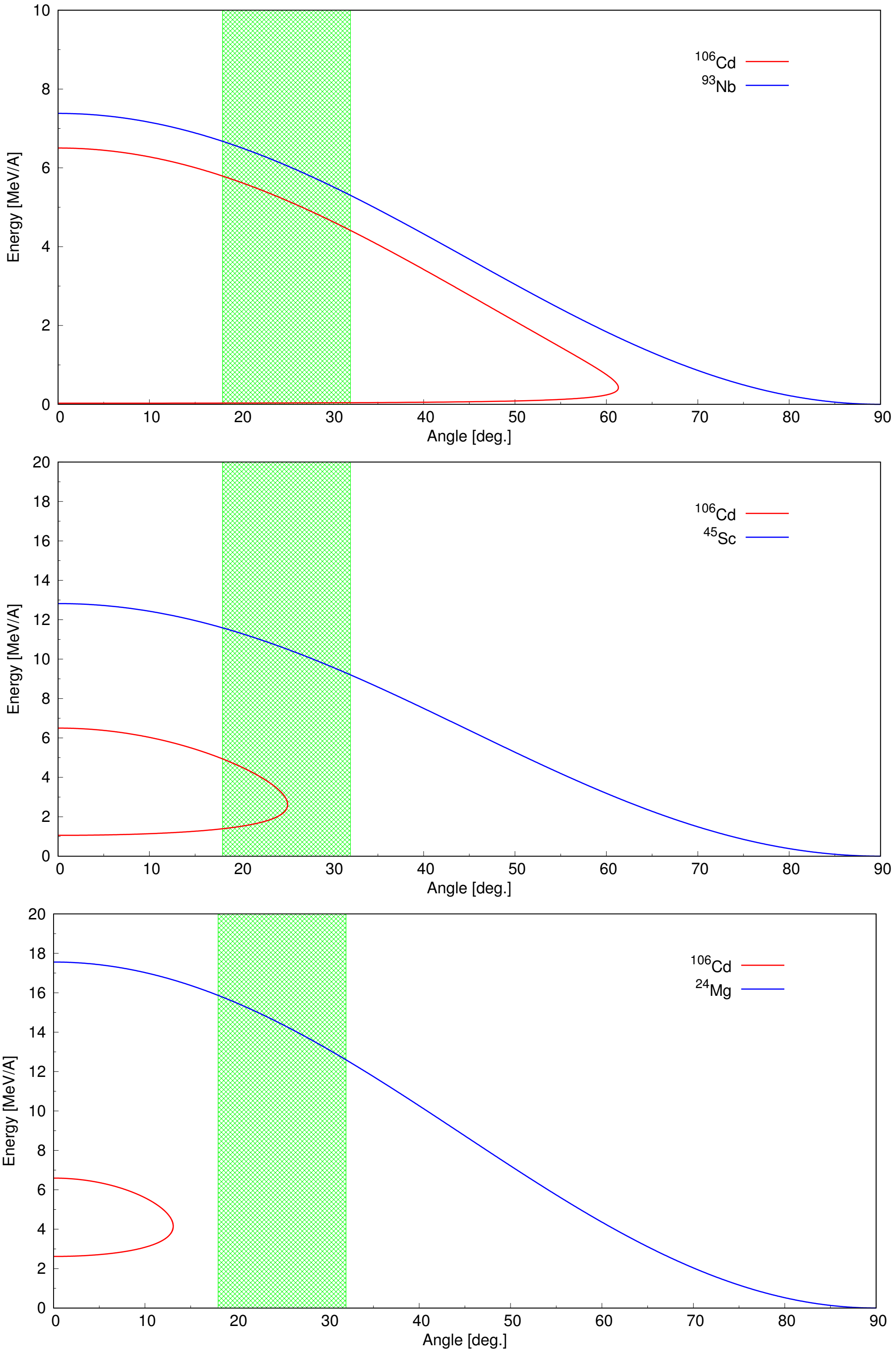

Figure A.3.: Beam (red) and degrader (blue) energy as function of the ion angle with respect to the beam-line direction, showing the VAMOS angular acceptance (gree). By using 2.9 mg/cm^2 of ^{93}Nb (top) and 2.3 mg/cm^2 of ^{45}Sc (middle), both beam and degrader ions reach the entrance MWPC; on the other hand, using 1.95 mg/cm^2 of ^{24}Mg, only degrader ions reach the spectrometer but at the same time their velocity would be very different from the beam-like one, allowing to reject the whole VAMOS event. The kinematics of the reaction is simulated with the software LISE++.

degrader foil. In addition to this, the employment of different material for target and degrader allows to take under control the status of the two foils during the experiment.

The degrader material was selected in order to reduce as much as possible the parasitic counting rate, caused by the reaction of the beam with the degrader itself. Then, the kinematic of the reaction was simulated for the three materials with the software LISE++ [143–146], by considering a thickness that would reduce the ^{108}Sn velocity by $\Delta\beta = 1\%$. As it is presented in Figure A.3, by using ^{93}Nb (2.9 mg/cm^2) or ^{45}Sc (2.3 mg/cm^2), both the degrader and beam ions would reach the entrance MWPC and most of them would also reach the IC. On the other hand, with ^{24}Mg (1.95 mg/cm^2) the reaction is so asymmetric that the beam ions would not reach the VAMOS entrance detector. Thus, according to these simulations, even if the ^{24}Mg foil contains a number of atoms that is twice the ones of the other materials, the detected γ ray would not be in coincidence with VAMOS.

Thus, ^{24}Mg was chosen as degrader material.

Thickness

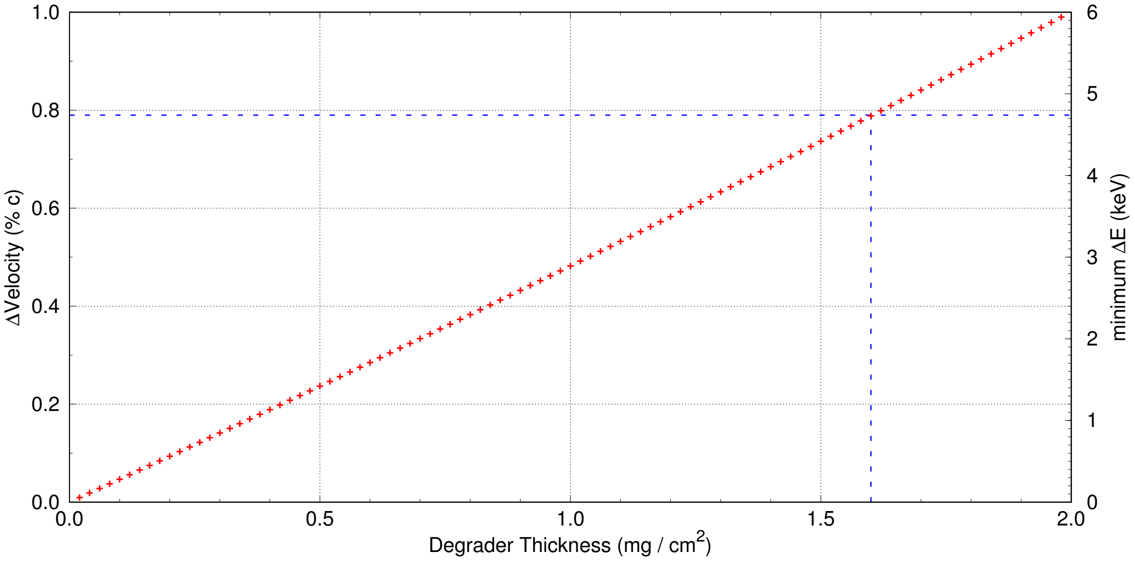

Figure A.4.: Recoil velocity difference as function of the ^{24}Mg degrader thickness. The y-axis on the right shows the minimum energy separation between the two components for the transition $2^+ \rightarrow 0^+$ of ^{108}Sn, taking into account the compact configuration of AGATA.

The degrader thickness directly depends on the energy separation between the two components of each γ-ray transition. While on one side a thicker degrader allows to clearly identify the two components, on the other side the energy loss should be compensated by increasing the beam energy that may entail a larger population of high-lying states with respect to those of interest. Moreover, even if Figure A.3 shows that ^{24}Mg would not be identified inside the spectrometer, the huge number of emitted γ rays (the number of atoms in the degrader is almost 10 times larger than those in the target) can still be randomly in coincidence with other detected particles, increasing the background.

In previous experiments, it has been proven that the AGATA in-beam energy resolution is around 5 keV at 1332 keV, as shown in Chapter 4. Thus, it was decided that the minimum energy separation should be approximately equal to the energy resolution. For the channels of interest the energy loss inside the degrader and the consequent velocity decrease was simulated as function of the material thickness with RangeLibC++. In Figure A.4 the trend of the velocity difference is presented; moreover, accounting the position of the AGATA detectors when the array is in compact configuration, the energy separation between the two components was estimated for the transition of interest in ^{108}Sn ($E_{2^+\rightarrow 0^+}$ = 1206.1 keV). For the chosen energy separation limit, the degrader thickness was chosen to be around 1.6 mg/cm^2.

A.3. Beam: energy

In the previous sections it has been underlined that the energy of the beam-like recoils had to be sufficient to reach the VAMOS focal plane: according to simulations, in order to have a good resolution of Z in the ionization chamber, the recoils energy should be more than 3.7 MeV/A. However, if the beam energy is too high, high-lying states might be populated failing the aim of the experiment: as it is discussed in Chapter 5, the nuclei of the studied region have a low-lying isomers so, if the excitation energy is too high, all the feeding might ends up in the isomer and therefore none of the states below the isomer would be directly populated. This condition would make the lifetime measurement impossible for the states of interest, as it happens in fusion-evaporation reaction (see Chapter 1).

Starting from the Z-identification constraint, the travel of the recoils inside VAMOS was simulated via both LISE++ and RangeLibC++: considering their energy loss inside all the detectors (gas, Mylar foils, etc.) described in Chapter 2, the energy of ^{108}Sn ions should be larger than 4 MeV/A at the entering into the MWPC. The same simulations confirmed that minimum beam energy, which allows the identification of Sn nuclei inside the IC, is 750 MeV.

In order to perform the experiment in safe conditions, the energy of the beam was chosen to be 20 MeV larger than the estimated value. Thus, a ^{106}Cd beam at 770 MeV was required[2] for the experiment.

---

[2] As discussed in Chapter 4, the beam energy was not enough for a clear identification of the fragments atomic number. In fact, just before the performed experiment the new VAMOS entrance detector (see Chapter 2) was mounted, so the energy loss of the fragments inside the spectrometer was underestimated.

B

Tracking Optimisation

In Chapter 2 the features of AGATA tracking algorithms were presented, underlining the necessity of optimising the performances according to the goal of the experiment. For this thesis OFT algorithm was used in the identification of the γ-ray path inside the array and the meaning of the three empirical parameters was described in Chapter 3.

This appendix focus on the graphs linked to the tracking parameters optimisation. The values of the three parameters were optimised in order to maximise at the same time both Peak-to-Total ratio (P/T) and tracking efficiency. Moreover, as explained in Chapter 3, it has been chosen to improve the tracking capabilities for the 1332 keV transition of ^{60}Co source, because the transitions of interest have an energy ranging between 900 and 1300 keV [101, 102, 131].

As the low-energy γ rays are mostly detected by photoelectric effect, in Figure B.1 the P/T ratio is almost constant for the 121 keV transition. On the other hand larger effects can be observed for the 1332 keV case: a small value of SigmaTheta, in fact, may exclude useful points from the clustering, treating these events as background. The rejection of such events has effect on both P/T and tracking efficiency. Therefore, the value of SigmaTheta was defined as the beginning of the *plateau* of the two variables.

The parameter MinProbSing sets a threshold in the energy acceptance for the single events, so that below this threshold all the low energy events are rejected by the figure of merit. However, while the figure of merit rejects more background events and improves the P/T with the threshold increasing, also good event are discarded as well. This behaviour can be observed in Figure B.2. For this reason the value of MinProbSing should be as low as possible and it was chosen to maximise the tracking efficiency at 1332 keV.

In the investigation of the optimal MinProbTrack value, the dependence of both P/T and tracking efficiency is less evident than the previous cases, as it is shown in Figure B.3. Moreover, while on one side the P/T slightly increases with MinProbTrack, on the other the efficiency has the opposite trend. Thus, the value of MinProbTrack was chosen by multiplying P/T by the tracking efficiency and then selecting the maximum.

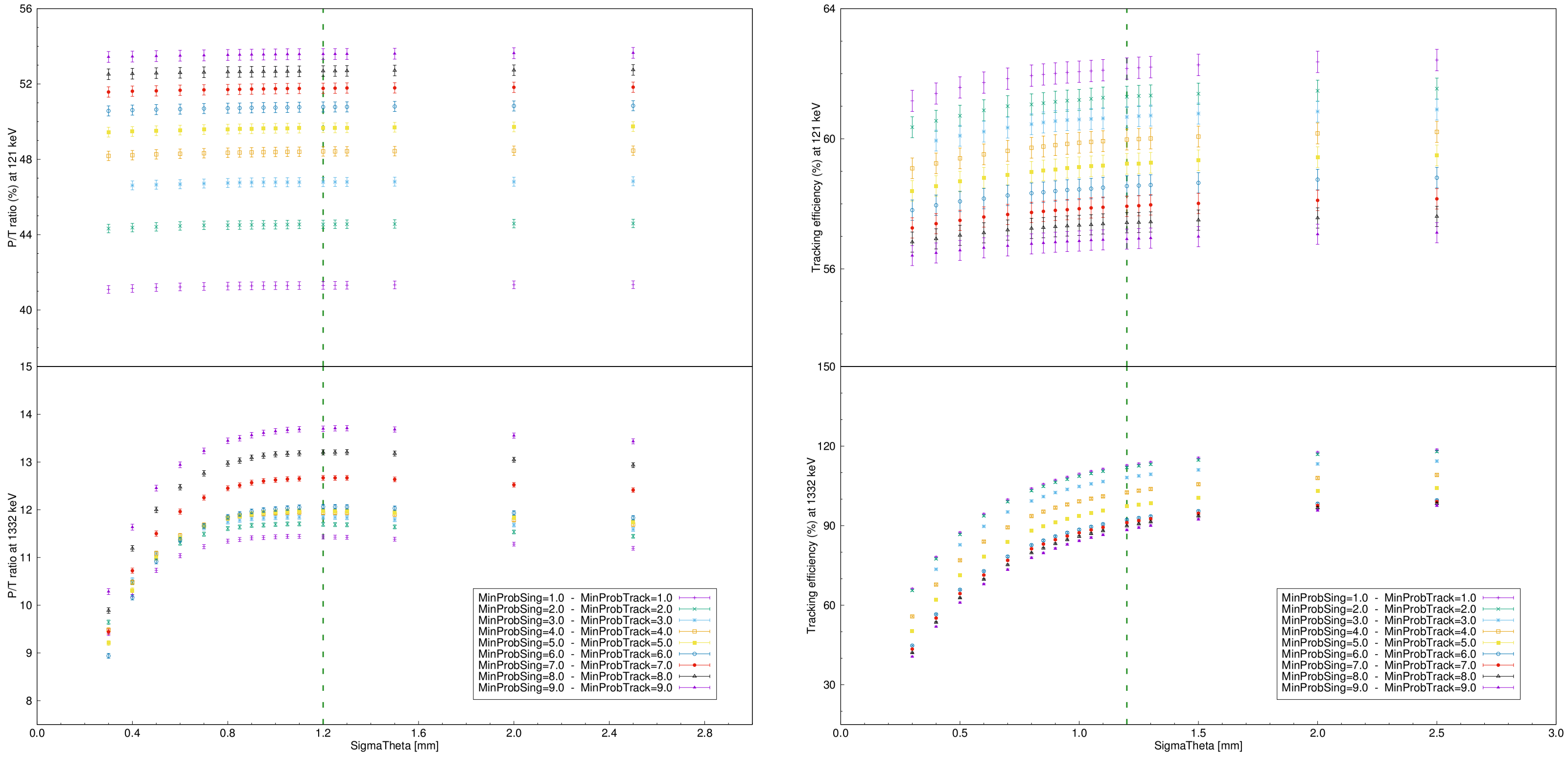

Figure B.1.: Tracking optimisation for OFT algorithm: SigmaTheta. (left) Peak-to-Total ratio (P/T) and (right) tracking efficiency as function of SigmaTheta for several combinations of the other two parameters. The tracking efficiency is defined as the ratio between the area measured with the tracking and the one without the tracking. Both P/T and efficiency are estimated at (top) 121 keV transition of ^{152}Eu and (bottom) 1332 keV of ^{60}Co. The green dashed line represents the optimal value of the parameter, chosen at the beginning of the plateau of both P/T and tracking efficiency.

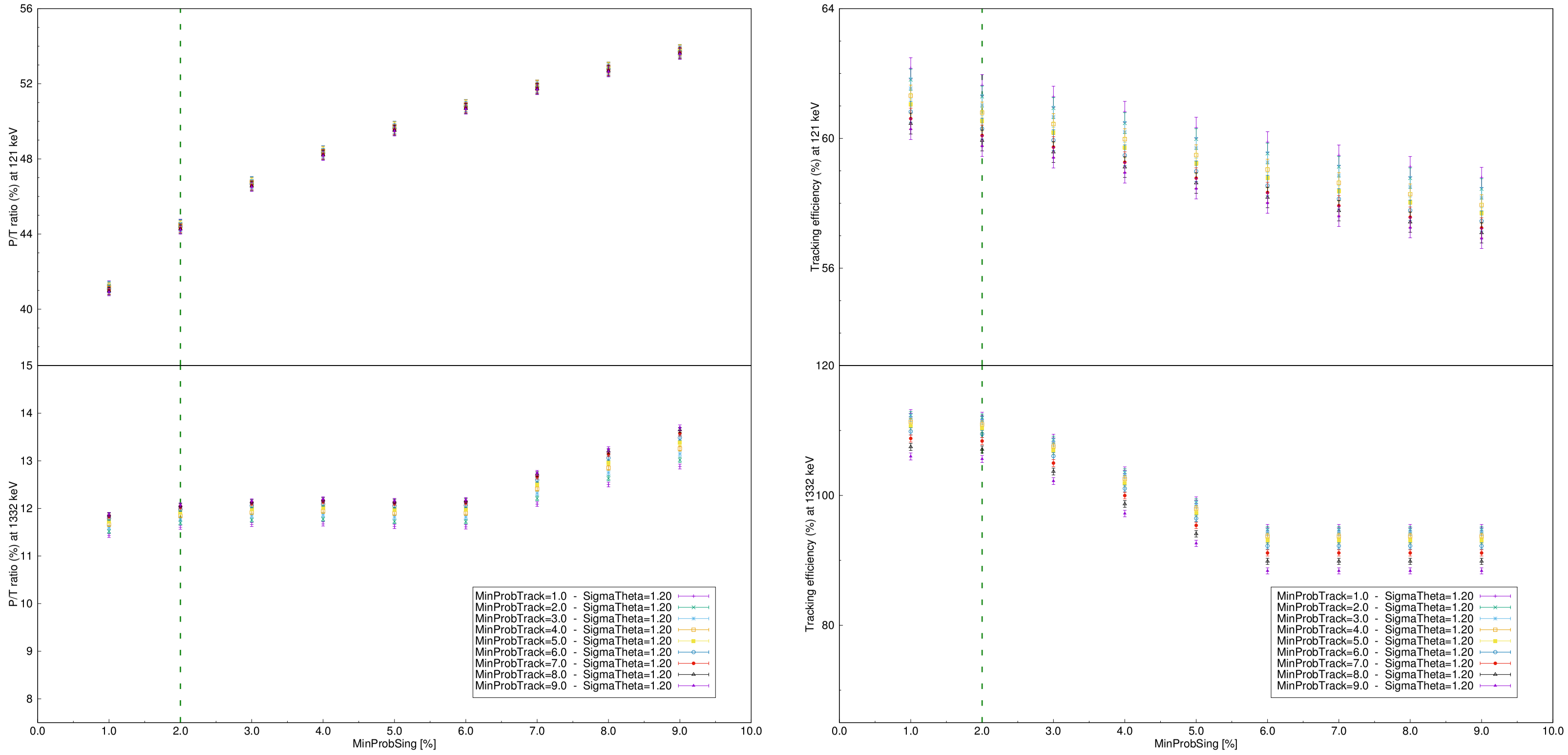

Figure B.2.: Tracking optimisation for OFT algorithm: MinProbSing. (left) Peak-to-Total ratio (P/T) and (right) tracking efficiency as function of MinProbSing for several combinations of the other two parameters. The tracking efficiency is defined as the ratio between the area measured with the tracking and the one without the tracking. Both P/T and efficiency are estimated at (top) 121 keV transition of ^{152}Eu and (bottom) 1332 keV of ^{60}Co. The green dashed line represents the optimal value of the parameter, chosen at the maximum tracking efficiency.

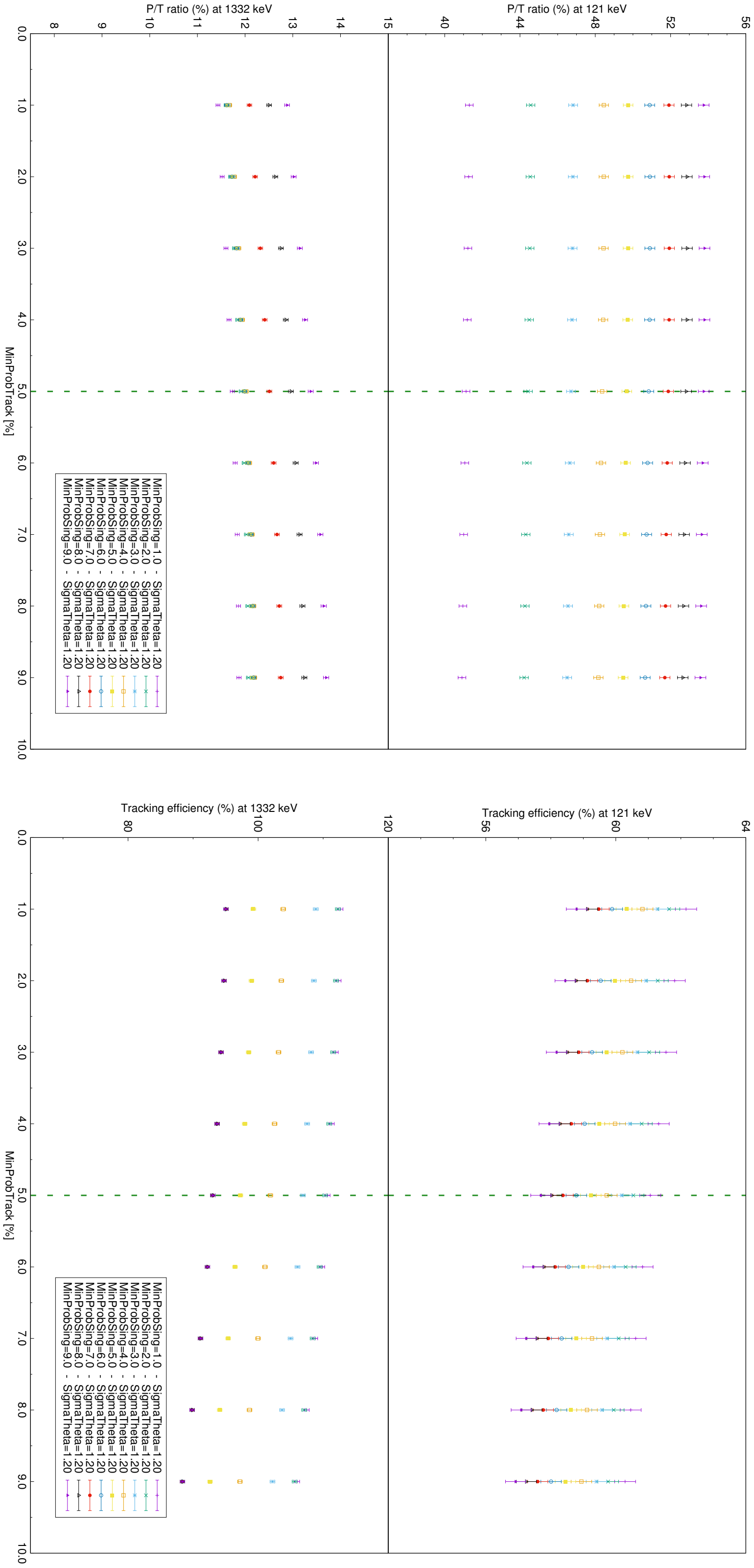

Figure B.3.: Tracking optimisation for OFT algorithm: MinProbTrack. (left) Peak-to-Total ratio (P/T) and (right) tracking efficiency as function of MinProbTrack for several combinations of the other two parameters. The tracking efficiency is defined as the ratio between the area measured with the tracking and the one without the tracking. Both P/T and efficiency are estimated at (top) 121 keV transition of ^{152}Eu and (bottom) 1332 keV of ^{60}Co. The green dashed line represents the optimal value of the parameter.

After the description of the optimisation procedure of the tracking parameters, it is worth mentioning what arises from the P/T ratios reported in the figures. These values are indeed much lower than the nominal one [103] or what expected from Compton-suppressed HPGe arrays, whose typical values are around $50-65\%$[1]. Because of the very busy AGATA campaign in GANIL, the reaction chamber was really activated by previous experiments and the time requested to reduce the activity to standard rates was too long. In fact, during the AGATA calibration runs which took place just before the beginning of the experiment, the rates of the background were around 2.5-3.5 kHz per crystal. Because of this large and not-uniform background, there is a bias in the evaluation of the P/T ratio, whose value is much lower than expected. However, despite of the presence of this bias, the described procedure for the optimisation of the tracking is still valid: the OFT algorithm has been proven effectively to reconstruct the path of the γ-ray, that were emitted not only by the radioactive sources, but also by the activated target chamber.

---

[1] P/T ratio is strongly dependent on the γ-ray multiplicity, so for the reported value the multiplicity is implicitly considered below 10.

Bibliography

[1] K. H. Maier and M. Rejmund. *Shell model interaction between proton holes and between proton holes and neutron particles around* ^{208}*Pb*. European Physical Journal A 14, 349 (2002).

[2] A. Sonzogni et al. *Nudat 2* (2016).

[3] R. F. Casten. *Nuclear structure from a simple perspective* (Oxford University Press Oxford, 2000).

[4] B. Bounthong. *Calculs microscopiques pour les noyaux exotiques de masse moyenne et lourde*. Ph.D. thesis, Université de Strasbourg (2016).

[5] J. Suhonen. *From nucleons to nucleus: concepts of microscopic nuclear theory* (Springer Science & Business Media, 2007).

[6] S. Bacca. *Structure models: from shell model to ab initio methods - A brief introduction to microscopic theories for exotic nuclei*. European Physics Journal Plus 131, 107 (2016).

[7] M. Mayer-Goeppert. *Nuclear configurations in the spin-orbit coupling model. I. Empirical evidence*. Physical Review 78, 16 (1950).

[8] M. Mayer-Goeppert. *Nuclear configurations in the spin-orbit coupling model. II. Theoretical considerations*. Physical Review 78, 22 (1950).

[9] M. Mayer-Goeppert and J. H. D. Jensen. *Elementary theory of nuclear shell structure* (Wiley, 1964).

[10] A. Bohr and B. Mottelson. *Nuclear structure: nuclear deformations*, volume 2 (World Scientific, 1998).

[11] E. Caurier, G. Martinez-Pinedo, F. Nowacki, A. Poves and A. P. Zuker. *The shell model as a unified view of nuclear structure*. Reviews of Modern Physics 77, 427 (2005).

[12] R. B. Wiringa and S. C. Pieper. *Evolution of nuclear spectra with nuclear forces*. Physical Review Letters 89, 182501 (2002).

[13] E. A. McCutchan, C. J. Lister, R. B. Wiringa, S. C. Pieper, D. Seweryniak, J. P. Greene et al. *Precise electromagnetic tests of ab-initio calculations of light nuclei: states in* ^{10}*Be*. Physical Review Letters 103, 192501 (2009).

[14] T. Otsuka, T. Suzuki, J. D. Holt, A. Schwenk and Y. Akaishi. *Three-body forces and the limit of oxygen isotopes.* Physical Review Letters 105, 032501 (2010).

[15] A. P. Zuker. *Three-body monopole corrections to realistic interactions.* Physical Review Letters 90, 042502 (2003).

[16] J. D. Holt, T. Otsuka, A. Schwenk and T. Suzuki. *Three-body forces and shell structure in calcium isotopes.* Journal of Physics G 39, 085111 (2012).

[17] W. A. Richter, M. G. Van der Merwe, R. E. Julies and B. A. Brown. *New effective interactions for the 0f1p shell.* Nuclear Physics A 523, 325 (1991).

[18] B. A. Brown and B. H. Wildenthal. *Status of the nuclear shell model.* Technical report, National Superconducting Cyclotron Laboratory and Department of Physics and Astronomy, Michigan State University (1988).

[19] R. V. Mau. *Mesons in nuclei*, volume 1 (North-Holland, Amsterdam, 1979).

[20] R. Machleidt, K. Holinde and C. Elster. *The Bonn meson-exchange model for the nucleon-nucleon interaction.* Physics Reports 149, 1 (1987).

[21] R. B. Wiringa, V. G. J. Stoks and R. Schiavilla. *Accurate nucleon-nucleon potential with charge-independence breaking.* Physical Review C 51, 38 (1995).

[22] K. A. Brueckner and D. Goldman. *Single particle energies in the theory of nuclear matter.* Physical Review 117, 207 (1960).

[23] K. A. Brueckner, J. L. Gammel and J. T. Kubis. *Calculation of single-particle energies in the theory of nuclear matter.* Physical Review 118, 1438 (1960).

[24] R. Machleidt and D. R. Entem. *Chiral effective field theory and nuclear forces.* Physics Reports 503, 1 (2011).

[25] D. R. Entem and R. Machleidt. *Accurate charge-dependent nucleon-nucleon potential at fourth order of chiral perturbation theory.* Physical Review C 68, 041001 (2003).

[26] S. Weinberg. *Three-body interactions among nucleons and pions.* Physics Letters B 295, 114 (1992).

[27] U. Van Kolck. *Few-nucleon forces from chiral Lagrangians.* Physical Review C 49, 2932 (1994).

[28] S. N. Yang and W. Glöckle. *Three-body mesonic retardation effect.* Physical Review C 33, 1774 (1986).

[29] S. A. Coon and J. L. Friar. *Pionic retardation effects in two-pion-exchange three-nucleon forces.* Physical Review C 34, 1060 (1986).

[30] M. Dufour and A. P. Zuker. *Realistic collective nuclear Hamiltonian.* Physical Review C 54, 1641 (1996).

[31] G. Hagen, M. Hjorth-Jensen, G. R. Jansen, R. Machleidt and T. Papenbrock. *Continuum effects and three-nucleon forces in neutron-rich oxygen isotopes.* Physical Review Letters 108, 242501 (2012).

[32] G. Hagen, M. Hjorth-Jensen, G. R. Jansen, R. Machleidt and T. Papenbrock. *Evolution of shell structure in neutron-rich calcium isotopes.* Physical Review Letters 109, 032502 (2012).

[33] E. Caurier and F. Nowacki. *Present status of shell model techniques.* In *Acta Physica Polonica B* (1999), volume 30, p. 705.

[34] E. Caurier and G. Martínez-Pinedo. *Frontier of shell model calculations.* Nuclear Physics A 704, 60 (2002).

[35] C. Lanczos. *An iteration method for the solution of the eigenvalue problem of linear differential and integral operators* (United States Governm. Press Office Los Angeles, CA, 1950).

[36] J. J. Ressler, R. F. Casten, N. V. Zamfir, C. W. Beausang, R. B. Cakirli et al. *Transition from the seniority regime to collective motion.* Physical Review C 69, 034317 (2004).

[37] P. Van Isacker. *Partial conservation of seniority in nuclei.* International Journal of Modern Physics E 20, 191 (2011).

[38] I. Talmi. *Simple models of complex nuclei*, volume 7 (CRC Press, 1993).

[39] R. Bass. *Nuclear reactions with heavy ions*, volume 11 (Springer, 1980).

[40] G. R. Satchler. *Introduction to nuclear reactions* (Springer, 1990).

[41] R. A. Broglia and A. Winther. *Heavy ion reactions* (Benjamin-Cummings, 1991).

[42] K. Rehm. *Quasi-elastic heavy-ion collisions.* Annual Review of Nuclear and Particle Science 41, 429 (1991).

[43] K. Bethge, G. Walter and B. Wiedemann. *Kernphysik: eine Einführung* (Springer-Verlag, 2008).

[44] K. Alder, A. Bohr, T. H. B. Mottelson and A. Winther. *Study of nuclear structure by electromagnetic excitation with accelerated ions.* Review of Modern Physics 28, 432 (1956).

[45] K. Alder, A. Winther and J. L. Gammel. *Electromagnetic excitation: theory of Coulomb excitation with heavy ions.* Physics Today 29, 63 (1976).

[46] A. Winther and K. Alder. *Relativistic Coulomb excitation.* Nuclear Physics A 319, 518 (1979).

[47] T. Glasmacher. *Intermediate-energy Coulomb excitation.* Nuclear Physics A 693, 90 (2001).

[48] L. Corradi, G. Pollarolo and S. Szilner. *Multinucleon transfer processes in heavy-ion reactions.* Journal of Physics G 36, 113101 (2009).

[49] C. H. Dasso, G. Pollarolo and A. Winther. *Systematics of isotope production with radioactive beams.* Physical Review Letters 73, 1907 (1994).

[50] V. E. Oberacker, A. S. Umar and R. Keser. *Microscopic DC-TDHF study of heavy-ion potentials and fusion cross sections.* In *Journal of Physics: Conference Series* (IOP Publishing, 2013), volume 420, p. 012132.

[51] R. Broda. *Private communication.*

[52] D. Montanari. *Reaction dynamics of neutron rich nuclei in Ca isotopes with heavy ions and gamma spectroscopy.* Ph.D. thesis, Universita degli Studi di Milano (2009).

[53] T. Mijatovic. *Study of heavy-ion reactions with large solid angle magnetic spectrometers.* Ph.D. thesis, University of Zagreb (2015).

[54] J. J. Valiente-Dobón. *Gamma-ray spectroscopy of neutron-rich nuclei populated via multinucleon-transfer reactions.* In *Basic Concepts in Nuclear Physics: Theory, Experiments and Applications* (Springer International Publishing, Cham, 2016), volume 182, p. 87.

[55] P. J. A. Buttle and L. J. B. Goldfarb. *Neutron transfer in heavy ion reactions.* Nuclear Physics 78, 409 (1966).

[56] P. Papadakis. *Combining in-beam γ-ray and conversion electron spectroscopy. The SAGE spectrometer.* Ph.D. thesis, University of Liverpool (2010).

[57] M. Siciliano. *Shape coexistence in the neutron-deficient nucleus ^{194}Po: gamma-ray and electron spectroscopic study employing the SAGE spectrometer.* Master's thesis, University of Padova (2013).

[58] U. Jakobsson. *A spectroscopic study of low-lying states in neutron-deficient astatine and francium nuclei.* Ph.D. thesis, University of Jyäskylä (2013).

[59] J. M. Blatt and V. F. Weisskopf. *Theoretical nuclear physics* (Springer Science & Business Media, 2012).

[60] K. S. Krane and D. Halliday. *Introductory nuclear physics* (Wiley New York, 1988).

[61] P. J. Brussaard and P. W. M. Glaudemans. *Shell-model applications in nuclear spectroscopy* (North-Holland Pub. Co., 1977).

[62] B. H. Brandow. *Linked-cluster expansions for the nuclear many-body problem.* Reviews of Modern Physics 39, 771 (1967).

[63] I. Hamamoto, H. Sagawa and X. Z. Zhang. *Quadrupole strength function and core polarization in drip line nuclei.* Nuclear Physics A 626, 669 (1997).

[64] R. du Rietz, J. Ekman, D. Rudolph, C. Fahlander, A. Dewald, O. Möller, B. Saha et al. *Effective charges in the fp shell.* Physical Review Letters 93, 222501 (2004).

[65] A. Gottardo, J. J. Valiente-Dobón, G. Benzoni, R. Nicolini, A. Gadea, S. Lunardi et al. *New isomers in the full seniority scheme of neutron-rich lead isotopes: the role of effective three-body forces.* Physical Review Letters 109, 162502 (2012).

[66] A. Poves, E. Pasquini and A. P. Zuker. *Quasiconfigurations: an approach to effective forces.* Physics Letters B 82, 319 (1979).

[67] L. Meitner, O. Hahn and F. Strassmann. *Über die umwandlungsreihen des urans, die durch neutronenbestrahlung erzeugt werden.* Zeitschrift für Physik 106, 249 (1937).

[68] H. R. Hulme, J. McDougall, R. A. Buckingham and R. H. Fowler. *The photoelectric absorption of γ-rays in heavy elements.* In *Proceedings of the Royal Society of London A* (JSTOR, 1935), volume 149, p. 131.

[69] F. F. Karpeshin, Y. N. Novikov and M. B. Trzhaskovskaya. *Internal conversion in hydrogen-like ions.* Physics of Atomic Nuclei 67, 217 (2004).

[70] M. Rysavỳ and O. Dragoun. *On the reliability of the theoretical internal conversion coefficients.* Journal of Physics G 26, 1859 (2000).

[71] T. Kibédi, T. W. Burrows, M. B. Trzhaskovskaya, P. M. Davidson and C. W. Nestor Jr. *Evaluation of theoretical conversion coefficients using BrIcc.* Nuclear Instruments and Methods in Physics Research A 589, 202 (2008).

[72] T. Kibédi, T. Burrows, M. Trzhaskovskaya, P. Davidson and C. W. Nestor Jr. *BrIcc2.3 website.*

[73] M. J. Berger, J. H. Hubbell, S. M. Seltzer, J. Chang, J. S. Coursey, R. Sukumar, D. S. Zucker and K. Olsen. *XCOM: photon cross-sections database* (2014).

[74] P. Duvauchelle, G. Peix and D. Babot. *Effective atomic number in the Rayleigh to Compton scattering ratio.* Nuclear Instruments and Methods in Physics Research B 155, 221 (1999).

[75] M. Kurudirek and M. Büyükyildiz. *Estimation of effective atomic number in the Rayleigh to Compton scattering ratio using different methods.* Nuclear Instruments and Methods in Physics Research A 820, 80 (2016).

[76] O. Klein and Y. Nishina. *Über die streuung von strahlung durch freie elektronen nach der neuen relativistischen quantendynamik von Dirac.* Zeitschrift für Physik 52, 853 (1929).

[77] M. Wang, G. Audi, F. Kondev, W. Huang, S. Naimi and X. Xu. *The AME2016 atomic mass evaluation (II). Tables, graphs and references.* Chinese Physics C 41, 030003 (2017).

[78] M. Bender, G. F. Bertsch and P. H. Heenen. *Global study of quadrupole correlation effects.* Physical Review C 73, 034322 (2006).

[79] A. Blazhev, M. Gorska, H. Grawe, J. Nyberg, M. Palacz, E. Caurier, O. Dorvaux, A. Gadea, F. Nowacki et al. *Observation of a core-excited $E4$ isomer in ^{98}Cd.* Physical Review C 69, 064304 (2004).

[80] C. B. Hinke et al. *Superallowed Gamow-Teller decay of the doubly magic nucleus* ^{100}*Sn.* Nature 486, 341 (2012).

[81] R. Kumar, P. Doornenbal, A. Jhingan, R. K. Bhowmik, S. Muralithar et al. *Enhanced* $0^+_{g.s.} \to 2^+_1$ *E*2 *transition strength in* ^{112}*Sn.* Physical Review C 81, 024306 (2010).

[82] I. O. Morales, P. Van Isacker and I. Talmi. *Generalized seniority and* $E2$ *transitions in the tin isotopes.* Physics Letters B 703, 606 (2011).

[83] A. Banu, J. Gerl, C. Fahlander, M. Górska, H. Grawe, T. R. Saito, H. J. Wollersheim, E. Caurier, T. Engeland, A. Gniady, M. Hjorth-Jensen, F. Nowacki et al. ^{108}*Sn studied with intermediate-energy Coulomb excitation.* Physical Review C 72, 061305 (2005).

[84] C. Vaman et al. $Z = 50$ *Shell gap near* ^{100}*Sn from intermediate-energy Coulomb excitations in even-mass* $^{106-112}$*Sn isotopes.* Physical Review Letters 99, 162501 (2007).

[85] J. Cederkäll, A. Ekström, C. Fahlander, A. Hurst, M. Hjorth-Jensen et al. *Sub-barrier Coulomb excitation of* ^{110}*Sn and its implications for the* ^{100}*Sn shell closure.* Physical Review Letters 98, 172501 (2007).

[86] A. Ekström, J. Cederkäll, C. Fahlander, M. Hjorth-Jensen et al. $0^+_{gs} \to 2^+_1$ *transition strengths in* ^{106}*Sn and* ^{108}*Sn.* Physical Review Letters 101, 012502 (2008).

[87] P. Doornenbal, P. Reiter, H. Grawe, H. J. Wollersheim et al. *Enhanced strength of the* $2^+_1 \to 0^+_{g.s.}$ *transition in* ^{114}*Sn studied via Coulomb excitation in inverse kinematics.* Physical Review C 78, 031303 (2008).

[88] A. Jungclaus, J. Walker, J. Leske, K. H. Speidel, A. E. Stuchbery, M. East et al. *Evidence for reduced collectivity around the neutron mid-shell in the stable even-mass Sn isotopes from new lifetime measurements.* Physics Letters B 695, 110 (2011).

[89] V. M. Bader, A. Gade, D. Weisshaar et al. *Quadrupole collectivity in neutron-deficient Sn nuclei:* ^{104}*Sn and the role of proton excitations.* Physical Review C 88, 051301 (2013).

[90] G. Guastalla, D. D. Di Julio, M. Górska, J. Cederkäll, P. Boutachkov, P. Golubev, S. Pietri, H. Grawe, F. Nowacki, K. Sieja et al. *Coulomb excitation of* ^{104}*Sn and the strength of the* ^{100}*Sn shell closure.* Physical Review Letters 110, 172501 (2013).

[91] P. Doornenbal, S. Takeuchi, N. Aoi, M. Matsushita, A. Obertelli, D. Steppenbeck, H. Wang et al. *Intermediate-energy Coulomb excitation of* ^{104}*Sn: moderate* $E2$ *strength decrease approaching* ^{100}*Sn.* Physical Review C 90, 061302 (2014).

[92] J. M. Allmond, A. E. Stuchbery, A. Galindo-Uribarri, E. Padilla-Rodal, D. C. Radford et al. *Investigation into the semimagic nature of the tin isotopes through electromagnetic moments.* Physical Review C 92, 041303 (2015).

[93] G. J. Kumbartzki, N. Benczer-Koller, K. H. Speidel, D. A. Torres, J. M. Allmond, P. Fallon et al. $Z = 50$ *core stability in* ^{110}*Sn from magnetic-moment and lifetime measurements.* Physical Review C 93, 044316 (2016).

[94] D. C. Radford et al. *Nuclear structure studies with heavy neutron-rich RIBS at the HRIBF.* In *Nuclear Physics A* (Elsevier, 2004), volume 746, p. 83.

[95] J. M. Allmond, D. C. Radford et al. *Coulomb excitation of* $^{124,126,128}Sn$. Physical Review C 84, 061303 (2011).

[96] R. Broda, C. T. Zhang, P. Kleinheinz, R. Menegazzo, K. H. Maier, H. Grawe, M. Schramm, R. Schubart, M. Lach and S. Hofmann. *Collisions between* ^{106}Cd *and* ^{54}Fe *at 30 MeV above the Coulomb barrier by high resolution* $\gamma - \gamma$ *coincidences.* Physical Review C 49, R575 (1994).

[97] R. Broda. *Spectroscopic studies with the use of deep-inelastic heavy-ion reactions.* Journal of Physics G 32, R151 (2006).

[98] J. J. Valiente-Dobón, D. Mengoni, A. Gadea, E. Farnea, S. M. Lenzi, S. Lunardi, A. Dewald, T. Pissulla, S. Szilner, R. Broda, F. Recchia et al. *Lifetime measurements of the neutron-rich* $N = 30$ *isotones* ^{50}Ca *and* ^{51}Sc*: orbital dependence of effective charges in the* fp *shell.* Physical Review Letters 102, 242502 (2009).

[99] A. Dewald, S. Harissopulos and P. Von Brentano. *The differential plunger and the differential decay curve method for the analysis of recoil distance Doppler-shift data.* Zeitschrift für Physik A 334, 163 (1989).

[100] A. Dewald, O. Möller and P. Petkov. *Developing the Recoil Distance Doppler-Shift technique towards a versatile tool for lifetime measurements of excited nuclear states.* Progress in Particle and Nuclear Physics 67, 786 (2012).

[101] M. Siciliano. *Study of quadrupole correlations in the neutron-deficient Sn and Cd region via lifetimes measurements.* In *Nuovo Cimento C* (APS, 2017), volume 40, p. 84.

[102] M. Siciliano, J. J. Valiente-Dobón, A. Goasduff, D. Bazzacco et al. *Study of quadrupole correlations in N=Z=50 region via lifetime measurements.* In *Acta Physica Polonica B* (2017), volume 48, p. 331.

[103] S. Akkoyun et al. *Agata-advanced gamma tracking array.* Nuclear Instruments and Methods in Physics Research A 668, 26 (2012).

[104] A. Wiens, H. Hess, B. Birkenbach, B. Bruyneel, J. Eberth, D. Lersch, G. Pascovici, P. Reiter and H. G. Thomas. *The AGATA triple cluster detector.* Nuclear Instruments and Methods in Physics Research A 618, 223 (2010).

[105] G. F. Knoll. *Radiation detection and measurement* (John Wiley & Sons, 1979).

[106] F. C. L. Crespi, F. Camera, O. Wieland et al. *A pulse shape analysis algorithm for HPGe detectors.* Nuclear Instruments and Methods in Physics Research A 570, 459 (2007).

[107] M. Descovich, P. Nolan et al. *The position response of a large-volume segmented germanium detector.* Nuclear Instruments and Methods in Physics Research A 553, 512 (2005).

[108] N. Goel, C. Domingo-Pardo, T. Habermann et al. *Characterisation of a symmetric AGATA detector using the γ-ray imaging scanning technique.* Nuclear Instruments and Methods in Physics Research Section A: Accelerators, Spectrometers, Detectors and Associated Equipment 700, 10 (2013).

[109] F. Recchia, D. Bazzacco, E. Farnea, A. Gadea, R. Venturelli et al. *Position resolution of the prototype AGATA triple-cluster detector from an in-beam experiment.* Nuclear Instruments and Methods in Physics Research A 604, 555 (2009).

[110] R. Venturelli and D. Bazzacco. *Adaptive Grid Search as Pulse Shape Analysis Algorithm for γ-Tracking and Results* . Technical report, Laboratori Nazionali di Legnaro (2004).

[111] B. Bruyneel, B. Birkenbach and P. Reiter. *Pulse shape analysis and position determination in segmented HPGe detectors: The AGATA detector library.* The European Physical Journal A 52, 1 (2016).

[112] P. Söderström, F. Recchia, J. Nyberg et al. *Interaction position resolution simulations and in-beam measurements of the AGATA HPGe detectors.* Nuclear Instruments and Methods in Physics Research A 638, 96 (2011).

[113] A. Lopez-Martens, K. Hauschild, A. Korichi, J. Roccaz and J. P. Thibaud. *γ-ray tracking algorithms: a comparison.* Nuclear Instruments and Methods in Physics Research A 533, 454 (2004).

[114] D. Bazzacco. *The Advanced Gamma Ray Tracking Array AGATA.* In *Nuclear Physics A* (2004), volume 746, p. 248.

[115] J. Gerl. *AGATA technical proposal.* Technical report, European Gamma Spectroscopy Community (2001).

[116] H. Savajols et al. *VAMOS: a VAriable MOde high acceptance Spectrometer.* Nuclear Physics A 654, 1027c (1999).

[117] H. Savajols. *VAMOS: A variable mode high acceptance spectrometer for identifying reaction products induced by SPIRAL beams.* Nuclear Instruments and Methods in Physics Research B 204, 146 (2003).

[118] M. Rejmund, B. Lecornu, A. Navin, C. Schmitt et al. *Performance of the improved larger acceptance spectrometer: VAMOS++.* Nuclear Instruments and Methods in Physics Research A 646, 184 (2011).

[119] M. Vandebrouck, A. Lemasson, M. Rejmund, G. Fremont, J. Pancin, A. Navin, C. Michelagnoli, J. Goupil, C. Spitaels and B. Jacquot. *Dual Position Sensitive MWPC for tracking reaction products at VAMOS++.* Nuclear Instruments and Methods in Physics Research A 812, 112 (2016).

[120] S. Pullanhiotan, A. Chatterjee, B. Jacquot, A. Navin and M. Rejmund. *Improvement in the reconstruction method for VAMOS spectrometer.* Nuclear Instruments and Methods in Physics Research B 266, 4148 (2008).

[121] H. Blok, E. A. J. M. Offermann, C. W. De Jager and H. De Vries. *Path reconstruction and resolution improvement in magnetic spectrometers.* Nuclear Instruments and Methods in Physics Research A 262, 291 (1987).

[122] M. Berz, K. Joh, J. A. Nolen, B. M. Sherrill and A. F. Zeller. *Reconstructive correction of aberrations in nuclear particle spectrographs.* Physical Review C 47, 537 (1993).

[123] D. Bazzacco. *Recal - subversion repository.*

[124] B. Bruyneel, P. Reiter, A. Wiens, J. Eberth, H. Hess, G. Pascovici, N. Warr et al. *Crosstalk corrections for improved energy resolution with highly segmented HPGe-detectors.* Nuclear Instruments and Methods in Physics Research Section A: Accelerators, Spectrometers, Detectors and Associated Equipment 608, 99 (2009).

[125] B. Bruyneel, P. Reiter, A. Wiens, J. Eberth, H. Hess, G. Pascovici, N. Warr, D. Weisshaar et al. *Crosstalk properties of 36-fold segmented symmetric hexagonal HPGe detectors.* Nuclear Instruments and Methods in Physics Research A 599, 196 (2009).

[126] D. Bazzacco. *xTalkSort - subversion repository.*

[127] L. S. Darken. *Role of disordered regions in fast-neutron damage of HPGe detectors.* Nuclear Instruments and Methods in Physics Research B 74, 523 (1993).

[128] T. J. Ross. *Neutron damage tests of a highly segmented Germanium detector.* Ph.D. thesis, University of Surrey (2009).

[129] J. N. Anno. *Notes on radiation effects on materials* (Hemisphere Publishing Corporation, Washington, DC, 1984).

[130] B. Bruyneel, B. Birkenbach, J. Eberth, H. Hess, G. Pascovici, P. Reiter, A. Wiens et al. *Correction for hole trapping in AGATA detectors using pulse shape analysis.* The European Physical Journal A 49, 1 (2013).

[131] M. Siciliano, J. J. Valiente-Dobón, A. Goasduff, D. Bazzacco, A. Lopez-Martens et al. *Lifetime measurement in* $Z = N = 50$ *region: optimization of OFT parameters.* Technical report, Laboratori Nazionali di Legnaro (2017).

[132] Z. Kis, B. Fazekas, J. Östör, Z. Révay, T. Belgya, G. L. Molnár and L. Koltay. *Comparison of efficiency functions for Ge gamma-ray detectors in a wide energy range.* Nuclear Instruments and Methods in Physics Research A 418, 374 (1998).

[133] D. C. Radford. *Radware05.*

[134] H. Bethe and J. Ashkin. *Passage of radiation through matter.* In *Experimental Nuclear Physics* (Wiley, NY, 1953).

[135] T. K. Alexander and A. Bell. *A target chamber for recoil-distance lifetime measurements.* Nuclear Instruments and Methods 81, 22 (1970).

[136] S. Saha, Y. K. Agarwal, M. Deshpande and A. Roy. *A method to study heavy ion reactions using position sensitive and Bragg curve spectroscopy detectors.* Nuclear Instruments and Methods in Physics Research A 335, 165 (1993).

[137] E. Clément, C. Michelagnoli, G. de France, H. J. Li, A. Lemasson, C. B. Dejean et al. *Conceptual design of the AGATA 1π array at GANIL.* Nuclear Instruments and Methods in Physics Research A 855, 1 (2017).

[138] A. Lemasson. *Private communication.*

[139] J. A. Winger, B. M. Sherrill and D. J. Morrissey. *INTENSITY: a computer program for the estimation of secondary beam intensities from a projectile fragment separator.* Nuclear Instruments and Methods in Physics Research B 70, 380 (1992).

[140] A. Leon, S. Melki, D. Lisfi, J. Grandin, P. Jardin, M. Suraud and A. Cassimi. *Charge state distributions of swift heavy ions behind various solid targets (*$36 \leq Z_p \leq 92$*, 18 MeV/u* $\leq E \leq$ *44 MeV/u).* Atomic Data and Nuclear Data Tables 69, 217 (1998).

[141] K. Shima, T. Ishihara and T. Mikumo. *Empirical formula for the average equilibrium charge-state of heavy ions behind various foils.* Nuclear Instruments and Methods in Physics Research 200, 605 (1982).

[142] G. Schiwietz and P. Grande. *Improved charge-state formulas.* Nuclear Instruments and Methods in Physics Research B 175, 125 (2001).

[143] O. Tarasov. *LISE++ website.*

[144] D. Bazin, O. Tarasov, M. Lewitowicz and O. Sorlin. *The program LISE: a simulation of fragment separators.* Nuclear Instruments and Methods in Physics Research A 482, 307 (2002).

[145] O. B. Tarasov and D. Bazin. *LISE++: design your own spectrometer.* Nuclear Physics A 746, 411 (2004).

[146] O. B. Tarasov and D. Bazin. *LISE++: radioactive beam production with in-flight separators.* Nuclear Instruments and Methods in Physics Research B 266, 4657 (2008).

[147] A. Winther. *GRAZING.*

[148] K. H. Schmidt, B. Jurado, C. Amouroux and C. Schmitt. *General description of fission observables: GEF model code.* Nuclear Data Sheets 131, 107 (2016).

[149] T. Mijatović, S. Szilner, L. Corradi, D. Montanari, Pollarolo et al. *Multinucleon transfer reactions in the* $^{40}Ar+^{208}Pb$ *system.* Physical Review C 94, 064616 (2016).

[150] D. Mengoni, J. J. Valiente-Dobón, E. Farnea, A. Gadea, A. Dewald and A. Latina. *Lifetime measurements of neutron-rich nuclei around* ^{48}Ca *with the CLARA-PRISMA setup.* The European Physical Journal A 42, 387 (2009).

[151] M. Siciliano, A. Goasduff, J. J. Valiente-Dobón, R. M. Pérez-Vidal et al. *Study of quadrupole correlations in the* $^{106,108}Sn$ *isotopes via lifetimes measurements.* Technical report, Laboratori Nazionali di Legnaro (2016).

[152] R. Yanez. *RangeLibC++.*

[153] A. B. Brown, C. W. Snyder, W. A. Fowler and C. C. Lauritsen. *Excited states of the mirror nuclei,* ^{7}*Li and* ^{7}*Be.* Physical Review 82, 159 (1951).

[154] H. Bateman. *The solution of a system of differential equations occurring in the theory of radioactive transformations.* In *Proceeding of the Cambridge Philosophical Society, Mathematical and Physical Sciences* (1910), volume 15, p. 423.

[155] D. Ward, H. R. Andrews, J. S. Geiger, R. L. Graham and J. F. Sharpey-Schafer. *Lifetimes for levels above the "rotational phase change" in* ^{158}*Er.* Physical Review Letters 30, 493 (1973).

[156] G. Böhm, A. Dewald, P. Petkov and P. Von Brentano. *The differential decay curve method for the analysis of Doppler shift timing experiments.* Nuclear Instruments and Methods in Physics Research A 329, 248 (1993).

[157] M. T. Esat, D. C. Kean, R. H. Spear and A. M. Baxter. *Mass dependence of the static quadrupole moments of the first* 2^+ *states in the cadmium isotopes.* Nuclear Physics A 274, 237 (1976).

[158] N. Boelaert, A. Dewald, C. Fransen, J. Jolie, A. Linnemann, B. Melon, O. Möller, N. Smirnova and K. Heyde. *Low-spin electromagnetic transition probabilities in* $^{102-104}$*Cd.* Physical Review C 75, 054311 (2007).

[159] G. A. Müller, A. Jungclaus, O. Yordanov, E. Galindo, M. Hausmann, D. Kast, K. P. Lieb, S. Brant, V. Krstić, D. Vretenar et al. *High-spin structure and electromagnetic transition strengths in* ^{104}*Cd.* Physical Review C 64, 014305 (2001).

[160] W. Andrejtscheff, M. Senba and Z. Z. Ding. *Multi-Quasiparticle Isomers in Nuclei with* $Z = 50$*.* Bulletin of the American Physical Society 27, DF13 (1982).

[161] M. Hass, H. H. Bertschat, C. Broude, E. Dafni, F. D. Davidovsky, G. Goldring and P. M. S. Lesser. *Mean lives and magnetic moments of high-spin levels in* ^{108}*Sn.* Nuclear Physics A 410, 317 (1983).

[162] T. Ishii, M. Ishii, K. Yanagida and M. Ogawa. *Nuclear Structure of* ^{109}*Sn.* Technical report, International Atomic Energy Agency (1988).

[163] W. Andrejtscheff, L. K. Kostov, P. Petkov, Y. S. Savane, C. Stoyanov, P. von Brentano, J. Eberth, R. Reinhardt and K. O. Zell. *Electric quadrupole transition strengths of the type* $6_1^+ \rightarrow 4_1^+$ *in* $^{106-112}$*Sn.* Nuclear Physics A 505, 397 (1989).

[164] A. Makishima, T. Ishii, M. Nakajima, M. Ogawa and M. Ishii. *Nuclear structure of the yrast* 6^+*,* 10^+ *and* 14^- *states in* ^{106}*Sn.* Zeitschrift für Physik A. 349, 133 (1994).

[165] G. Auger, J. M. Lagrange, M. Pautrat and J. Vanhorenbeeck. *High-spin states in* ^{107}*Sn and* ^{107}*In isotopes.* Nuclear Physics A 426, 109 (1984).

[166] T. Ishii, A. Makishima, K. Koganemaru, Y. Saito, M. Ogawa and M. Ishii. *High-spin states in* ^{107}*Sn.* Zeitschrift für Physik A 347, 41 (1993).

[167] L. Käubler, H. Prade, J. Reif, R. Schwengner, G. Winter, H. Grawe, J. Heese, H. Kluge, K. H. Maier, R. Schubart et al. *In-beam study of* ^{109}*Sn.* Physica Scripta 1995, 266 (1995).

[168] R. S. Chakrawarthy and R. G. Pillay. *High spin states in* ^{109}*Sn.* Physical Review C 54, 2771 (1996).

[169] L. Käubler, H. Schnare, D. B. Fossan et al. *Collective structures and smooth band termination in* ^{109}*Sn.* Zeitschrift für Physik A 356, 235 (1996).

[170] I. Dankó, Z. Dombradi, Z. Gacsi, J. Gulyas, A. Krasznahorkay, N. Sandulescu, J. Blomqvist and R. Liotta. *Low-lying states of* ^{109}*Sn from the* ^{106}*Cd* $(\alpha, n\gamma)$ *reaction.* Nuclear Physics A 646, 3 (1999).

[171] T. Trivedi, P. C. Srivastava, D. Negi and I. Mehrotra. *Shell model description of* $^{102-108}$*Sn isotopes.* International Journal of Modern Physics E 21, 1250049 (2012).

[172] *ANTOINE website.*

[173] F. Nowacki. *Private communication.*

[174] A. P. Zuker, J. Retamosa, A. Poves and E. Caurier. *Spherical shell model description of rotational motion.* Physical Review C 52, R1741 (1995).

[175] A. M. Stefanini, L. Corradi, G. Maron, A. Pisent, M. Trotta, A. Vinodkumar et al. *The heavy-ion magnetic spectrometer PRISMA.* Nuclear Physics A 701, 217 (2002).

[176] G. Montagnoli, A. M. Stefanini, M. Trotta, S. Beghini, M. Bettini, F. Scarlassara, V. Schiavon, L. Corradi et al. *The large-area micro-channel plate entrance detector of the heavy-ion magnetic spectrometer PRISMA.* Nuclear Instruments and Methods in Physics Research A 547, 455 (2005).

[177] S. Beghini, L. Corradi, E. Fioretto, A. Gadea, A. Latina, G. Montagnoli, F. Scarlassara, A. Stefanini, S. Szilner, M. Trotta et al. *The focal plane detector of the magnetic spectrometer PRISMA.* Nuclear Instruments and Methods in Physics Research Section A: Accelerators, Spectrometers, Detectors and Associated Equipment 551, 364 (2005).

[178] D. Testov, A. Goasduff, L. Grassi, D. Mengoni et al. *Light charged particle detector EUCLIDES for the GALILEO campaign.* Technical report, Laboratori Nazionali di Legnaro (2015).

[179] K. Hadyńska-Klek, M. Rocchini, A. Nannini, J. J. Valiente-Dobón, D. Mengoni, D. Testov, B. Melon et al. *SPIDER: a new charge particle detector for the Coulomb excitation studies with GALILEO.* Technical report, Laboratori Nazionali di Legnaro (2016).

[180] D. Mengoni, J. A. Dueñas, M. Assié, C. Boiano, P. R. John et al. *Digital pulse-shape analysis with a TRACE early silicon prototype.* Nuclear Instruments and Methods in Physics Research A 764, 241 (2014).

[181] Ö. Skeppstedt, H. A. Roth, L. Lindström, R. Wadsworth, I. Hibbert, N. Kelsall, D. Jenkins, H. Grawe, M. Górska, M. Moszyński, Z. Sujkowski, D. Wolski, M. Kapusta, M. Hellström, S. Kalogeropoulos, D. Oner, A. Johnson, J. Cederkäll, W. Klamra, J. Nyberg, M. Weiszflog, J. Kay, R. Griffiths, J. Garces Narro, C. Pearson and J. Eberth. *The EUROBALL neutron wall - design and performance tests of neutron detectors.* Nuclear Instruments and Methods in Physics Research A 421, 531 (1999).

[182] T. Hüyük, A. Di Nitto, G. Jaworski, A. Gadea, J. J. Valiente-Dobón, J. Nyberg, M. Palacz, P. A. Söderström, J. R. Aliaga-Varea et al. *Conceptual design of the early implementation of the NEutron Detector Array (NEDA) with AGATA.* The European Physical Journal A 52, 55 (2016).

[183] *Media INAF website.*

[184] *SPES project website.*

[185] A. Andrighetto, L. Biasetto, M. Manzolaro, P. Benetti, S. Carturan, P. Colombo, F. Gramegna, G. Meneghetti, B. Monelli, G. Prete et al. *The SPES project at LNL.* In *American Institute of Physics Conference Proceedings* (AIP Publishing, 2009), volume 1099, p. 728.

[186] G. Prete, A. Andrighetto, J. Esposito, P. Mastinu and J. Wyss. *The SPES project: a second generation ISOL facility.* In *Physics Procedia* (2012), volume 26, p. 274.

[187] E. Kugler. *The ISOLDE facility at the CERN PS Booster.* Nuclear Instruments and Methods in Physics Research B 79, 322 (1993).

[188] A. Herlert. *The ISOLDE facility.* Nuclear Physics News 20, 5 (2010).

[189] *SPIRAL2 project website.*

[190] M. Lewitowicz. *The SPIRAL2 project.* In *American Institute of Physics Conference Proceedings* (American Institute of Physics Publishing, 2007), volume 891, p. 91.

[191] S. Gales. *SPIRAL2 at GANIL: next generation of ISOL facility for intense secondary radioactive ion beams.* Nuclear Physics A 834, 717C (2010).

[192] P. Spiller and G. Franchetti. *The FAIR accelerator project at GSI.* Nuclear Instruments and Methods in Physics Research A 561, 305 (2006).

[193] S. Szilner. *Private communication.*

[194] C. Toepffer. *Q-value dependence of multinucleon transfer reactions.* Physical Review Letters 27, 872 (1971).

[195] A. Y. Abul-Magd, K. El-Abed and M. El-Nadi. *The Q-value dependence of the cross section of heavy ion reactions.* Physics Letters B 39, 166 (1972).

[196] Y. Alhassid, R. D. Levine, J. S. Karp and S. G. Steadman. *Information-theoretic analysis of energy disposal in heavy-ion transfer reactions.* Physical Review C 20, 1789 (1979).

[197] C. Rodríguez-Tajes, F. Farget, X. Derkx, M. Caamaño, O. Delaune, K.-H. Schmidt, E. Clément, A. Dijon, A. Heinz, T. Roger et al. *Transfer reactions in inverse kinematics: An experimental approach for fission investigations.* Physical Review C 89, 024614 (2014).

[198] A. Goasduff, J. J. Valiente-Dobón, S. Lunardi, F. Haas, A. Gadea et al. *Counting rate measurements for lifetime experiments using the RDDS method with the new generation γ-ray array AGATA.* Nuclear Instruments and Methods in Physics Research A 758, 1 (2014).

List of Figures

1.1. Measured excitation energy of the first 2^+ state as a function of the proton and neutron numbers for all the known even-even nuclei. In proximity of the shell closures (black rectangles) the excitation energy rapidly increases. Data taken from Reference [2]. 11

1.2. Schematic drawing of the Hilbert space truncation. Adapted from Reference [4]. 13

1.3. Single-particle levels when the spin-orbit term is added to the harmonic oscillator Hamiltonian. Figure taken from References [9, 10] and then corrected for the erroneous effect of the V_{so} term on the $2s_{1/2}$ orbital. 15

1.4. Hierarchy of the nuclear forces inside the chiral perturbation theory, classified according to the chiral order ν and described as a function of $\left(\frac{Q}{\Lambda_\chi}\right)^\nu$ (see text). Solid and dashed lines represent nucleons and pions, respectively. Small dots, large solid dots, solid squares and solid diamonds denote vertices of interaction index equal to 1, 2, 3 and 4 respectively. Taken from Reference [24]. 19

1.5. Number of non-zero matrix elements (given by the colour axis) considering full $0\hbar\omega$ valence spaces as a function of the proton and neutron numbers. For $N, Z > 40$ ($l = 3$ major shell) the dimensions of the matrices exceed the capacity of standard computers when using the full major shell, illustrating the importance of the space truncation in this region. The rectangles with black outline represents the shell closures. 21

1.6. (Left) Calculated $B(E2; J \to J-2)$ values for seniority conserving (full dots) and non-conserving (open dots) transitions as a function of the fractional filling of the main shell. (Right) Schematic illustration of $B(E2; J \to J-2)$ plotted against $B(E2; 2^+ \to 0^+)$ for seniority- and collectivity-dominated transitions. Figure adapted from Reference [36]. 22

1.7. Classification of heavy-ion collisions as a function of the impact parameter. Figure adapted from Reference [43]. 23

1.8. Microscopic Density-Constrained Time-Dependent Hartree-Fock study of ^{48}Ca+^{132}Sn at the energy $E_{c.m.} = 140$ MeV, showing a contour plot of the mass density at internuclear distance $R = 10.4$ fm. During the formation of the "neck" between the reaction fragments, the nucleons transfer takes place entailing an exchange of mass and momentum. Figure taken from Reference [50]. . . . 25
1.9. (left) Schematic design of the angular momentum transfer in the case of transfer reactions between a target t and a projectile p at energies close to the Coulomb barrier. The angular momenta of the orbiting nucleons of the initial l_i and final state l_f would be perpendicular to the scattering plane and their projections will have opposite sign. (right) Schematic representation of the states populated in the plane excitation energy versus angular momentum degrees of freedom for the two regimes described in the text: small relative velocities ($E_{rel} \ll E_F$) and higher transfer energies ($E_{rel} \approx E_F$). The region of population for fusion-evaporation reactions has been depicted for comparison. Figure adapted from Reference [54]. 27
1.10. Different steps of a fusion-evaporation reaction ending up in the ground state of the newly formed nucleus. The average time scale of each step in case of heavy compound-nucleus formation is indicated. Taken from References [56, 57]. 29
1.11. (a) Schematic illustration of the fusion-evaporation cross-section with respect to the excitation energy of the compound nucleus. The cross section of fusion and fission rises with increasing energy; as the fission cross section becomes more competitive with the increasing excitation energy of the compound nucleus, the fusion-evaporation cross section starts to decrease. As example, the neutron-evaporation channels have been added, while the $2n$ channel is presented by a dashed line as the fusion barrier cuts this exit channel. (b) The de-excitation path to the yrast line of the final nucleus, produced in the entry region through the evaporation of neutrons from the compound nucleus. The $4n$ evaporation channel has been drawn as an example and the arrows from the entry region downward denote emitted γ rays. Taken from Reference [58]. 30
1.12. Diagrams explaining the first-order expansion of the Equation 1.30: because of the emission or absorption of a quantum gamma of character ε and momentum L, a core particle is excited into an unoccupied orbit and creates a particle-hole state; then this $p-h$ states later recombines in a scattering process with the single particle outside the core. Figure adapted from Reference [61]. 33
1.13. Mass absorption coefficient of electromagnetic radiation in germanium ($Z = 32$) as a function of the γ-ray energy. The coloured lines represent the different interaction mechanisms. Data taken from Reference [73]. 36
1.14. Experimental γ-ray energy spectrum for ^{137}Cs radioactive source. The large peak at 662 keV is due to the γ ray emitted after the beta decay of the nucleus, while the little bump at around 480 keV is the *Compton edge* caused by the backward-scattered γ rays that escape from the germanium detector. . 38
1.15. Systematics of the $Z = 50$ proton shell gap as a function of the neutron number. The experimental values are taken from Reference [77]. 40

1.16. Systematics for even-even Sn nuclei of mass numbers between $A = 102$ and $A = 130$ showing the partial level schemes up to the seniority isomers. For neutron-deficient Sn isotopes with $A \leq 112$ the presence of the 6^+ isomer with lifetimes larger than 1 ns suggests the typical seniority for the $(g_{7/2})^{v=2}$ configuration. For heavier Sn isotopes, whose 10^+ states have a long lifetime of the order of few μs, such state can also be identified as a seniority isomer arising from the neutron orbital $(h_{11/2})^{v=2}$. Levels of the same spin and positive parity are connected by dashed lines. Figure adapted from Reference [81]. 41

1.17. Reduced transition probability $B(E2)$ systematics along the whole Sn isotopic chain for (top) $4^+ \rightarrow 2^+$ and (bottom) $2^+ \rightarrow 0^+$ transitions. The “adopted” results for the neutron-rich isotopes are taken from Reference [2], while for the neutron-deficient region the results are taken from References [81, 83–93]. The rapid change in the $B(E2)$ values at $N = 64$ seems to be related to the neutron subshell closure [81]. 42

2.1. Sketch of the GANIL facility. The beams coming from the 5 cyclotrons are distributed in the different experimental area. The experiment described in this work took place in the experimental hall G1, using the VAMOS-AGATA setup. 46

2.2. Design of the geodesic geometry for the 4π solid angle coverage array. The white line represent a ATC detector, counting one (R,G,B) triplet of crystals. The figures is adapted from Reference [103]. 47

2.3. AGATA technical drawings. Dimensions of the (R,G,B) types of the AGATA asymmetric crystals, composing an ATC detector. The figure is adapted from Reference [103]. 48

2.4. AGATA triple cluster detectors. (left) Drawing of an AGATA crystal with its electrical segmentation into 36 segments, 6 rings of 6 segments each. (right) AGATA detector with graphically-edited transparent end cap, showing the three HPGe encapsulated crystals and their electronics. Figure taken from Reference [104]. 49

2.5. During the experiment, the AGATA array was composed by 24 crystals and it was placed in compact configuration around the reaction chamber. 50

2.6. Comparison between the simulated signal shape (circles) and the measured one (solid line), obtained with ^{137}Cs source. The signals displayed in the different panels are the net charge signal of the segment on which the measure is focused and the 8 transient signals given by its 8 neighbour segments. Figure taken from Reference [106]. 51

2.7. Simulated traces for an AGATA detector: (top) the core signal for different radii and (bottom) the transient signals induced in a non-hit neighbouring segment. Colour code as indicated in the inset of the right graph. The slice is at 40.25 mm from the front of the detector. The figure is adapted from Reference [111]. 52

2.8. Interaction position resolution (W_p) as function of the γ-ray energy for different interaction mechanisms: photoelectric effect (blue), Compton scattering (red) and pair production (green). The error bars are due to statistical errors only. The figure is adapted from Reference [112]. 52

2.9. The relevant γ-ray interaction mechanisms in matter and the features exploited by the tracking algorithms. Figure taken from Reference [114]. . . . 54

2.10. Interaction positions and cluster identification in a 4π germanium shell as considered by the tracking algorithm. Figure taken form Reference [115]. . . 54

2.11. Schematic drawing of VAMOS. At the entrance of the spectrometer the dual position sensitive MWPC measures the direction of the recoils. This detector together with a MWPPAC placed at the focal plane measures the TOF of the fragments. The recoil position and direction at the focal plane are provided by the two DC. Just after the DC an IC is placed to measure the energy loss and total kinetic energy of the reaction products, which allows the identification of their atomic number. 56

2.12. (left) Schematic view of the dual position-sensitive multi-wire proportional counter (MWPC) placed as VAMOS entrance detector. In the inset the expansion of the three wire planes illustrating the wire plane orientation and spacings. (right) Front and back views of the detector assembly. Figure adapted from Reference [119]. 57

2.13. Schematic view of the VAMOS focal plane detection system, indicating the direction for increasing values of the magnetic rigidity Bρ. The picture has been adapted from Reference [118]. 58

2.14. Cologne plunger for deep-inelastic reactions: (left) design and (right) installation inside the reaction chamber. The green and red arrows represent the beam and recoils direction, respectively. The scheme on the left is taken from Reference [100]. 61

2.15. Recoil Distance Doppler-Shift method. After the reaction, the excited nucleus leaves the target with a velocity β_S. The fragment loses energy inside the degrader material, decreasing its velocity down to the velocity β_U, that is directly measured by the magnetic spectrometer and then used for correcting the Doppler shift. Because of the two different velocities of the fragments, for every γ-ray transition two components are present: the energy of the γ rays emitted after the degrader would be properly Doppler corrected, while the energy would be shifted at lower values for those emitted before the degrader. 62

3.1. Central contact energy as function of the segment and of the summed segments (SSg) energy for crystal 03A. This crystal has segment 12 (central pad) which is broken, so its charge is collected by the neighbouring segments (border pads). In addition, the SSg matrix (top-left pad) shows that the energy of the summed segments is lower than the CC energy (orange dashed line): indeed this HPGe has segment 02 that is lost. 67

3.2. Central contact energy as function of the energy of segment 05 for crystal 10C. Having a variable gain, this segment is unstable. 68

3.3. Central contact energy as function of the segment and of the summed segments (SSg) energy for crystal 12B. This crystal has segment 05 (central pad) which is broken, so its charge is collected by the neighbouring segments (border pads). In addition to that, segment 11 (central-top pad), which is one of the neighbouring, has unstable gain as it can be identified by the presence of three different structures. The comparison between the central contact and sum energy of the segments (top-left pad) shows the presence of the two issues: the several structures reveal the presence of a broken segment, while the unstable one entails the SSg energy to be lower than the CC energy (orange dashed line). 68

3.4. Comparison between different PSA grid search for the crystal 00C: hit pattern projection on xy-plane (top) and xz-plane (bottom). For *Random* grid the interaction position is a random point inside the firing segment. For *Adaptive* [110] and *AdaptiveTwoHits* grids the algorithm stops searching the interaction point, as soon as a minimum of χ^2 is found; moreover *AdaptiveTwoHits* accepts the contemporaneous presence of two hits in the same segment. For *Full* grid the interaction point is search inside the whole database. 70

3.5. Neutron damage correction of crystal 12C: the 1408 keV peak of ^{152}Eu, before (red) and after (black) the correction. Neutron damage induces defects inside the crystal lattice of the germanium detector, reducing the charge collection efficiency. These defects causes the presence of a tail on the lower energy part of the γ-ray peak. 71

3.6. AGATA relative efficiency as function of γ-ray energy without (blue) and with (red) tracking, measured with ^{152}Eu. In order to reduce the X-rays coming mostly from the beam and the target, 5 mm thick Cu absorbers were placed in front of the detectors. The comparison between the relative efficiency without (squares) and with (stars) the absorbers shows a decrease at energies below 400 keV. The efficiency curve without the tracking has been normalised to 1 for the 1408 keV transition energy. Taken from References [101, 131]. 73

3.7. Energy loss in IC-pad 02 (row A) as function of the validated time-stamp (VTS). Due to the gas pressure changing with the external temperature, the variation of ion energy loss can be observed. 75

3.8. Spectra of the central pads for the four different rows in the IC. The red area represents the events rejected in order to exclude pile up. 76

3.9. IC signals as function of the horizontal focal plane position: (left) raw signals after the time-alignment correction where also the lower and upper thresholds have been applied, (right) the signals after the gain matching. 77

3.10. Energy loss ΔE_{AB} in the first two IC rows as function of the total energy loss E_{TOT} (calibrated IC signal summed up the four rows). From the matrix the atomic number of the fragment will be defined. In the green-dashed rectangle a second structure is clearly visible and it is due to those events where the signal is missing from line A or line B. 78

3.11. Energy loss in the first two IC rows ΔE_{AB} as function of the total energy loss E_{TOT} (calibrated IC signal summed up the four rows), after requiring the trajectory conditions of Equation 3.3. 79

3.12. DC signals as function of each channel: (left) raw signals and (right) the signals after the gain matching. The fragments trajectory is reconstructed if at least two non-consecutive rows fire. 80

3.13. Schematic drawing of the drift chambers (DC) along the xz- (left) and yz-plane, showing trajectory requirement and focal plane coordinates reconstruction. The event is considered valid only if at least two non-consecutive DC rows fire. Then the focal plane position (x_f,y_f), the inclination angles in horizontal (θ_f) and vertical planes (ϕ_f) are extrapolated considering a straight trajectory of the ion. 81

3.14. Hit pattern of the first (left) and second (right) MWPC entrance detectors. . 82

3.15. Time alignment of the MWPPAC: per each pad of this focal plane detector an offset is added to the measured TOF. In order to be more sensitive in the procedure, the time alignment was done looking at the mass number over charge state (A/q) ratio as function of the focal plane horizontal position. The two graphs represent the A/q ratio before (top) and after (bottom) the alignment. 83

3.16. Amplitude of the induced tension signal as function of the motor positions. In order to calibrate the feedback system of the plunger, the calibration procedure was repeated ranging from the contact point (green-dashed line) up to the sensitivity limit of the device. 85

3.17. Inverse of the induced charge as function of the motor positions. For small target-degrader separation the trend is linear, so the position of the contact point ($1/Q(x) = 0$) can be extrapolated with a linear fit (red line). The plunger zero offset is given by the distance between the extrapolated and the measured contact point positions (green lines). Figure taken from Reference [101]. 85

4.1. Difference between the timestamp of AGATA ($TStrack$) and the VAMOS one (VTS) as a function of the ions TOF, showing all the events when a particle and a γ ray were detected in coincidence. In the timestamp difference it is possible to distinguish between the different bunches of the beam, delivered by the cyclotron with a period of ≈110 ns. In order to exclude random coincidences, a time condition (coloured in the plot) was set. 88

4.2. Energy loss in the first two IC rows (ΔE_{AB}) as function of the total energy loss E_{TOT}, showing the gates on the atomic number for all the identified ions. In the experiment the ^{106}Cd beam at the energy of 770 MeV impinged onto ^{92}Mo target, while ^{24}Mg foil was used as a degrader for the RDDS method. The beam-like ions were obtained by the reaction ^{106}Cd+^{92}Mo, while the nuclei in the Ni region were mostly produced in the ^{106}Cd+^{24}Mg reaction. . . 89

4.3. Energy loss in the first two IC rows (ΔE_{AB}) as function of the total energy loss E_{TOT}, focusing the attention on the beam-like fragments. The Z resolution was at the limit for the nuclei in this region. Especially difficult was the selection of the atomic number close to the overwhelming inelastic channels (i.e. $\pm 1p$ channels). 90

4.4. Charge states as function of the validated time-stamp (VTS). Even after correcting the energy loss fluctuations in the ionization chamber, the same time correction has to be set directly to the charge state. 91

4.5. Normalised yields of the charge states for the identified ^{106}Cd. The experimental values are compared with different empirical formulas: (green) Winger [139], (brown) Leon [140], (blue) Shima [141] and (purple) Schiwietz [142]. The empirical predictions were calculated by using LISE++ [143–146], considering the reaction products at focal plane. Measured and calculated yields are normalised setting the maximum value equal to 1. 92

4.6. Schematic draw of the focal-plane detection system along the xz-plane, showing in particular the IC Mylar window (red line) which is supported by the vertical nylon wires (black dots). Despite the presence of the wires, the Mylar foil is bent because of the different operating pressure of the DC and IC. By knowing the horizontal angle at the focal plane (see Figure 2.13), the reaction products energy loss can be corrected. 93

4.7. Atomic mass identification for the gate on $Z = 46$. (left) A/q spectra for the different charge states, showing in red the events that were rejected for reducing the background. (right-top) Calibrated mass as a function of the focal-plane horizontal position. The coloured region represents the 2D gates, while the grey-scale points are the rejected events. (right-bottom) Calibrated mass spectrum, showing in green the gates that were defined for the different atomic mass numbers. 95

4.8. Yields of the nuclei, identified by the VAMOS spectrometer in coincidence with AGATA, as a function of their proton and neutron numbers. The beam-like ions were obtained by the reaction of the ^{106}Cd beam with the ^{92}Mo target, while the nuclei in the Ni region were mostly produced by the ^{106}Cd impinging onto the ^{24}Mg degrader. The position of the beam and target nuclei are highlighted by the purple and blue circles, respectively. 96

4.9. Yields of the even-even beam-like nuclei as a function of their proton and neutron numbers. The yields were estimated from the efficiency-corrected peak area of the $2^+ \rightarrow 0^+_{g.s.}$ transition. 97

4.10. Normalised yield of the fusion-fission reaction of the ^{106}Cd beam with the ^{92}Mo target, calculated by the reaction code GEF [148]. In the simulation the compound nucleus ^{198}Th with the excitation energy $E_x = 120$ MeV were considered and secondary processes like particle evaporation were also added. In the graph the highest yield is normalised to 1. 98

4.11. Normalised yield of the MNT reaction of the ^{106}Cd beam impinging onto the ^{92}Mo target at the energy of 770 MeV. The calculation, performed with the reaction code GRAZING [147], was also considering secondary processes, such as particle evaporation. In the graph the highest yield is normalised to 1. 98

4.12. Total Kinetic Energy Loss (TKEL) distribution, obtained by gating on ^{108}Sn (red) and ^{104}Pd (blue). The two nuclei were populated via different reaction mechanisms and this affected the distribution of the TKEL. The distributions are normalised by scaling their maximum value to 1. 99

4.13. Gamma-ray energy spectrum for ^{60}Ni before (top) and after (bottom) performing the Doppler correction. The FWHM of the 1332 keV peak is 5.3 keV, which is just $\approx$ 30% higher than what had been obtained with radioactive sources. 100

4.14. Comparison between the reaction fragments velocity (blue) directly measured by VAMOS and (red) the energy-loss corrected one for the ^{106}Cd after the reaction. Because of the energy loss in such materials, the velocity that should be used for the Doppler correction is $\Delta\beta/\beta \approx 4\%$ larger than what was measured by the VAMOS spectrometer. 101

4.15. Schematic drawing of the experimental setup, showing the AGATA (red) and VAMOS (black) frames of reference. 102

4.16. Doppler-corrected γ-ray energy of ^{60}Ni as a function of the offset along the z-axis to the set position of AGATA. The optimal value of the offset is obtained by maximising the amplitude and improving the energy resolution of the peak at 1332 keV. From the procedure it results that the offset is -3.5 mm. 103

4.17. The major contribution to the Q-value uncertainty is given by the energy loss inside the target. (left) According to the position where the reaction takes place inside the target, the beam and the fragment lose energy differently. Then, considering that usually the reaction point in the target is unknown, the Q-value can be calculated under certain assumption: in the analysis, the reactions were supposed to take place in the middle of the target. (right) Inside the target both beam and reaction-fragment will straggle within the target. 104

4.18. Representation of a possible level-feeding pattern: the levels k populate the level of interest i, which deexcites via transitions to the levels h. Taken from Reference [100]. 106

4.19. Schematic drawing explaining the basics of the coincidence method. By gating on the shifted component of the feeder B, the transition of interest A would have both shifted and unshifted components; on the other hand, by gating on B_u, all the A-transition γ rays would be emitted after the degrader. Adapted from Reference [100]. 107

5.1. Doppler-corrected γ-ray energy spectrum, obtained gating on ^{106}Cd, for all the plunger distances. The most intense transitions of both ^{106}Cd and ^{92}Mo are identified and labelled. 112

5.2. Prompt Doppler-corrected γ-γ matrix for ^{106}Cd for all the plunger distances. By gating on a certain transition it is possible to observe the γ rays detected inside a coincidence time window of 6 ns and then determine the partial level scheme of the populated nuclei. 113

5.3. Lifetime measurement of the ^{106}Cd first 2^+ state via the coincidence procedure, performed by gating on the shifted component of the $4^+_1 \rightarrow 2^+_1$ transition. (left) Normalised area as function of the target-degrader distances for the $2^+_1 \rightarrow 0^+_{g.s.}$ transition, showing (red line) the fitting function used for the Decay Curve Method. (right) Lifetime of the 2^+ state as function of the target-degrader distances, obtained via the Differential Decay Curve Method: the solid line represents the average value, the dashed lines are the corresponding error bars and the grey area marks the region outside the sensitivity of DDCM. The final results are summarized for the two methods in Table 5.1. 113

5.4. (left) Doppler-corrected γ-ray energy spectrum gated on ^{104}Cd for all the plunger distances. The spectrum is compared with the one obtained by gating on the Q-value (green). For graphical reasons, the statistics of the Q-value gated spectrum is multiplied by a factor 5. Despite the clear mass identification, contamination (red) from the inelastic-scattered ^{106}Cd beam is still present. All the identified transitions of the beam-like ion are shown and (right) reported in the level scheme of the ^{104}Cd. 115

5.5. Doppler-corrected γ-ray energy spectrum for ^{104}Cd, gating on the Q-value for reducing the feeding from high-spin transitions (see text). For the three distances the lowest-lying transitions are shown (blue): the feeding from the states above the 4^+ state is practically negligible. Despite of the additional constraint on the reconstructed Q-value, there are still ^{106}Cd contaminations (red). 116

5.6. Normalised unshifted area as function of the target-degrader distance for (left) $4^+_1 \rightarrow 2^+_1$ and (right) $2^+_1 \rightarrow 0^+_{g.s.}$, showing (red line) the fitting function used for the Decay Curve Method. The area is normalised to the sum of shifted and unshifted areas. The obtained lifetimes are $\tau_{eff}(4^+) = 3.0(3)$ ps and $\tau(2^+) = 8.0(5)$ ps. 116

5.7. Inelastic-scattered beam contamination in the Sn isotopic chain. (left) Fragments total energy (E_{TOT}) as function of the γ-ray Doppler-corrected energy, requiring the $Z = 50$ identification: the $2^+ \rightarrow 0^+$ transition of ^{106}Cd indicates that is possible to reduce the contamination by requiring the condition (dashed red line) $E_{TOT} < 500$MeV. (right) Mass spectrum of the Sn isotopic chain with (blue) and without (red) the condition for reducing the ^{106}Cd contamination: the peaks related to ^{106,109}Sn have a sensible reduction, while the rest of the statistics remains practically untouched. 118

5.8. (left) Doppler-corrected γ-ray energy spectrum in coincidence with ^{108}Sn, summed for all the plunger distances. All the identified transitions are reported in the level scheme of ^{108}Sn (right). 120

5.9. Doppler-corrected γ-ray energy spectrum for ^{108}Sn, after gating on the Q-value to reduce the feeding from high-spin states (see text). For each plunger distance the $4^+ \rightarrow 2^+$ (blue lines show the centroids) and $2^+ \rightarrow 0^+$ (red lines show the centroids) transitions are shown, presenting for both of them the shifted (dashed) and unshifted (solid) components. 121

5.10. Normalised area as function of the target-degrader distances for the $4^+ \to 2^+$ (left) and $2^+ \to 0^+$ (right) transitions, obtained from the spectra of Figure 5.9. The lifetimes $\tau(4^+) = 3.6(5)$ ps and $\tau(2^+) = 0.76(8)$ ps are extracted from the fitting curve (solid red) via the Decay Curve Method (DCM). 122

5.11. Lifetime measurement of the first (left) 4^+ and (right) 2^+ state in ^{108}Sn as function of the target-degrader distance, obtained via the Differential Decay Curve Method: the solid line represents the fitting function, while the dashed ones are the error bars. The lifetimes result to be $\tau(4^+) = 3.67(12)$ and $\tau(2^+) = 0.7(2)$ ps. In the graphs the points in the method sensitive region are shown. 122

5.12. Distribution of the 4^+ state lifetime, obtained simulating the peak area of the 6^+ isomeric state and then performing the measurement via DDCM. The green solid line represent the mean value of the distribution. The resulting lifetime is $\tau(4^+) = 3.7(2)$ ps. 123

5.13. (left) Doppler-corrected γ-ray energy spectrum for ^{106}Sn for all the plunger distances. Despite the constraint on the fragments total energy (E_{TOT}), contaminations from the inelastic-scattered ^{106}Cd beam (red) and In isotopes (orange) are still present. All the identified transitions belonging to ^{106}Sn are shown and reported in the level scheme (right). 125

5.14. Normalised area as function of the target-degrader distances for the $2^+ \to 0^+$ transition. The lifetimes $\tau(4^+) = 5.2(39)$ ps and $\tau(2^+) = 1.3(7)$ ps are extracted from the fitting curve (solid red) via the Decay Curve Method (DCM). 126

5.15. Level scheme of the ^{107}Sn reported by Ishii *et al.* in Reference [166], showing the neutron-coupled and the negative parity bands. 127

5.16. Part of the ^{109}Sn level scheme reported by Käubler *et al.* in Reference [169], showing the high-spin structures of 5 different bands. 127

5.17. Doppler-corrected γ-ray energy spectrum for ^{107}Sn, summing up all the statistics. No contamination from ^{106}Cd beam are present, but several peaks due to ^{107}In transitions (orange) are observed. When the assignment was possible, the identified transitions of the beam-like ion are shown. 128

5.18. Doppler-corrected γ-ray energy spectrum for ^{109}Sn, summing up all the statistics. Despite the constraint on the fragments total energy (E_{TOT}), contamination (red) from the inelastic-scattered ^{106}Cd beam is still present; in addition also contamination (orange) from ^{109}In are visible. When the assignment was possible, the identified transitions of the beam-like ion are shown. 128

6.1. Reduced transition probability $B(E2)$ systematics along the Sn isotopic chain for (top) $4^+ \to 2^+$ and (bottom) $2^+ \to 0^+$ transitions. The results discussed in this thesis (black dots) are compared with previous experiments. The "adopted" results for the neutron-rich isotopes are taken from Reference [2], while for the neutron-deficient region the results are taken from References [81, 83–93]. 130

6.2. Comparison between the experimental low-lying states in ^{106,108}Sn with LSSM calculations, obtained with SnETMod [171] and Z50BonnC [172] interactions. In the calculations, ^{100}Sn was defined as core and the neutrons model space consisted of the $1d_{5/2}$, $0g_{7/2}$, $1d_{3/2}$, $2s_{1/2}$ and $0h_{11/2}$ orbitals. 131

6.3. Calculated proton Effective Single-Particle Energies (ESPE) as a function of the neutron number. The LSSM predictions were obtained considering the ^{90}Zr closed-shell core (see text). Figure taken from Reference [83]. 133

6.4. Comparison of the measured $B(E2; 2^+ \to 0^+)$ values with LSSM predictions, considering ^{90}Zr as closed-shell core (see text). The results discussed in this thesis (black dots) are compared with previous experiments: the "adopted" results for the neutron-rich isotopes are taken from Reference [2], while for the neutron-deficient region the results are taken from References [81, 83–93]. The LSSM predictions are taken from Reference [83]. 133

6.5. Experimental $B(E2)$ values for the $4^+ \to 2^+$ and $2^+ \to 0^+$ transitions together with LSSM predictions, considering a ^{80}Zr closed-shell core (see text). The results discussed in this thesis (black dots) are compared with previous experiments: the "adopted" results for the neutron-rich isotopes are taken from Reference [2], while for the neutron-deficient region the results are taken from References [81, 83–93]. The different lines represent the LSSM calculations: the solid line represents the $B(E2)$ prediction obtained from the seniority truncation $v \leq 8$, while the dashed lines are the theoretical results where no seniority truncation has been considered and three different sets of effective charges are used. 135

6.6. Relative occupation numbers of protons (top) and neutrons (bottom) for the 0^+, 2^+ and 4^+ states of ^{106,108}Sn, given with respect to the occupation numbers of ^{106}Sn (left), i.e. $\pi : (g_{9/2})^{10}(d_{5/2})^0(g_{7/2})^0(d_{3/2})^0(s_{1/2})^0$, $\nu : (g_{9/2})^{10}(d_{5/2})^6(g_{7/2})^0(d_{3/2})^0(s_{1/2})^0(h_{11/2})^0$, and to the ones of ^{108}Sn (right), i.e. $\pi : (g_{9/2})^{10}(d_{5/2})^0(g_{7/2})^0(d_{3/2})^0(s_{1/2})^0$, $\nu : (g_{9/2})^{10}(d_{5/2})^6(g_{7/2})^2(d_{3/2})^0(s_{1/2})^0(h_{11/2})^0$. The theoretical predictions are given by the LSSM calculations, considering a ^{80}Zr core. The hatched colors represents the full-seniority predictions, while the solid ones are given by the truncated seniority calculation. 139

7.1. P70 proton cyclotron at the Laboratori Nazionali di Legnaro for the SPES project. The primary proton beam will be accelerated up to the energy of 70 MeV and impinge onto a uranium carbide target, producing several exotic species via proton-induced fission; then, the radioactive nuclei will be reaccelerated by the ALPI super-conductive radio-frequency linear accelerator up to an energy of about 10 MeV/A, to be delivered to the experimental apparata. Taken from Reference [183]. 143

7.2. GRAZING code calculations for the production cross sections of target-like nuclei in multi-nucleon transfer reactions as a function of transferred protons and neutrons. The results refer to the collision of Rb isotopes on ^{208}Pb at energies about 20% above the nominal Coulomb barrier. The panels correspond to the heavy binary partner in the reactions: from the top they are ^{76}Rb+^{208}Pb, ^{87}Rb+^{208}Pb, ^{94}Rb+^{208}Pb and ^{98}Rb+^{208}Pb. Taken from Reference [193]. 144

A.1. Comparison between (left) direct and (right) inverse kinematics for ^{106}Cd+^{92}Mo, fixing $E_i^{c.m.} = 351.5$ MeV. Both ^{108}Sn (red) and its binary partner ^{90}Zr (blue) fly in the direction of the spectrometer. However, for inverse kinematics the ^{108}Sn fragments have the energy that is $\approx$100 MeV higher than the one produced in the direct reaction, providing a better identification at the ionization chamber. The VAMOS angular acceptance is highlighted in green, placing the spectrometer at the grazing angle. 149

A.2. Total Kinetic Energy Loss (TKEL) as function of the target thickness, simulated for the central trajectory (red) and taking into account the VAMOS angular acceptance (blue). The TKEL dispersion is estimated considering the difference between the maximum and minimum values. The green dashed lines represent the chosen thickness for the experiment. 150

A.3. Beam (red) and degrader (blue) energy as function of the ion angle with respect to the beam-line direction, showing the VAMOS angular acceptance (gree). By using 2.9 mg/cm^2 of ^{93}Nb (top) and 2.3 mg/cm^2 of ^{45}Sc (middle), both beam and degrader ions reach the entrance MWPC; on the other hand, using 1.95 mg/cm^2 of ^{24}Mg, only degrader ions reach the spectrometer but at the same time their velocity would be very different from the beam-like one, allowing to reject the whole VAMOS event. The kinematics of the reaction is simulated with the software LISE++. 152

A.4. Recoil velocity difference as function of the ^{24}Mg degrader thickness. The y-axis on the right shows the minimum energy separation between the two components for the transition $2^+ \rightarrow 0^+$ of ^{108}Sn, taking into account the compact configuration of AGATA. 153

B.1. Tracking optimisation for OFT algorithm: SigmaTheta. (left) Peak-to-Total ratio (P/T) and (right) tracking efficiency as function of SigmaTheta for several combinations of the other two parameters. The tracking efficiency is defined as the ratio between the area measured with the tracking and the one without the tracking. Both P/T and efficiency are estimated at (top) 121 keV transition of ^{152}Eu and (bottom) 1332 keV of ^{60}Co. The green dashed line represents the optimal value of the parameter, chosen at the beginning of the plateau of both P/T and tracking efficiency. 156

B.2. Tracking optimisation for OFT algorithm: MinProbSing. (left) Peak-to-Total ratio (P/T) and (right) tracking efficiency as function of MinProbSing for several combinations of the other two parameters. The tracking efficiency is defined as the ratio between the area measured with the tracking and the one without the tracking. Both P/T and efficiency are estimated at (top) 121 keV transition of ^{152}Eu and (bottom) 1332 keV of ^{60}Co. The green dashed line represents the optimal value of the parameter, chosen at the maximum tracking efficiency. 157

B.3. Tracking optimisation for OFT algorithm: MinProbTrack. (left) Peak-to-Total ratio (P/T) and (right) tracking efficiency as function of MinProbTrack for several combinations of the other two parameters. The tracking efficiency is defined as the ratio between the area measured with the tracking and the one without the tracking. Both P/T and efficiency are estimated at (top) 121 keV transition of ^{152}Eu and (bottom) 1332 keV of ^{60}Co. The green dashed line represents the optimal value of the parameter. 158

List of Tables

1.1. Electromagnetic transition rates. The transition probabilities T are in s^{-1}, the energies E are in MeV, $B(EL)$ in $\mathrm{e}^2\mathrm{fm}^{2L}$ and $B(ML)$ in $\mu_N^2\mathrm{fm}^{2L-2}$. . . . 32

2.1. Optimal features of VAMOS for mass-dispersive mode operation 55
2.2. Nominal performances of the MWPC detector. 57

3.1. Comparison between the FWHM of the sum energy of all the segments before and after the neutron damage correction, measured at 1408 keV peak of ^{152}Eu. Only those detectors that needed the correction are reported in the table. 72
3.2. The OFT algorithm depends on 3 empirical parameters that can be chosen following the requirements of the experiment: the reported values are optimised for the 1332 keV transition of the ^{60}Co source. 73
3.3. Nominal plunger positions and absolute target-degrader distances with their errors. The statistical error is the root mean square of the fluctuation of the foils separation with respect to the nominal position. The total error has the contributions from the statistical error and the systematic error. 86

5.1. Lifetime of the 2_1^+ state of ^{106}Cd: the results obtained via the DCM and DDCM are compared to the literature adopted value [157]. 114
5.2. Comparison between the measured lifetime of both 2_1^+ and 4_1^+ states in ^{104}Cd with results reported in literature. Results ^{a} are taken from [159] and ^{b} come from [158]. 117
5.3. Direct feeding measured from the γ-ray spectra of Figure 5.9. 119
5.4. Direct feeding measured from the γ-ray spectra of Figure 5.13. 124

6.1. Reduced transition probabilities for the low-lying $2^+ \to 0^+$ and $4^+ \to 2^+$ transitions of ^{106,108}Sn. The values, extracted from the lifetimes measured in this work, are shown together with those obtained via Coulomb excitation measurement [81, 83, 84, 86]. The results are reported in e^2fm^4. 130

6.2. Reduced transition probabilities for the low-lying $2^+ \rightarrow 0^+$ and $4^+ \rightarrow 2^+$ transitions in ^{106,108}Sn, calculated with the SnETMod [171] and Z50BonnC [172] interactions. In the calculations, the core was ^{100}Sn and the neutrons model space consisted of $g_{7/2}dsh_{11/2}$ orbitals. The results are given in units of e^2fm^4. 132

A.1. The experimental setup was optimised to populate ^{108}Sn isotopes, which correspond to the $+2p-2n$ channels of the proposed multi-nucleon transfer reaction: the beam, target and degrader combination was carefully chosen after simulations. 148
A.2. Ground-state to ground-state Q-value for multi-nucleon transfer reaction, populating the $+2p$ and $+2p-2n$ channels that correspond to ^{108}Sn and ^{106}Sn, respectively. The values are reported for the different target-material options. 148
A.3. Optimum Q-value for different target material, estimated via Equation A.1. . 149